UNIVERSITÀ DEGLI STUDI DI TRIESTE

UNIVERSITÀ DEGLI STUDI DI TRIESTE

XXXIV CICLO DEL DOTTORATO DI RICERCA IN NANOTECNOLOGIE

Carbon nanodots and molecular machines as bottom-up approaches to nanotechnology

Settore scientifico-disciplinare: **CHIM/06**

DOTTORANDO
SIMONE DI NOJA

COORDINATORE
PROF. ALBERTO MORGANTE

SUPERVISORE DI TESI
PROF. MAURIZIO PRATO

CO-SUPERVISORE DI TESI
DR. GIULIO RAGAZZON

ANNO ACCADEMICO 2020/2021

Summary

Summary **3**

Abbreviations **5**

Abstract **7**

Riassunto **9**

Chapter 1 Nanotechnology: an overview **12**

1.1 Top-down approach 13

1.2 Bottom-up approach 14

1.3 Carbon nanomaterials 17

1.4 Carbon nanodots 18

1.5 Bottom-up pathways for amino-functionalized CNDs 19

1.6 Supramolecular chemistry 22

1.7 Molecular machines and devices 23

1.8 Artificial molecular machines 25

1.9 Energetically-demading transport 29

Chapter 2 Transfer of axial chirality endows carbon nanodots with circularly polarized luminescence **35**

2.1 Introduction 35

2.2 Results and Discussion 36
2.2.1 Synthesis and characterization of CNDs-1 36
2.2.2 Synthesis and characterization of CNDs-2 41

2.3 Conclusions 51

2.4 Experimental section 52
2.4.1 General information 52
2.4.2 Synthetic details, characterization and collection of spectra 54
Synthesis of CNDs-*S*-1 and CNDs-*R*-1 54
Survey of synthetic parameters for CNDs-2 57

Size exclusion chromatography analysis of CNDs-*S*-2 58
Characterization of CNDs-*R*-2 59
Synthesis of CNDs in absence of chiral diamine 60

Chapter 3 Control on dissipative kinetics enhances the functionality of a minimal molecular machine 62

3.1 Introduction 63

3.2 Results and discussion 65

3.3 Conclusions 78

3.4 Experimental section 78
3.4.1 General information 78
3.4.2 General method for chemically fueled operations with asymmetric axle 1bH^+ 79
3.4.3 Synthetic details, characterization and collection of spectra 80
Synthesis of symmetric axle 1a$H^+PF_6^-$ 80
Synthesis of asymmetric axle 1b $H^+PF_6^-$ 89

Conclusions 116

References 118

Ringraziamenti 132

Abbreviations

AFM	Atomic force microscopy
Arg	*L*-Arginine
aq.	Aqueous
ATP	Adenosine triphosphate
ATR	Attenuated total reflectance
Boc_2O	Di-tert-butyl dicarbonate
$CBPQT^{4+}$	Cyclobis(paraquat-p-phenylene)
CHX	Cyclohexane
CNMs	Carbon-based nanomaterials
CNDs	Carbon nanodots
CNTs	Carbon nanotubes
CPL	Circularly polarized luminescence
DB24C8	Dibenzo-24-crown-8
DCM	Dichloromethane
DMF	*N*,*N*-dimethyl formamide
DMSO	Dimethyl sulfoxide
ECD	Electronic circular dichroism
EDA	Ethylene diamine
EDTA	Ethylenediaminetetraacetic acid
eq.	Equivalents
FTIR	Fourier-transform infrared spectroscopy
g_{abs}	Absorption dissymmetry factor
g_{lum}	Luminescence dissymmetry factor
HRMS	High resolution mass spectrometry
IPCA	5-oxo-1,2,3,5-tetrahydroimidazo[1,2-α]pyridine-7-carboxylic acid

MeOH	Methanol
MIMs	Mechanically interlocked molecules
MW	Microwave
N-CNDs	Nitrogen-doped carbon nanodots
NDA	Naphthalene dianhydride
P_1-*t*-Bu	P_1-*t*-Bu-tris(tetramethylene)
PE	Petroleum ether
PS	Photosensitizer
QY	Quantum yield
r.t.	room temperature
SEC	Size exclusion chromatography
τ_C	Correlation lifetime
τ	Emission lifetime
TCA	Trichloroacetic acid
TFA	Trifluoroacetic acid
TfOH	Trifluoromethane sulfonic acid or triflic acid
TLC	Thin layer chromatography
TEM	Transmission electron microscopy
THF	Tetrahydrofuran
TsCl	Tosyl chloride
UV	Ultraviolet
UV-Vis	UV-Visible
XPS	X-ray photoelectron spectroscopy

Abstract

The field of nanotechnology, a broad discipline committed to the design, control and manipulation of matter at the nanoscale, has advanced tremendously in the last decades. The final goal of nanotechnology is the development of novel materials, possessing at least one dimension between 1-100 nm. The controlled manipulation of materials at the nanoscale allows conveying new features, which can be dramatically different from those of their corresponding bulk counterparts. Two strategies can be adopted for the fabrication of nanomaterials. Top-down approach consists in the miniaturization of larger materials into nanomaterials; while bottom-up method relies on controlled reactions of atoms and molecular precursors to assemble complex nanomaterials. Interest in the latter strategy is growing due to the possibility to fabricate tailored nanomaterials with fine-tuned properties from molecularly engineered "building blocks".

The *fil rouge* of this thesis is the use of a rational bottom-up approach to build novel structures at the nanoscale, using two different strategies: a traditional bottom-up approach to obtain materials with nanometric dimensions, and a supramolecular-based approach to build molecular systems performing tasks at the nanoscale.

Chapter 1 provides, initially, a general overview of nanotechnology and of respective top-down and bottom-up strategy. An emphasis on the bottom-up methods will be given. After, the synthetic bottom-up approaches for the synthesis of carbon nanomaterials, and in particular carbon nanodots, will be described, and some notable examples will be discussed. Lastly, a complementary approach to the fabrication of nanomaterials will be described, based on supramolecular chemistry. A considerable attention will be given to the synthesis and functioning of one of the most common family of systems used in this domain: artificial molecular machines. Through some specific examples, their operation will also be discussed.

Chapter 2 presents the synthesis, purification, and characterization of a family of atropoisomeric carbon nanodots, *via* bottom-up microwave-assisted method. Contrary to other hydrophilic carbon nanodots, these nanoparticles display solubility in organic solvents. Depending on the chirality of the enantiomer employed, these chiral particles show specular profile in the UV-Visible region, as detected by electronic circular dichroism. Remarkably, one class of these carbon nanodots shows circularly polarized luminescence. Contrary to the literature precedents on carbon nanodots, this advanced optical property is observed in solution, without needing any chiral external matrix. As evidenced by morphological and chiroptical experiments, the axial chirality is

transferred from molecular to the nanoscale. In this way, this property is directly encoded within nanomaterial structure, without the need for post-functionalization steps.

Chapter 3 presents the synthesis and characterization of a symmetric and an asymmetric molecular axle. Both bear a recognition site for a macrocycle, allowing the formation of pseudorotaxane. Its terminal part can be dynamically stoppered, gaining control on the pseudorotaxane formation. The threading/dethreading operation in response to acid-base inputs was studied, confirming machine operation according to a ratchet mechanism, leading to the energetically-demanding trapping of the macrocycle in a high-energy state. The peculiar choice of molecular stopper allowed controlling the dethreading kinetics, ranging from obtaining kinetically-trapped out-of-equilibrium state to rapid equilibration. The solvent in which the operation occurs is fundamental in controlling the dethreading kinetics. Tuning this parameter, the machine can experience either a rapid equilibration or an observable dissipative relaxation, revealing the directional exploration of a square reaction network underlying machine operation, which can be repeated multiple times *in situ*.

Riassunto

Il campo della nanotecnologia, un'ampia disciplina impegnata nella progettazione, controllo e manipolazione della materia alla scala del nanometro, è progredito enormemente negli ultimi decenni. L'obiettivo finale della nanotecnologia è lo sviluppo di nuovi materiali, che devono possedere almeno una dimensione compresa tra 1 e 100 nm. La manipolazione controllata e precisa dei materiali su scala nanometrica consente di donare nuove caratteristiche ai nanomateriali, che possono essere notevolmente diverse da quelle delle loro corrispondenti controparti bulk. Due diverse strategie possono essere adottate per la fabbricazione di nanomateriali. L'approccio top-down consiste nella miniaturizzazione di materiali *bulk* in nanomateriali; mentre il metodo bottom-up si basa su reazioni controllate di singoli atomi, precursori molecolari e macromolecolari per assemblarli in nanomateriali complessi. L'interesse per quest'ultima strategia sta crescendo a causa di numerosi vantaggi, tra tutti la messa a punto di nanomateriali con proprietà su misura, da "mattoncini" ingegnerizzati a livello molecolare.

Il *fil rouge* di questa tesi è l'uso di un approccio razionale bottom-up per costruire nuove strutture su scala nanometrica, utilizzando due diversi tipi di strategie basate su questo tipo di metodo: un approccio tradizionale bottom-up per ottenere materiali con dimensioni nanometriche e un approccio supramolecolare per costruire sistemi molecolari che compiono una funzione su scala nanometrica.

Il *Capitolo 1*, in una prima parte, fornisce una panoramica generale delle nanotecnologie e i suoi due rispettivi approcci ad essa: la strategia top-down e la strategia bottom-up. Particolare enfasi sarà data ai metodi bottom-up. Nella seconda sezione verranno descritti gli approcci sintetici bottom-up per la sintesi di nanomateriali di carbonio, ed in particolare di nanodots di carbonio. Nella terza sezione verrà descritto un altro tipo di approccio alla fabbricazione di nanomateriali, basato sulla chimica supramolecolare. Una notevole attenzione sarà rivolta alla sintesi e al funzionamento di uno dei più comuni sistemi molecolari utilizzati in questa classe: le macchine molecolari artificiali. Verrà anche discusso il loro funzionamento attraverso alcuni esempi specifici.

Il *Capitolo 2* mostra la sintesi, la purificazione e la caratterizzazione di una famiglia di nanodots di carbonio atropoisomerici, ottenuti utilizzando un metodo bottom-up assistito da microonde. Al contrario di altri nanodots di carbonio idrofilici, queste nanoparticelle mostrano solubilità in solventi organici. Inoltre, a seconda della chiralità dell'enantiomero impiegato, i nanodots mostrano uno spettro speculare nella regione UV-Visibile, come rilevato dal dicroismo circolare elettronico. Sorprendentemente, una

classe di questi nanodots di carbonio mostra luminescenza circolarmente polarizzata. A differenza di altri nanodots riportati in letteratura, questa proprietà ottica avanzata è osservata in soluzione, senza l'utilizzo di alcuna matrice chirale. Come evidenziato da esperimenti morfologici e chirottici, la chiralità assiale viene trasferita da molecolare a nanoscala. In questo modo, questa proprietà viene codificata direttamente all'interno della struttura del nanomateriale, senza ulteriori passaggi di post-funzionalizzazione.

Il *Capitolo 3* mostra la sintesi e la caratterizzazione di un asse molecolare simmetrico e di uno asimmetrico. Entrambi possiedono un sito di riconoscimento per un macro ciclo etere corona, che consente la formazione di pseudorotassani. La parte terminale dell'asse può essere bloccata dinamicamente, ottenendo il controllo sulla formazione dello pseudorotassano. È stata studiata l'operazione di infilamento/sfilamento in risposta a stimoli acido-base, confermando il funzionamento della macchina secondo il cosiddetto meccanismo di *ratchet*, che conduce all'intrappolamento dell'anello in uno stato ad alta energia. La scelta peculiare del frammento molecolare dell'estremità ha mostrato la possibilità di controllare la cinetica di sfilamento, potendo passare da uno stato fuori dall'equilibrio cineticamente intrappolato fino a un equilibrio rapido. È importante sottolineare che il solvente in cui avviene l'operazione è di fondamentale importanza nel controllo della cinetica di sfilamento. Modificando questo parametro, la macchina può raggiungere un rapido equilibrio oppure può dare un rilassamento dissipativo, che conferma un network di reazione che opera in modo direzionale alla base del funzionamento della macchina, che può essere ripetuta più volte *in situ*.

Chapter 1

Nanotechnology: an overview[1]

Nanotechnology is an intersectorial discipline rooted in the fields of physics, chemistry, biology, medicine, and engineering. The principal aim of this branch of science is to develop and fabricate new materials at the nanoscale (with at least one dimension in the size range of about 1-100 nm), in order to perform defined tasks. These new (nano)materials can be assembled from individual atoms, distinct molecules and also macromolecular building blocks; besides, nanostructures can also be obtained by breaking down (*i.e.* ablating, cutting, edging) bulk materials up to structures at the nanoscale.

The controlled and precise manipulation of nanomaterials both at the atomic and molecular level, allows conveying novel properties and features, which can be dramatically different from those of their corresponding bulk counterparts, *e.g.*, thermal, electrical, mechanical properties. For this reason, in the last decades, the interest in the field of nanotechnology has kept increasing. From an academic point of view, nanotechnological investigations help to better understand several phenomena that occur in the gap between atoms and bulk materials. Besides, the vast and versatile library of nanomaterials that is being explored has the potential to find solutions to several urgent problems related to, *e.g.*, healthcare, energy storage, environment and many others.[1] This goal can be accomplished also because nanomaterials have witnessed a deep evolution, gaining more and more complexity.[2] Nanomaterials can be divided into different families. Historically, we can distinguish four generations.[3] The first and the second generation consist respectively of passive and active nanostructures. Within the first category, coatings and additives usually used in paints are found. These materials are also used in cosmetic applications. The second generation involves, for instance, electronic devices, sensors, drugs, and chemical delivery systems. The third generation is based on nanosystems in which multiple nanomaterials are assembled to complementarily exploit their properties in the new hybrids. Finally, the fourth generation consists of heterogeneous molecular nanosystems, where every component is engineered at the molecular level in order to *ad hoc* display specific features.[2] The fabrication of objects and materials at the nanoscale can be accomplished through two different approaches:[4–6]

[1] This chapter is partially adapted from Garrido, M., Gualandi, L., Di Noja, S., Filippini, G., Bosi, S., Prato, M. Synthesis and applications of amino-functionalized carbon nanomaterials. *Chem. Commun.*, **2020**, 56, 12698-12716 with permission from the Royal Society of Chemistry.

- Top-down approach: nanomaterials and nanostructures can be realized after a miniaturization process of large and bulk materials, until the desired shape and dimensions are obtained
- Bottom-up approach: nanomaterials and nanostructures can be achieved using atoms or molecules precursors as tiny bricks.

1.1 Top-down approach

The top-down approach for the fabrication of nanomaterials consists in processes involving the miniaturization of bulk materials, in order to reproduce tailored defined structures at the nanoscale.
Top-down strategy is the most common method employed by scientists to tune and engineer microscale and larger scale systems in an arbitrary fashion.[7] A prominent example is the fabrication of refined microelectronic chips and integrated circuits, where the patterning does not rely on a previous self-assembly process. Among the various processes, lithography is the most exploited technique to obtain such nanostructures. Lithography is named photolithography when optical sources – ultraviolet (UV) light up to X-rays – are employed, accessing nanomaterials with dimensions ranging from 100 to 10 nm; otherwise, smaller dimensions can be accessed by scanning-beam lithography, exploiting electrons or ions, reaching defined patterns with dimensions smaller than 10 nm.[8] A well-known example of the potential of this approach is depicted in Figure 1.1, displaying a bull in miniature modelled by photopolymerization.[9]

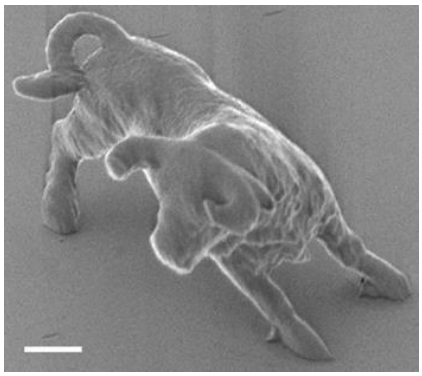

Figure 1.1. Scanning electron micrograph of a bull in miniature, mould on the microscale, obtained via *top-down* approach. Republished with permission of *Nature* from "Finer features for functional microdevices", Kawata S. *et al.*, 412, **2001**; permission conveyed through Copyright Clearance Center, Inc.

Other techniques can involve the use of mechanically printed molds, made of polymers or metals. In this case, specific portions of these molds can be removed selectively by plasma etching technique. While top-down approaches give access to several advantages in the case of refined nanostructures, they also have some drawbacks.

Firstly, the fabrication of nanomaterials with these techniques becomes challenging as the dimensions become smaller. Secondly, the nanomaterials are created by addition and subtraction of patterned structures, leading to a large amount of waste. Thirdly, top-down-based nanomaterials are often prepared in clean rooms and specialized laboratories, increasing the cost of the whole process. These disadvantages are a limitation to the use top-down approach for the fabrication of architectures at the nanoscale.[10]

1.2 Bottom-up approach

The bottom-up approach for the synthesis of nanomaterials consists in the manipulation of atoms and molecules to realize structures at the nanoscale. Molecules can be considered as the smallest bricks existing.[11] Importantly, researchers can engineer these molecular building blocks in order to control their self-assembly in a specific manner and consequently to build nanomaterials building unit-by-building unit. Indeed, as Prof. Richard Feynman said: *"when we have some control of the arrangement of things on a molecular scale, we will get an enormously greater range of possible properties that substances can have"*.[12] As a matter of fact, downsizing a material to the nanoscale can convey new and tailored properties to the final nanostructure. Compared to top-down approaches, bottom-up methods present several advantages. Bottom-up strategy can afford materials with high accuracy with respect to top-down approach, due to a higher control over the dimensions of the obtained products. Moreover, the wasted by-products are fewer with respect to the nanostructures fabricated with top-down methods. Besides, the produced nanomaterials can be also embedded in bulk materials in a straightforward manner. Lastly, bottom-up strategies are an easy way approach to nanotechnology, for the reason that either clean rooms or expensive instruments are not necessary, but are simply needed molecules in solutions, which are routinely used in the vast majority of wet chemistry laboratories. These advantages have positively favoured the investigation of bottom-up nanomaterials, opening them up to new fields of applications.[10,13]

From a chemical perspective, bottom-up strategies for nanotechnology represent a mix of materials chemistry with organic and inorganic chemistry. Among nanomaterials made with bottom-up strategy, the simplest ones are nanoparticles and nanocrystals. This kind of nanostructures are simply made from molecules reacting together to form a new chemical species, where their final properties are encoded within the molecular structure of the precursors employed. Moreover, also the surface of the nanomaterials can be modified and engineered in turn, endowing the final nanomaterial with new features. Remarkably, these characteristics can be dramatically different from the ones present in their corresponding bulk materials, paving the way to a number of new applications. Although atoms could also be employed, the vast majority of nanostructures are built from (macro)molecules, predominantly due to their chemical

stability. Moreover, molecules are useful elementary units because they can be handled in an easier way in research laboratories, compared to atoms. Besides, the structure of the molecules – and consequently their physico-chemical properties – can be engineered to build larger structures, either by covalent interactions or by self-assembling processes.

In the field of bottom-up approach, two different "philosophies" can be encountered. The first strategy relies on the reaction of molecular species in order to fabricate nanomaterials with increased size, put together with strong covalent bonds. The step from the molecular to the nanoscale results in nanostructures retaining molecular features, but also possessing new functionalities. This kind of approach is extremely versatile, due to the possibility to tune the structure of the starting molecular precursors through small changes, unlocking a number of diverse applications. Finally, for practical applications, these nanomaterials can also be included into solid-state matrices, retaining or even improving the nanomaterial (their) features[14] (Figure 1.2). Carbon-based nanomaterials (CNMs) represent a widely studied class of nanomaterials obtained with this approach. Among CNMs, carbon nanodots (CNDs) have attracted the interest of the scientific community due to their unusual properties, *e.g.* their simple synthesis, their straightforward solubility in a number of solvents, their photoluminescence, and their fine-tuned properties. The possibility to engineer CNDs, endowing them with novel features, will be discussed in *Chapter 1.3-1.5* and *2*. Usually, the uniqueness of this kind of nanomaterials relies in properties such as their exotic morphologies, uncommon electrical and mechanical features, rare photophysical features, etc. Nonetheless, with this strategy the dimensions of the nanomaterials often cover a broad distribution, hampering the possibility of using them in practical applications requiring high levels of structural control. Besides, this kind of nanostructures lack in performing complex tasks, such as transport,[15] extension/contraction,[16] synthesis,[17] etc.
To tackle the aforementioned limitations, a second strategy based on the use of molecularly-defined nanomaterials can be taken into account. In this case, molecules bearing engineered moieties, are designed to interact with each other, leading to self-assembly processes. Moreover, this kind of strategy is highly versatile, because it allows using a number of different molecular fragments (*e.g.* inserting hydrophobic and hydrophilic motifs on the same molecule). These molecular systems may not be linked by strong covalent bonds, but instead they could be held together by supramolecular forces *i.e.* weak interactions. The cooperation between the different components is highly efficient and can result in the arrangement in a specific manner. The controlled disposition facilitates the emergence of functional nanostructures built molecule-by-molecule, enabling them to perform to complex tasks,[18] whose outcomes can also have macroscopic effects (Figure 1.2).[19–21] The use of supramolecular interactions as a bottom-up approach to build molecularly-defined structures will be discussed in *Chapter 1.6-1.9* and *3*.

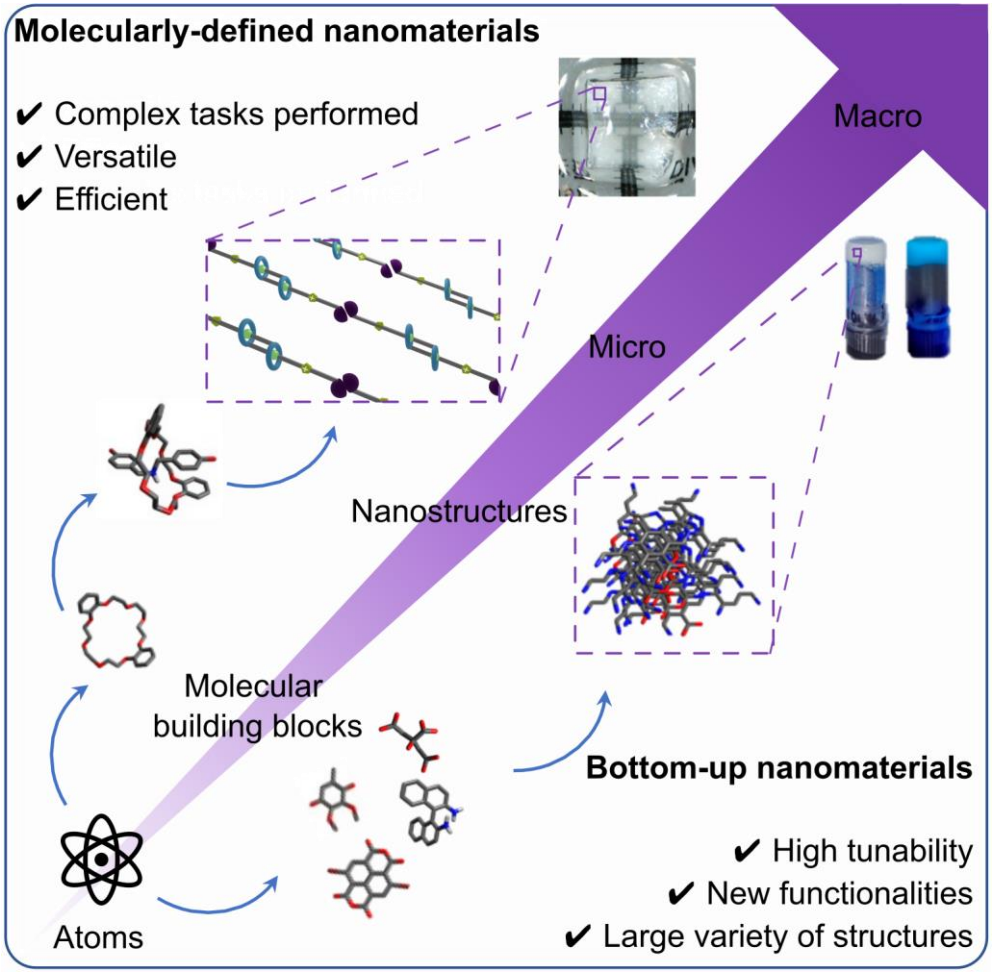

Figure 1.2. Bottom-up approaches from the atomic to the macroscopic level. On the right side, traditional bottom-up strategy to build materials with nanometric dimensions. On the left side, bottom-up approach towards nanomaterials based on supramolecular chemistry. Part of the image is reprinted with permission from *J. Am. Chem. Soc.* **2017**, 139, 42, 14825–14828. Copyright 2022 American Chemical Society. Part of the image is reprinted with permission from *ACS Nano* **2018**, 12, 2, 1296–1305. Copyright 2022 American Chemical Society.

1.3 Carbon nanomaterials

CNMs have played a major role in the field of nanotechnology. Indeed, the discovery of fullerenes in 1985 represented a breakthrough in the study of nanomaterials. Fullerene (or C_{60}) (Figure 1.3a), the first molecular carbon allotrope,[22] is deeply different from other allotropic forms of carbon, namely graphite and diamond. Indeed, C_{60} is the first molecular CNM made of a discreet number of carbon atoms. After the identification of fullerenes, new carbon-based nanoforms have been welcomed in the CNMs family: from carbon nanotubes (CNTs) (Figure 1.3b)[23,24] to graphene (Figure 1.3c),[25] and, more recently, with the advent of CNDs.[26] The aforementioned CNMs are the most common, though more exotic nanoforms can be considered too, from carbon nano-onions to carbon nanohorns, nanocones, and nanodiamonds.[27] During recent years, CNMs have gained the limelight of the scientific scene due to their interesting physicochemical properties.

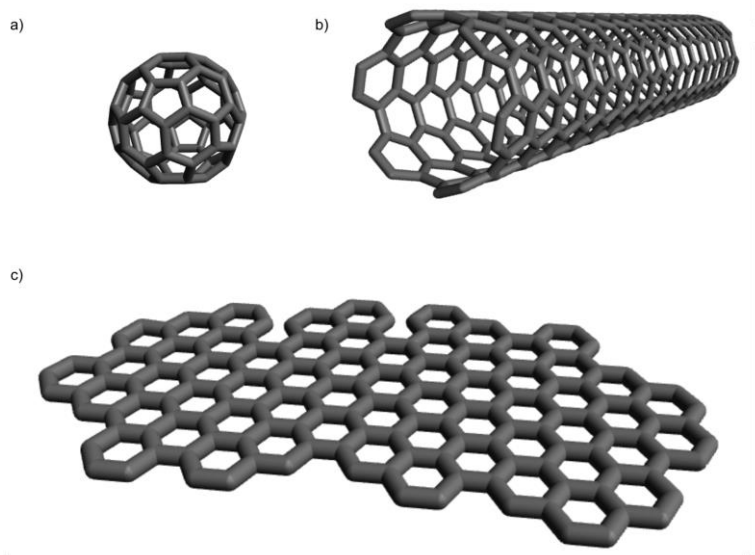

Figure 1.3: Schematic depiction of important CNMs. a) C_{60} b) CNT c) graphene. All these structures may serve as starting point for the preparation of more complex systems. CNMs not to scale.

However, a major drawback of CNMs in their pristine form is their difficult manipulation and strong tendency to aggregation in most common solvents.[28] For this reason, many efforts have been dedicated in the chemical functionalization of carbon nanoforms, with the scope of transforming CNMs into species resembling simpler organic derivatives. This attempt is due firstly to an easier handling of CNMs and, importantly, to the preparation of highly engineered *ad hoc* nanostructures for practical applications. In fact, the features of carbon-based nanostructures can be easily designed and fine-tuned through the chemical functionalization of their surfaces, improving their solubility, and allowing their employment in different technological applications.

1.4 Carbon nanodots

CNDs are one of the latest of CNMs discovered, consisting of quasi-spherical nanoparticles with diameters typically below 10 nm.[29] Their elemental constituents are mainly carbon, hydrogen, and oxygen, but other atoms like nitrogen or sulfur are often encountered.[30] Their discovery dates back to 2004 when, Scrivens *et al.* noticed this highly fluorescent and fast-moving material in the electrophoresis plate, while analysing the production residues of CNTs by arc discharge.[26] Since then, CNDs have witnessed a growing interest from the scientific community, because of their peculiar photoluminescent (PL) properties (excitation dependent fluorescent emission), biocompatibility, and low production costs. The aforementioned characteristics make CNDs privileged candidates for a vast number of applications.

The optical properties of CNDs are usually associated to either to the delocalized band structure resulting from the newly formed graphitic core or to the presence of photoluminescent molecular-like chromophores.[31] Nonetheless, both effects might contribute to the overall PL features, depending on the nature of the material.[32,33] The mechanisms underlying the formation of CNDs is still under debate in the scientific community, but general hints deriving from the large amount of data on this topic indicate that condensation, polymerization and aromatization play a predominant role.[34] Nowadays many synthetic protocols have been developed to obtain CNDs, but all of them can be ascribed to two main approaches: top-down and bottom-up methods.[35] The former is achieved by high energy treatment of large carbon structures (*e.g.*, CNTs, amorphous carbon, graphite, etc.). Typical protocols include arc discharge,[36] laser ablation,[37] and electrochemical oxidation.[38] Instead, the bottom-up methodologies exploit the thermal treatment of small molecular precursors and are achieved by MW-assisted,[39] solvothermal and pyrolytic methods.[40] Both top-down and bottom-up approaches present advantages; however, through the bottom-up method, it is possible to employ a wider variety of precursors, achieving a greater control over the resulting material and a fine-tuning of their properties while aiming for a specific application.[31] It is worth to mention that CNDs are the sole CNMs that can be prepared entirely from bottom-up strategy, without the need of post-functionalization. For instance, fullerene, CNTs and graphene can be prepared first *via* top-down methods and then have to be functionalized *via* bottom-up strategy to ease their handling, their solubility and their use in technological applications.[28] On the contrary, CNDs can be synthetized using an entirely bottom-up approach: indeed, starting from the proper choice of molecular precursors, the features of the building blocks would possibly be transferred from the molecular scale to the nanoscale.[41] The materials obtained with bottom-up synthesis are generally derived by solvothermal treatment, due to the versatility and low production costs that this approach offers.[42] Among the hydro- and solvothermal methods, that historically relied on the use of an autoclave and often require long reaction times, the microwave (MW)-assisted procedures have rapidly emerged as a reference in terms of reaction time, energy consumption, and reproducibility.[43] In the last few years, numerous syntheses of CNDs have been reported. Some examples of the wide variety of

substrates from which CNDs were obtained include carbohydrates,[44] amino acids,[45] ethylenediaminetetraacetic acid (EDTA),[46] citric acid[47] and raw materials.[48] Depending on the materials used for the synthesis and the heteroatoms present in their structure, several functional groups can be obtained on the surface of the resulting material.

1.5 Bottom-up pathways for amino-functionalized CNDs

The possibility of introducing heteroatoms in CNDs significantly widens the range of possible CNDs that can be obtained.[49] Doping with heteroatoms dramatically influences the properties of the final material and N, O, P, B, and S are the elements most frequently reported for the doping.[50] Materials obtained by nitrogen doping, referred to as nitrogen-doped CNDs (N-CNDs), show very interesting characteristics (Figure 1.4). They are usually obtained by hydro- or solvothermal treatment of nitrogen-containing molecules, like amino acids or EDTA. N-CNDs can be obtained also by multicomponent synthesis, in which a precursor without nitrogen atoms (*e.g.*, citric acid, glucose, etc.) is allowed to react in the presence of a doping agent (*e.g.*, EDTA, urea, etc.) to afford CNDs.[51]

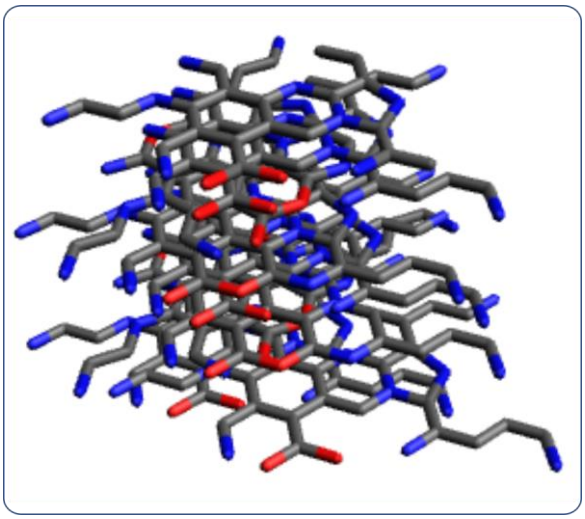

Figure 1.4: Schematic depiction of a N-doped carbon nanodot.

In these systems, which were studied in great detail if compared to others, heteroatom doping results in improved PL characteristics that were associated with the formation of molecular-like fluorophores or to N-centered defects of graphitic domains.[42,52] Further studies evidenced how molecular fluorophores are produced in the reaction of citric acid and ethylene diamine (EDA) at 200°C. Amidation and cyclization reactions led to the formation of 5-oxo-1,2,3,5-tetrahydroimidazo[1,2-α]pyridine-7-carboxylic acid (IPCA), which is a highly fluorescent molecule and was detected in the analysis of the reaction products by the means of different techniques. IPCA was identified as the responsible of the luminescent properties of the material, albeit it is still unclear if it is covalently bonded to the polymeric chains of these CNDs or absorbed in their structure. This study

also enlightened the need for reliable purification protocols to eliminate low molecular weight impurities, as well as larger particles deriving from the synthesis of N-CNDs.[53,54] The use of a doping agent is usually associated with an increase of the PL features, a trend also linked to the amount of nitrogen introduced in the system. As an example, it was observed that the quantum yield (QY) of N-CNDs, obtained from citric acid in the presence of different doping agents, increases dramatically. In this study, three different doping agents were assessed: ammonium hydroxide, EDA, and diethylenetriamine. The non-doped CNDs were characterized by a QY lower than 1%, while CNDs were characterized by an increased QY of 15.6% and 56.8% by using EDA and diethylenetriamine, respectively.[39] Synthetic protocols of N-CNDs using *L*-arginine (Arg) and EDA (Figure 1.5a) were reported.[43,55] In one case, the use of a doping agent resulted in excellent PL characteristics of the so-obtained material, which was characterized by a diameter of 2.5 ± 0.8 nm as determined via atomic force microscopy (AFM). The overall QY was 17% and, after separation by the means of size exclusion chromatography (SEC), it was obtained a fraction of N-CNDs with higher luminescence (QY of 46%). The presence of primary amino groups on the surface of N-CNDs was detected with the Kaiser test. This analysis evidenced the presence of 1350 μmol/g amino groups. Moreover, these surface functionalities conferred to the as obtained N-CNDs excellent solubility in water and mild solubility in organic solvents like *N,N*-dimethyl formamide (DMF) and dimethyl sulfoxide (DMSO). However, as indicated by X-ray photoelectron spectroscopy (XPS), different types of nitrogen are also present in the structure. Despite obtaining more detailed structural information still represents a challenge, the authors were able to establish the different contributions of Arg and EDA in the resulting material. Comparative nuclear magnetic resonance (NMR) experiments performed on materials obtained with ^{13}C labelled precursors evidenced how Arg contributes mainly to the signals associated with aromatic domains, while ethylenediamine was found to be responsible for the signals attributed to aliphatic groups.[43,56]

Surface functionalities of CNDs play a critical role in the chemistry of these nanoparticles, and thus in their chemical and photophysical behaviour.[57] CNDs usually bear a number of reactive molecular moieties, such as alcohols, carboxylic acids, and amines, that can be exploited for further functionalization, leading to the spontaneous coupling of CNDs with other nanostructures to form novel nanohybrids.[58–61] In addition, several examples of covalent functionalization are described in literature and exploit the well-known chemistry of the amino group, like *e.g.* the reaction between amines and thiocyanates,[62] acyl chloride derivatives[63] and with activated carboxylates by exploiting coupling with (1-ethyl-3-)3-dimethylaminopropyl(carbodiimide) and *N*-hydroxysuccinimide agents.[64,65] This versatile toolbox for post-synthetic functionalization has been widely used for the derivatization of CNDs allowing the synthesis of nanohybrids with unique properties. As an example, this method was used for the synthesis of nanohybrids between N-CNDs with different kind of dyes [66–68] and metallic complexes.[69]

Besides the post-functionalization, the concept of using a molecular doping agent to fine-tune the properties of the resulting CNDs has proven to be a highly convenient and flexible route. Indeed, several examples of one-pot functionalization were reported and, in this context, the versatile reactivity of the amino group played a major role in these syntheses. Leveraging the principles of bottom-up strategy, CNDs with unique features can be obtained, such as particle chirality. In the synthesis of CNDs with Arg and EDA, the chirality of the amino acid is lost due to high temperature (above 200°C) that results in racemization of the chiral core precursor. The replacement of EDA with chiral (*R*,*R*)- or (*S*,*S*)-cyclohexanediamine resulted in the retention of chirality in the obtained CNDs (Figure 1.5b).[70] Both electronic and vibration dichroism analyses were conducted, and the chiral nature of this kind of N-CNDs, albeit with low intensity signals, was detected. On the other hand, circularly polarized luminescence (CPL) remained elusive, probably due to an insufficient interaction of the chiral precursors with the emitting chromophore. Nonetheless, the introduction of chirality in this nanomaterial opens up exciting perspectives for their exploitation in fields where chirality is a crucial aspect, like medicinal chemistry, sensing, bioimaging, chiral induction, catalysis and protein interaction.[71–73]

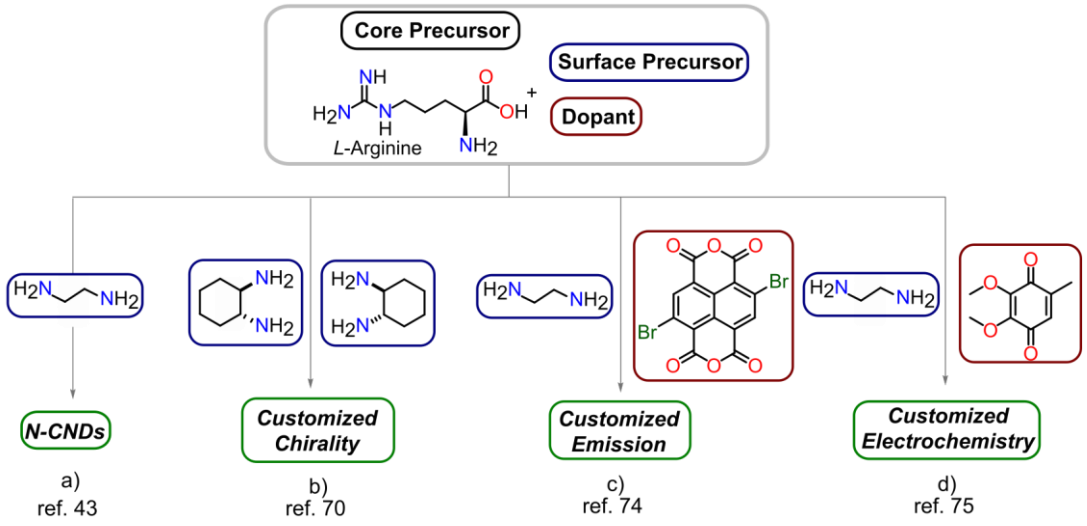

Figure 1.5. Schematic representation of modular bottom-up approach for the synthesis of engineered CNDs, using Arg as core precursor: a) from Arg and EDA b) one-pot doping with a chiral diamine c) one-pot doping with brominated NDA, d) one-pot doping with quinones.

White light-emitting CNDs were obtained by reaction of Arg, EDA, and naphthalene dianhydrides (NDA) in an MW-assisted protocol.[74] The reaction of the amino groups with the anhydride moieties, affording the corresponding imides, allowed fine-tuning the emission color of the material, ranging from blue to orange. When bromine core-substituted NDA were used, aromatic nucleophilic substitution between amino groups and the bay positions of NDA contributed to the CNDs formation and by tuning the equivalents (eq.) of precursors the authors were able to obtain white light-emitting

CNDs (Figure 1.5c). The one-pot functionalization of CNDs can be exploited not only for the tailoring of the chiral and optical properties of these materials. It was also shown how the introduction of quinones in the Arg/EDA based CNDs synthesis can influence the redox characteristics of the resulting material (Figure 1.5d). The formation of imines between amines and quinones and their consequent inclusion in the CNDs structure resulted in the modulation of their redox potential, from -1.52 to -2.04 V vs SCE (standard calomel electrode).[75] It has been demonstrated that fine-tuning of electrochemical properties can be an useful pathway to the exploitation of CNDs for solar-driven reactions or as photocatalysts.[49,76,77] Besides, CNDs have been used also as aminocatalysts, taking advantage of the abundant amino groups present on the surface of these nanoparticles.[72] Importantly, the amount and the type of surface functional groups of the CNDs can be engineered, choosing accurate molecular building blocks. In light of these considerations, we thought it could be possible to extend the toolbox of CNDs' properties, obtaining a nanomaterial able to emit CPL, exploiting a bottom-up approach using proper molecular precursors. The combination of chirality and fluorescence properties in CNDs is the purpose of part of this Thesis, where the synthesis, purification and characterization of CPL–active CNDs is reported (*Chapter 2*).

1.6 Supramolecular chemistry

The bottom-up fabrication of nanostructures based on supramolecular chemistry has been a predominant topic of interest for almost 40 years. Going to the source, supramolecular chemistry may be described as the "*chemistry beyond the molecule, bearing on the organized entities of higher complexity that result from the association of two or more chemical species held together by intermolecular forces*".[78] This is the most accepted definition of supramolecular chemistry, reported by Jean-Marie Lehn, Nobel laureate in Chemistry in 1987 along with Charles Pedersen and Donald J. Cram "*for their development and use of molecules with structure-specific interactions of high selectivity*".[79]

Supramolecular chemistry relies on the concept of self-assembly and pre-organization through *molecular recognition, i.e.* "*the ability of a molecule to recognize and associate with another molecule based on the presence of complementary chemical functionalities*".[80,81] Supramolecular chemistry, through molecular recognition, is a tool for the construction of new chemical entities where the individual properties of single precursors are still maintained, while at the same time other unique features arise from the interaction of the components. The vast majority of supramolecular systems are driven by non-covalent interactions (*e.g.* hydrogen and coordination bonding, ionic, donor-acceptor, hydrophobic, van der Waals etc.). Leveraging on these forces, it is possible to design building block able to freely self-organize together without the help of external stimuli. Indeed, by mastering intermolecular weak interactions and by tuning the molecular backbone of the species employed, it has been possible to develop novel

sophisticated systems able to perform tasks at the nanoscale.[82] Hence, it is natural to portray supramolecular chemistry as a strategy for the construction of nano-architectures, following the principles of bottom-up nanotechnology. Indeed, the bottom-up fabrication of functional materials by spontaneous self-assembly merges precise molecular scale design with tailored supramolecular tasks.
A considerable influence for nanoscientists comes from Nature, where several biological systems are extremely complicated machines built together in a supramolecular fashion.[83] The most known example is represented by deoxyribonucleic acid (DNA). This structure is a double sequence-controlled polymer[84] composed by several molecular building blocks, *i.e.* nucleotides. Weak hydrogen bond interactions drive the self-assembling of the two strands of the DNA, allowing the formation of the double helix. Inspired by natural world, able to develop complex architectures from scratch, researchers aspire to better understand the operation of these systems to reinvent them in artificial systems. In this sense, nanotechnology helps making progresses along this way, taking advantage of supramolecular forces as a bottom-up strategy to build structures which are molecularly-defined at the nanoscale. This assumption is practically translated in the design and synthesis of a vast library of man-made supramolecular materials[19], like supramolecular polymers[85], peptide fibers[86], artificial cells,[87] etc. In these examples, the controlled arrangement of molecular fragments helps in the formation of nanostructured functional materials able to perform tasks at the nanoscale. In addition to the cited cases, artificial molecular machines are one of the most exploited strategy of bottom-up approach to build nanomaterials having properties encoded within the molecular structure itself.[88,89]

1.7 Molecular machines and devices

Since decades, scientist engaging with nanotechnology have found in Nature a source of inspiration for their work. At the molecular level, Nature exploits a number of molecular building blocks, putting them together in order to build complex, but highly efficient, nanodevices called *molecular machines*.[88] One definition that can be used to illustrate what is a molecular machine is the following: *"a multicomponent molecular system with defined energy input that is capable of performing a measurable and useful secondary function reversibly either at the nanoscale or, if amplified through collective action, at larger scales"*.[90] For instance, there are a plethora of naturally occurring machines able to convert an external energy input into a function, *e.g.* the directionally controlled movement of their components.[91] One of the most important example of biological machine is represented by the adenosine triphosphate (ATP) synthase enzyme. ATP synthase is a transmembrane protein localized in the mitochondrial membrane. It exerts a fundamental function, since it is responsible for the synthesis of ATP, employed as an energy source in all cellular functions.

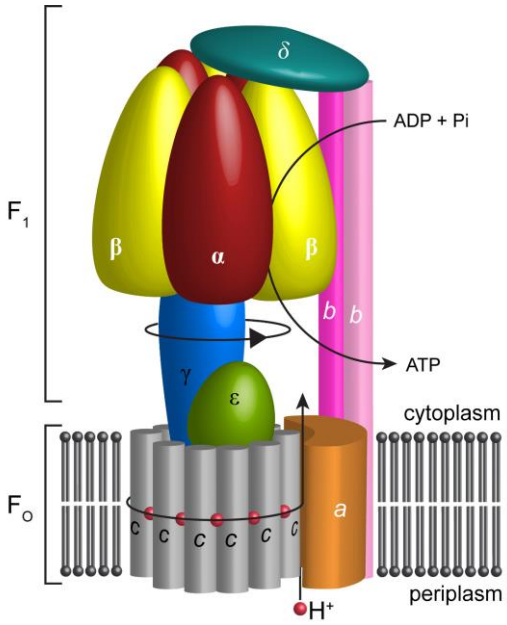

Figure 1.6. Schematic representation of ATP synthase, illustrating the rotary motor (F_0) and stator (F_1) sub-components. Republished with permission of *ELife Sciences Publications, Ltd* from "Cryo-EM reveals distinct conformations of E. coli ATP synthase on exposure to ATP", Sobti M. *et al.*, 8, **2019**; permission under the terms of the Creative Commons Attribution License.[92]

This elaborate bio-machine can be sort into four units (Figure 1.6). In the F_0 domain, composed by subunits c and subunit a, the proton translocation occurs. The rotation of the rotor, formed by γ and ε subunits, within F_1 domain is driven by the proton gradient across the membrane, passing along the F_0 domain. The F_1 domain, composed by α/β subunits, is the location where ATP synthesis takes place. The proton gradient drives conformational changes in α/β subunits, powering a turbine-like movement used to synthetize ATP molecules. Globally, the domains are still hold thanks to a stator, formed by subunits b and δ. Remarkably, the catalyzed process of ATP synthase is also reversible (*i.e.*, if ATP is cleaved, the rotor pumps protons against the pH gradient).[93] Prof. Richard Feynman and K. Eric Dexler, respectively in the lecture "There's plenty of room at the bottom" and in the book "Engines of Creation : The Coming Era of Nanotechnology",[12,94] envisioned the possibility to use molecules for the construction of operating machines, like the ones embedded in our bodies. In this sense, scientists have been putting substantial efforts to recreate nanodevices and machines artificially. Despite the analogy with macroscopic machines is plain, the classic forces that dominate bulk machines are negligible for nanodevices. As an example, gravity and friction – controlling the world at the macroscale – can be considered irrelevant on nanometric systems. On the contrary, Brownian motion fully governs the operation of these machines at the nanoscale.[95] It must be pointed out that in biological systems, Brownian motion is swindled by the global cooperative effect of each components. Scientist have overcome this "obstacle" carefully designing chemical precursors, using

supramolecular chemistry as a powerful tool to mimic biological linear and rotary machines.[96]

1.8 Artificial molecular machines

The advancement of nanotechnology has included progresses in the fabrication of artificial molecular devices, mimicking the natural ones.
As already mentioned, artificial molecular machines can be considered as one of the most studied cases, using a bottom-up approach, to build molecularly-defined materials of nanodimensions, where the final properties are encoded within the molecular structure itself. Undoubtedly, artificial molecular machines are inspired by their biological counterpart.[97] They can be made up either by a single molecule or formed starting from a *supermolecule*.[98,99] A supermolecule is formed when a spontaneous assembly occurs between a cavitand molecule (also known as macrocycle or *host*) – namely crown ethers[100], cyclodextrins[101], etc. – and a *guest* molecule. The guest, in some cases called also *thread* or *axle*, can be a rod-shaped molecule. Since the thread molecular building block possesses a specific recognition motif for the host molecule, it will insert into the cavitand forming a molecular complex. It is important to point out that the self-assembly of the two building blocks is energetically favoured, due to an energetic stabilization of the newly formed *supermolecule*, also called pseudorotaxane. At this point, if the extremities of the thread molecule are reacted covalently to insert two sterically hindered groups that prevent macrocycle dethreading, a *rotaxane* is formed. A second situation takes place when the two extremities are linked together, forming a *catenane*. In both cases, this kind of molecules are defined as Mechanically Interlocked Molecules (MIMs) and are ubiquitous in the field of artificial molecular machines (Figure 1.7).[102,103] Remarkably, even if the recognition site of the thread is switched off by an external input, the bulky groups – known as stoppers – or the thread itself will prevent the slipping of the host molecule. Nanodevices can be formed by a single component, or by multiple molecules interacting with each other. Despite the simplicity in handling a single building block, the use of multiple components is preferred due to the versatility in the bottom-up design of the molecular structure, and consequently in the final functions of the nanosized molecular system.[104–106] Motion of a component (*e.g.* the macrocycle) with respect to the other (*e.g.* the axle) is one of the most studied functions present in artificial molecular machines. When the axle is provided with two (or more) identical recognition sites (also called *stations*), the motion is just a shuttling of the macrocycle with respect to the thread.[107] On the other hand, when there are recognition sites having a different binding affinity for the host molecule, the movement may be controlled. Indeed, when a proper energy source is supplied – in the form of chemical, light or redox inputs[108] – the relative affinity of the macrocycle for the two stations can drastically change. As a consequence, the host molecule will move towards the (former) less efficient site. The initial state can be restored, if an opposite energy input is provided.[109]

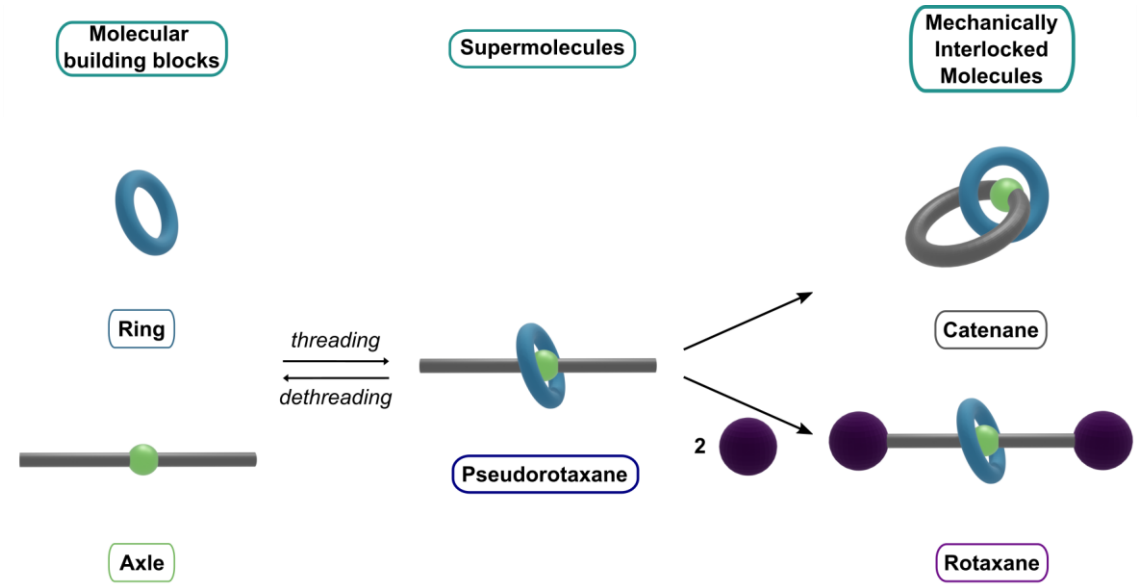

Figure 1.7. Schematic representation of a simple pseudorotaxane and derived mechanically interlocked molecules.

The shuttling function has been exploited in several examples of artificial molecular machines, nonetheless artificial nanodevices still lack in showing useful functions to be employed for practical applications in the near future.[110,111] In fact, despite the great progresses in the field, artificial nanomachines barely reach the performances of naturally occurring counterpart. To tackle this problem, researchers are moving in different directions. For instance, through the synthesis of more elaborate molecular machines, with a high degree of dissymmetry, in order to catch up the complexity of biological nanomachines performing practical functionalities.[112] Besides, in order to have molecular machines able to compete with already existing technologies, researchers are studying to reproduce two peculiar behaviours of biological nanomachines operations: unidirectionality and autonomy.[113,114] Unidirectionality is a key point in the description of nanodevices able to perform useful tasks. To explain this behaviour, it is important to recap some general concepts. Chemical species are mostly studied when they are in a state of equilibrium. From an energetic point of view, the equilibrium state is defined as a thermodynamic absolute minimum. In this framework, when a MIM possesses two recognition sites, the macrocycle will be located on the station having the lowest minimum energy. Nonetheless, after a proper energy source is provided, the energy of the first state can be increased and the ring can shuttle to the second unchanged station. Thus, the system has adapted to a new equilibrium condition. The system can go back to its initial state, if another energetic stimulus (opposite to the first one) is supplied. However, despite controlling the motion of the macrocycle, useful work cannot be extracted, because the accomplished work will be erased as soon as the "destabilizing" stimulus is turned off. Such an artificial molecular machine is defined as *molecular switch* (Figure 1.8a).[114] In order to extract useful work out of molecular motion, it is necessary to build *molecular motors.* These systems associate the relative

movement of its components, in response to an external stimuli, to a cyclic reaction network, which is travelled in a directional fashion .[114–116] This kind of systems, exploiting Brownian motion of molecules, operate according to the so-called ratchet mechanisms (Figure 1.8b).

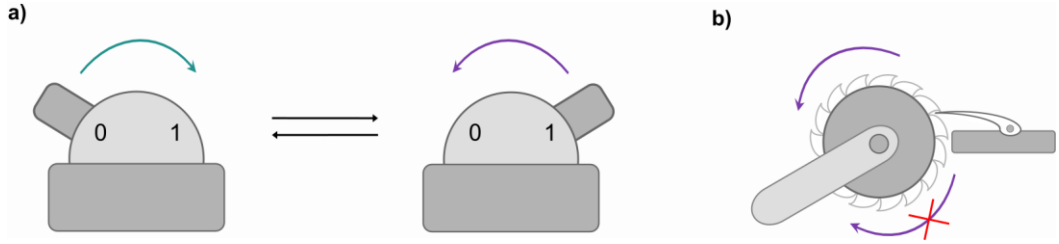

Figure 1.8. Schematic representation and operation of a) a macroscopic switch device and b) a macroscopic ratchet mechanism. In the first case, both clockwise and counterclockwise directions are allowed whereas in the second case the operation is unidirectional.

Ratchet mechanisms are widely used by biological structures present in Nature, like the transmembrane protein ATP synthase, the kinesin protein, and Na^+/K^+ ATPase pump. Exploiting the energy supplied by ATP hydrolysis, these proteins transport ions or molecules against concentration gradients, *i.e.* in the direction opposite to that deriving from equilibrium thermodynamics. In the field of nanotechnology, ratchet mechanisms were popularized by Prof. Richard Feynman, who highlighted that random Brownian motion of molecules can be converted into directed motion against gradient concentration.[117] This concept has paved the way to the potential use of ratchet-based systems for *e.g.* the energy storage or the realization of endergonic processes, all at the nanoscale level. In 1999, the first example of an artificial ratchet-based system was reported by Feringa and coworkers (Figure 1.9).[118] It consists of a sterically hindered chiral alkene molecule, endowed with a photoswitchable double bond. Upon light irradiation, one of the two components can unidirectionally rotate along the double bond. After UV light irradiation, the (*P*,*P*)-*E* isomer photoisomerizes to the (*M*,*M*)-*Z* isomer. Due to its instability, this isomer undergoes to a second chirality switching already at room temperature (r.t.), giving the (*P*,*P*)-*Z* isomer. However, this last structure is not stable under UV light and it will undergo another photoconversion, affording the (*M*,*M*)-*E* form. High temperature will result in the last chiral inversion, giving back the initial (*P*,*P*)-*E*. This pioneering work has paved the way to the synthesis of different generations of molecular motors[119,120] and to the bottom-up design of smart nanomaterials, which include motors as building blocks.[115,121,122] It is noteworthy to mention that ratchet mechanisms can be operated also with supramolecular systems.

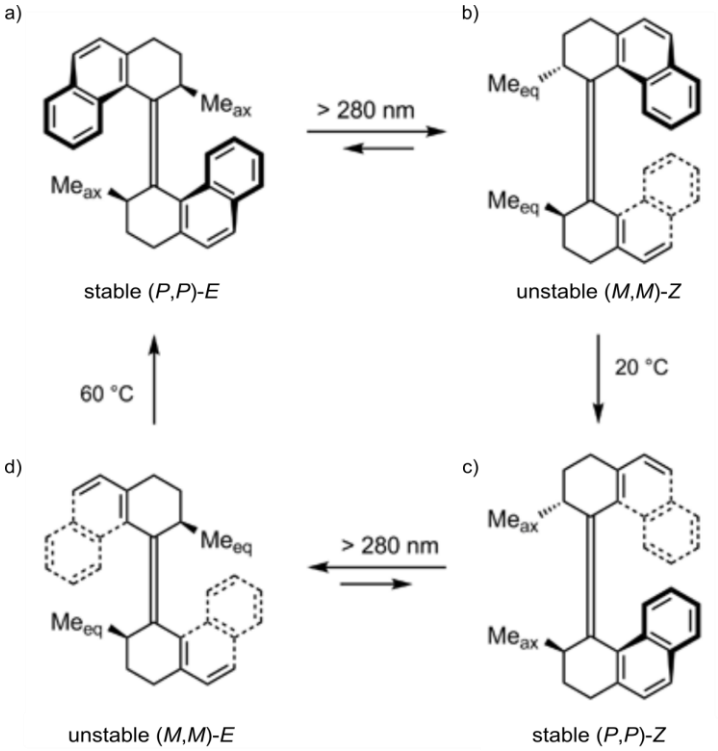

Figure 1.9: Molecular structure and operation for the unidirectional motion of the molecular motor by Feringa. [118]

Few years after Feringa's motor, Leigh and coworkers reported a supramolecular artificial device system operating according to a ratchet mechanism. (Figure 1.10).[123]

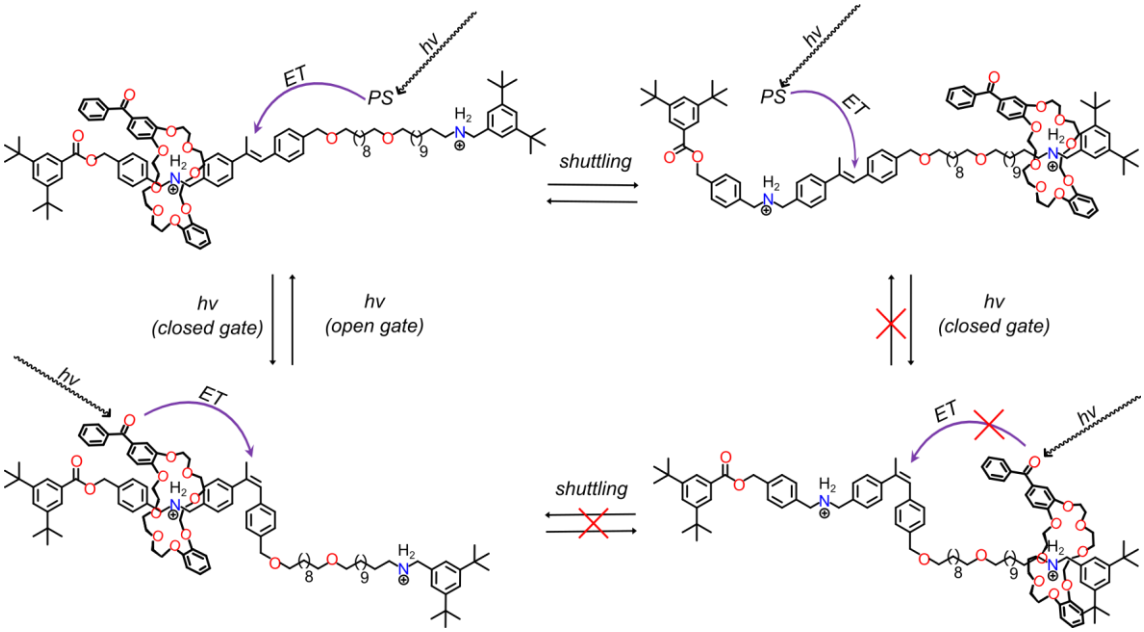

Figure 1.10: Scheme of operation of the molecular ratchet reported by Leigh.[123] The purple arrows represent the distance-dependant energy transfer from benzophenone moiety to methylstilbene gate. PS represents the benzil photosensitizer.

The asymmetric rotaxane comprises two ammonium sites, where a macrocycle bearing a benzophenone moiety can accommodate; in between them, a photoswitchable methylstilbene functional group separates the ammonium stations. When the methylstylbene is in its *E*-isomer, the ring can shuttle between the two ammonium stations, resulting in a statistical distribution (Figure 1.9, top left and top right). Upon light irradiation, *E*-isomer can be converted into its *Z*-isomer after energy transfer from a benzil photosensitizer (PS). In this condition, the free shuttling of the ring is hampered by the photoswitching of the methylstilbene, which now act as a light-controlled gate barrier for the macrocycle. When the macrocycle is on the ammonium station near the gate, upon irradiation of the benzophenone moiety, another energy transfer can occur from the benzophenone to the methylstilbene (Figure 1.9, bottom left). This process can reopen the gate, allowing the ring to shuttle again. On the contrary, if the macrocycle is on the ammonium station far from the methylstilbene, energy transfer does not happen (Figure 1.9, bottom right). Consequently, the gate will remain closed and the population of this rotaxanes co-conformation will increase over time, driving the system away from the initial statistical distribution.

The development of nanodevices implementing a ratchet mechanism is far from being simple. Indeed, it requires a careful design of each molecular fragment in every component.[114,122,124,125] It is paramount to carefully engineer a nanomachine with the correct energy profile, both in the presence and in absence of fuel addition, in order to make it work. In particular, to drive machine motion in one direction, a kinetic selectivity between backward and forward motion must be precisely designed, in order to have the right disposition of energy minima and maxima to afford a unidirectional pathway.[126,127] Lastly, a valuable advancement in the development of autonomous MIMs is their autonomous operation.[125,128,129] Looking at biomolecular machines, it is possible to observe that they work under a continuous supply of energy.[91] From an energetic point of view, these nanodevices could go back and forth from the initial to the final state relentlessly. Achieving this kind of operation is still challenging. In fact, most of artificial molecular machines need to be provided opposite inputs, in order to perform a series of repeated cycles, and only few examples of autonomous operation have been reported.[118,125,130,131] All the aforementioned characteristics, namely structural complexity, unidirectionality and autonomy, would be appealing for the construction of efficient, and performative artificial molecular machines.[132]

1.9 Energetically-demading transport

In the last decades, the domain of artificial molecular machines has been flourishing and the literature of this field is vast. Considerable efforts were dedicated to developing artificial systems resembling biomolecular devices. An important aspect of these natural machines is the ability to pump (*i.e.* shuttle) molecules against a concentration gradient. This characteristic endows the achievement of energetically-demading (*i.e.* endergonic) processes, resulting from the operation of efficient molecular ratchet mechanisms.

Despite the deep knowledge in the synthesis of artificial molecular machines, the field of energetically-demanding molecular pumps is still in its infancy.[133]
To realize a prototype of molecular pump, in 2014, Credi and coworkers designed a pseudo-rotaxane composed by an asymmetric axle and a crown ether macrocycle.[130,134] The axle component possesses a photoswitchable azobenzene at one end, a cyclopentyl moiety as a pseudostopper at the other end, while in the middle, an ammonium station acting as a recognition site for the crown ether. When the azobenzene is in the form of *E*-isomer, the threading of the macrocycle occurs from that side and a thermodynamic equilibrium is reached with the formation of a pseudo-rotaxane. After the threading, the energy profile of the system can be modulated by light irradiation. Indeed, *E*-azobenzene can be converted into its *Z*-isomer, which has a more pronounced steric hindrance with respect to the *E* counterpart. The photoisomerization increases the energetic barrier for dethreading through azobenzene. Isomerization also destabilizes the system, leading to dethreading of the ring over the cyclopentyl side, thus affording the unidirectional transit of the macrocycle according to a ratchet-mechanism. Remarkably, due to the intrinsic properties of azobenzene, the system can be switched back to its initial state with the same light. This allows, under continuous irradiation, an autonomous unidirectional threading and dethreading, which brings the system to a dissipative out-of-equilibrium state, which can revert during the time to an equilibrium situation, if the energy supplied removed (Figure 1.11).

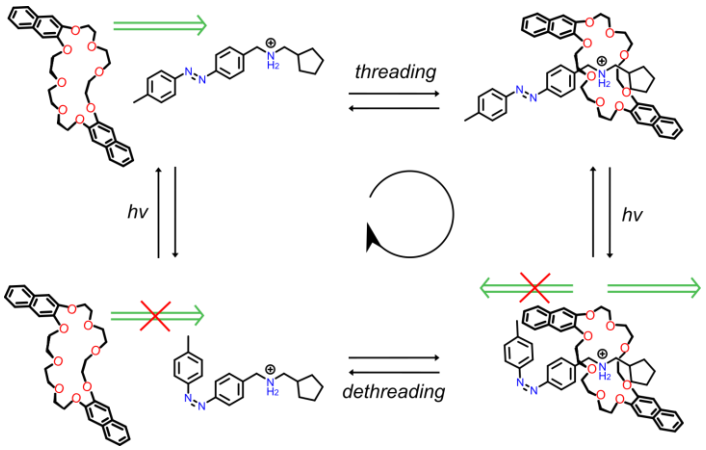

Figure 1.11: Scheme of the operation cycle of the molecular pump operated by light irradiation by Credi.[130] Green arrows represent the direction covered by the macrocycle.

The authors later demonstrated that the dethreading kinetics can also be controlled either by moving the azobenzene moiety from para to meta position,[135] or by the insertion of another stopper with different size, namely a 2,4-dimethylphenyl moiety.[136] In the latter case, an important feature of the system is the possibility to further functionalize the stopper side, increasing the length of the system, allowing it being embedded into more complex molecular devices.
Light irradiation is widely employed as external energy stimulus in molecular pumps,[137] but it is not the only one. Stoddart and co-workers reported several examples of ratched-

based artificial molecular machines able to operate in response to redox stimuli.[138] The authors demonstrated that it was possible to obtain a ratchet mechanism by redox changes in a [2]pseudorotaxane.[139] The redox inputs are able to drive a tetracationic ring, namely a cyclobis(paraquat-*p*-phenylene) ($CBPQT^{4+}$), in one direction relative to a charged axle, showing a switchable bipyridinium recognition site and a pyridinium, acting as a switchable and high energy steric barrier. After a reduction step, bipyridinium site and the $CBPQT^{4+}$ are reduced to their radical cation form, producing a change in the energetic profile of the system.

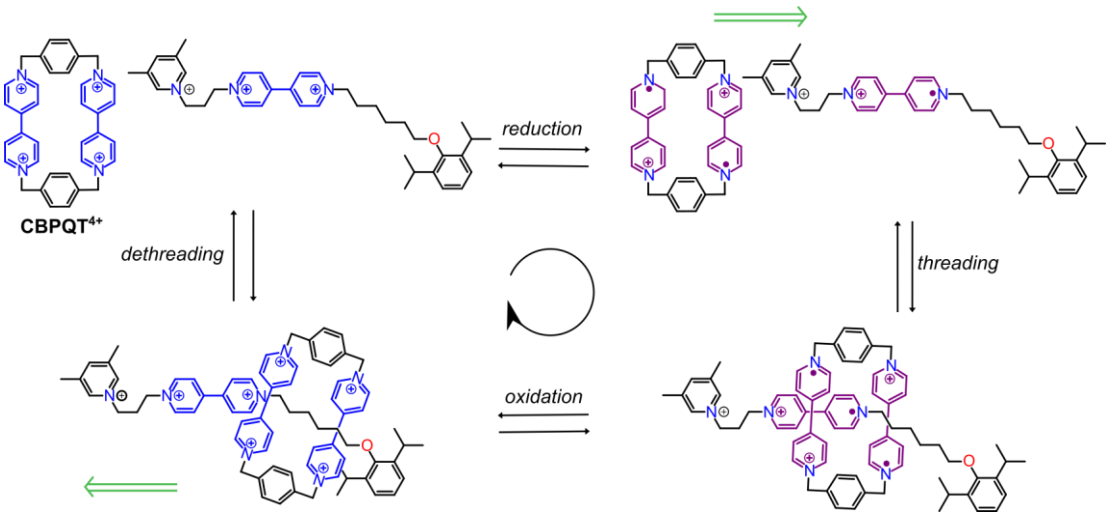

Figure 1.12. Scheme of the operation cycle of the energy-demanding supramolecular machine operated by redox stimuli by Stoddart.[139] Green arrows represent the direction covered by $CBPQT^{4+}$.

This change in their electronic structure leads to the threading of the macrocycle onto the axle, with the formation of the pseudorotaxane. A subsequent oxidation leads the system to a high-energy out-of-equilibrium state. NMR study confirms a dissipative kinetics of the system, which experience a dethreading of the $CBPQT^{4+}$ with respect to the axle during the time (Figure 1.12). Leveraging on this knowledge, Stoddart's group designed a library of synthetic supramolecular pumps able to act in a repetitive manner.[140] The first and most prominent example of these machines comprises different and important elements in its molecular structure. In this case, the $CBPQT^{4+}$, the pyridinium steric barrier and the bipyridinium recognition site are used in combination with a pumping cassette, namely an oligomethylene chain, and a steric speed bump (isopropyl phenyl moiety). The mechanism is similar to the previous example: after reduction and oxidation steps, a high-energy [2]pseudorotaxane is formed. However, due to strong coulombic repulsions, the macrocycle does not revert immediately to its initial state, rather it crosses the isopropylphenyl steric barrier and allocate it onto the pumping cassette site. Remarkably, the operation can be repeated twice: indeed, the clever bottom-up engineering of the molecular structure allows the system to carry a second macrocycle from the solution to the ring collection moiety, hampering at the same time the shuttling of the first $CBPQT^{4+}$ to the reduced viologen, thanks to the

isopropylphenyl steric barrier. This approach has paved the way to several artificial molecular machines controlled under redox stimuli, from simple structures up to the incorporation in polymeric structures and onto solid surfaces. [141,142]

Lastly, besides light and electrical stimuli, also chemical fuels can be exploited to operate artificial molecular machines. In this framework, Leigh's group has been reporting ratchet-based molecular machines showing unidirectional movement.[123,125,143,144] Among the prominent examples of artificial molecular pumps reported by his group, there are rotary and linear motors driven by pulses of a chemical fuels, *i.e.* acid-base inputs. (Figure 1.13).[145]

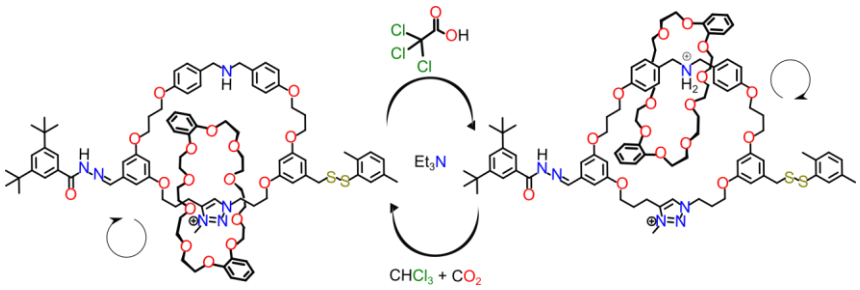

Figure 1.13. Scheme of the directional cycle of catenane operated by TCA fuel by Leigh.[145]

In this study, the authors report catenanes working as rotary molecular motors. The catenane possesses a dibenzyl ammonium site and a triazolium station, used for the recognition of a crown ether macrocycle. Moreover, an acid-labile hydrazone moiety and a base-labile disulfide gate blocker complete the structure. When the system is in an acidic environment, the threading of the crown ether ring occurs. The movement is allowed because the energetic barrier of the hydrazone is dynamically lowered and raised, due to the dynamic reaction of the starting hydrazide and aldehyde to form a hydrazone. As soon as the solution becomes basic, the dibenzyl ammonium station is deprotonated and the ring relocates onto the triazolium site, due to a greater binding affinity with respect to the amine site. The shuttling is permitted by the dynamic exchange of the disulfide site under basic conditions and, at the same time, the kinetic stability of the hydrazone barrier in the same condition. Every step of the operation was demonstrated by NMR spectroscopy, after accurate separation of the rotaxane. Remarkably, the pH change is carried out using trichloroacetic acid (TCA), an organic molecule prone to decomposition into chloroform and carbon dioxide, following its deprotonation. The use of TCA makes the process proceed spontaneously upon addition of acid, and the whole operation can be repeated a number of times, unlocking the possibility to perform subsequent cycles onto the same system. In the same study, a double-functionalized linear axle with a molecular structure similar to the catenane was also employed (Figure 1.14).

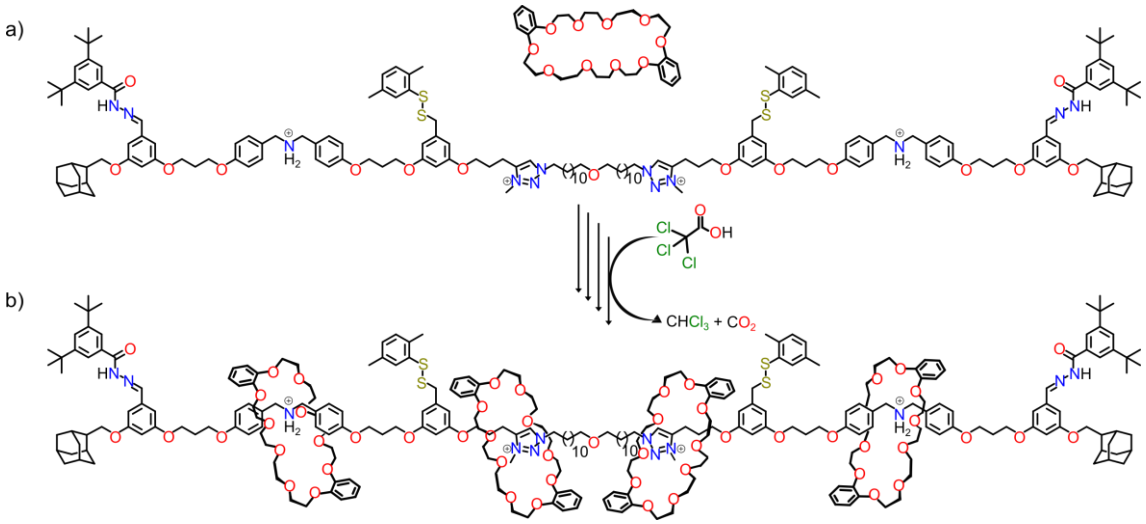

Figure 1.14. Directional pumping of macrocycle crown ethers onto a double linear axle. The threading is powered by four subsequent TCA fuel pulses.[145].

Also in this case, the system possesses the same molecular fragments aforedescribed: a hydrazone barrier as terminal unit, a dibenzylamonium and a triazolium recognition site separated by a disulfide barrier. All these units are located in the two halves of the thread with a specular symmetry. In this system, the ratcheting of four macrocycles from solution onto the axle was demonstrated, obtaining a high-energy out-of-equilibrium rotaxane. The general design of this system was also adapted to operate a pumping against a concentration gradient from solution onto the surface of polymeric beads.[146] In this study, Leigh and coworkers mechanically trapped crown ether rings in a higher-energy, out-of-equilibrium state, paving the way to the storage and release of energy (and information) operated by artificial molecular nanostructures.

Despite the great improvement in the field, the proposed examples are often require a high degree of synthetic complexity.[112] To effectively compete with the present nanotechnologies, artificial molecular machines should be simple both in design and in their operation, maintaining their functionality. In this framework, the purpose of part of this Thesis is the design, bottom-up synthesis, and characterization of a simple ratchet-based molecular machine that can operate according to a ratchet mechanism. Its operation in response to acid/base inputs was studied and the major results are reported in *Chapter 3*.

Chapter 2

Transfer of axial chirality endows carbon nanodots with circularly polarized luminescence[2]

2.1 Introduction

CNDs are a fascinating class of nanoparticles, which can be produced *via* bottom-up methods, and offer tunable features. One of the reasons why CNDs received considerable attention from the scientific community is their luminescence, which has been the focus of numerous studies.[33,147] In most cases, desirable luminescent properties are combined with water solubility, facilitating their use in biological applications.[148,149] However, while much less explored, CNDs soluble in non-polar organic solvents are highly desirable for technological applications, *e.g.* in optoelectronic devices.[150] To date, the few non-polar CNDs reported have been usually obtained via a hot-injection method.[151,152] This method is reminiscent of the synthesis of inorganic quantum dots, requiring high temperature and inert atmosphere, and so far proved less versatile than the consolidated bottom-up strategies employed in the synthesis of hydrophilic CNDs.[153]

The underdevelopment of non-polar CNDs in comparison with their water soluble analogues is evident also from the lack of chiral non-polar CNDs.[154–157] On this basis, we approached the preparation of chiral and non-polar CNDs leveraging the solvothermal treatment of small molecular precursors.[56,158,159] Indeed, the appropriate selection of starting materials, doping agents, and synthetic conditions affords CNDs with tailored structural and optical properties.[31,33,70,160,161] Expanding the solvothermal strategies to non-polar solvents would be desirable, because it can significantly increase the pool of molecular dopants that can be employed, leading to engineered advanced functionalities. In particular, it could facilitate the development of CNDs exhibiting CPL, without the need for a chiral matrix. Indeed, to date all the studies reporting CPL from CNDs employed chiral matrices,[162] known to impart CPL even to achiral molecular fluorophores, as opposite to controlling the nanoparticle chirality directly.[163–167] To achieve CPL, we reasoned that a promising strategy would be to employ atropoisomeric precursors. Atropoisomers are molecules that are chiral by virtue of restricted rotation around a single bond, *i.e.*, they are axially chiral.[168–170] Such

[2] This chapter is derived-with permission-from Di Noja, S., Amato, F., Zinna, F., Di Bari, L., Ragazzon, G., Prato, M. Transfer of Axial Chirality to the Nanoscale Endows Carbon Nanodots with Circularly Polarized Luminescence., *Angew. Chem. Int. Ed.* Wiley. **2022**, e202202397. I am particularly grateful to Dr. Francesco Zinna and Prof. Lorenzo Di Bari from the University of Pisa for performing CPL measurements on **CNDs-2**.

precursors have not been previously employed for the preparation of CNDs, possibly due to their non-polar nature. However, atropoisomeric units such as binaphthyls are frequently employed as CPL emitters and have high thermal racemization barriers, which are desirable features to achieve CNDs that display CPL.[171,172] Herein, we report the synthesis and the properties of novel non-polar chiral CNDs derived from atropoisomeric precursors, resulting in CNDs that display intrinsic CPL, good processability in organic solvents, and prolonged thermal stability.

2.2 Results and Discussion

2.2.1 Synthesis and characterization of CNDs-1

To realize atropoisomeric CNDs, we employed citric acid in combination with either (*S*)-1,1'-binaphtyl-2,2'-diamine or its (*R*)-atropoisomer. Citric acid was selected for its consolidated ability to afford CNDs under several synthetic conditions.[53,173] Binaphthyl diamines were chosen because diamines are frequently used as doping agents in CND synthesis, and the naphthyl groups could impart hydrophobicity to the resulting CNDs.[174] Moreover, these axially chiral precursors have high thermal stability, with a rotational energy barrier $\Delta G^{\ddagger}$ equal to 178.4 kJ/mol and with a racemization half-life of 23 h at 250 °C.[175] Using DMF as solvent was critical for the success of our synthetic procedure, because DMF can solubilize the atropoisomeric diamine, allowing it to react. The molecular precursors are mixed and reacted in a MW for 300 s at 240 °C. The obtained crude is filtered to remove large particles, and the filtrate is precipitated with cold diethyl ether, affording **CNDs-1**, as a powder stable in its dried form. (Figure 2.1, top reaction arrow) Morphological and structural characterization were carried out using AFM, Attenuated total reflection – Fourier-Transform Infrared spectroscopy (ATR-FTIR), XPS and thermogravimetric analysis (TGA).

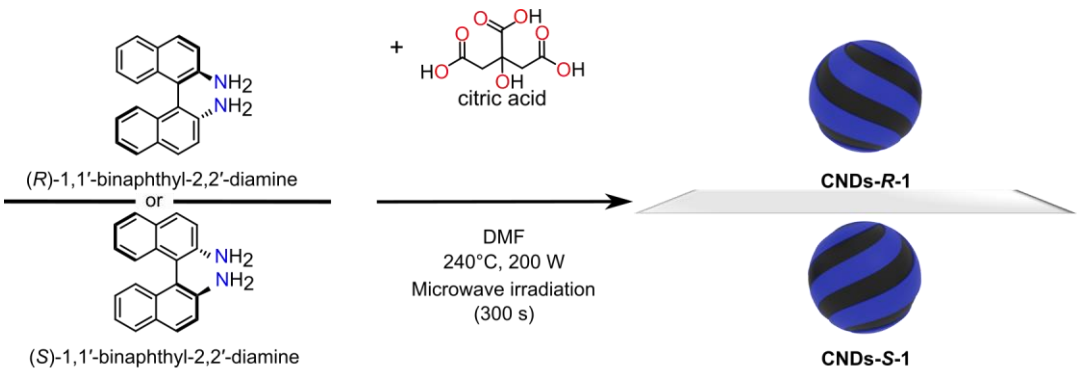

Figure 2.1. Synthesis of atropoisomeric **CNDs-1**.

AFM experiments revealed particles ranging from 2.5 to 5.3 nm, with a mean size of 3.5 nm (Figure 2.2a-b). ATR-FTIR spectrum of **CND-1** shows diverse functional groups similar to the ones of diamine molecular precursor (Figure 2.2c-d). In particular, a broad band peaking at 3366 and 3085 cm^{-1} can be assigned to the N-H stretching. The low

intensity of this band and the disappearance of the sharp peaks at 3475 and 3382 cm^{-1} of the starting diamine (Figure 2.2d) suggest the reaction of -NH_2 groups with the citric acid to form **CND-1**. Going to smaller wavenumbers, the peaks at 1709, 1498 and 1385 cm^{-1} are indicative of C=O, C-N/C=C and C-O bonds, respectively. Moreover, the signals at 816 and 760 cm^{-1}, representative of C-H bending of the aromatic unit, indicates the presence of the binaphthyl moiety. The peaks are slightly shifted with respect to the starting diamine, corroborating the reaction of the molecular precursors to form a new chemical entity.

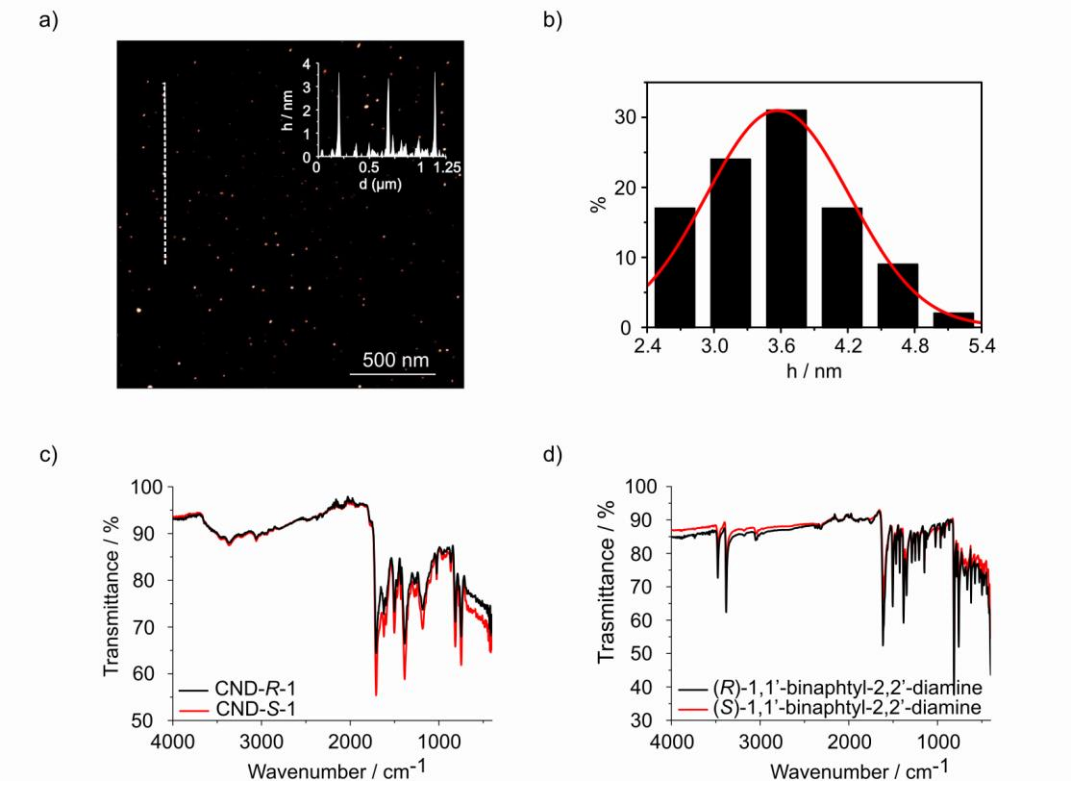

Figure 2.2. a) Tapping mode AFM of **CNDs-*R*-1** deposited on a mica substrate; inset is the height profile along the white solid line. b) Size histogram of AFM height data, with distribution fit (red curve) based on a Gaussian distribution. Statistical analysis is carried out on 100 nanoparticles. c) ATR-FTIR spectra of **CNDs-*R*-1** (black line) and **CNDs-*S*-1** (red line). d) ATR-FTIR spectra of (*R*)-1,1'-binaphthyl-2-2'-diamine (black line) and (*R*)-1,1'-binaphthyl-2-2'-diamine (red line) reported as comparison.

The chemical composition of **CNDs-1** was also investigated by XPS survey (Figure 2.3). The spectra of both **CNDs-*R*-1** and **CNDs-*S*-1** confirm the presence of carbon, nitrogen and oxygen inside the structure of the nanoparticles. The elements are in a C/N/O percentage ratio of 80.4/5.3/14.3 and 80.4/5.6/14.0, respectively for **CNDs-*R*-1** and **CNDs-*S*-1**. The deconvolution of the peaks for C1s shows in both **CNDs-1** the abundance of C=C bonds, ascribed to the presence of binaphthyl-derived moieties. As shown by ATR-FTIR, also XPS confirms the presence of C-N and C=O bonds (Figure 2.3 and Table 2.1).

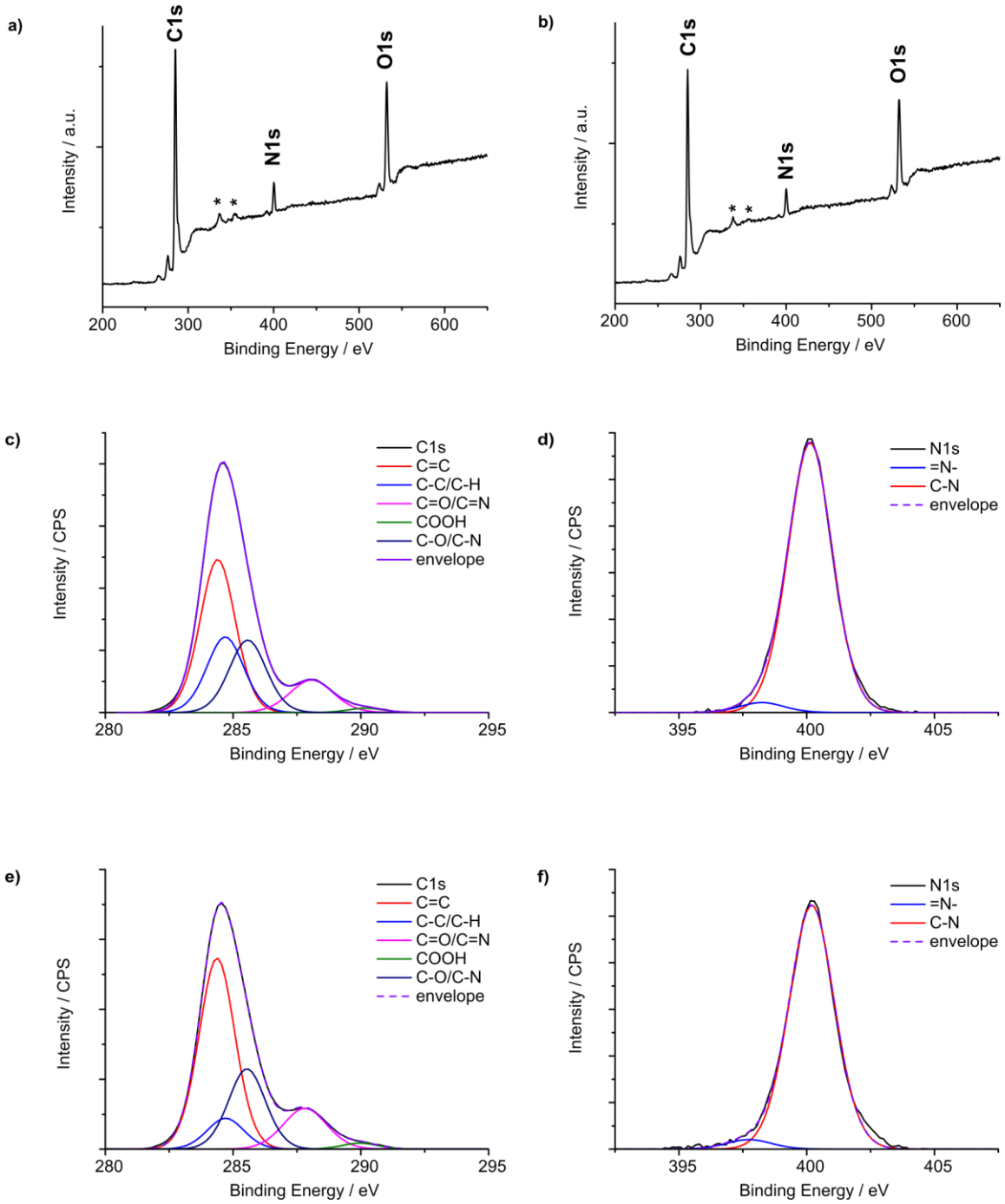

Figure 2.3. XPS survey of a) **CNDs-*R*-1**, b) **CNDs-*S*-1** showing the C1s, N1s and O1s peaks (* from gold substrate Au4d3, Au4d5 and Au4p). c, d) Deconvoluted C1s and N1s spectra of **CNDs-*R*-1**; e, f) deconvoluted C1s and N1s spectra of **CNDs-*S*-1**.

Table 2.1. XPS percentage of C, N, and O atoms and their deconvoluted components in **CNDs-*R*-1** and **CNDs-*S*-1**, as determined by XPS measurements.

	CNDs-*R*-1	**CNDs-*S*-1**
C%	**80.4**	**80.4**
C=C	43.5	52.9
C-C/C-H	22.4	8.8
C=O/C=N	11.4	13.7
COOH	1.2	1.7
C-O/C-N	21.5	22.9
N%	**5.3**	**5.6**
=N-	3.6	3.7
C-N	96.4	96.3
O%	**14.3**	**14.0**

Thermogravimetric analysis indicates a moderate weight loss up to 200 °C, potentially due to decarboxylation. A second loss peak is found at 250°C followed by a significant weight loss between 400 °C and 450 °C, attributed to Csp^3-rich domains.[176] The residual 42% and 43% weight at 700 °C, for **CNDs-*R*-1** and **CNDs-*S*-1** respectively, can be attributed to the abundance of aromatic fragments present inside the structure of the nanodots, which do not decompose in inert atmosphere at high temperature. (Figure 2.4) A residual mass value analogously appears in other members of CNMs, like graphene and carbon nanotubes.[177] The values are in accordance with XPS and FT-IR analyses.

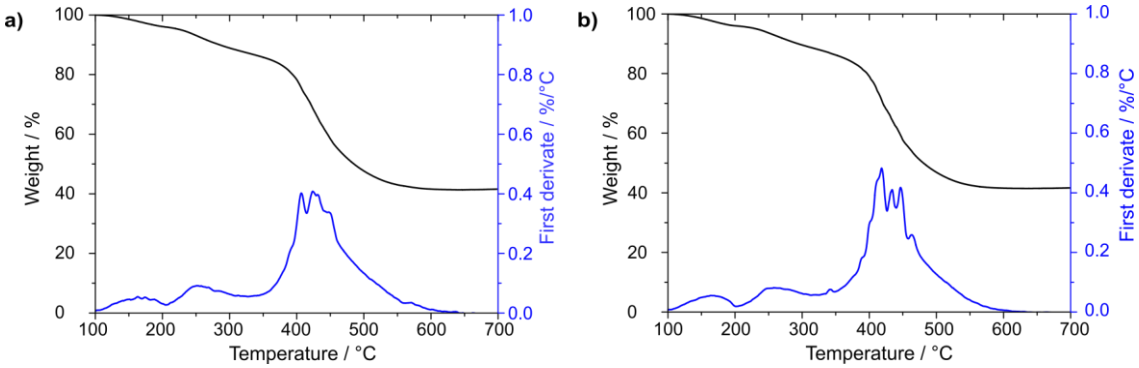

Figure 2.4. Thermogravimetric analysis (black line) and its first derivative (blue line) of a) **CNDs-*R*-1** and b) **CNDs-*S*-1**. Analyses performed under Nitrogen atmosphere.

Subsequently, chiroptical characterization of **CNDs-1** was carried out to study their photophysical properties. UV-visible (UV-Vis) absorption spectra in chloroform ($CHCl_3$) of both **CNDs-1** are identical and present absorption bands extending up to 450 nm, with a maximum peak at 285 nm, possibly related to π-π* electronic transition (Figure 2.5b). Importantly, electronic circular dichroism (ECD) of **CNDs-*S*-1** and **CNDs-*R*-1** displayed opposite and specular spectra, having a maximum at 287 nm

(Figure 2.5b), and for both **CNDs-1**, at 287 nm, the absorption dissymmetry factor (g_{abs}) is $|8.0|\times10^{-4}$. In a previous example, it has been demonstrated that the synthesis with racemic mixture of chiral precursors leads to no chiroptical activity.[70] In this case, the outcome would give a material with potentially different physicochemical properties, due to the formation of diastereoisomers, besides enantiomers. Therefore, this option was not further investigated. **CNDs-1** emit in the blue region of the spectrum, showing a wavelength-dependent emission profile, typical of this class of CNMs (Figure 2.5c-d). Both **CNDs-1** emit with a maximum emission intensity at 387 nm, regardless of the starting atropoisomer employed.

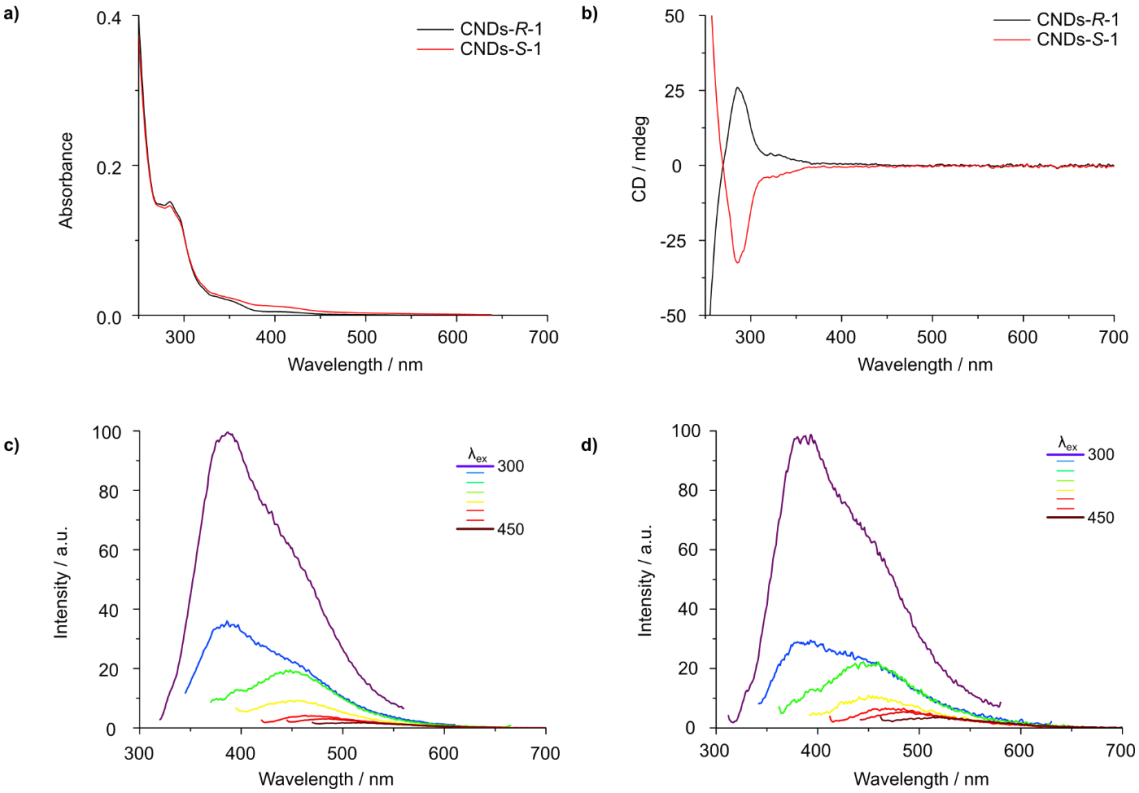

Figure 2.5. (a) UV-Vis spectra of **CNDs-*R*-1** (black line) and **CNDs-*S*-1** (red line); (b) ECD spectra of **CNDs-*R*-1** (black line) and **CNDs-*S*-1** (red line); (c) and (d) Fluorescence emission spectra of **CNDs-*R*-1** and **CNDs-*S*-1** recorded at different excitation wavelengths. Experiments performed in $CHCl_3$ at r.t., at concentrations between 0.01 and 0.05 mg/mL.

Despite the straightforward protocol of synthesis and the simple purification of these atropoisomeric carbon nanoparticles, **CNDs-1** showed unsatisfactory optical features. In fact, due to technical issues, CPL in the blue region of the visible spectrum could not be recorded. For this reason, we were prompted to obtain atropoisomeric CNDs with red-shifted emission.

2.2.2 Synthesis and characterization of CNDs-2

In order to improve the optical properties of atropoisomeric CNDs, we explored the use of doping agents. Upon screening of several carbonyl compounds (see Experimental section **2.4.2**), we selected 1,4-benzoquinone as a suitable doping agent because it can participate in CNDs formation and can react with aromatic amines as Michael acceptor at both position 2 and 5, promoting the formation of extended conjugated polymer structures.[75,178] Thus, (*S*)- or (*R*)- atropoisomeric 1,1'-binaphthyl-2,2'-diamine, citric acid and an optimized amount of benzoquinone were mixed in DMF and heated up to 240 °C in a MW reactor (see Figure 2.6 and Experimental section **2.4.2**).

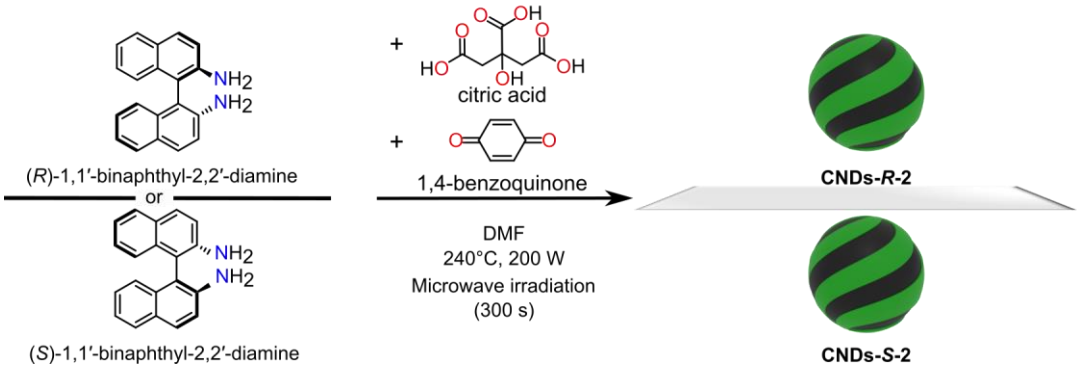

Figure 2.6. Synthesis of atropoisomeric **CNDs-2**.

Simple mixing of benzoquinone with the other precursors afforded a burgundy color mixture. This color change was not observed for **CNDs-1**, indicating that 1,4-benzoquinone reacts with atropoisomeric amines already at r.t. The mixture turned into a dark brown solution upon MW treatment. The crude was filtered to remove any large particle, and **CNDs-2** were precipitated from Et_2O. The effective removal of small molecules using this straightforward purification procedure was confirmed by thin-layer chromatography (TLC) analysis and ^{1}H-NMR. Further validation of the purification procedure was obtained performing an additional SEC separation, which afforded fractions having similar optical properties, indicating material homogeneity (see Figure 2.7 and Experimental section **2.4.2**).[43,179]

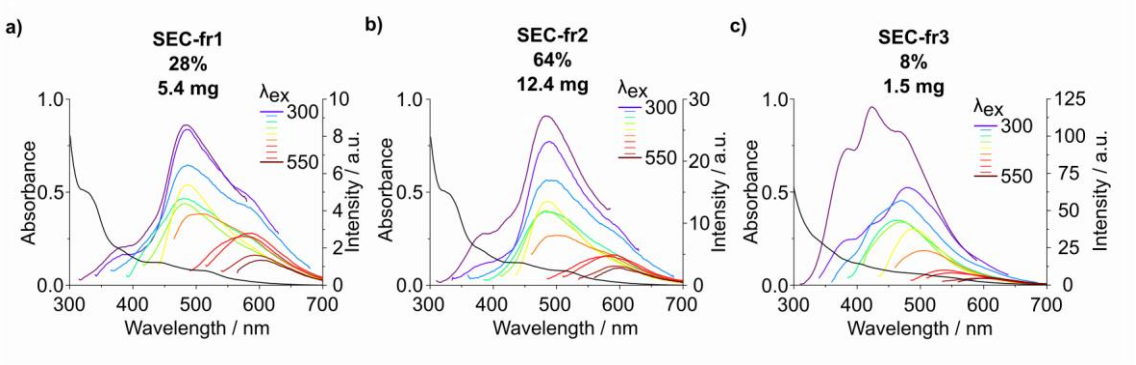

Figure 2.7. UV-Vis and fluorescence emission spectra of a) SEC-fr1, b) SEC-fr2 and c) SEC-fr3 recorded at different excitation wavelengths. Experiments performed in $CHCl_3$ at r.t.

The obtained CNDs, termed **CNDs-*S*-2** or **CNDs-*R*-2**, are soluble (*e.g.* > 20 mg/mL) in common polar organic solvents, such as DMF, DMSO, $CHCl_3$, and dichloromethane (DCM), indicating good processability. Partial solubility in water can also be achieved. Structural and morphological information on atropoisomeric **CNDs-2** was obtained by transmission electron microscopy (TEM), AFM, XPS, ATR-FTIR, and nuclear magnetic resonance (NMR) analysis. TEM analysis of **CNDs-*S*-2** reveals particles having a mean size of 3.5 nm (Figure 2.8a), consistently smaller than other CNDs synthetized using citric acid as core precursor (mean size of 15 nm).[180] The quasi-spherical nature of **CNDs-*S*-2** was confirmed by AFM analysis, which showed a uniform height distribution centered at 3.6±0.5 nm, fully consistent with the TEM data (Figure 2.8b-c). ^{1}H-NMR of **CNDs-*S*-2** in $CDCl_3$ displays broad signals in the aromatic (8.5-6.5 ppm) and aliphatic (3.5-1 ppm) regions of the spectrum, together with a less intense broad signal at ca. 6 ppm, pointing at the inclusion of all precursors and, at the same time, at the absence of molecular species (Figure 2.7d). Indeed, broad signals are coherent with the formation of particles, leading to H atoms experiencing different environments and slow rotation.[54] Analogous results are observed for **CNDs-*R*-2** (see Experimental section **2.4.2**).

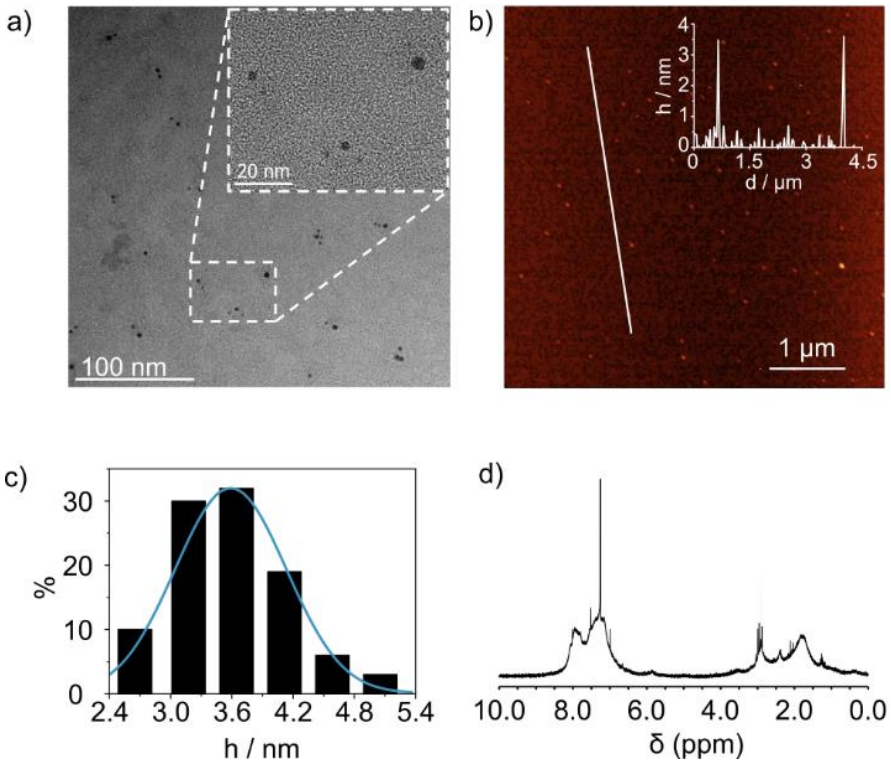

Figure 2.8. a) TEM image of **CNDs-*S*-2**: inset is the dashed area at higher magnification. b) Tapping mode AFM of **CNDs-*S*-2** deposited on a mica substrate; inset is the height profile along the white solid line. c) Size histogram of AFM height data, with distribution fit (blue curve) based on a Gaussian distribution. Statistical analysis is carried out on 100 nanoparticles. d) ^{1}H-NMR ($CDCl_3$, 400 MHz, r.t.) of **CNDs-*S*-2**.

The chemical composition of **CNDs-2** was investigated by XPS analysis (Figure 2.9 and Table 2.2). XPS survey for **CNDs-*S*-2** and **CNDs-*R*-2** indicate effective nitrogen inclusion into the nanomaterial, with 5.6% N, 12.5% O, and 81.9% C and 5.7% N, 14.2% O, and 79.5% C observed for **CNDs-*R*-2** and **CNDs-*S*-2**, respectively.

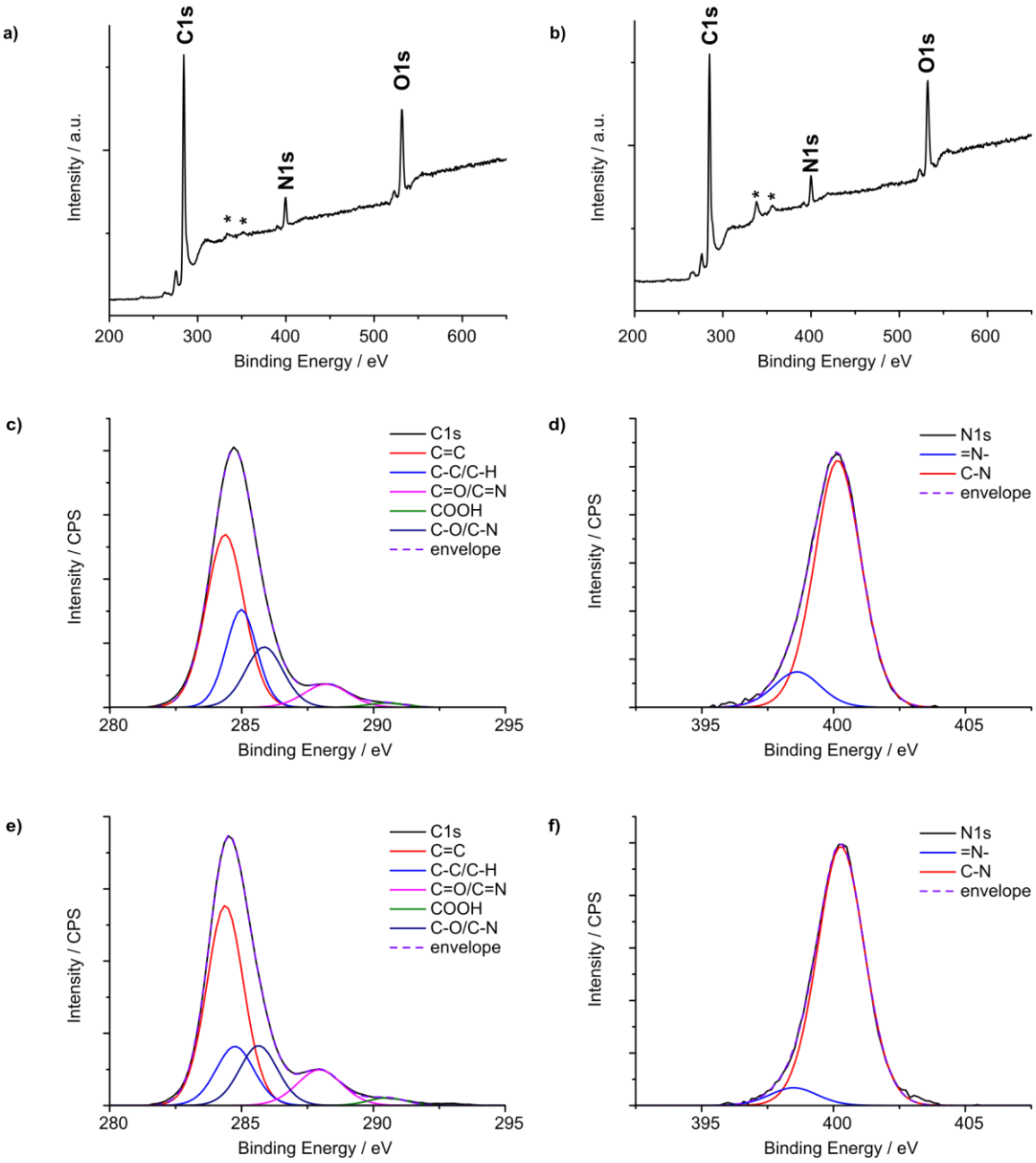

Figure 2.9. XPS survey of a) **CNDs-*R*-2** and b) **CNDs-*S*-2**, showing the C1s, N1s and O1s peaks (* from gold substrate Au4d3, Au4d5 and Au4p). c, d) Deconvoluted C1s and N1s spectra of **CNDs-*R*-2**; e, f) deconvoluted C1s and N1s spectra of **CNDs-*S*-2**.

Deconvolution of C1s peak indicates that ca. 50% of C participate in C=C bonds and reveals the presence of residual COOH groups. Analysis of N1s peak indicates amino groups as the main component associated with N, with an increase in C=N bonds observed upon benzoquinone addition, *i.e.*, in comparison with **CNDs-1** (see Figure 2.3 and Table 2.1 for comparison).

Table 2.2. XPS percentage of C, N, and O atoms and their deconvoluted components in **CNDs-*R*-2** and **CNDs-*S*-2** as determined by XPS measurements.

	CNDs-*R*-2	**CNDs-*S*-2**
C%	**81.9**	**80.0**
C=C	50.3	53.5
C-C/C-H	23.0	16.3
C=O/C=N	7.9	11.6
COOH	1.2	2.1
C-O/C-N	17.5	16.5
N%	**5.6**	**5.7**
=N-	12.6	6.4
C-N	87.4	93.6
O%	**12.5**	**14.3**

Coherent information is obtained from ATR-FTIR by comparison with the starting materials (Figure 2.2d). The two sharp N-H stretching signals of the diamine precursor at 3475 and 3382 cm^{-1} disappeared, with new signals observed between 1618 and 1573 cm^{-1}, in the region of N-H bending. The presence of binaphthyl units is confirmed by the distinctive strong signals at 815 and 749 cm^{-1}, assigned to the out-of-plane bending of aromatic C-H bonds, which are slightly shifted with respect to the starting diamine.[181] The presence of carbonyl functional groups is indicated by an intense signal at 1707 cm^{-1}, which originates mainly from citric acid, as revealed by the comparison with **CNDs-1**, obtained in the absence of benzoquinone, which nevertheless show a similar peak at 1709 cm^{-1}(Figure 2.2c).

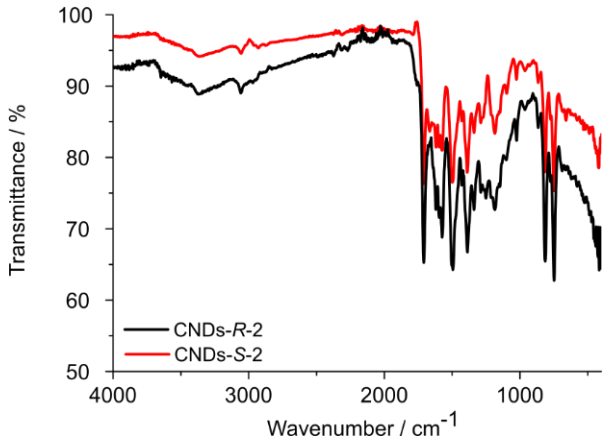

Figure 2.10. ATR-FTIR spectra of **CNDs-*R*-2** (black line) and **CNDs-*S*-2** (red line).

The UV-Vis absorption spectra of **CNDs-*S*-2** and **CNDs-*R*-2** in $CHCl_3$ (Figure 2.11a) display broad absorption bands extending into the visible region up to 600 nm. Non-structured shoulders appear at 285 and 425 nm, possibly ascribed to n-π* and π-π* electronic transitions. Since starting diamine does not absorb above 400 nm (Figure 2.11b), **CNDs-2** formation affords low-energy optical transitions in the visible region. The new band was tentatively ascribed to an extended conjugation of the atropoisomeric moiety reacting with 1,4-benzoquinone, already at r.t. The ECD spectra of **CNDs-*S*-2** and **CNDs-*R*-2** in $CHCl_3$ (Figure 2.11c) demonstrate the chiral nature of atropoisomeric **CNDs-2**. Indeed, the two spectra have equal intensity and opposite sign. The ECD spectrum displays the low-energy transition in the visible characteristic of atropoisomeric **CNDs-2**.

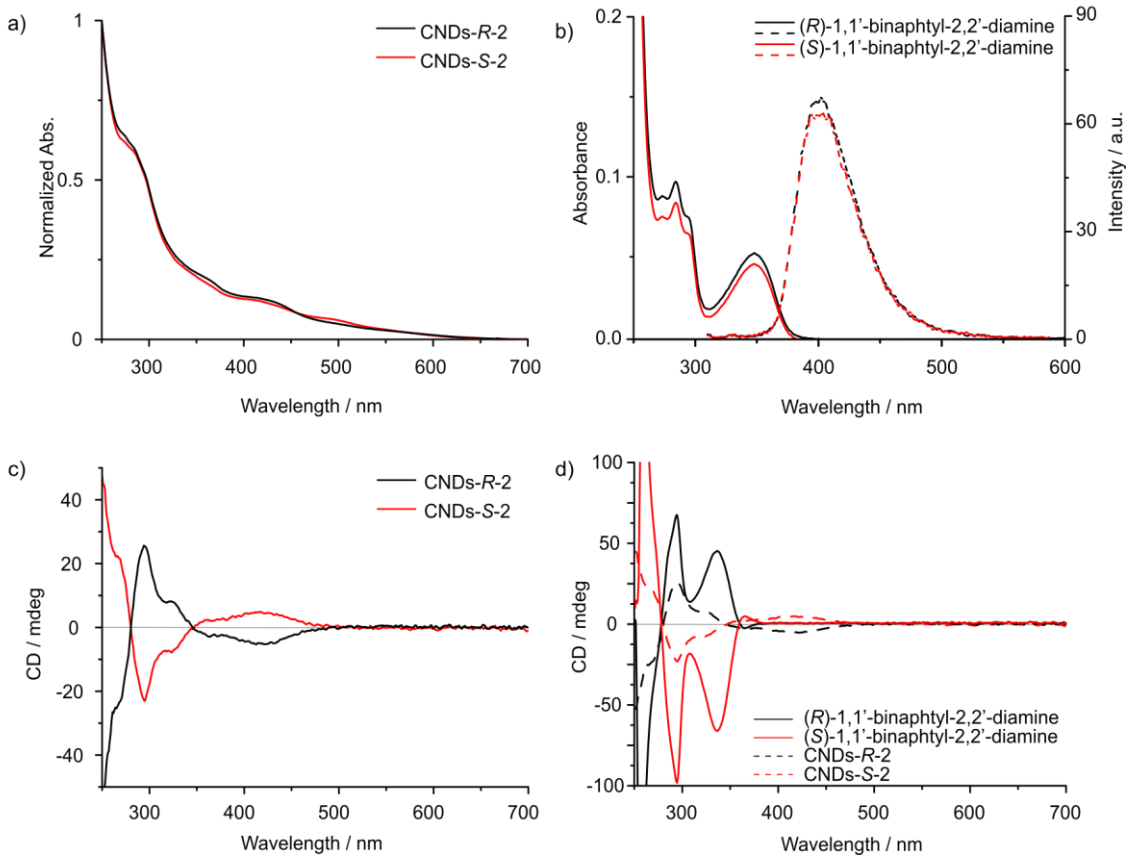

Figure 2.11. a) UV-Vis spectra of **CNDs-*R*-2** (black line) and **CNDs-*S*-2** (red line) in $CHCl_3$. b) UV-Vis spectra (solid lines) and fluorescence emission spectra (dashed lines) of (*R*)- (black line) and (*S*)-1,1′-binaphthyl-2,2′-diamine (red line). Fluorescence emission spectra are recorded at λ_{ex}=300 nm, with a maximum peak at λ_{em}=400 nm c) ECD spectra of **CNDs-*R*-2** (black line) and **CNDs-*S*-2** (red line) in $CHCl_3$. d) ECD spectra of (*R*)- (black solid line) and (*S*)-1,1′-binaphthyl-2,2′-diamine (red solid line). As reference, ECD spectra of **CNDs-*R*-2** (black dashed line) and **CNDs-*S*-2** (red dashed line) are reported. Experiments performed in $CHCl_3$ at r.t..

This new band, centered around 417 nm, is associated with a g_{abs} of $|4.6|\times10^{-4}$. For comparison, in the starting diamine the most red-shifted ECD band (336 nm) was

associated to a g_{abs} of $|2.6|\times10^{-3}$ (Figure 2.11d). Thus, axial chirality is effectively transferred to the nanomaterial. A higher g_{abs} was recorded for **CNDs-1** with respect to **CNDs-2** ($|8.0|\times10^{-4}$ vs. $|4.6|\times10^{-4}$). The difference in g_{abs} between the two families of CNDs is hardly due to a thermal racemization of the binaphthyl unit. Indeed, the reaction temperature profiles are very similar for **CNDs-1** and **CNDs-2**. This experimental evidence suggests that g_{abs} values are governed by variations in the dihedral angle of the binaphthyl unit rather than thermal racemization, as reported in literature.[182] Screening of synthetic parameters also supports the same conclusion. Indeed, a survey of synthesis temperature and time suggests that temperature-induced racemization is not relevant up to 240 °C and reveals that longer reaction times afford higher g_{abs} values (see Experimental section **2.4.2**). The emission spectra of **CND-*S*-2** show a main emission band in the green region, peaking at 480 nm and displaying an excitation wavelength-dependent profile (Figure 2.12). Since the starting diamine emits in the blue region, with an emission centered at 400 nm (Figure 2.11b), **CNDs-*S*-2** formation leads to a significant bathochromic shift of the emission (80 nm). Less intense emissions extending up to 650 nm are also observed, typical of CNDs.

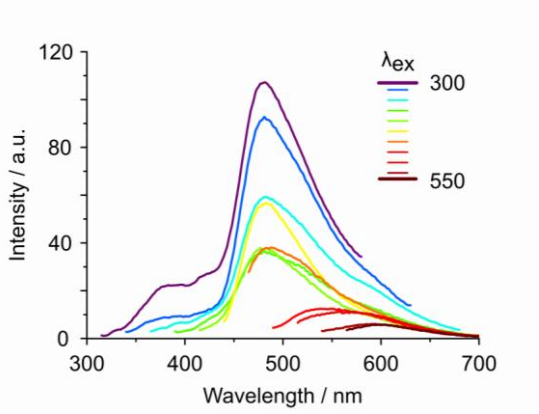

Figure 2.12. Fluorescence emission spectra of **CNDs-*S*-2** recorded at different excitation wavelengths in $CHCl_3$. Experiments performed at r.t., at concentrations between 0.01 and 0.05 mg/mL.

The conjugation effect sustained by the addition of 1,4-benzoquinone was ascertained by experiments in multiple solvents in which atropoisomeric dots are soluble. Indeed, if an hypothetical charge-transfer effect upon light irradiation occurs, the photophysical properties of CNDs would depend strongly on solvent polarity. (Figure 2.13 and Table 2.3). Using the polarity scale introduced by Reichardt[183] for solvatochromic compounds, it is possible to see a trend in g_{abs}. The dissymmetry factor increases up to $|6.0|\times10^{-4}$ in highly polar organic solvents, such as DMF or ethanol, with increasing polarity (as well as the ability of the solvent to participate in H-bonding interactions). On the contrary, the maximum emission wavelength does not change significantly upon changing the solvent polarity. On the base of this experimental evidence, the red-shift in the emission of **CNDs-2** with respect to **CNDs-1** can be ascribed to an extended conjugation, rather than a charge-transfer effect.

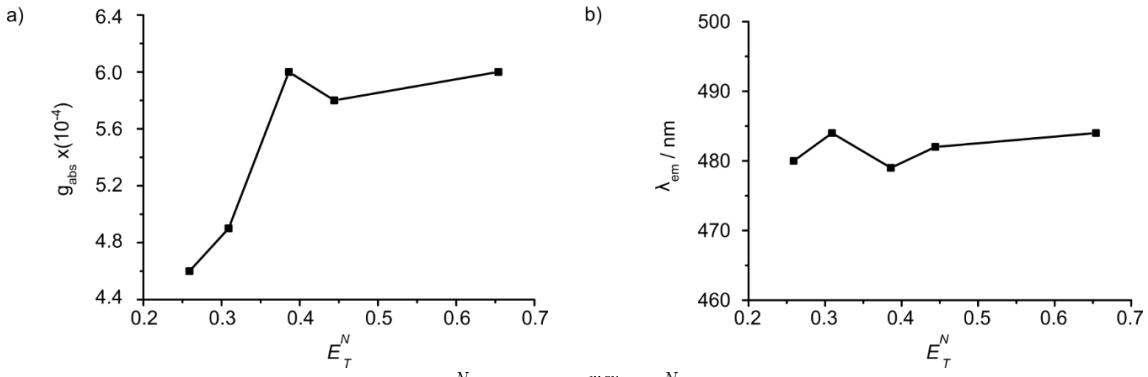

Figure 2.13: Plots of g_{abs} (at 417 nm) *vs* E_T^N (left) and λ_{exc}^{max} *vs* E_T^N (right).

Table 2.3. Values of g_{abs}, λ_{em}, and τ_{ave} obtained for **CNDs-2** in different solvents. Polarity indexes E^N_T are taken from ref. [183].

Solvent	E_T^N	$\lvert g_{abs} \rvert$ ($\times 10^{-4}$)	λ_{em}
$CHCl_3$	0.259	4.6	480
DCM	0.309	4.9	484
DMF	0.386	6.0	479
DMSO	0.444	5.8	482
EtOH	0.654	6.0	484

The fluorescence spectrum of **CNDs-2** shows an emission dependent from the excitation wavelength. To further analyse this behaviour, the relative QY was measured. Accordingly, the luminescence QY changes with the excitation wavelength, ranging from 0.6% at 350 nm down to 0.45% at 450 nm for **CNDs-*S*-2**, in correspondence of the lowest-energy chiral absorption band. Similar results were observed for atropoisomeric **CNDs-*R*-2**, with a value of 0.6% at 350 nm and of 0.35% at 450 nm (Figure 2.14).

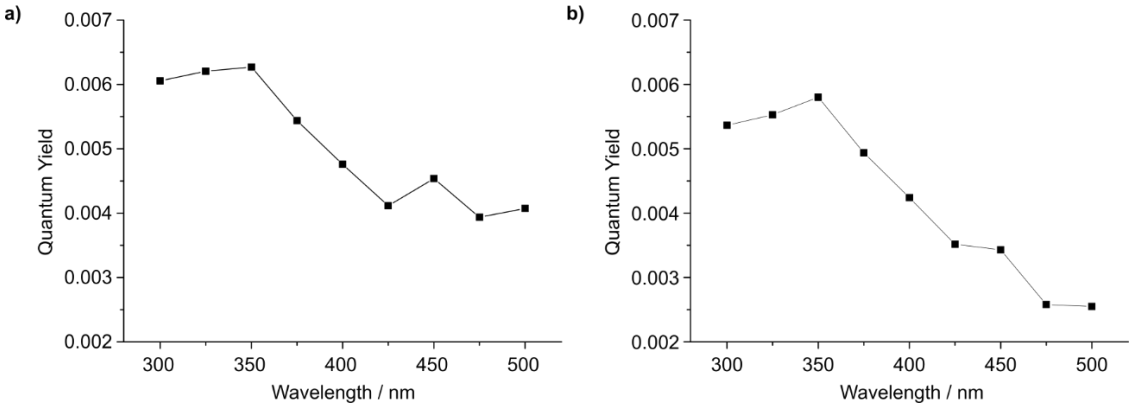

Figure 2.14. Relative QY of a) **CNDs-*S*-2** and b) **CNDs-*R*-2** measured upon changing the excitation wavelength.

Remarkably, upon 365 nm irradiation, **CNDs-2** samples displayed opposite CPL bands centered around 500 nm, negative for **CNDs-*R*-2** and positive for **CNDs-*S*-2**, which

retrace the luminescence profiles (Figure 2.15a). Luminescence dissymmetry factors (g_{lum}) are fairly constant throughout the emission region. Average g_{lum} values were estimated as the ratio between the integral of CPL and the integral of total intensity spectrum calculated in the 420-640 nm range, providing $g_{lum} = +3.6 \cdot 10^{-4}$ and $-3.4 \cdot 10^{-4}$ for **CNDs-*S*-2** and **CNDs-*R*-2**, respectively (Figure 2.15b).

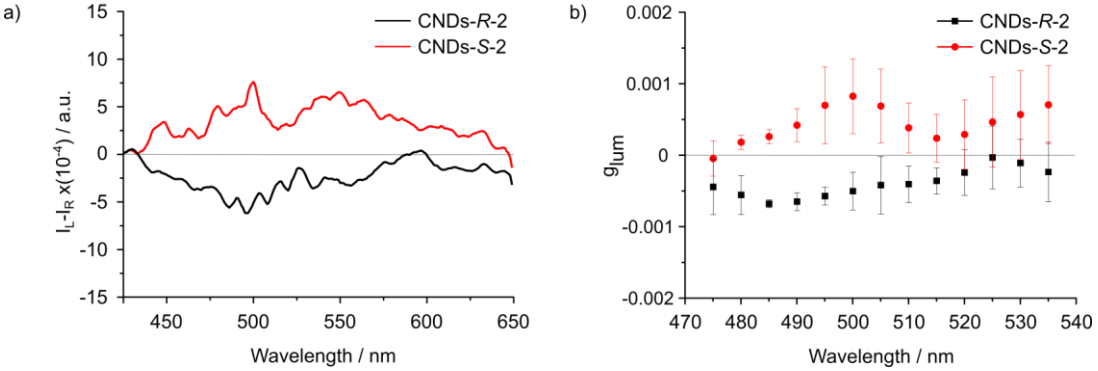

Figure 2.15. a) CPL spectra of **CNDs-*R*-2** (black line) and **CNDs-*S*-2** (red line) in CH_2Cl_2, excited at 365 nm. b) g_{lum} of **CNDs-*R*-2** (black circle points) and **CNDs-*S*-2** (red circle points) *vs* wavelength. Note that g_{lum} is noisy on the spectral edges where emission intensity becomes vanishing small. Experiments were performed at r.t., at concentrations between 0.01 and 0.05 mg/mL.

Such values are in line with the respective g_{abs} of the most red-shifted Cotton effect in the ECD spectra (417 nm, see Figure 2.11c). This indicates a similar stereochemistry of the ground and emitting excited state.[172] The CPL measurements were performed in DCM, which offers a low viscosity. However, similar results were obtained in a more polar and viscous solvent, such as DMF (Figure 2.16). In DMF, the g_{lum} of **CNDs-*R*-2** and **CNDs-*S*-2** are $-3/+4 \cdot 10^{-4}$. These values are similar to the ones measured in DCM, indicating that the solvent nature does not significantly change the CPL response.

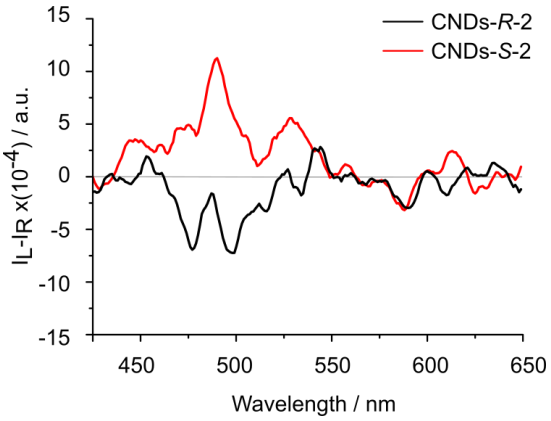

Figure 2.16. CPL spectra of **CNDs-*R*-2** (black line) and **CNDs-*S*-2** (red line) in DMF, excited at 365 nm.

In order to understand the noisy nature of the spectra, we must consider the intrinsic presence of fluorescence linear anisotropies, due to a rotational correlation time (τ_c)

bigger than or comparable with lifetime, inherent to large size systems. Indeed, in the case of **CNDs-2**, through Stokes-Einstein equation, it can be estimated a τ_c~2-3 ns for the average particle (r~1.74 nm) in DCM. This value must be compared with the emission lifetime (τ), 2.7 ns (Figure 2.17 and Table 2.4). $\tau \sim \tau_c$ indicates that the particles retain a significant part of their photoselection because of inefficient tumbling. In order to avoid linear contributions, a particular experimental setup was adopted. The complete description of the setup is reported in the Experimental section **2.4.1**.

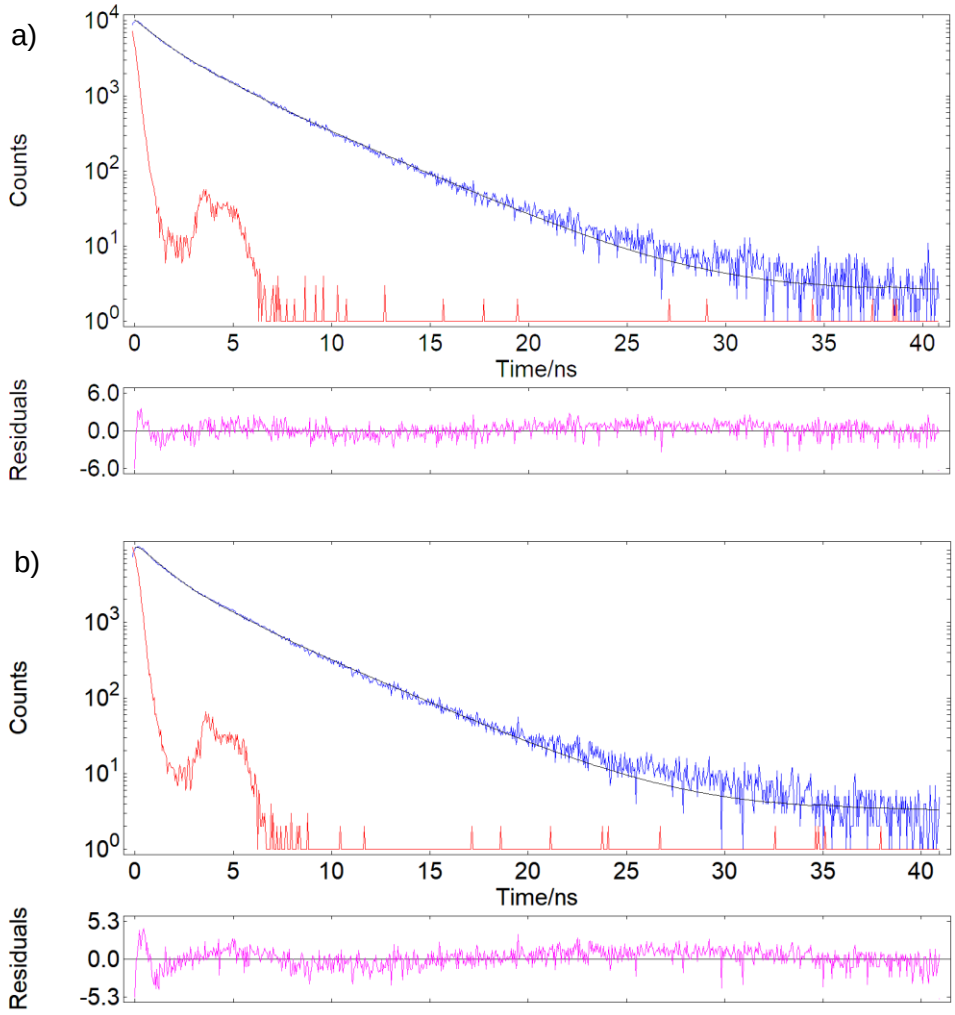

Figure 2.17. Fluorescence decay curve of a) **CNDs-*R*-2** and b) **CNDs-*S*-2** in DCM (λ_{exc} = 375 nm, λ_{em} = 490 nm). The blue curves correspond to the sample fluorescence decay, the red curves correspond to the instrument response function – used to fit the fluorescence decays – and the black curves correspond to the best fit, with their respective residuals (magenta lines).

Table 2.4. Fitting parameters of the fluorescence decay curves.

Sample	A_1	$\tau_1 \pm 0.1$ (ns)	A_2	$\tau_2 \pm 0.1$ (ns)	τ_{ave} (ns)
CNDs-*R*-2	0.07	1.51	0.03	3.86	2.74
CNDs-*S*-2	0.07	1.36	0.03	3.86	2.73

To investigate the role of 1,1'-binaphtyl-2,2'-diamine in CPL generation, we have prepared CNDs in its absence (see Experimental Section **2.4.2**). The obtained achiral material emits at a different wavelength (465 nm) with respect to atropoisomeric **CNDs-2** and has a more pronounced excitation-dependent emission, suggesting that the chiral diamine participates directly to the formation of fluorophores responsible of CPL. On the other hand, 1,1'-binaphtyl-2,2'-diamine alone displays CPL activity in the UV/violet region with a maximum around 395 nm and g_{lum} of $-9 \cdot 10^{-4}$ and $+8 \cdot 10^{-4}$ for *R*-and *S*-enantiomer respectively (Figure 2.18).

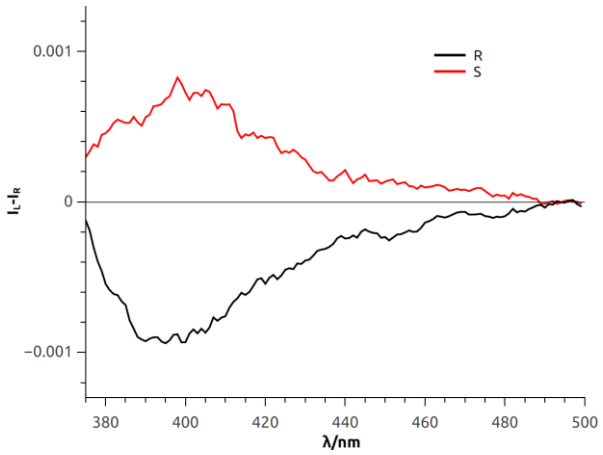

Figure 2.18. CPL spectra of (*R*)- (black line) and (*S*)-1,1′-binaphthyl-2,2′-diamine (red line) in CH_2Cl_2, excited at 365 nm.

Thermogravimetric analysis of **CNDs-2** indicates a moderate weight loss up to 350 °C, possibly due to decarboxylation reactions, followed by a significant weight loss above 400 °C, which might be attributed to Csp^3-rich domains (Figure 2.19a)[176]. A residual 43% weight at 700 °C for both **CNDs-2** further substantiates the abundance of aromatic structures, in full agreement with XPS analysis. On the basis of the negligible weight loss observed at 100 °C, we tested the thermal stability of **CNDs-2** in time. Even after 150 h at 100 °C under air, the g_{abs} of **CNDs-*S*-2** and **CNDs-*R*-2** remained unchanged (Figure 2.19b). Remarkably, while the g_{lum} values are lower than other nanostructured systems, this is the first case in which thermal stability could be investigated.[184–188] The stability of atropoisomeric **CNDs-2**, combined with their good processability, makes this type of nanoparticles suitable candidates for technological applications of CPL under harsh conditions.

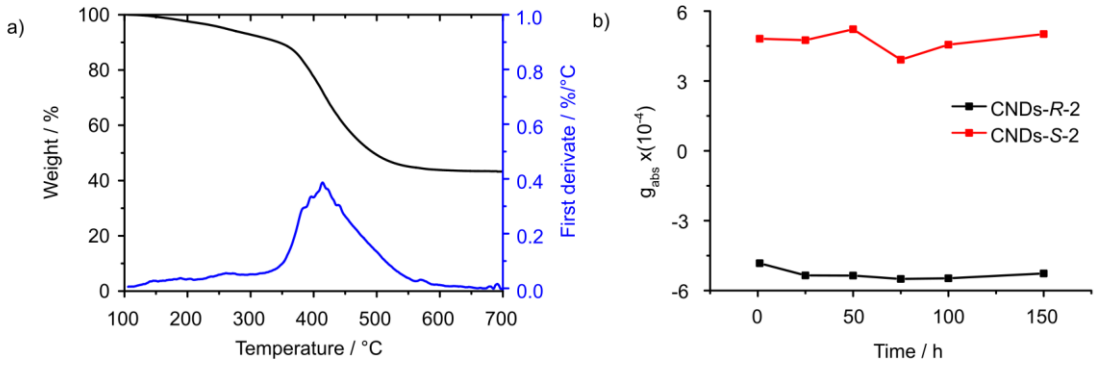

Figure 2.19. Thermal characterization of **CNDs-2**. a) Thermogravimetric analysis of **CNDs-*S*-2** (black line) and its first derivative (blue line). Analysis performed under Nitrogen atmosphere b) g_{abs} of **CNDs-*R*-2** (violet squares) and **CNDs-*S*-2** (green squares) after thermal treatment at 100°C in an oven for the indicated time.

2.3 Conclusions

In conclusion, two families of atropoisomeric CNDs were synthetized *via* bottom-up strategy, using citric acid, binaphthyl diamine, and eventually a dopant as molecular precursors. CNDs were purified and fully characterized with a number of morphological and photophysical techniques. Experimental evidence showed that axially chiral information is retained in the synthesis of CNDs, as assessed by ECD spectroscopy. Importantly, a rational choice of molecular building blocks affords carbon-based nanoparticles displaying CPL as an intrinsic property. Indeed, by preparing novel non-polar chiral CNDs from atropoisomeric precursors, the axial chirality of the starting material is extended from molecular to nanoscale, resulting in nanomaterials displaying CPL. Achieving intrinsic CPL from an easily processable and thermally stable nanoparticle demonstrates the potential of engineering nanomaterials at the molecular level to obtain advanced functionalities.[2]

2.4 Experimental section

2.4.1 General information

MW synthesis was performed on a CEM Discover-SP, using 10 mL glass MW vials. The synthetic protocols could be reproduced also on an Anton Paar 400 MW reactor. NMR spectra were recorded on Varian 400 spectrometer (^{1}H: 400 MHz). UV-Vis measurements were carried out on PerkinElmer Lambda 35 UV-Vis spectrophotometer. All the spectra were recorded at r.t. using 10 mm path-length cuvettes. AFM images were obtained with a Nanoscope IIIa, VEECO Instruments. As a general procedure, AFM analyses were performed using tapping mode with a HQ:NSC19/ALBS probe (80 kHz; 0.6 N/m) (MikroMasch) from drop cast of samples in ethyl acetate diluted solution (concentration in the order of μg/mL) on an exfoliated mica substrate. The obtained AFM images were analyzed in S3 Gwyddion 2.58, using Profile extraction tool and Find peaks function. Statistical analysis was carried out on one hundred nanoparticles. TEM images were acquired on Jeol, JEM 2100, Japan, at 200 kV. The TEM is equipped with Gatan camera and DigitalMicrographs software. Samples were drop cast from an ethyl acetate diluted solution (concentration in the order of μg/mL) on top of a copper grid (copper-grid-supported carbon film), purchased from Ted Pella, Inc. Finally, the solvent was removed in vacuum. ATR-FTIR was performed on a Shimadzu IRAffinity-1S equipped with a QATR-10 with diamond crystal. Typically, spectra were recorded with 4 cm^{-1} resolution and 60 scans accumulation. ECD spectra were recorded using Jasco J-810 at 20 °C. Conditions were as follows: scanning rate 100 nm/min, data pitch 1 nm, Digital Integration Time (D.I.T.) 2 s, 3 accumulations. Luminescence lifetimes were measured with an Edinburgh Instruments FS5 time-correlated single-photon counting spectrofluorimeter, exciting the sample at 375 nm with a picosecond pulsed diode laser (EPL-375 Edimburgh Instruments).

For TLC analysis, Merck pre-coated TLC plates (silica gel 60 GF254, 0.25 mm) were employed, using UV light as the visualizing agent (254 nm). For filtration, Merck Omnipore 0.1 μm PTFE Membrane filters (25 mm) were employed. Organic solutions were concentrated under reduced pressure on a Büchi rotatory evaporator. XPS experiments were performed on a SPECS Sage HR 100 spectrometer with a non-monochromatized X ray source (Magnesium Kα line of 1253.6 eV energy and 252 W), placed perpendicular to the analyzer axis and calibrated using the 3d5/2 line of Ag with a full width at half maximum (FWHM) of 1.1 eV. The selected resolution for the spectra was 15 eV of Pass Energy and 0.15 eV/step. All measurements were made in an ultra-high vacuum chamber at a pressure around $8 \cdot 10^{-8}$ mbar. Samples were prepared drop casting a dispersion of the samples in chloroform on gold slides prepared in house and allowing to dry overnight. CasaXPS software (version 2.3.16 PR1.6) was used for data analysis. Survey spectra were employed to calculate relative atomic composition of all elements present in the samples.

General procedures and materials. CNDs were synthesized in glass MW vials. Commercial reagents and solvents were used as purchased from Sigma-Aldrich or VWR and used as received, without further purification, unless otherwise stated. Citric acid, (*S*)-1,1'-binaphthyl-2,2'-diamine, (*R*)-1,1'-binaphthyl-2,2'-diamine and 1,4-benzoquinone are all commercially available. QY measurements were performed with quinine sulphate in 0.10 M H_2SO_4 (literature QY 0.54 at 360 nm)[43] as standard and **CNDs-*S*-2 or CNDs-*R*-2** in $CHCl_3$ solution. The fluorescence QY were calculated according to the Equation 1

$$\Phi_x = \Phi_{st} \frac{I_x}{I_{st}} \frac{A_{st}}{A_x} \frac{n_x^2}{n_{st}^2}$$

I is the measured integrated fluorescence emission intensity. *A* is the absorbance value, *n* is the refractive index of the solvent and Φ is the QY. The index *x* is referred to the sample, and the index *st* is referred to the standard. The absorbance of the standard and the sample were measured with A<0.1 at the excitation wavelength. The QY was calculated at different excitation wavelengths by taking advantage of the following proportion:

$$\Phi_{exc} \propto \frac{I_{exc}}{A_{exc}}$$

Where the subscript *exc* indicates a specific excitation wavelength. The estimated experimental error on QY is 25%.

CPL measurements were carried out with a home-made spectrofluoropolarimeter.[189] In the current configuration the setup is optimized for visible measurements (400-750 nm), while efficient measurements in the UV region are out of range, due to emission monochromator grating efficiency. This experimental limitation prevented the observation of CPL from **CNDs-1** which may also be CPL-active. The samples were dissolved in CH_2Cl_2 and displayed absorbance 0.25 at 420 nm. A 365 nm LED was used as the excitation source, employing a 90° geometry. The excitation light was linearly polarized parallel to the detection direction. Acquisition parameters were: band-with ~10 nm, scan-speed 1 nm/sec, integration time 8 sec, photomultiplier voltage 600 V, accumulations 20 for spectra in CH_2Cl_2 and 10 for spectra in DMF. $CHCl_3$ was employed in the optical characterization because of its ease of processing (lower boiling point) and UV-cutoff at shorter wavelengths with respect to DMF. This allowed also consistency with NMR characterization, performed in $CDCl_3$. The CPL measurements were performed in DCM, which offers a low viscosity, beneficial in increasing the tumbling rate of the molecules therefore minimizing photoselection. The photoselection may indeed affect measurements since the τ_c (estimated 2-3 ns, based on the size of **CNDs-2**) in CH_2Cl_2 is similar to recorded τ (2.7 ns for **CNDs-2**, Figure 2.17 and Table 2.4). In order to avoid linear contributions, the sample is excited with a 90° geometry, linearly polarizing the excitation source along the detection direction. In this way only

the few molecules that at a given instant do not contribute to fluorescence linear anisotropies are excited. This experimental setup effectively eliminates such linear anisotropies, but it comes at the cost of significantly reducing the photons available for detection. It was noted that even a much polar and completely different solvent such as DMF gives similar CPL spectra (Figure 2.16), indicating that the solvent nature does not significantly change the CPL response.

2.4.2 Synthetic details, characterization and collection of spectra

Synthesis of CNDs-*S*-1 and CNDs-*R*-1

Either (*S*)- or (*R*)-1,1'-binaphthyl-2,2'-diamine (75 mg, 0.264 mmol, 1 eq.) and citric acid (76 mg, 0.396 mmol, 1.5 eq.) were dissolved in DMF (250 μL) and then heated at 240°C, 80 psi and 200 W for 300 seconds. In the process of MW heating, the solution changes color from pale pink to brown as a result of formation of **CNDs-1**. The solution was diluted with DMF and filtered through a 0.1 μm microporous membrane to remove possible large aggregates. The solution was collected and 50 mL of cold diethyl ether were added in order to induce CNDs' precipitation. The precipitate was filtered through a 0.1 μm microporous membrane and washed with 50 mL of Et_2O, giving a pale pink powder (**CNDs-*S*-1**: 18 mg, **CNDs-*R*-1**: 17 mg).

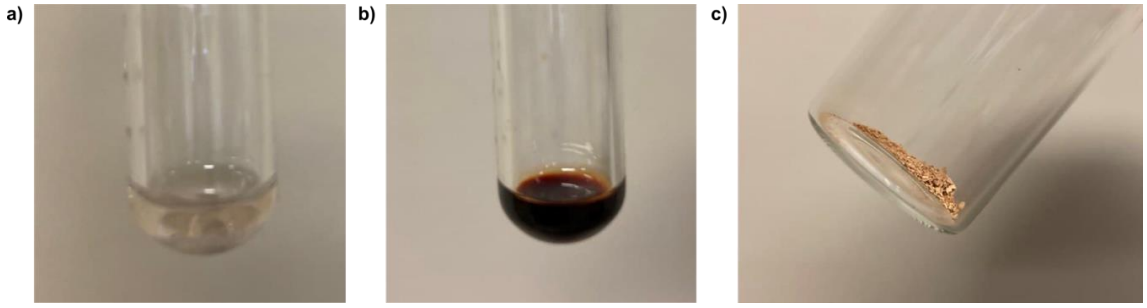

Figure 2.20. Photographs of the vials a) before and b) after MW-heating process and (c) the final **CNDs-1** after precipitation in cold Et_2O and subsequent filtration.

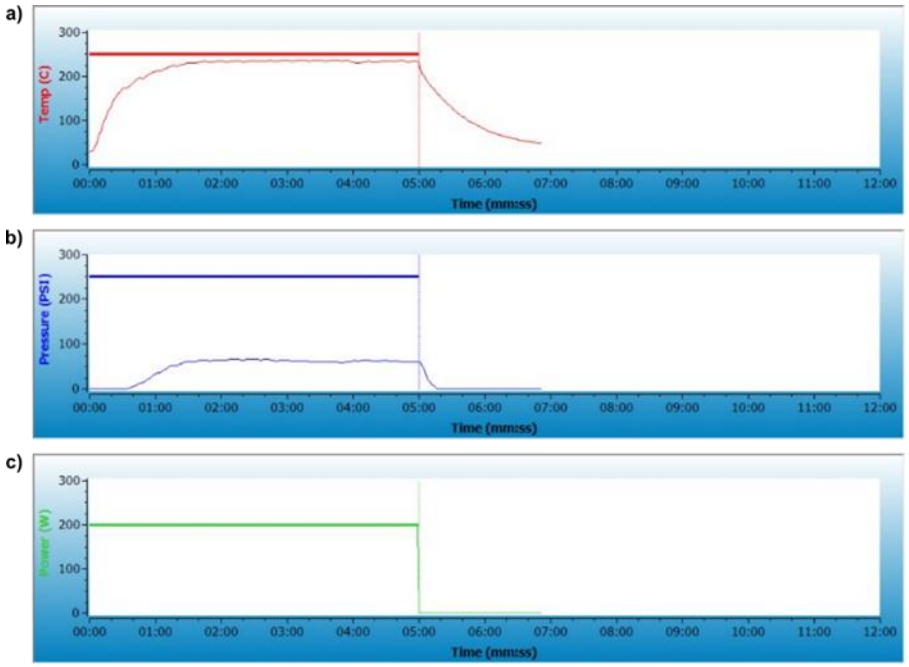

Figure 2.21. Typical a) temperature, b) pressure and c) power profiles recorded during MW-heating process for the synthesis of **CNDs-1**.

Synthesis of CNDs-*S*-2 and CNDs-*R*-2

Either (*S*)- or (*R*)-1,1'-binaphthyl-2,2'-diamine (75 mg, 0.264 mmol, 1 eq.) and citric acid (76 mg, 0.396 mmol, 1.5 eq.) 1,4-benzoquinone (28.5 mg, 0.264 mmol, 1 eq.) were dissolved in DMF (250 μL) and then heated at 240°C, 100 psi and 200 W for 300 seconds. In the process of MW heating, the solution changes color from burgundy to dark brown as a result of formation of CNDs. The solution was diluted with DMF and filtered through a 0.1 μm microporous membrane to remove possible large aggregates. The solution was collected and 50 mL of cold diethyl ether were added in order to induce CNDs' precipitation. The precipitate was filtered through a 0.1 μm microporous membrane and washed with 50 mL of Et_2O, giving a brown powder (**CNDs-*S*-*2***: 41 mg, **CNDs-*R*-*2***: 42 mg). The effective removal of side products is confirmed by TLC. CHX:EtOAc 7:3 or DCM:MeOH 95:5 were employed. Using the former eluent, **CNDs-2** have an R_f of 0, while other impurities can be identified only in the crude (at higher R_f), but not in the final product. The latter eluent reveals a uniform, broad, stripe with R_f of ca. 0.5. It is possible to solubilize **CNDs-2** in water at spectroscopic concentrations by dissolving them first in DMSO and then adding an aliquot of the obtained solution in water.

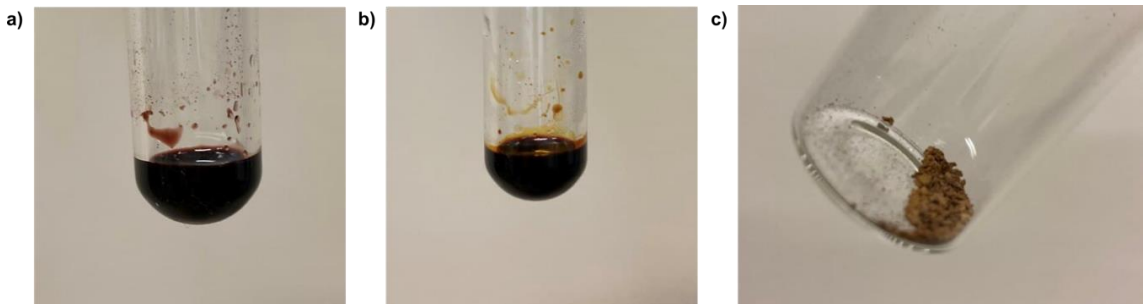

Figure 2.22. Photographs of the vials a) before and b) after MW-heating process and c) the final **CNDs-2** after precipitation in cold Et_2O and subsequent filtration.

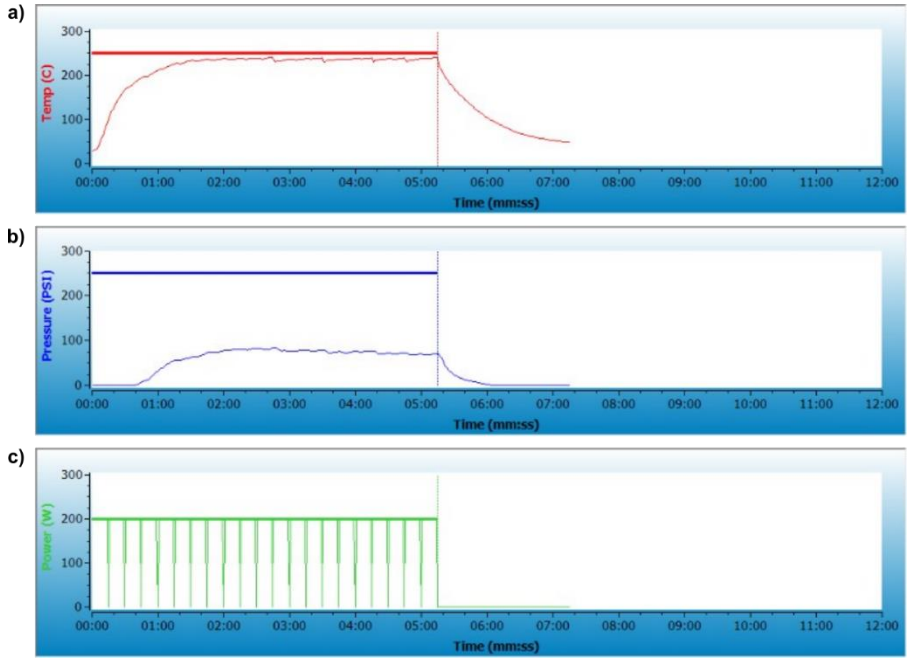

Figure 2.23. A typical a) temperature, b) pressure and c) power profiles recorded during MW-heating process for the synthesis of **CNDs-2**.

Screening of the doping agents for CNDs-2

As a general procedure, the screening of different dopant agents was carried out following the same synthetic protocol of **CNDs-2**, replacing 1,4-benzoquinone with 2,3-dimethoxy-5-methyl-1,4-benzoquinone, 1,4-naphthoquinone or terephthalaldehyde.

Table 2.5. Mass and g_{abs} values obtained upon the addition of a dopant different from 1,4-benzoquinone.

Dopant	mmol/mass added	g_{abs} *(10^{-4})	Solid color	mass (mg)
1,4-benzoquinone	0.264 mmol/28.5 mg	4.6 (λ=417 nm)	brown	41
2,3-dimethoxy-5-methyl-1,4-benzoquinone	0.264 mmol/48 mg	-6.8 (λ=291 nm)	brown	27
1,4-naphthoquinone	0.264 mmol/41.7 mg	-2.3 (λ=285 nm)	brown	11
Terephthalaldehyde [a)]	0.264 mmol/28 mg	5.4 (λ=291 nm)	yellow	54

[a)] This reaction was carried out using (*R*)-1,1′-binaphthyl-2,2′-diamine, the others with (*S*)-1,1′-binaphthyl-2,2′-diamine.

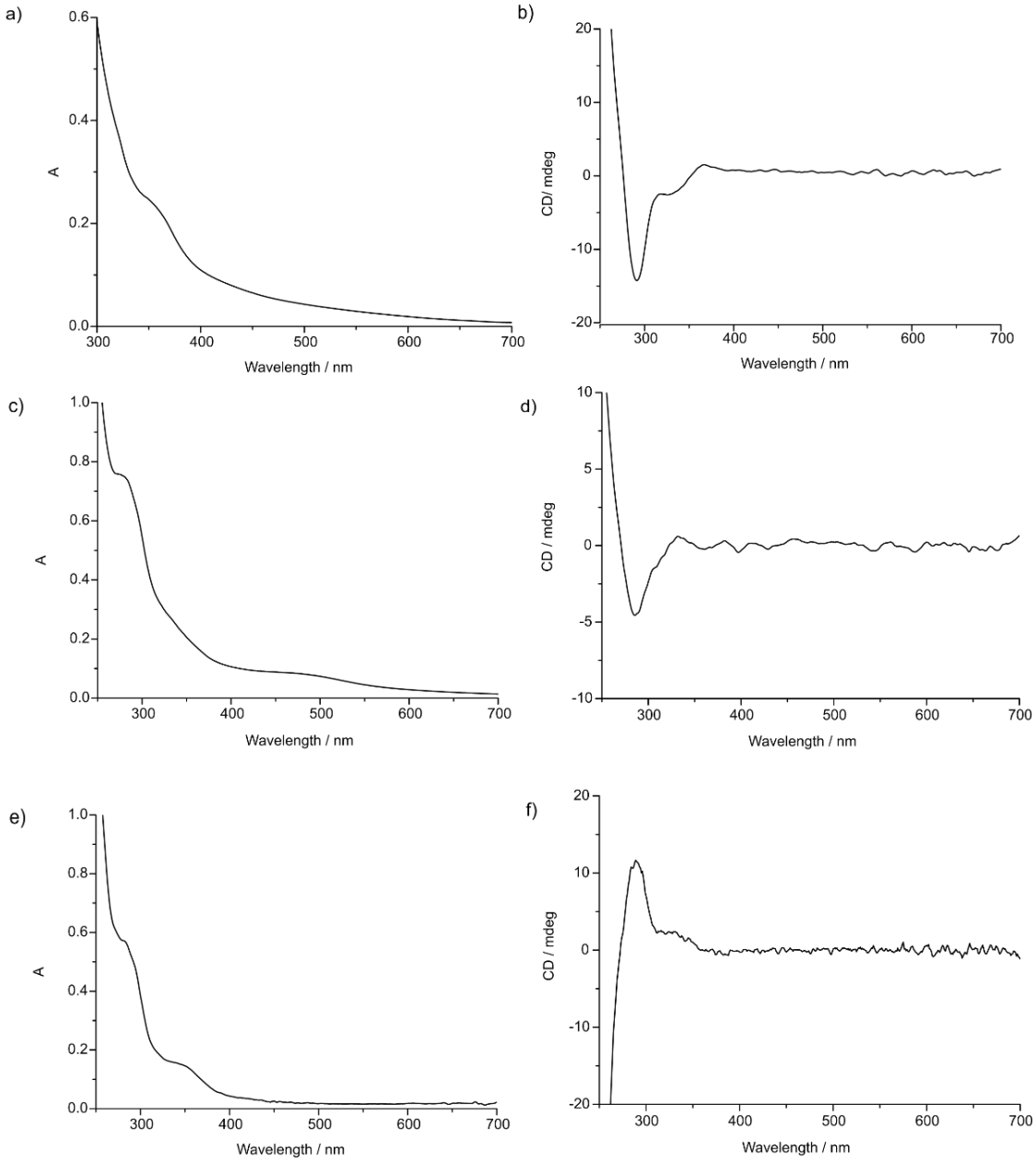

Figure 2.24. UV-Vis and ECD spectra of CNDs from a, b) 2,3-dimethoxy-5-methyl-1,4-benzoquinone; c, d) 1,4-naphthoquinone; e, f) terephthalaldehyde. Spectra recorded in $CHCl_3$.

Survey of synthetic parameters for CNDs-2

As a general procedure, citric acid (76 mg, 0.396 mmol, 1.5 eq), (*S*)-1,1′-binaphthyl-2,2′-diamine (75 mg, 0.264 mmol, 1 eq.) and benzoquinone (28.5 mg, 0.264 mmol, 1 eq.) and were dissolved in DMF (250 µL) and then reacted at 240°C, 200 W for 300 seconds. In the process of MW heating, the solution changes color from burgundy to dark brown as a result of formation of CNDs. The solution was diluted with DMF and

filtered through a 0.1 μm microporous membrane to remove possible large aggregates. The solution was collected and 50 mL of cold Et_2O were added in order to induce CNDs' precipitation. The precipitate was filtered through a 0.1 μm microporous membrane and washed with 50 mL of Et_2O, giving a brown solids. In the case of entry (E), MW power was set at 300 W in order to reach a higher temperature.

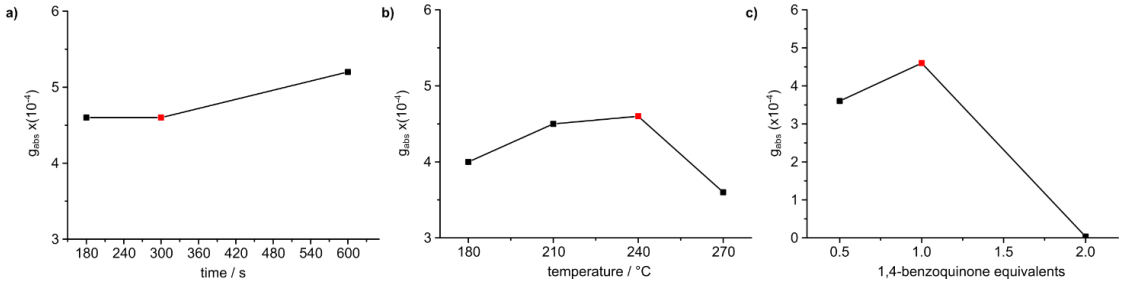

Figure 2.25. Trend of the g_{abs} calculated at 417 nm in function of (a) time, (b) temperature and (c) eq. of 1,4-benzoquinone. Red squares indicate the standard synthesis conditions.

Table 2.6. Mass and g_{abs} values measured at 417 nm obtained upon modifying one synthetic parameter, either time, temperature or eq. of 1,4-benzoquinone.

	Modified parameter	Value (unit)	g_{abs} *(10^{-4})	mass (mg)
	none	240 (°C), 200 (W), 300 (s)	4.6	41
A.	time	180 (s)	4.6	40
B.	time	600 (s)	5.2	43
C.	temperature	180 (°C)	4.0	34
D.	temperature	210 (°C)	4.5	32
E.	temperature	270 (°C)	3.6	64
F.[a)]	amount of BQ	0.5 (eq.)	-3.6	24
G.	amount of BQ	2.0 (eq.)	0.03	65

a) This reaction was carried out using (*R*)-1,1′-binaphthyl-2,2′-diamine.

Size exclusion chromatography analysis of CNDs-*S*-2

For SEC separation, a column packed with Sephadex LH-20 in DMF operating at atmospheric pressure was employed. **CNDs-*S*-2** (19.4 mg) were dissolved in DMF (2 mL) and separated by SEC. Three fractions named SEC-fr1, SEC-fr2 and SEC-fr3 were obtained, according to their elution time. Finally, DMF was removed under reduced pressure, obtaining three oils. (SEC-fr1: 5.4 mg, SEC-fr2: 12.4 mg, SEC-fr3: 1.5 mg). All fractions display the typical excitation-dependent emission profile, with minor differences consistent with the presence of slightly different families of CNDs.[43]

Characterization of CNDs-*R*-2

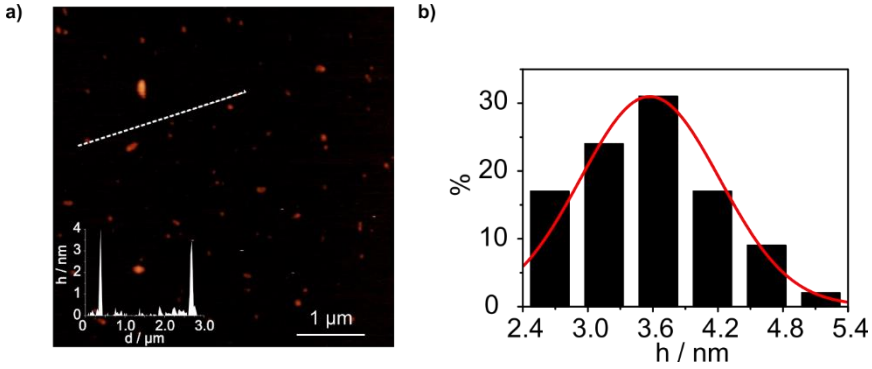

Figure 2.26. a) Tapping mode AFM of **CNDs-*R*-2** deposited on a mica substrate; inset is the height profile along the white dashed line. b) Size histogram of AFM height data, with distribution fit (red curve) based on a Gaussian distribution. **CNDs-*R*-2** possess a mean size of 3.6±0.6 nm, based on a statistic of 100 nanoparticles.

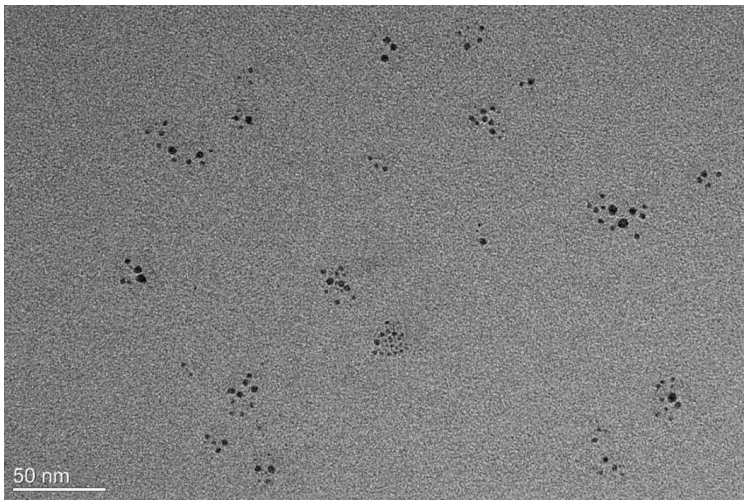

Figure 2.27. TEM image of **CNDs-*R*-2.**

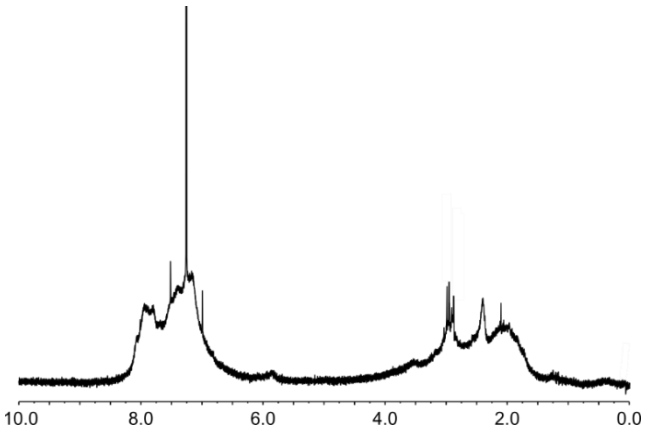

Figure 2.28. ^{1}H-NMR ($CDCl_3$, 400 MHz, r.t.) of **CNDs-*R*-2.**

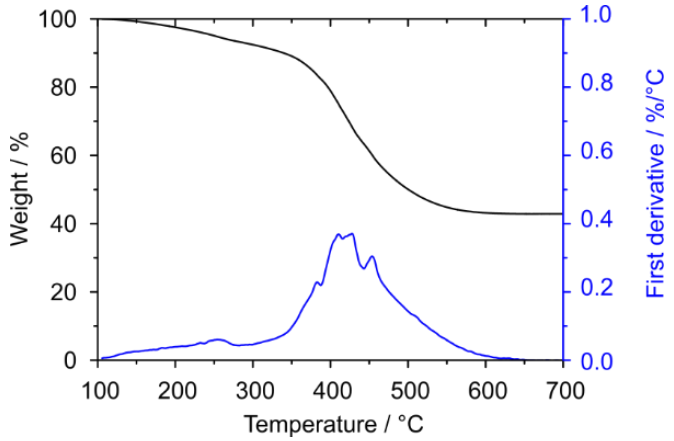

Figure 2.29. Thermogravimetric analysis of **CNDs-*R*-2** (black line) and its first derivative (blue line).

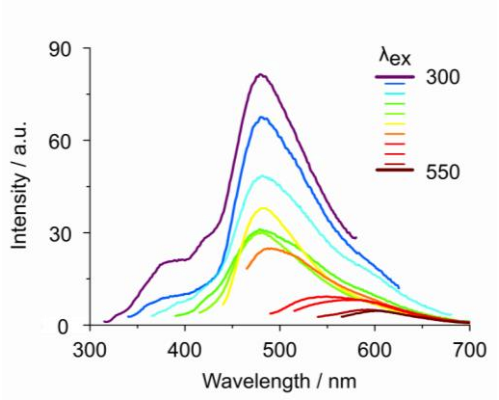

Figure 2.30. Fluorescence emission spectra of **CNDs-*R*-2** recorded at different excitation wavelengths in $CHCl_3$. Experiments performed at r.t., at concentrations between 0.01 and 0.05 mg/mL.

Synthesis of CNDs in absence of chiral diamine

Citric acid (76 mg, 0.396 mmol, 1.5 eq.) and benzoquinone (28.5 mg, 0.264 mmol, 1 eq.) were dissolved in DMF (250 μL) and then heated at 240°C, 200 W for 300 seconds. In the process of MW heating, the solution changes color from yellow to brown as a result of formation of CNDs. The solution was diluted with DMF and filtered through a 0.1 μm microporous membrane to remove possible large aggregates. The solution was collected and 50 mL of cold Et_2O were added in order to induce CNDs' precipitation. The precipitate was filtered through a 0.1 μm microporous membrane and washed with 50 mL of Et_2O, giving a black solid (11 mg). Due to poor solubility of **CNDs-BQ** in $CHCl_3$, the optical characterization was performed in DMSO. As it can be seen, both the absorption and the luminescence spectra are profoundly different between **CNDs-BQ** and **CNDs-2** sample.

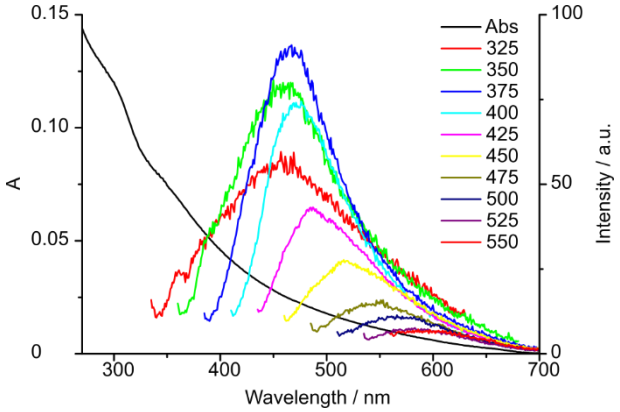

Figure 2.31. UV-Vis absorption and emission spectra of **CNDs-BQ** recorded in DMSO. The excitation wavelengths are shown inside the figure.

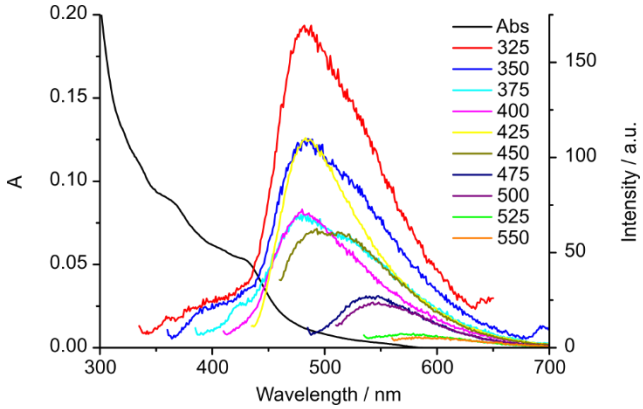

Figure 2.32. UV-Vis absorption and emission spectra of **CNDs-*S*** recorded in DMSO. The excitation wavelengths are shown inside the figure.

Chapter 3

Control on dissipative kinetics enhances the functionality of a minimal molecular machine[3]

3.1 Introduction

Since decades, scientists engaging with nanotechnology have found in Nature a source of inspiration for their work.[83] Indeed, the development of artificial molecular nanotechnologies, similar to those encountered in living organisms, is envisioned as an important technological advancement.[96,110] To this regard, artificial molecular machines have held the limelight of the scientific community, due to their potential to bridge the gap between natural and artificial world.[113,114,138,190,191] The term "molecular machine"[114,138] encompasses a broad range of molecular architectures, having different level of functionality. The simplest case is represented by molecular switches, that interconvert between two states as a consequence of perturbed environmental conditions.[111,121] At higher level of complexity,[192] we find systems that can undergo a cyclic sequence of chemical reactions. The ability to perform cyclic reaction sequences is particularly relevant, because it enables endergonic processes. Indeed, from the point of view of the underlying physics, cyclic chemical reaction networks that are traveled unidirectionally represent a clear demarcation point between chemical reaction networks that can or cannot absorb work from the environment, operating as molecular ratchets.[118,123,124,193,194] Thus, cyclic reaction sequences are a prerequisite to perform more elaborated tasks, such as directional motion and progressivly driving chemical systems away from equilibrium.[190,195] As a general example of cyclic chemical reaction network we consider a square reaction scheme for pseudorotaxane assembly that can be traveled unidirectionally upon alternating acid-base stimuli, leading to energetically-demanding transport (Figure 3.1). This choice stems from the simplicity of pH changes as stimuli to power molecular machinery, and the importance of simplicity for the progress of the field.[112] When the axle is deprotonated – state *i* – the components are thermodynamically disassembled, however, protonation of the axle forms a recognition site for the ring – in state *ii* – leading to thermodynamically favored assembly in state *iii*. Addition of a base will ultimately revert the system to state *i*, but this process can occur *via* either state *i* or state *iv*. Indeed, dethreading from protonated state *iii*, followed by deprotonation of the uncomplexed axle might take place, given the reversibility of self-assembly processes, and the high basicity of basic sites encircled by macrocycles,

[3] This chapter is adapted from "Control on dissipative kinetics enhances the functionality of a minimal molecular machine" Di Noja, S.; Garrido, M.; Gualandi, L.; Ragazzon, G.; *manuscript in preparation*. I am particularly grateful to Dr. Lorenzo Gualandi for the synthesis of symmetric axle **1a** and for the preliminary operation studies using that axle; to Dr. Marina Garrido for the synthesis of some non-commercial hydrazides and the UV-Vis measurements on model compounds.

an established effect in MIMs.[196–198] Importantly, in this scenario dethreading occurs *via* the microscopic reverse process of threading under acidic conditions; therefore, the machine would not complete a cyclic reaction sequence, which is essential to be able to perform work on the environment.

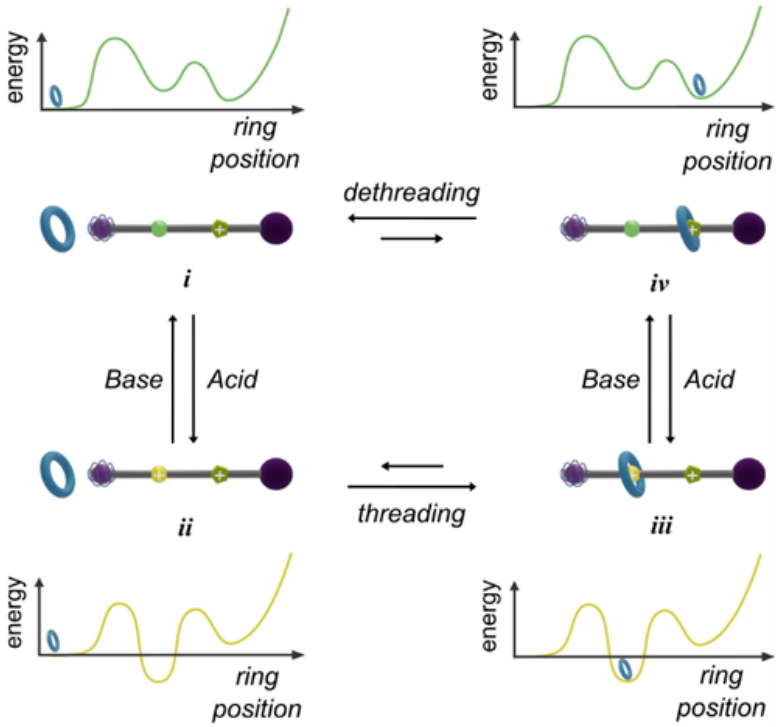

Figure 3.1. Minimal scheme for the operation of a molecular ratchet mechanism driven by the alternation of acid and base inputs, leading to the energetically demanding transport of a macrocycle onto a thermodynamically unfavoured recognition site. Yellow sphere and olive pentagonal prism stations serve as recognition units, while violet spheres represent (pseudo)stoppers.

To engineer a cyclic operation sequence, it is critical to control dethreading kinetics, observing the relaxation from high-energy state *iv* to state *i*. Such a dynamics is considered a dissipative process, of high current interest in relation to transient supramolecular assemblies.[199–206] Engineering a dissipative dynamics in a crown-ether rotaxane is challenging, because it is known that subtle changes in stopper structure lead to large changes in the threading/dethreading kinetics, resulting in a sharp transition from pseudorotaxane to rotaxane-like character of the complex, an effect termed "all-or-nothing" substituent effect.[207,208] So far, studies that approached self-assembly kinetics investigated the threading processes affording thermodynamically stable complexes, whereas the dethreading kinetics from high-energy states – which are expected to be significantly different – remained essentially unexplored.[139] In this Chapter, it is studied the dethreading process from high-energy states in a minimalistic machine powered by acid-base stimuli. Control on its operation was gained, obtaining kinetically-trapped or dissipative states on-demand, which allowed performing repeated ratcheting cycles.

3.2 Results and discussion

To advance the understanding of minimal molecular ratchets, our design was based on a molecular pump module developed by Leigh and coworkers, capable to accumulate multiple macrocycles in a high-energy interlocked structure, upon a sequence of acid-base stimuli.[145,146] The operating mechanism in action is based on the self-assembly of a crown-ether macrocycle onto a dibenzyl ammonium ion, which is one of the most extensively studied recognition motifs in the domain of molecular machines.[16] A key design element is a benzaldehyde terminal of the axle component, which under acidic conditions can react with an hydrazide to form a hydrazone in dynamic equilibrium with the separated components. If the hydrazide bears sufficiently bulky groups, the hydrazone acts as a stopper, affording a rotaxane. Under basic conditions, the dibenzylammonium recognition site and hydrazone dynamicity are lost. As a consequence, the crown-ether remains threaded in a kinetically-trapped high-energy state.[145,146] In the reported architectures, this phenomenon is coupled with crown ether shuttling over a disulfide-controlled speed bump, which has opposite kinetic features with respect to hydrazone, i.e., it is dynamic under basic conditions, resulting in the directional motion of the macrocycle along the axle.[145,146] Leveraging Leigh's design, **1a**H^+ was prepared as a minimal molecular ratchet capable of energetically-demanding transport. Axle **1a**H^+ comprises two key functional elements: a dibenzylammonium recognition site and symmetric terminal aldehydes. The synthesis of **1a**H^+ is achieved using a convergent 6-step strategy, having an overall yield of 34% (see Figure 3.2 and Experimental section **3.4.3**).

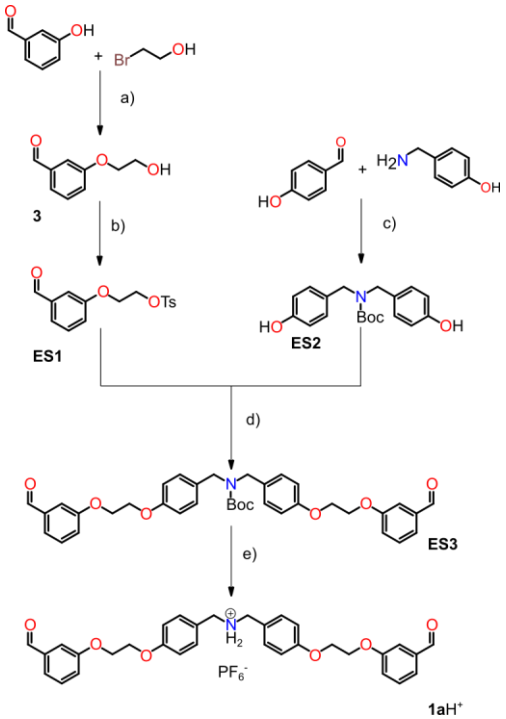

Figure 3.2. Scheme reaction for the synthesis of symmetric axle **1a**H^+. a) 2-Bromoethanol, NaOH, H_2O, reflux 12 h; b) TsCl, NEt_3, DCM, r.t.; c) (1) Na_2SO_4, MeOH (2) $NaBH_4$, MeOH/THF 1:1 (3) Boc_2O, $NaHCO_3$, MeOH, r.t.; d) K_2CO_3, DMF, 80°C, 16 h; e) TFA, DCM, r.t. then NH_4PF_6 (aq.) THF, r.t., 1 h.

As macrocyclic component we selected the extensively used crown ether dibenzo-24-crown-8 (**DB24C8**, Figure 3.3), which is known to have a high affinity for dibenzylammonium ion in non-polar organic solvents.[209]

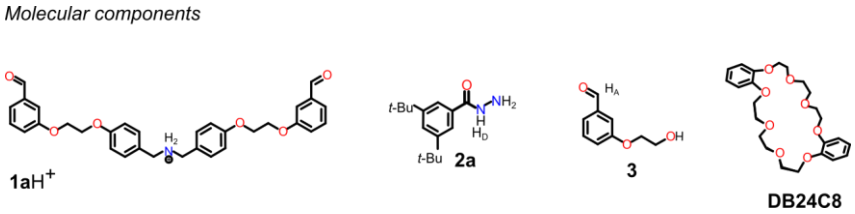

Figure 3.3. Molecular structure of investigated compounds for the operation of symmetric axle **1a**H^+ as a molecular ratchet.

Addition of **DB24C8** to **1a**H^+ in CD_3CN resulted in the formation of pseudorotaxane [**1a**H^+⊂**DB24C8**], as evidenced by the upfield shift in the protons of macrocycle both in the aromatic (*e.g.* from 6.91 to 6.81 ppm, Figure 3.4c-e, green panel) and in the aliphatic region (*e.g.* 4.10, 3.80 and 3.69 ppm to 4.05, 3.77 and 3.59 ppm, respectively, Figure 3.4 c-e, blue panel). In agreement with previous reports, as increasing amounts of **DB24C8** were added , the resonances of uncomplexed **1a**H^+ shlightly shifted towards lower frequencies (*e.g.* from 7.04 to 7.02 ppm) disclosing the underlying rapid equilibrium associated with ion pair formation between **1a**H^+ and its counterion PF_6^-.[210]

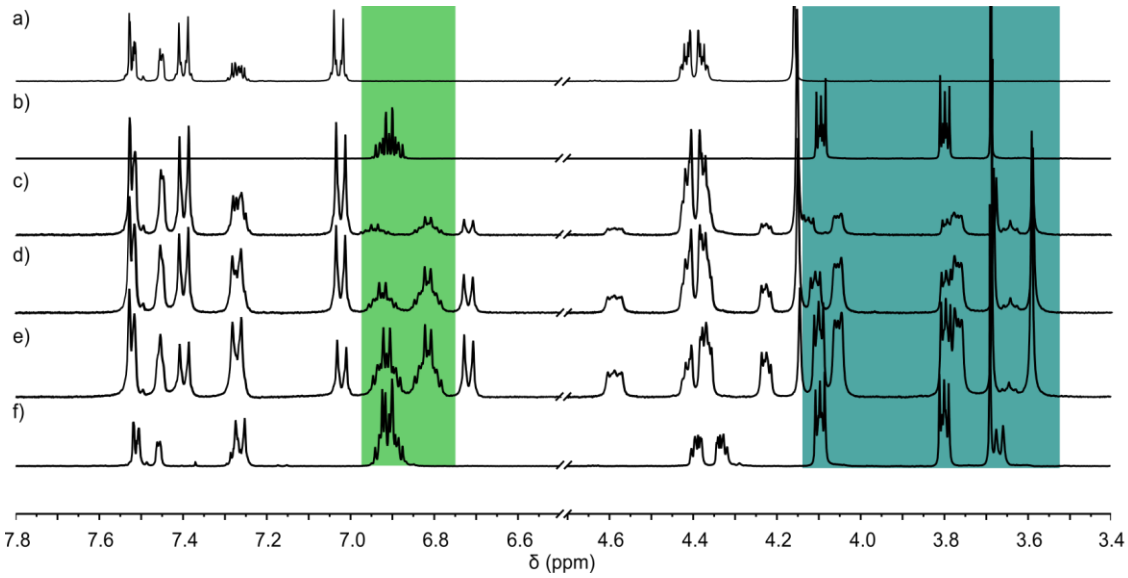

Figure 3.4. Partial ^{1}H-NMR spectra (500 MHz, CD_3CN) of a) **1a**H^+, b) **DB24C8.** Formation of pseudorotaxane [**1a**H^+⊂**DB24C8**] from **1a**H^+ upon addition of c) 0.33, d) 0.5 and e) 1 eq. of **DB24C8**. f) Dethreading of **DB24C8** upon addition of 1.1 eq. of P_1-*t*-Bu to sample e). Concentration of both **1a**H^+ and **DB24C8** and components is 6 mM.

Addition of 1.1 eq. of phosphazene base P_1-*t*-Bu-tris(tetramethylene) (P_1-*t*-Bu) resulted in complete dethreading, as revealed by the disappearance of signals associated with pseudorotaxane and the appearance of peaks related to free deprotonated **1a** species (Figure 3.3f). Both threading and dethreading processes occurred in a period of time

shorter than the one required to record an NMR spectrum, indicating that benzaldehyde terminals do not provide a significant kinetic barrier for **DB24C8** slippage on this time scale. Having established the ability of **1a**H^+ to thread **DB24C8**, we focused our attention on hydrazone stopper features, selecting hydrazide **2a** as starting point (Figure 3.5a), which was already employed to stopper the larger dibenzo-30-crown-10 macrocycle.[145] Optimization studies associated with hydrazone formation were performed using commercially available 3-(2-hydroxyethoxy)benzaldehyde (**3**, Figure 3.5a), which served as a minimal model of **1a**H^+ terminals.

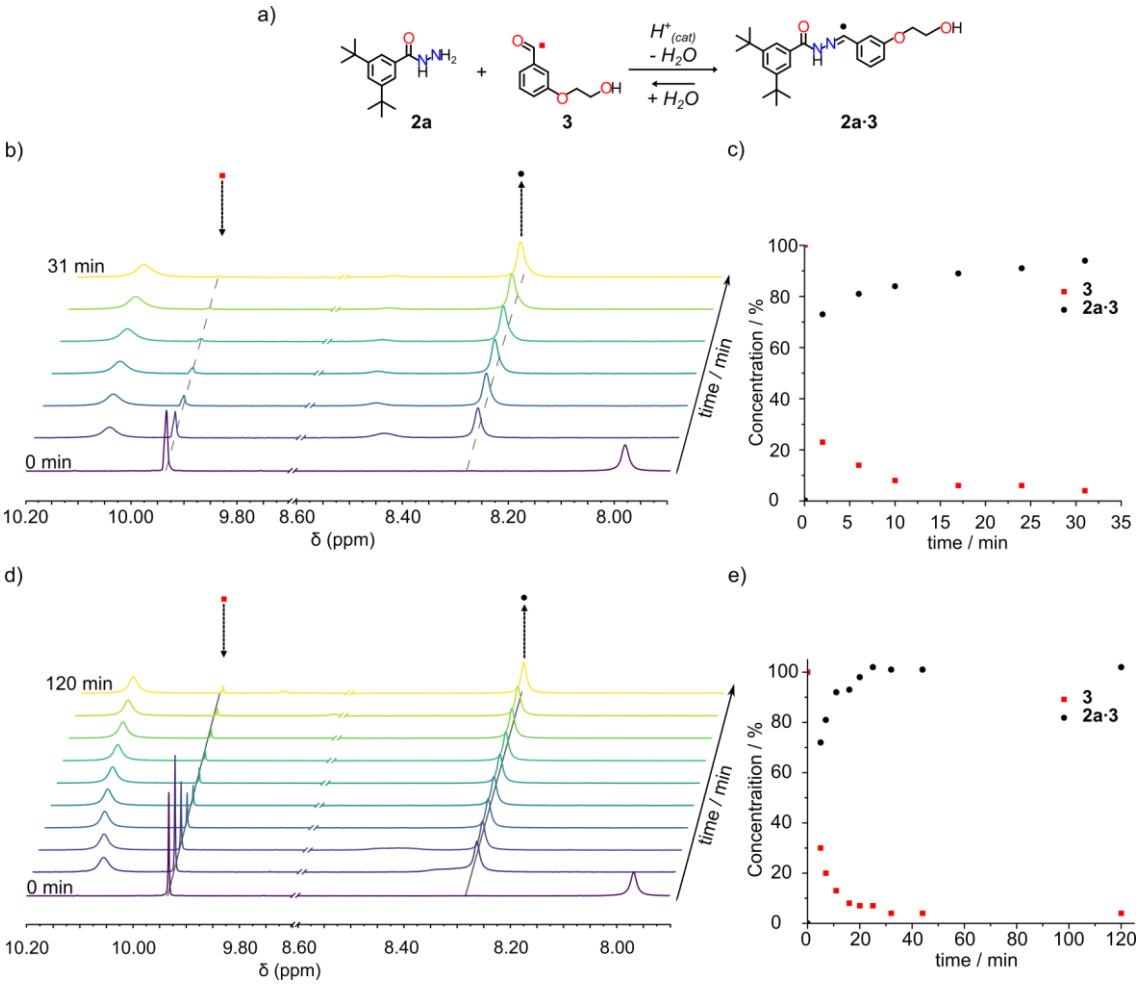

Figure 3.5. a) Schematic representation of the formation of **2a**·**3** from **2a** and **3**. b) Partial stacked ^{1}H-NMR (500 MHz, $CDCl_3$:CD_3CN 3:1) spectra of the reaction between **2a** and **3** (6 mM) to form **2a**·**3** in the presence of b) 0.2 eq. TCA or d) 0.05 eq. TfOH. Spectra from purple to yellow represent the reaction monitored at b) 0, 2, 6, 10, 17, 24 and 31 minutes after the addition of 0.2 eq. TCA and d) at 0, 5, 7, 11, 16, 20, 25, 32, 44 and 120 minutes after the addition of 0.05 eq. TfOH. e) Normalized concentration of **3** (red squares) and **2a**·**3** (black circles) during the time after the addition of c) 0.2 eq. TCA and e) 0.05 eq. TfOH. Concentrations determined from the integration of signals at 9.93 (for **3**) and 8.26 ppm (for **2a**·**3**).

Solutions of **3** and hydrazide **2a** (6 mM of both components) were kinetically stable over time, showing no evidence of hydrazone formation under neutral conditions. The nucleophilic addition of hydrazide could be promoted by addition of acids, such as TCA

or triflic acid, CF_3SO_3H (TfOH). In particular, a screening of experimental conditions indicated that hydrazone formation **2a**·**3** could take place quantitatively (>95%) either upon addition of 0.05 eq. of TfOH over ca. 90 min or of 0.2 eq. of TCA over 30 min. (Figure 3.5b-e). When using higher amounts of acid, the extent of hydrazone formation **2a**·**3** was lower, possibly due to hydrazone hydrolysis becoming a competitive process. Hydrazone formation could be monitored also via UV-vis absorption spectroscopy, following the formation of a new absorption band at 295 nm (Figure 3.6). By using absorption spectroscopy, we could confirm hydrazone formation even at a concentration of 120 µM for both components, and observed that the rate of hydrazone formation under the employed conditions is strongly dependent on the total concentration of acid. Indeed, in the presence of 222 µM TCA the reaction did not proceed, while in the presence of 14.76 mM TCA, the kinetic of hydrazone formation was comparable to that observed using 6 mM components. Control experiments excluded the relevance of light-induced isomerization of hydrazone under our experimental conditions. Indeed, we observed identical outcomes when performing hydrazone formation reaction in the dark or under ambient light.

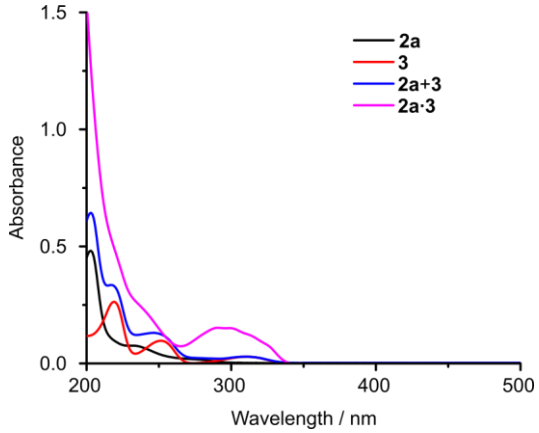

Figure 3.6. UV-Vis spectra of **2a** (black line), **3** (red line), the mixture of **2a** and **3** (blue line) and **2a**·**3** (magenta line) after 90 minutes, upon addition of TCA (14.76 mM) to the mixture of **2a** and **3**. Experiments performed in CH_3CN, 120 µM, r.t.

By combining pseudorotaxane self-assembly with hydrazone formation it was possible to obtain the complex **1a**·**2a**$_2H^+$, which however remains stable in CD_3CN only for a few minutes, after which the solution becomes slightly turbid. Addition of **DB24C8** to **1a**·**2a**$_2H^+$ promoted precipitation, indicating that pure CD_3CN is not an optimal solvent for the present system. Since **1a**·H^+ is not well soluble in pure $CDCl_3$, we identified $CDCl_3$:CD_3CN 3:1 as a suitable mixed solvent system, which could ensure the solubility of both **1a**H^+, and **1**·**2a**$_2H^+$ alone and in the presence of **DB24C8**. To obtain a high-energy state, 1.1 eq. of phosphazene base P_1-*t*-Bu were added to preassembled [**1a**·**2a**$_2H^+$⊂**DB24C8**]. Contrary to what was observed in the absence of **2a**, the signals of uncomplexed **DB24C8** did not increase their intensity, with evidence from ^{1}H-NMR spectroscopy pointing at the deprotonation of [**1a**·**2a**$_2H^+$⊂**DB24C8**], to afford a high-

energy rotaxane [**1a**·**2a**$_2$⊂**DB24C8**], in which **DB24C8** resides onto the hydrazone moiety (Figure 3.7). However, the need to operate in mixed solvent system and the lack of indicative peaks in the ^{1}H-NMR complicated *in situ* monitoring machine operation.

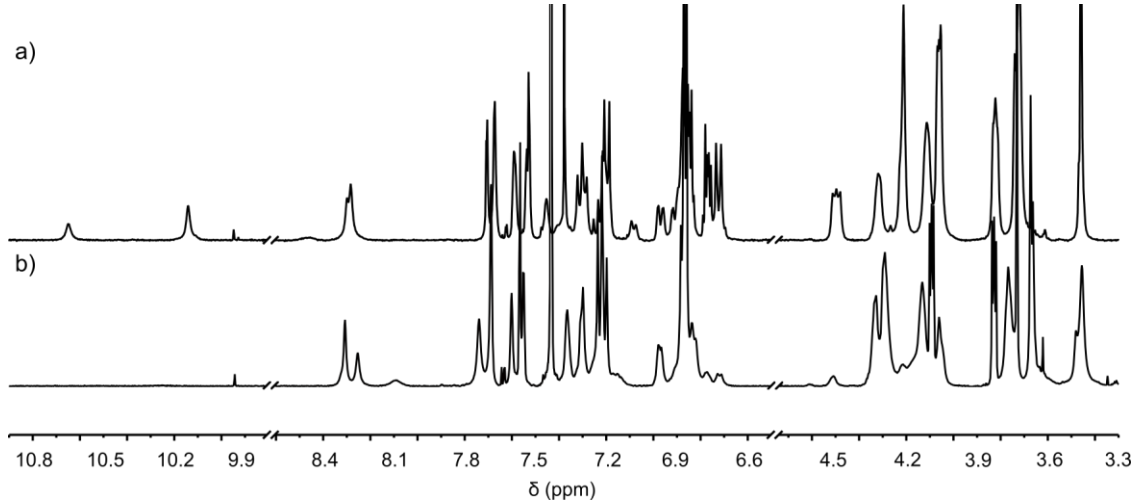

Figure 3.7 Partial ^{1}H-NMR spectra (500 MHz, $CDCl_3$:CD_3CN 3:1) of a) [**1a**·**2a**$_2$H$^+$⊂**DB24C8**] and b) [**1a**·**2a**$_2$⊂**DB24C8**] upon addition of 1.1 eq. of P_1-*t*-Bu.

To improve systems solubility and monitoring, we prepared axle **1b**H$^+$. This molecular machine has a size of ca. 3.5 nm in its fully extended conformation, and would operate according to the reaction scheme in Figure 3.8.

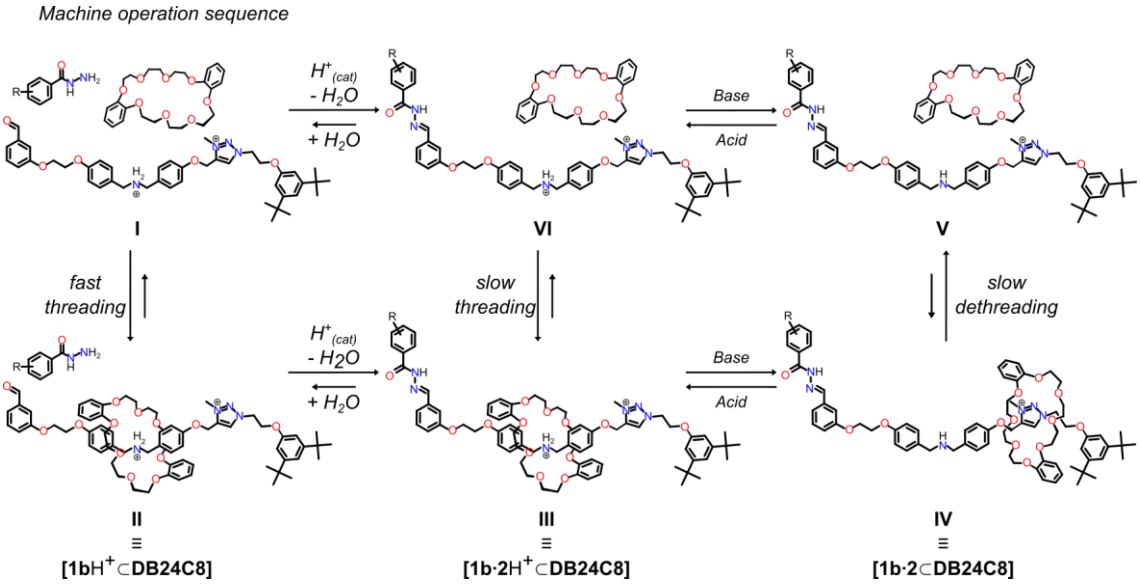

Figure 3.8. Reaction network for the operation of **1b**H$^+$ and a generic hydrazide **2** leading to kinetic trapping of **DB24C8** in high-energy state (IV) as a result of sequential acid-base additions.

Using this asymmetric axle (state I), the formation of pseudorotaxane [**1b**H$^+$⊂**DB24C8**] (state II) and, after dynamic stoppering of the hydrazone, the subsequent generation of rotaxane [**1b**·**2a**H$^+$⊂**DB24C8**] (state III) can be followed. Exploiting acid-base inputs,

the threading/dethreading process was studied. Depending on the size of -R moiety onto hydrazide **2**, the system can undergo directly to a rapid equilibration (state V) or to an energetically-demanding pumping of the ring onto the triazolium station [**1b**·**2a**⊂**DB24C8**] (state IV), confirming machine operation according to a ratchet mechanism. Moreover, if -R has proper dimensions, the system can experience a dissipative dethreading kinetics, revealing a square reaction network underneath the machine operation, which goes from state III to state V *via* state IV. Using an opposite acid/base input, the process can be performed multiple times, pushing the system from state V to VI and realizing a full cycle of threading and dethreading *via* states (III→IV→V→VI→VI). **1b**H^+ can be obtained with an overall 9% yield as a result of a convergent 8-step synthesis, based on the preparation of an asymmetryc dibenzylammonium core having a pendant propargyl moiety, and subsequent click reaction to afford a triazolium secondary station upon methylation (Figure 3.9 and Experimental section **3.4.3**).

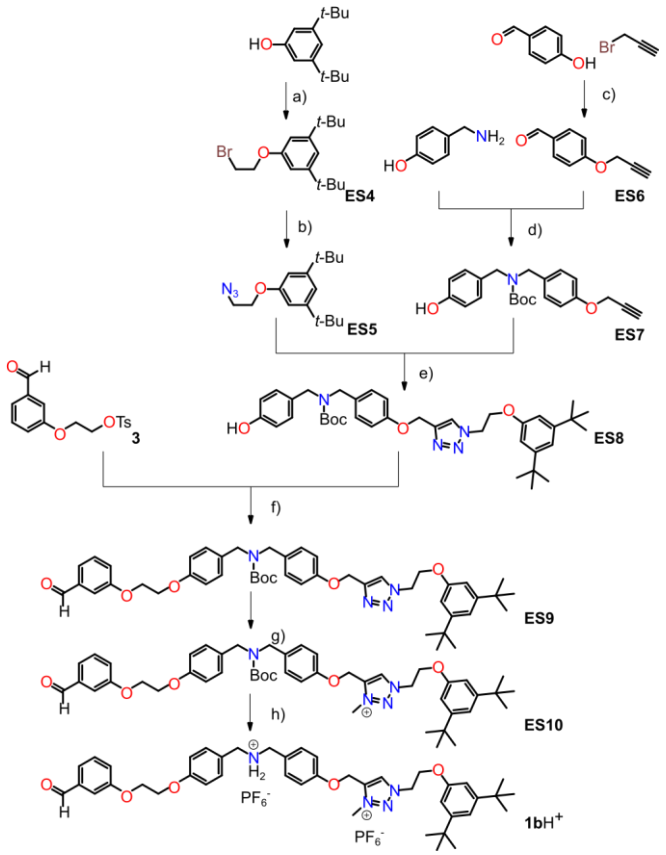

Figure 3.9. Scheme reaction for the synthesis of symmetric axle **1b**H^+.a) K_2CO_3, CH_3CN, reflux, 18 h; b) NaN_3, DMF, r.t., 24 h; c) K_2CO_3, CH_3CN, reflux, 2 h d) (1) Na_2SO_4, MeOH, reflux, 18 h (2) $NaBH_4$, MeOH/THF 1:1, r.t., 6 h; (3) Boc_2O, $NaHCO_3$ MeOH, r.t., 6 h; e) $[Cu(CN)_4]PF_6$, 2,6 lutidine, DCM, r.t., 24 h; f) K_2CO_3, DMF, 80°C, 24 h; g) MeI, 40°C, 8 d; h) TFA, DCM, r.t., 4 h then NH_4PF_6 (aq.) THF, r.t., 18h.

The as-synthetized axle **1b**H^+ has an additional positive charge, improving the solubility in CD_3CN, which was complete under all employed experimental conditions. The triazolium moiety, along with ethylene chain attached to it, offered distinctive ^{1}H-NMR

signals for H_B, H_C, H_D, and H_E (Figure 3.10-I), facilitating *in situ* monitoring of machine operation.[211] Indeed, a stability constant of 225 M^{-1} in CD_3CN for the assembly of [**1b**H^+⊂**DB24C8**] was obtained from the integral ratio of the peaks at 5.32 ppm and 5.14 ppm, ascribed to H_B in uncomplexed and complexed **1b**H^+ (Figure 3.10-II). Hydrazone formation occurred effectively upon addition of hydrazide **2a** and 0.05 eq. of TfOH, as indicated in the ^{1}H-NMR spectrum by the disappearance of H_A signal at 9.99 ppm and the progressive rise of the H_F signal of **2a** in [**1b**·**2a**H^+⊂**DB24C8**] at 10.26 ppm (Figure 3.10-III). Addition of 1.1 eq. of P_1-*t*-Bu to [**1b**·**2a**H^+⊂**DB24C8**] afforded the high-energy complex [**1b**·**2a**⊂**DB24C8**], as evidenced by the disappearance of the H_B signal at 5.14 ppm and the appearance of a new set of peaks, including a singlet at 9.11 ppm and a singlet at 4.73 ppm, relative to H_C and H_B, along with two triplets at 5.45 and 4.70, relative to H_D and H_E (Figure 3.10-IV). The obtained high-energy, kinetically-trapped state was stable in solution for at least 48 h at r.t., during which the ^{1}H-NMR spectra remained unchanged, indicating the high kinetic stability of [**1b**·**2a**⊂**DB24C8**].

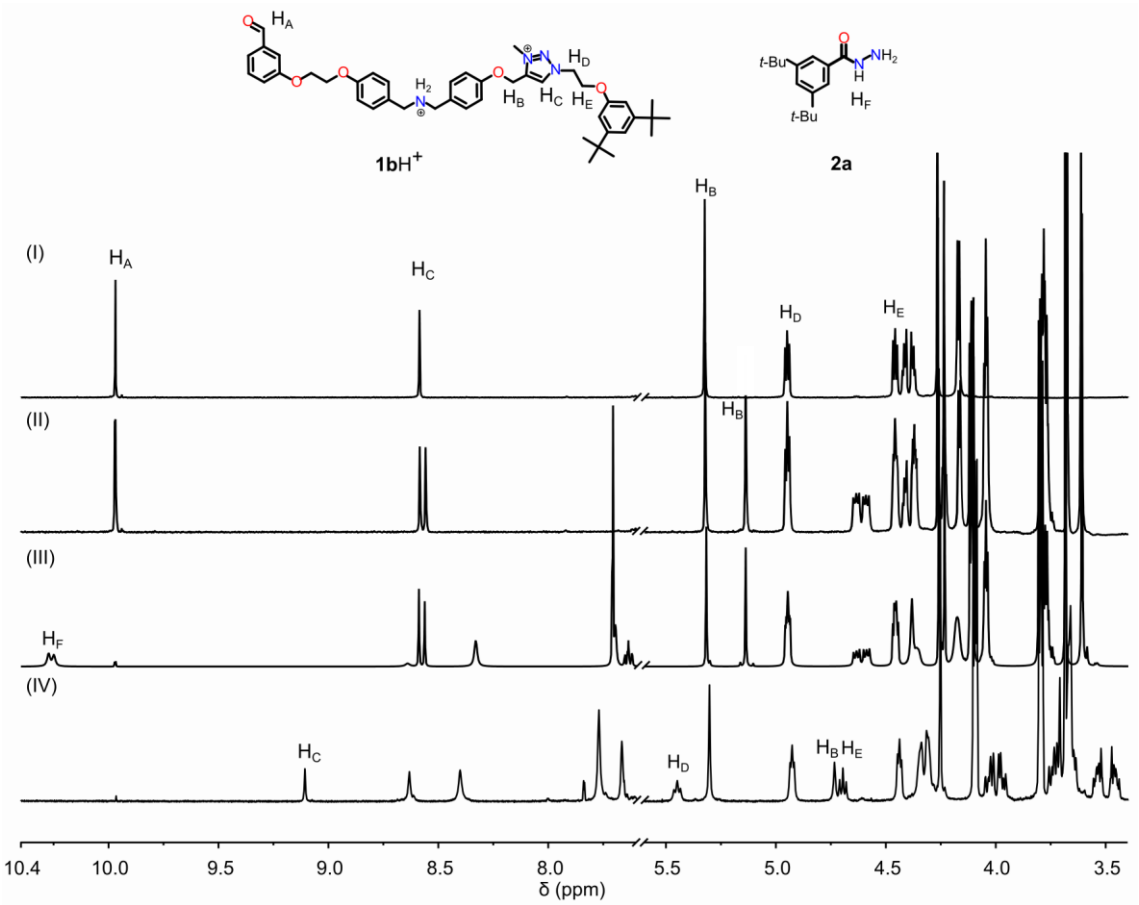

Figure 3.10. Partial ^{1}H-NMR spectra (500 MHz, CD_3CN) describing states I – IV (Figure 2b) for axle **1b**H^+ and hydrazide **2a**. (I) 7.2 mM axle **1b**H^+ alone, (II) upon addition of 1 eq. of **DB24C8**, (III) upon subsequent addition of 1 eq. of hydrazide **2a** and 0.05 eq. of TfOH to form [**1b**·**2a**H^+⊂**DB24C8**], and (IV) upon subsequent addition of 1.1 eq. of P_1-*t*-Bu to form [**1b**·**2a**⊂**DB24C8**].

We then turned our attention to controlling the relaxation kinetics from high-energy states IV to V, corresponding to the dethreading of **DB24C8** from deprotonated axles of type **1b**·**2**. We therefore subjected **1b**H^+ to reaction sequences from state I to state IV using hydrazides **2a**-**2l** (Figure 3.11).

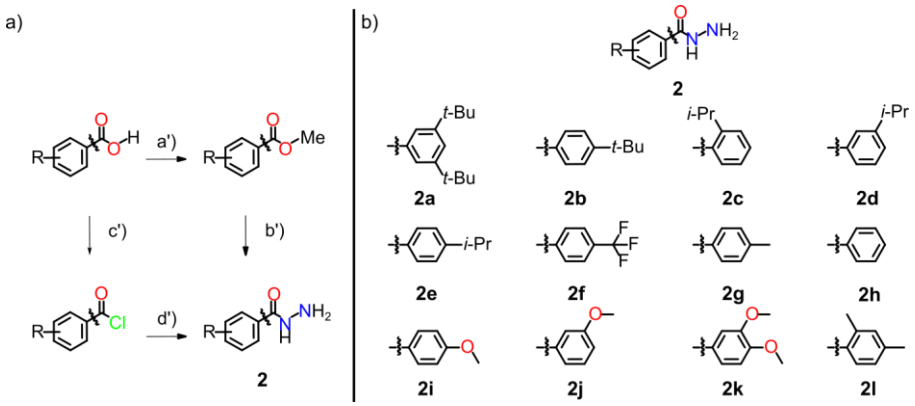

Figure 3.11. a) Generic scheme reaction for the synthesis of hydrazides **2** a') concentrated H_2SO_4, MeOH, reflux, 16 h; b') $NH_2NH_2{\cdot}H_2O$, MeOH, reflux, 3 d; c') $SOCl_2$, reflux, 3 h; d') $NH_2NH_2{\cdot}H_2O$, MeOH, reflux. b) Molecular structure of investigated hydrazides **2**.

Hydrazides **2a**-**2e** were selected because they have a progressive decrease in steric hindrance and offer the possibility to investigate the effect of changing *i*-Pr position on the phenyl ring. Hydrazide **2f** was selected because trifluoromethyl (CF_3) group is an isostere of *i*-Pr.[212] Hydrazides **2i**-**2k** provide information on methoxy substitutions, while hydrazide **2l** can be compared with **2g** and **2h** to gain insights on methyl substituents. The investigated hydrazides displayed a sharp all-or-nothing substituent effect in terms of dethreading kinetics to afford state V (Table 3.1).

Table 3.1. Kinetic data for the dethreading of **DB24C8** from [**1b**·2H$^+$⊂**DB24C8**] type complexes upon addition of 1.1 eq. of P_1-*t*-Bu in CD_3CN. at 298 K.

Hydrazide **2**	k_{out} [s^{-1}][a]	$t_{1/2}$ [min][b]	$\Delta G^{\ddagger}$ [kJ mol^{-1}][a,c]
2a	$<3.0\times10^{-7}$	$>3.9\times10^{4}$	>110.2
2b	$<3.0\times10^{-7}$	$>3.9\times10^{4}$	>110.2
2c	$<3.0\times10^{-7}$	$>3.9\times10^{4}$	>110.2
2d	$>1.9\times10^{-2}$	<0.6	<82.8
2e	$>1.9\times10^{-2}$	<0.6	<82.8
2f	$>1.9\times10^{-2}$	<0.6	<82.8
2g	$>1.9\times10^{-2}$	<0.6	<82.8
2h	$>1.9\times10^{-2}$	<0.6	<82.8
2i	$<3.0\times10^{-7}$	$>3.9\times10^{4}$	>110.2
2j	$>1.9\times10^{-2}$	<0.6	<82.8
2k	$>1.9\times10^{-2}$	<0.6	<82.8
2l[d]	–	–	–

[a] Apparent dethreading rate constant. Upper and lower bound values were calculated assuming a first-order kinetic with a residual fraction of complex of 0.05 after 160 s or 0.95 after 48 h for fast and slow processes, respectively. [b] Half-life of the complex, calculated as $t_{1/2} = \ln 2/k_{out}$. [c] Calculated from the measured rate constants using the relationship $\Delta G^{\ddagger} = -RT \ln(k_{out}\, h/k_B\, T)$, where R, h, and k_B correspond to the gas, Planck and Boltzmann constants. [d] Not investigated due to poor solubility in CD_3CN.

Indeed, high-energy structures of the [**1b**·**2**⊂**DB24C8**] obtained from hydrazides **2a**-**2c** and **2i** were stable over time, and no changes were observed over at least 48h in the ^{1}H-NMR spectrum. In sharp contrast, addition of P_1-*t*-Bu to pseudorotaxanes obtained from hydrazides **2d**-**2h** and **2j**-**2k** lead to the formation of respective **1b**·**2** adducts in a period of time shorter than the one required to record an NMR spectrum (ca. 160 s). On the basis of the present experimental data, it is not possible to unambiguously determine if the formation of state V from III occurred via intermediate IV or VI. To observe a dissipative kinetics associated with relaxation from state IV to state V, ensuring that the molecular machine performs a cyclic reaction sequence, we focused our attention on *i*-Pr substituted hydrazides **2c**-**2e**: the fact that **2c** afforded kinetically trapped state IV, while **2d** and **2e** afforded the equilibrium state V rapidly, was taken as an indication that dethreading was likely close to an experimentally accessible kinetics, having $t_{1/2}$ in the minutes to hours time-scale.[213] By comparing literature data on the threading kinetics of pseudorotaxanes based on dibenzylammonium/crown-ether recognition, we observed that when an analogous axle was investigated in CD_3CN or DCM, the threading rates were similar in the two solvents, while complex thermodynamic stability was much

higher in DCM (ca. 105 M^{-1} *vs.* 102 M^{-1}).[130,134] We reasoned that by stabilizing the studied pseudorotaxanes thermodynamically we could modulate the dethreading kinetics, slowing it down to a desirable rate. Indeed, it was already demonstrated that solvents have profound effects on supramolecular architectures,[214] and in particular on the performance of molecular machines.[135,215–217] Therefore, we decided to exploit this effect to operate in the mixed solvent system $CDCl_3$:CD_3CN: 3:1, because $CDCl_3$ is a less competitive solvent for hydrogen bonding interactions with respect to CD_3CN. An experimental confirmation of this feature was the increased association constant for pseudorotaxane **[1b**H^+**⊂DB24C8]**, from 225 M^{-1} to 1800 M^{-1}. We thus focused on hydrazides affording pseudorotaxanes which dethreaded rapidly in CD_3CN, measuring their dethreading kinetics in the mixed solvent system (Table 3.2). In contrast with previous experiments performed in CD_3CN, when **2e** and **2l** were employed, it was possible to observe a dissipative dethreading kinetics from state IV to state V. Indeed, the addition of 1.1 eq. of P_1-*t*-Bu to [**1b**·**2e**H^+**⊂DB24C8**] afforded the high-energy complex [**1b**·**2e⊂DB24C8**], state IV, as evidenced by the shift of the peaks related to the complex species.

Table 3.2. Kinetic data for the dethreading of **DB24C8** from [**1b**·**2**H^+**⊂DB24C8**] type complexes upon addition of 1.2 eq. of P_1-*t*-Bu in the mixed solvent CD_3CN:$CDCl_3$ 3:1 at 298 K.

Hydrazide **2**	k_{out} [s^{-1}][a]	$t_{1/2}$ [min][b]	$\Delta G^{\ddagger}$ [kJ mol^{-1}][a,c]
2d	$>1.9\times10^{-2}$	<0.6	<82.8
2e	$(6.7\pm0.7)\times10^{-3}$	1.7	85.4
2f	$>1.9\times10^{-2}$	<0.6	<82.8
2l	$(1.07\pm0.03)\times10^{-5}$	1110 (18.5 h)	101.4

[a] Apparent dethreading rate constant. Upper and lower bound values were calculated assuming a first-order kinetic with a residual fraction of complex of 0.05 after 160 s for fast processes. [b] Half-life of the complex, calculated as $t_{1/2} = \ln 2/k_{out}$. [c] Calculated from the measured rate constants using the relationship $\Delta G^{\ddagger} = -RT \ln(k_{out}\, h/k_B\, T)$, where R, h, and k_B correspond to the gas, Planck and Boltzmann constants.

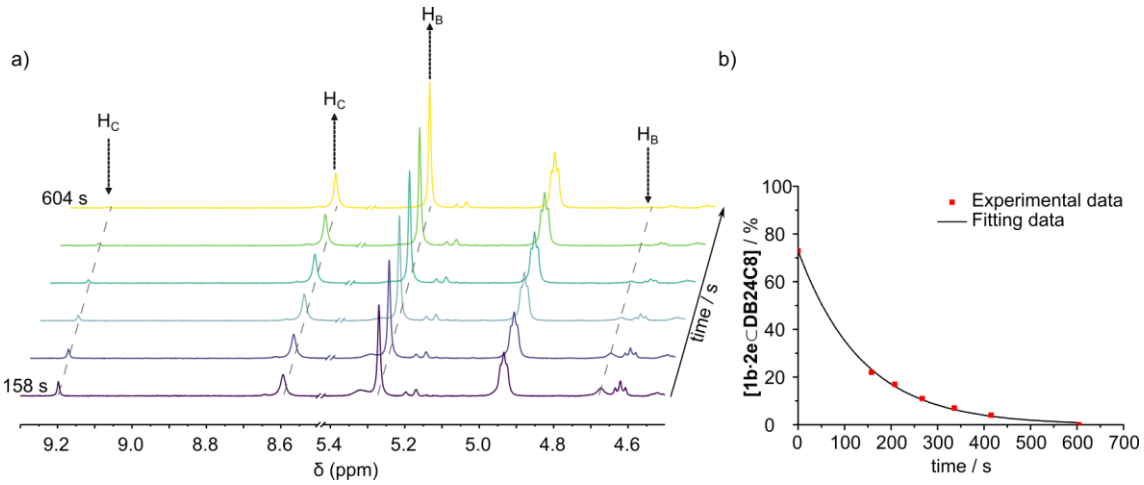

Figure 3.12. Observation of the dethreading of a) **[1b·2e⊂DB24C8]** and during the time. a) Partial ^{1}H-NMR (500 MHz, $CDCl_3$:CD_3CN 3:1) stacked spectra of **[1b·2e⊂DB24C8]** (5.25 mM) upon addition of 1.1 eq. of P_1-*t*-Bu to **[1b·2eH$^+$⊂DB24C8].** Spectra from purple to yellow represent the complex monitored at 158, 208, 267, 336, 415 and 604 s after the addition of the base. b) Concentration of **[1b·2e⊂DB24C8]** (red squares) during the time after the addition of the base, determined from the integration of H_B signals at 5.26 and 4.61 ppm, related respectively to the uncomplexed and complex species. Solid black line refers to the data fit, performed according to a first-order kinetic equation.

Secondly, by the progressive decreasing in intensity of these signals (Figure 3.12), due to the dethreading of **DB24C8** and the formation of **1b·2e**. For [**1b·2e⊂DB24C8**], it is possible to observe the complete dethreading in less than 10 minutes. Nonetheless, the dethreading kinetics depends critically on both the dimension and position of hydrazide substituents: as a matter of fact, for [**1b·2d⊂DB24C8**], and [**1b·2f⊂DB24C8**], obtained with 3-isopropyl benzohydrazide and with 4-trifluoromethyl benzohydrazide respectively, the dethreading occurs in a time shorter than NMR timescale also in the mixed solvent system $CDCl_3$:CD_3CN 3:1. Instead, for [**1b·2l⊂DB24C8**], the process advances in nearly 3 days (Figure 3.13).

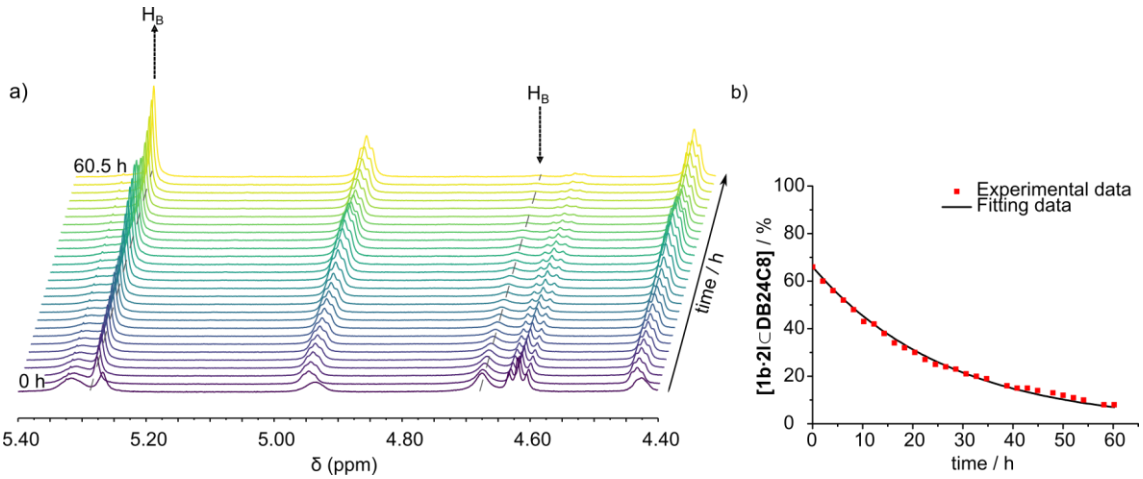

Figure 3.13. Observation of the dethreading of a) **[1b·2l⊂DB24C8]** and during the time. a) Partial ^{1}H-NMR (500 MHz, $CDCl_3$:CD_3CN 3:1) stacked spectra of **[1b·2l⊂DB24C8]** (5.25 mM) upon addition of 1.1 eq. of P_1-*t*-Bu to **[1b·2lH$^+$⊂DB24C8].** Spectra from purple to yellow represent the complex monitored every 65 minutes after the addition of the base. b) Concentration of **[1b·2e⊂DB24C8]** (red squares) during the time after the addition of the base, determined from the integration of H_B signals at 5.27 and 4.62 ppm, related respectively to the uncomplexed and complex species. Solid black line refers to the data fit, according to a first-order kinetic equation.

Fitting of the dethreading data confirmed that the process follows a first-order kinetics, with dethreading constants of $(6.7\times10^{-3}\pm0.7)\times10^{-3}$ s^{-1} and $(1.07\pm0.03)\times10^{-5}$ s^{-1} obtained when using hydrazide **2e** and **2l**, respectively (Table 3.2). Overall, these data demonstrate that by using a suitable solvent system it is possible to go from state III to state V *via* state IV. Leveraging the observed dissipative kinetics, we addressed the possibility to perform multiple times a complete cycle of threading and dethreading via states (III→IV→V→VI→III). Initially, state VI was prepared by reacting axle **1b**H$^+$ and hydrazide **2e** in the presence of 0.05 eq. of TfOH. Then, addition of 1 eq. of **DB24C8**, afforded [**1b**·**2e**H$^+$⊂**DB24C8**], which formed over 90 h, as evidenced by ^{1}H-NMR spectra (Figure 3.14).

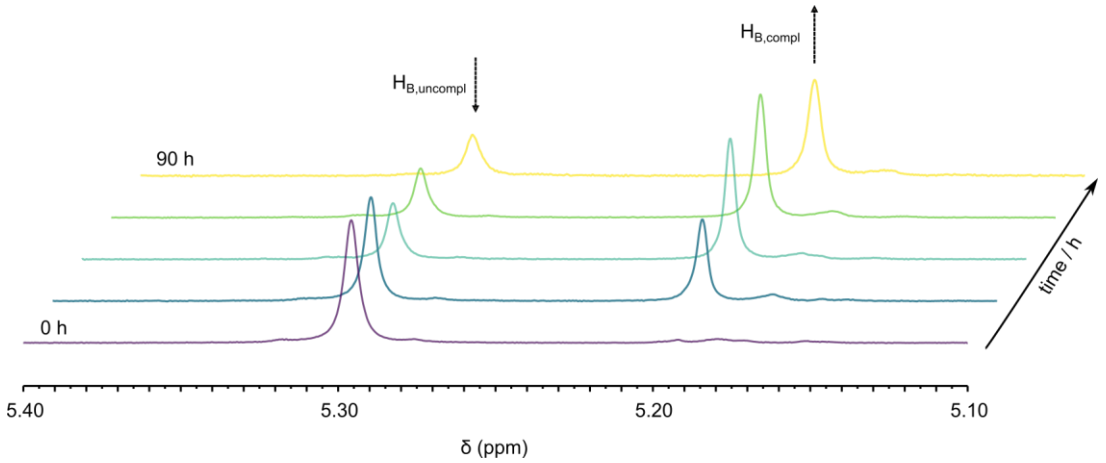

Figure 3.14. ^{1}H-NMR (500 MHz, $CDCl_3$:CD_3CN 3:1) – Partial stacked spectra of **1b**H^+**·2e** (5.25 mM) upon addition of 1 eq. of **DB24C8** to form **[1b·2e**H^+**⊂DB24C8]**. Spectra from purple to yellow represent the complex monitored at 0, 24, 46, 60, and 90 h after the addition of the ring.

Under the present experimental conditions, state III is likely formed directly *via* threading from state VI, *i.e.*, hydrazone dynamic formation does not play a role, because in an identical experiment performed using bulky hydrazide **2a** no threading was observed. Addition of 1.05 eq. of P_1-*t*-Bu to [**1b·2e**H^+**⊂DB24C8**], state III, afforded IV, which relaxed spontaneously to **1b·2e** and **DB24C8**, as evidenced by the convergence of the H_B peaks to a single signal at 5.27 ppm. Next, 1.1 eq. of TfOH is added, to reform the ammonium station of **1b**H^+, thus [**1b·2e**H^+**⊂DB24C8**]. Under these conditions it was possible to perform three subsequent cycles (III→IV→V→VI→III, Figure 3.15) powered by the addition of TfOH and P_1-*t*-Bu. The formation of [**1b·2e**H^+**⊂DB24C8**] for the fourth cycle could not be realized, presumably due to a progressive hydrolysis reaction of hydrazone to form starting aldehyde.

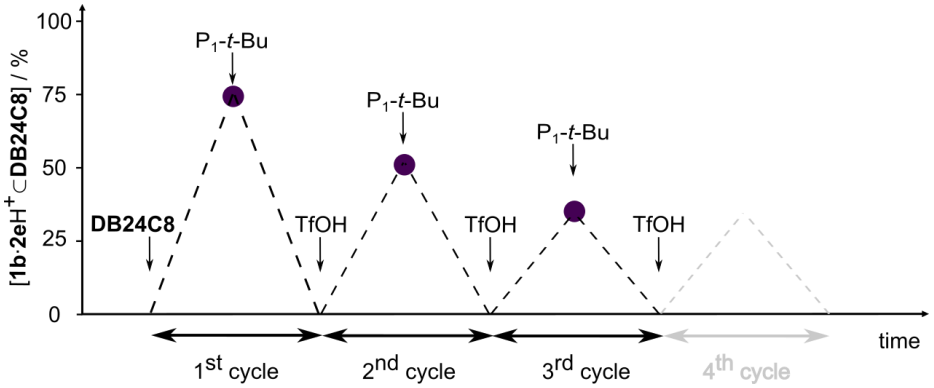

Figure 3.15 Repeated acid-base cycles ratcheting **DB24C8** onto **1b·2e** thread to form [**1b·2e⊂DB24C8**]. Conditions: CD_3CN:$CDCl_3$ 3:1, 5.4 mM, subsequent additions of 1.1 eq. base P_1-*t*-Bu and 1.05 eq. of TfOH. The reported values are an average of at least two independent experiments. Lines are intended as guide to the eye.

3.3 Conclusions

In conclusion, a minimal molecular machine powered by acid-base inputs capable of energetically demanding transport according to an energy ratchet mechanism was studied. On-demand selection of stoppering units allowed controlling the dethreading kinetics over four orders of magnitude, from a stable kinetically trapped state to a rapid equilibration. Remarkably, the careful selection of solvents allowed fine-tuning dethreading kinetics, making it possible to observe a dissipative relaxation, thus gaining direct evidence on machine exploring the square reaction network in a directional fashion. By operating the machine under such dissipative condition, it was possible to repeat the operation cycle of the machine three times, while observing it experimentally. Our work illustrates that solvent has profound effects on the operation of molecular machines, and it is possible to tailor these effects, leading to enhanced functionality.

3.4 Experimental section

3.4.1 General information

Materials, methods and instruments

Unless otherwise stated, all reagents and solvents were purchased from commercial sources and used as received, unless otherwise stated. Commercial reagents included hydrazides **2b**, **2e**, **2f**, **2g**, **2h**, **2i, 2j** and macrocycle **DB24C8**. Other hydrazides were synthetized from corresponding carboxylic acid or esters. Reactions were performed in anhydrous conditions under Argon atmosphere unless otherwise stated. TLC analysis was performed on Merck silica gel TLC Al foils with fluorescent indicator 254 nm (0.25 mm thick, 60 F254, Merck, Germany) and visualized using UV lamp (254 and 365 nm) and standard laboratory stains (ninhydrin alcoholic solution, potassium permanganate aqueous solution (aq.) and 2,4-dinitrophenylhydrazine solution). Column chromatography was carried out on silica gel (Merck silica gel 60 0.040-0.063 mm). Vacuum filtrations were carried out with polytetrafluoroethylene (PTFE) membranes having pore size 0.45 μm.

NMR experiments were performed on Varian INOVA 400 or 500 MHz, and on Bruker UltraShield Plus Avance III spectrometer400 MHz at 298 K, using partially deuterated solvents as internal standards. Chemical shifts (δ) are expressed in ppm and are referred to the residual non-deuterated solvent peak. Spin multiplicities are reported as singlet (s), doublet (d), triplet (t), quartet (q), multiplet (m) and broad (b) with proton-proton coupling constants (*J*) given in Hz. ESI-MS mass spectrometry measurements were performed on Bruker microTOF-Q, Bruker Esquire 4000 and Bruker HTCultra. UV-Vis measurements were carried out on a Cary 5000 Spectrometer (Varian), using 1 mm path quartz cuvettes.

The complete assignment of all the proton and carbon resonances for products **1a**$H^+PF_6^-$ and **1b**$H^+PF_6^-$ was allowed by a combination of 1D (^1H, ^{13}C) and 2D NMR (COSY, HSQCAD, HMBCAD) experiments.
The stability constants (K_a) were obtained from the ^1H NMR spectra of equimolar solutions ($6 \cdot 10^{-3}$ M) of the ring **DB24C8** and either axle **1a**$H^+PF_6^-$ or **1b**$H^+PF_6^-$, at r.t., using the single-point method.[218,219] The concentration of all the species at equilibrium was determined using the initial concentrations and the integration of the protons of the complexed and uncomplexed species. The stability constant K_a was calculated according to a 1:1 binding model with the equation:

$$K_a = [\mathbf{1}\subset\mathbf{DB24C8}] / [\mathbf{DB24C8}][\mathbf{1b}]$$

The experimental error on the value of the stability constant was estimated to be ±20%.
Data fitting of the exponential kinetics was performed using a home-made Python code according to a first-order differential equation. The function used is minimize(chi_squared, [0.01], args=(t, c[0], c), with method 'Nelder-Mead'.

3.4.2 General method for chemically fueled operations with asymmetric axle 1bH^+

Detailed analysis of the kinetics of rotaxanes were performed in CD_3CN or in mixed solvent systems $CDCl_3$:CD_3CN 3:1. When employed, $CDCl_3$ is purified on an alumina pad to remove any acidic impurity. When mixed solvent system is studied, solution of acid TfOH and phosphazene P_1-*t*-Bu are always prepared in bare CD_3CN, to avoid possible superior acidity in the first case and collateral reaction of the base with the solvent in the second case.

In a typical experiment, a standard 5 mm NMR tube was charged with a solution of asymmetric axle compound **1b** (3.59 mg in 500 μL, 3.6 μmol, 7.2 mM solution). Subsequently, 60 μL (3.6 μmol, 1 eq.) of a **DB24C8** macrocycle solution (8.07 mg in 300 μL, 18 μmol, 60 mM) is added and a first spectrum is immediately recorded, followed by a second one after 300 s, to ensure the complete equilibration. Then, 100 μL (3.6 μmol, 1 eq.) of hydrazide **2** (250 μL, 9 μmol, 36 mM) and 2.5 μL (0.18 μmol, 0.05 eq.) of TfOH (1 mL, 72 μmol, 72 mM) are added. The spectrum is checked until the disappearance (*i.e.* integration <5%) of the peak ascribed to the aldehyde (9.99 ppm). The final concentration after all the additions is 5.4 mM. Spectra are recorded after every new addition. Then, 22 μL (0.378 μmol, 1.1 eq.) of phosphazene base solution P_1-*t*-Bu (200 μL, 35 μmol, 175 mM) is added to the NMR tube and quickly mixed. The tube is inserted into the NMR spectrometer, which is tuned, matched, locked and shimmed and a first spectrum is recorded. The whole operation was estimated to take 158 s. The final concentration after all the additions is 5.25 mM.

3.4.3 Synthetic details, characterization and collection of spectra

Synthesis of symmetric axle 1a$H^+PF_6^-$

Synthesis of 3.

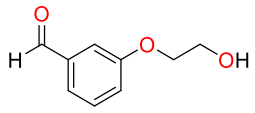

3

NaOH (56.4 mg, 1.41 mmol, 1 eq.) was added to a dispersion of 3-hydroxybenzaldehyde (172.2 mg, 1.41 mmol, 1 eq.) in 0.6 mL of water. As the base was added, the colour of the dispersion turned from colorless to yellow and the mixture started to solubilize. Once all the aldehyde was solubilized, 2-bromoethanol (176.2 mg, 1.41 mmol, 1 eq.) was added dropwise and the solution was heated at reflux for 7 h. After this time, the solution was basified to pH ≈ 10 with KOH (10% aq.) and extracted with EtOAc. Then, the combined organic layers were extracted with brine, dried with Na_2SO_4, filtered and concentrated under reduced pressure. The obtained oil was purified by column chromatography, using PE/EtOAc (8/2) as eluent mixture. The final product was obtained as an oil (183 mg, 78%). ^{1}H-NMR (500 MHz, $CDCl_3$), δ: 9.94 (s, 1H), 7.48-7.36 (m, 3H), 7.21-7.17 (m, 1H), 4.13 (m, 2H), 3.98 (m, 2H), 2.54 (s, 1H). ^{13}C-NMR (126 MHz, $CDCl_3$), δ: 192.2, 159.2, 137.8, 130.2, 123.9, 121.9, 112.9, 69.5, 61.2. HRMS (m/z) calculated for $C_9H_{10}O_3^+$ 166.0702, found 167.0703.

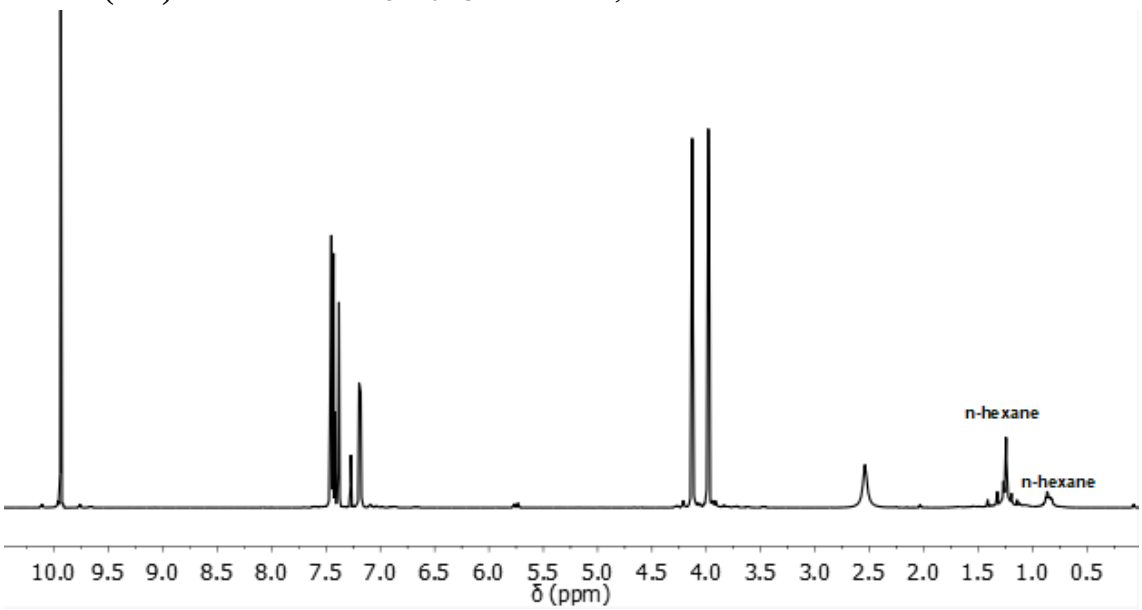

Figure 3.16. ^{1}H-NMR (500 MHz, $CDCl_3$) of **3.**

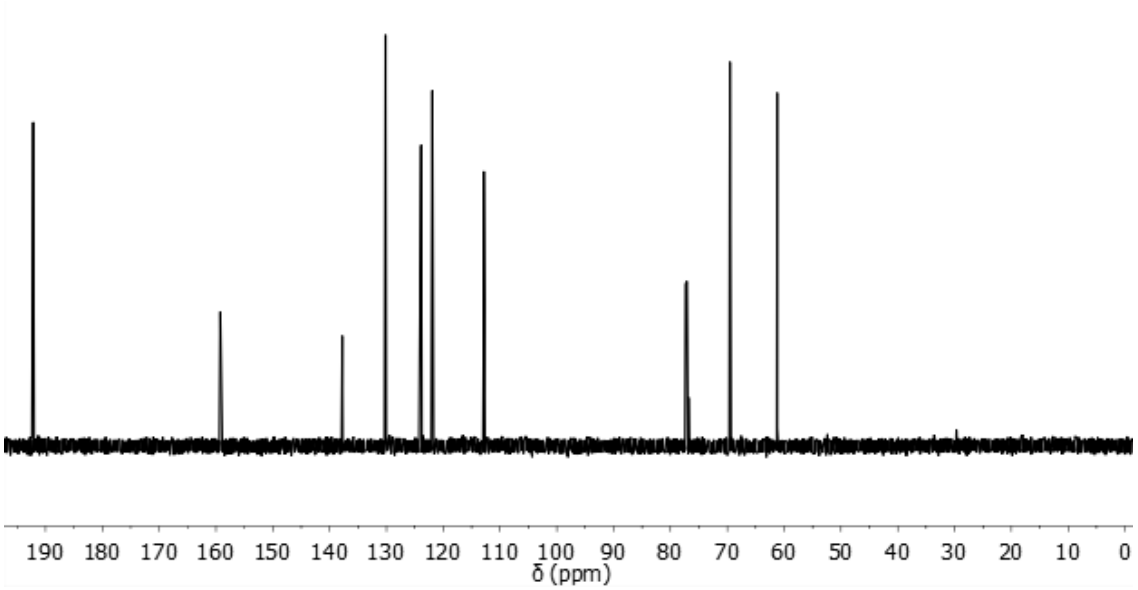

Figure 3.17. ^{13}C-NMR (126 MHz, $CDCl_3$) of **3**.

Synthesis of ES1.

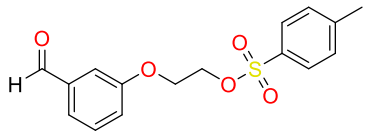

ES1

Compound **3** (148 mg, 0.89 mmol) was dissolved in dry DCM and triethyl amine (186 µL, 1.33 mmol, 1.5 eq.) was added. The reaction mixture was then cooled to 0 °C. TsCl (186 mg, 0.97 mmol, 1.1 eq.) was dissolved in 10 mL of dry DCM and added dropwise to the reaction mixture. The mixture was allowed to reach r.t. and left to stir overnight. 30 mL of NaOH 1 M were added to the reaction mixture, which was stirred for 20 min, after which it was let separate in two phases. The aqueous phase was extracted two more times with 30 mL of DCM. The combined organic layers were dried over Na_2SO_4 and filtered. The solvent was removed in vacuo. The product was isolated after column chromatography (SiO_2, eluent PE/EtOAc 9:1 to 7:3) to afford **ES1** as a white solid (194 mg, 67%). ^{1}H-NMR (400 MHz, $CDCl_3$) δ: 9.94 (s, 1H), 7.82-7.80 (m, 2H), 7.47-7.40 (m, 2H), 7.35-7.33 (m, 2H), 7.25-7.24 (m, 1H), 7.08-7.05 (m, 1H), 4.41-4.38 (m, 2H), 4.21,4.19 (m, 2H), 2.44 (s, 3H). ^{13}C-NMR (100 MHz, $CDCl_3$) δ: 191.92, 158.66, 145.18, 137.85, 132.91, 130.27, 130.00, 128.09, 124.26, 121.92, 112.82, 77.16, 68.02, 65.76, 21.76. HRMS (m/z) calculated for $C_{16}H_{16}O_5SNa^+$ 343.0611, found 343.0611.

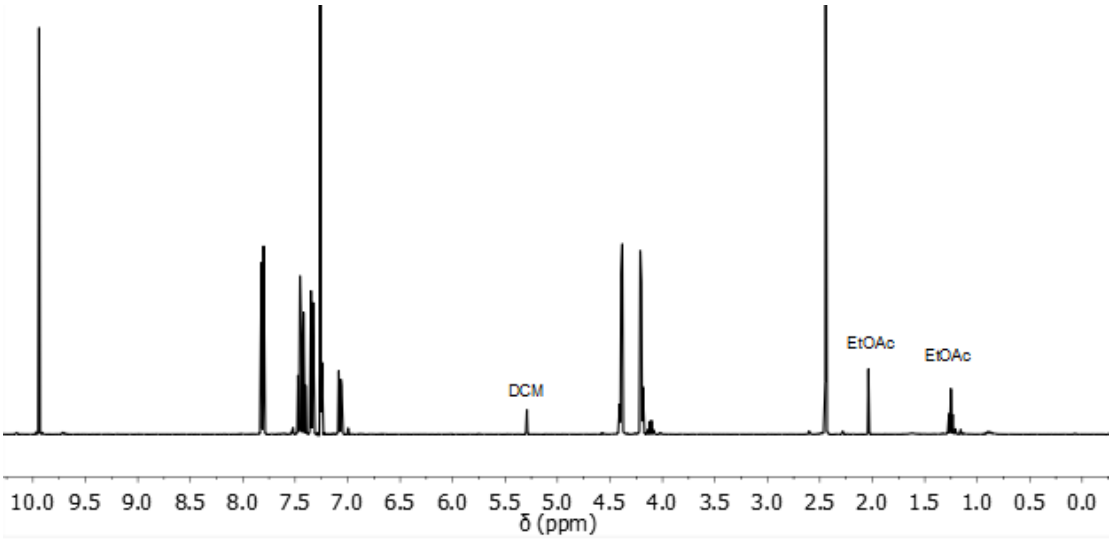

Figure 3.18. ^{1}H-NMR (400 MHz, $CDCl_3$) of **ES1**.

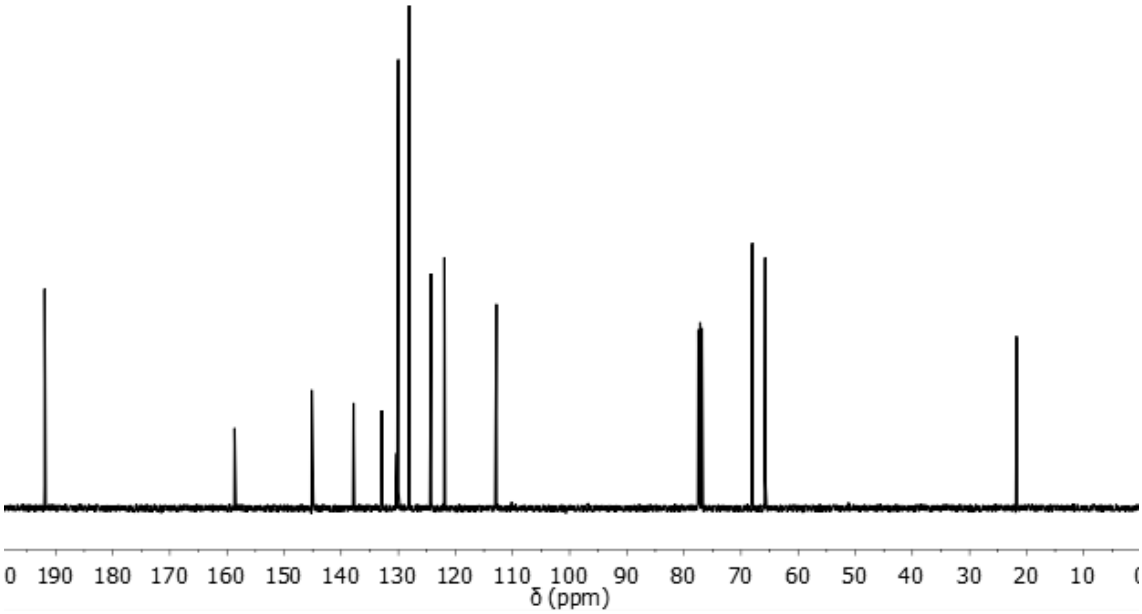

Figure 3.19. ^{13}C-NMR (100 MHz, $CDCl_3$) of **ES1**.

Synthesis of ES2.

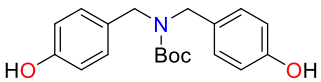

ES2

4-hydroxy benzylamine (490 mg, 3.97 mmol) and 4-hydroxy benzaldehyde (534 mg, 4.38 mmol, 1.1 eq.) were dissolved in anhydrous MeOH (80 mL), Na_2SO_4 was added

and the reaction mixture was heated to reflux overnight. The formation of the imine intermediate was checked via TLC (eluent: DCM/MeOH 9:1). The reaction mixture was filtered, concentrated under reduced pressure to ~60 mL, and then diluted with dry THF (60 mL). $NaBH_4$ was added in 5 portions over 1 h. The reaction mixture was then stirred at r.t. for 1 h and the process of the reaction checked via TLC. Once complete, the reaction was quenched with saturated NH_4Cl (10 mL). The organic solvents were then removed in vacuo. The residue was diluted with 125 mL of H_2O and the pH adjusted to 9 with NaOH. The aqueous phase was extracted with 3×150 mL EtOAc, washed with water, and then with brine. The organic phase was dried over Na_2SO_4, filtered and the solvent removed in vacuo to afford intermediate amine compound as a yellowish solid (yield assumed quantitative) that was used without further purification in the next step. Then, 500 mg of intermediate amine compound (2.18 mmol) were dissolved in dry MeOH (12 mL) and $NaHCO_3$ (732 mg, 8.72 mmol, 4 eq.) was added. Boc_2O (520 mg, 2.39 mmol, 1.1 eq.) was dissolved in 10 mL of dry MeOH and added dropwise to the reaction mixture that was stirred for 3 h and the progress of the reaction checked via TLC (eluent PE/EtOAc 7:3). MeOH was removed in vacuo and the residue resuspended in 100 mL H_2O. The aqueous phase was extracted with 3 × 20 mL EtOAc, the reunited organic phases washed with 60 mL of brine, dried over Na_2SO_4, filtered and the solvent removed under reduced pressure. The product was isolated after column chromatography (SiO_2, eluent PE/EtOAc 7:3) to afford **ES2** as a white solid. (355 mg, 47%). ^{1}H-NMR (500 MHz, DMSO-d_6,) δ: 9.33 (s, 2H), 7.01 (brd, 4H), 6.73-6.70 (m, 4H), 4.17-4.13 (brd, 4H), 1.41 (s, 9H). ^{13}C-NMR (126 MHz, DMSO-d_6) δ: 156.49, 155.02, 128.86, 128.21, 115.19, 78.96, 48.30-47.90, 28.12-28.08. HRMS (m/z) calculated for $C_{19}H_{23}NO_4Na^+$ 352.1519, found 352.1518.

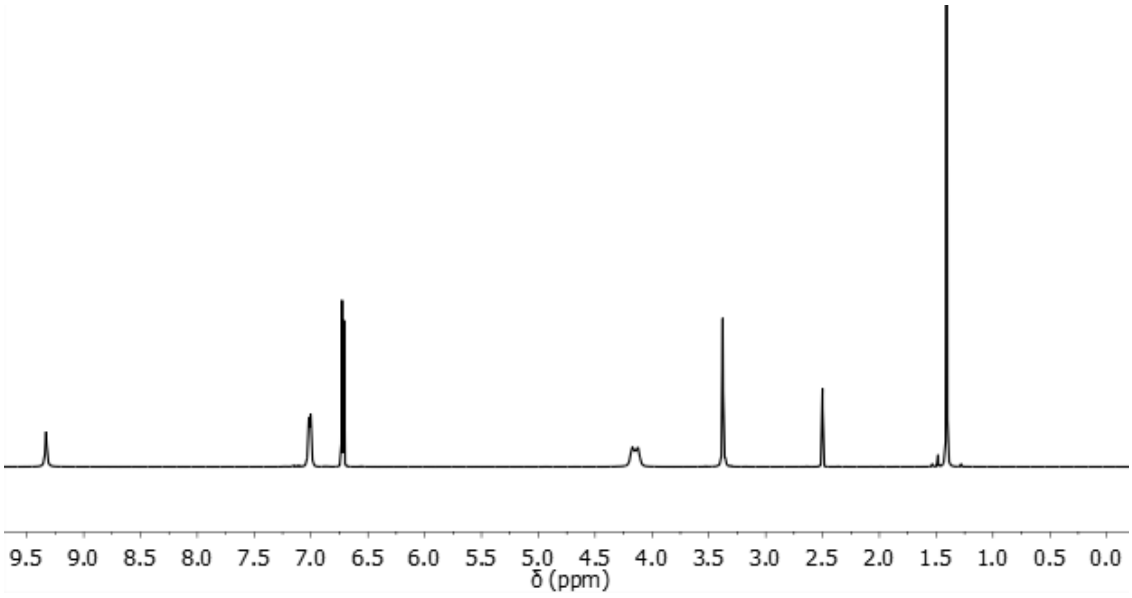

Figure 3.20. ^{1}H-NMR (500 MHz, DMSO-d_6) of **ES2**.

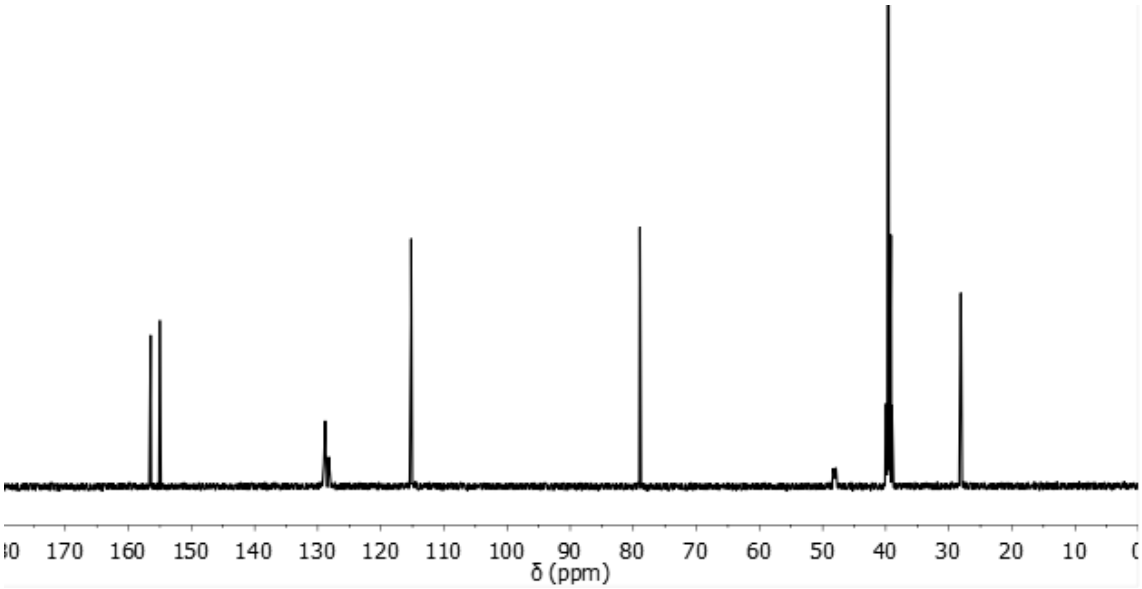

Figure 3.21. ^{13}C-NMR (126 MHz, DMSO-d_6) of **ES2**.

Synthesis of ES3.

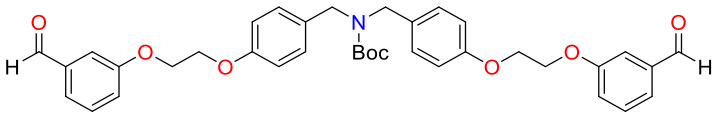

ES3

Compound **ES2** (84.6 mg, 0.257 mmol) and K_2CO_3 (106 mg, 0.771 mmol, 3 eq.) were suspended in 4 mL of dry DMF. Compound **ES1** (247 mg, 0.771 mmol, 3 eq.) was dissolved in 4 mL of dry DMF and added dropwise to the reaction mixture, which was then heated to 80 °C for 16 h. After this time, the reaction was cooled to r.t., DMF was removed under reduced pressure and the residue suspended in H_2O (50 mL). The aqueous phase was extracted with EtOAc (3 × 50 mL). The organic phases were collected, dried over Na_2SO_4, filtered, and the solvent was removed under reduced pressure. The target compound was isolated via column chromatography (SiO_2, eluent DCM/EtOAc 98:2 to 9:1) to afford **ES3** as a white solid. (112 mg, 70%). ^{1}H-NMR (400 MHz, CD_2Cl_2) δ: 9.97 (s, 2H), 7.50-7-48 (m, 4H), 7.45-7.44 (m, 2H), 7.27-7.22 (m, 2H), 7.17-7.15 (brm, 4H), 6.92-6.89 (m, 4H), 4.41-4.38 (m, 4H), 4.35-4.33 (m, 4H), 4.29 (brs, 4H), 1.48 (s, 9H) ^{13}C-NMR (100 MHz, CD_2Cl_2) δ: 192.42, 159.85, 158.35, 156.29, 138.55, 131.48, 130.75, 129.70, 124.08, 122.29, 115.07, 113.56, 80.27, 67.54, 67.11, 54.00, 48.76, 28.74. HRMS (m/z) calculated for $C_{37}H_{39}NO_8Na^+$ 648.2568, found 648.2566.

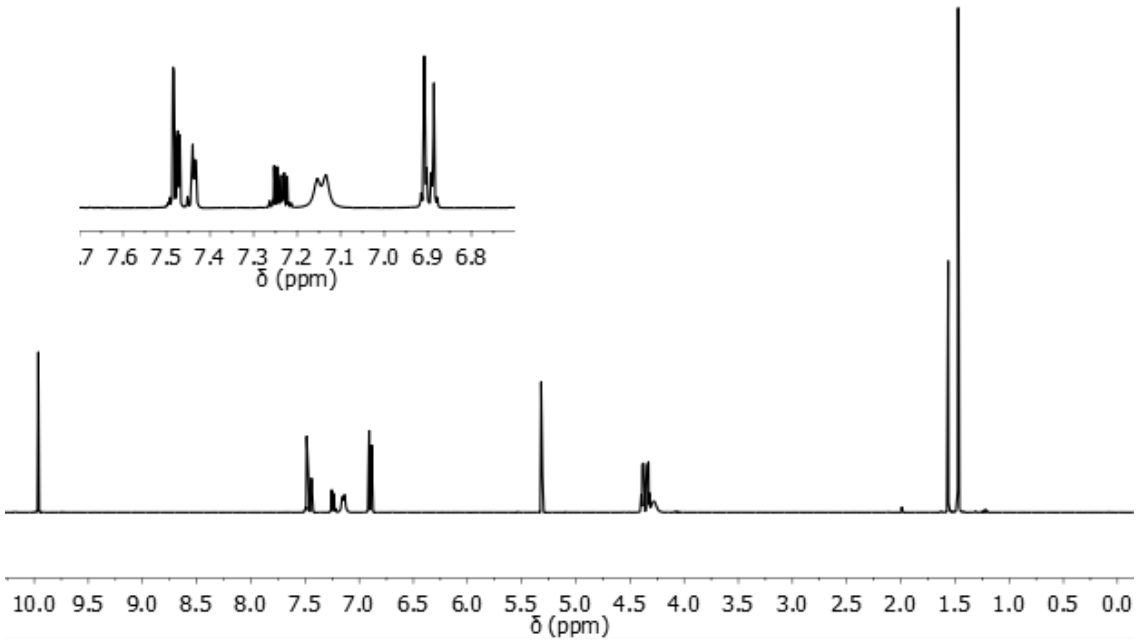

Figure 3.22. ^{1}H-NMR (400 MHz, CD_2Cl_2) of **ES3**.

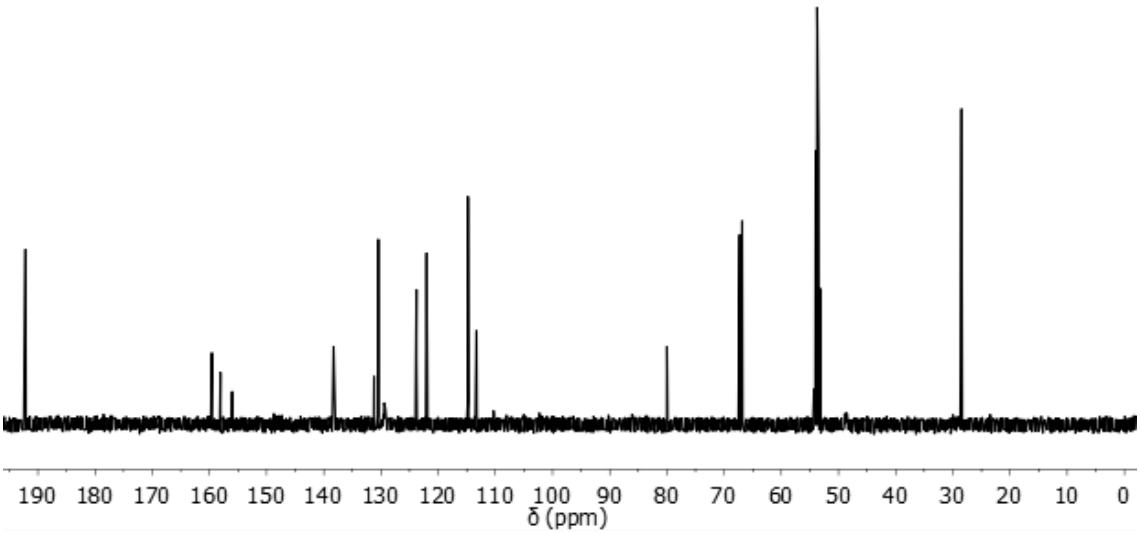

Figure 3.23. ^{13}C-NMR (100 MHz, CD_2Cl_2) of **ES3**.

Synthesis of 1a$H^+PF_6^-$.

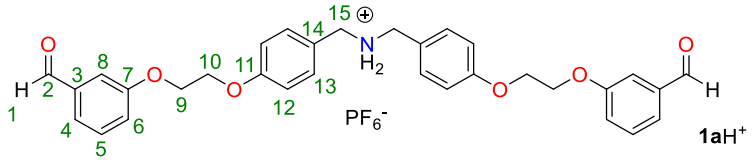

Compound **ES3** (20 mg, 0.031 mmol) was dissolved in 2 mL of dry DCM and trifluoroacetic acid (TFA) (0.600 mL) was added. The solution was stirred for 2h, after which DCM and excess of TFA were removed under reduced pressure. The residue was dissolved in 1 mL of THF and a saturated NH_4PF_6 solution (4 mL) was added dropwise while stirring. A white precipitate appeared, and the suspension was stirred for 1 additional hour. The suspension was filtered and the solid washed several times with water. Compound **1a**$H^+PF_6^-$ was obtained as an off-white solid (20 mg, 96%). ^{1}H-NMR (400 MHz, CD_3CN) δ = 9.99 (s, 2H, 1), 7.56 – 7.51 (m, 4H, 4+6), 7.47 (m, 2H, 8), 7.45 – 7.39 (m, 4H, 13), 7.29 (m, 2H, 5), 7.07 – 7.01 (m, 4H, 12), 4.45 – 4.38 (m, 8H, 9+10), 4.15 (s, 4H, 15). ^{13}C-NMR (100 MHz, CD_3CN) δ = 193.32 (2), 160.63 (11), 160.17 (7), 139.10 (3), 132.85 (13), 131.38 (4/6), 124.04 (4/6), 123.68 (14), 122.33 (5), 115.89 (12), 114.34 (8), 67.84 (9/10), 67.65 (9/10), 51.69 (15). HRMS (m/z) calculated for $C_{37}H_{39}NO_6^+$ 526.2224, found 526.2194 $(M\text{-}PF_6^-)^+$.

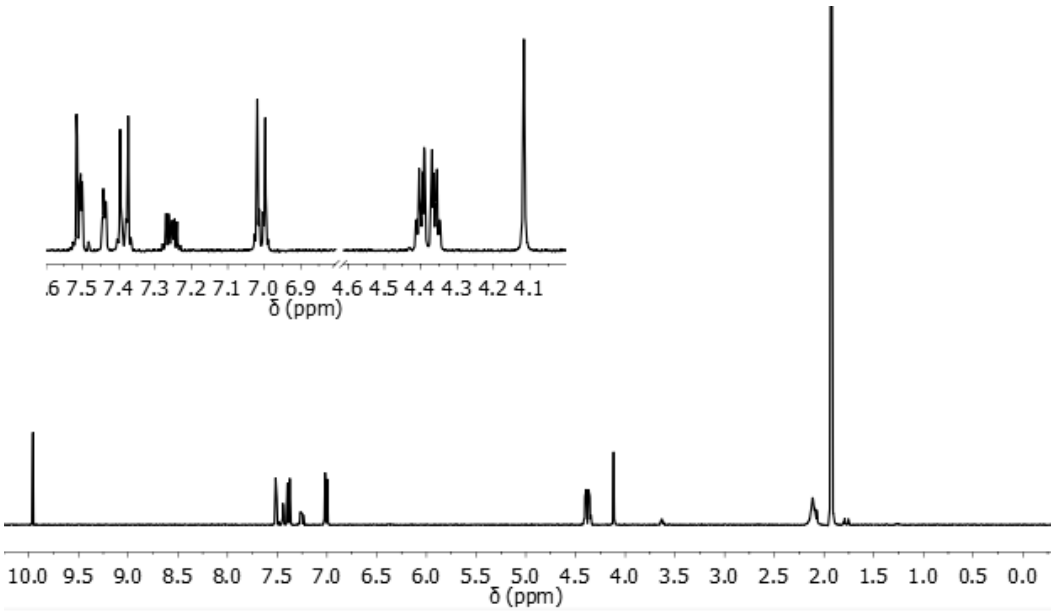

Figure 3.24. ^{1}H-NMR (400 MHz, CD_3CN) of **1a**H^+.

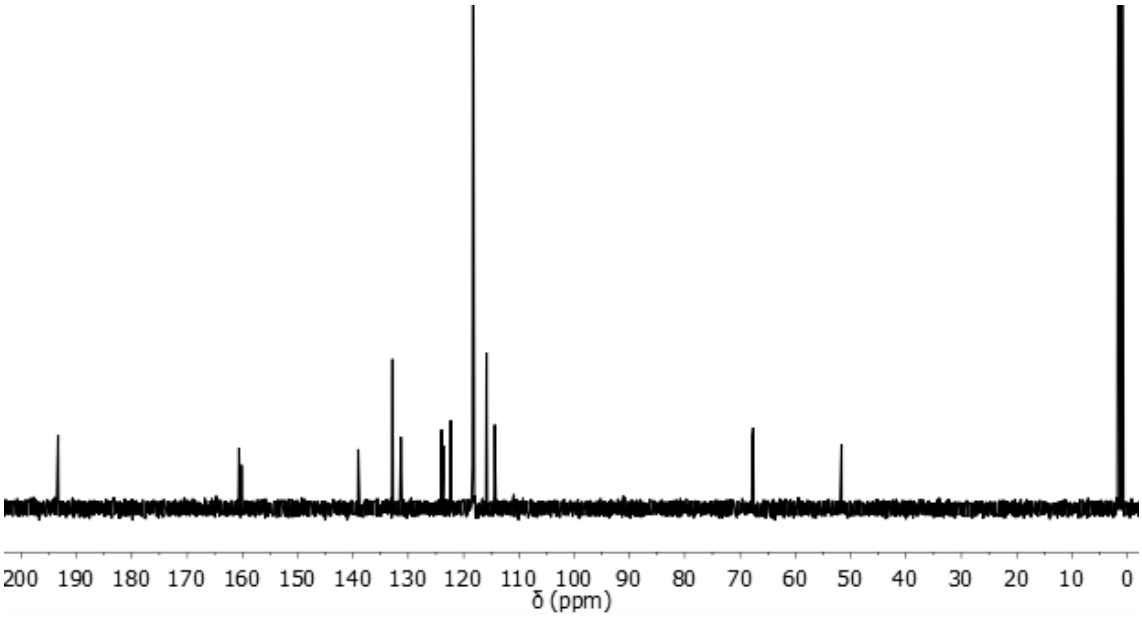

Figure 3.25. ^{13}C-NMR (100 MHz, CD_3CN) of **1a**H$^+$.

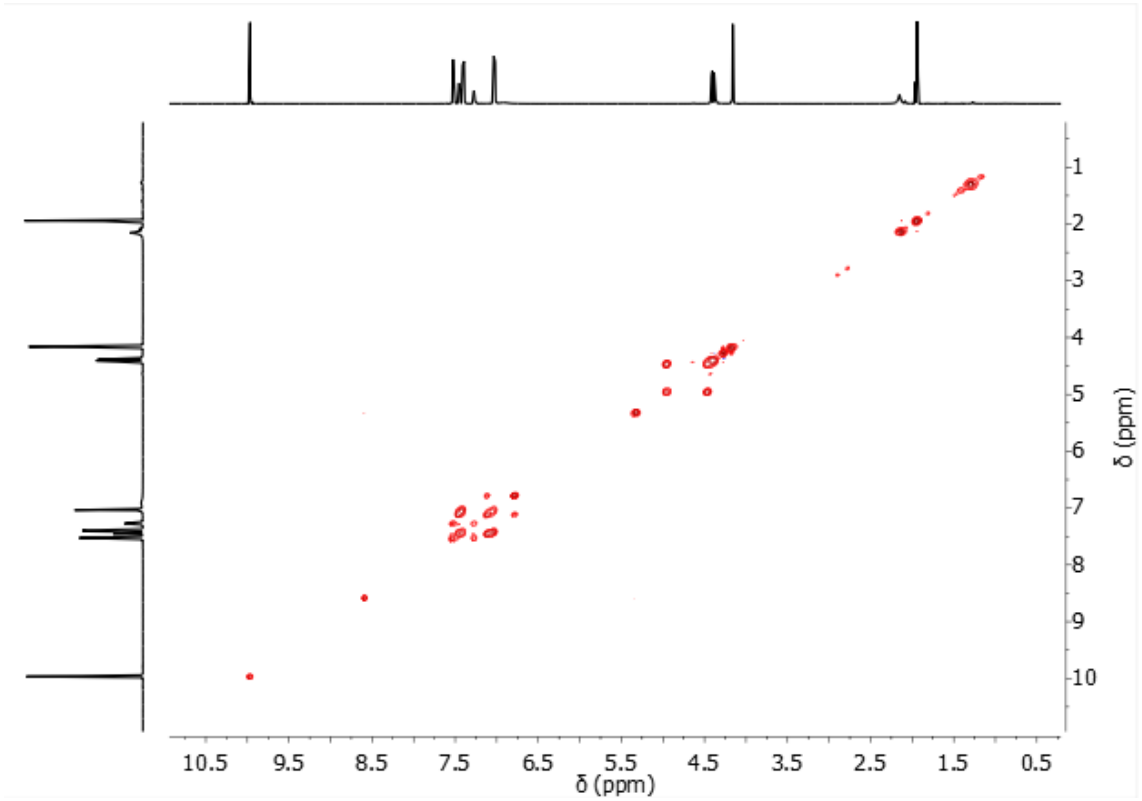

Figure 3.26. ^{1}H-^{1}H COSY (126 MHz, CD_3CN) of **1a**H$^+$.

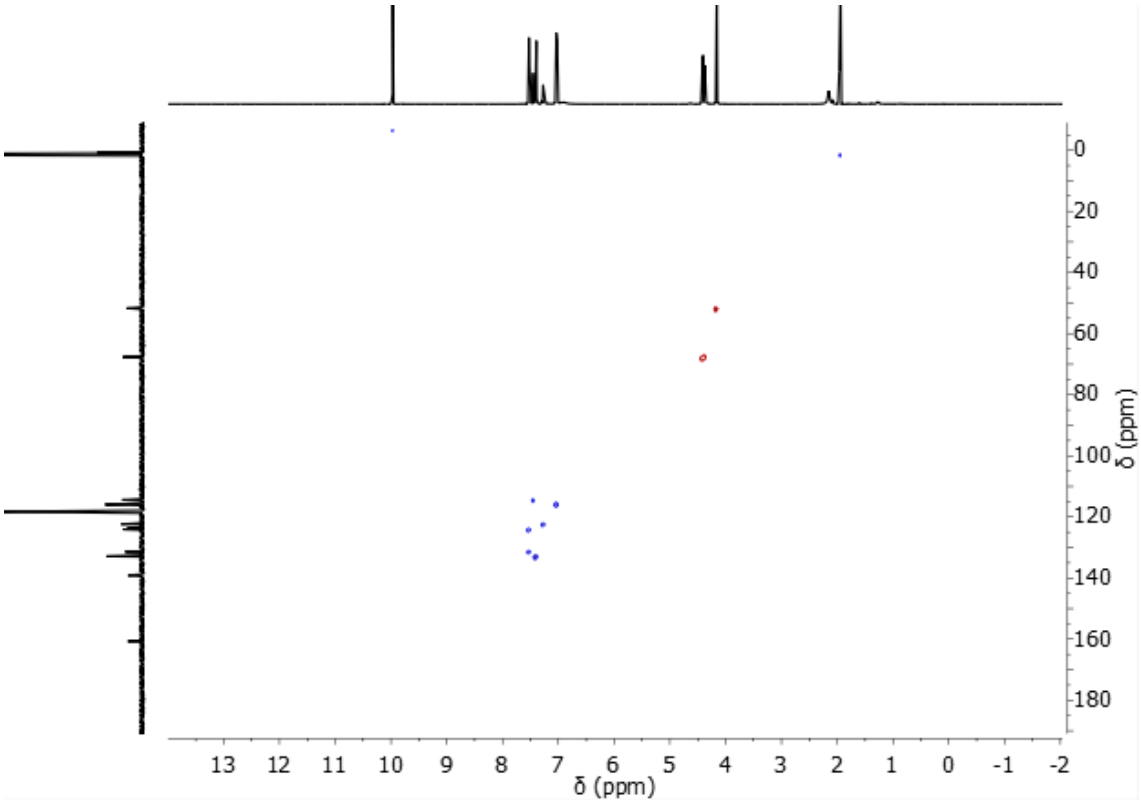

Figure 3.27. ^{1}H-^{13}C HSQCAD (CD_3CN) of **1a**H^+.

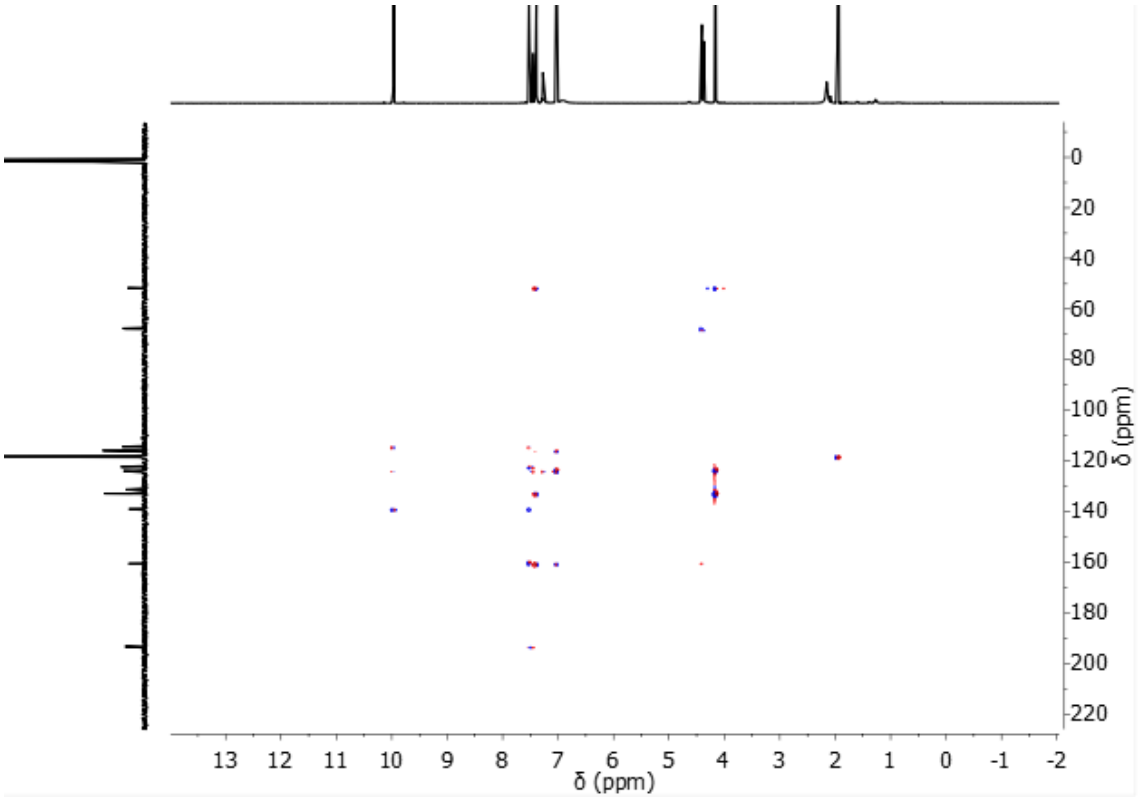

Figure 3.28. ^{1}H-^{13}C HMBCAD (CD_3CN) of **1a**H^+.

Synthesis of asymmetric axle 1b $H^+PF_6^-$

Synthesis of ES4.

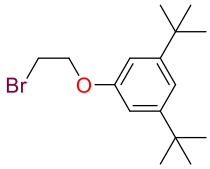

ES4

3,5-di-*tert*-butylphenol (619 mg, 3 mmol) and K_2CO_3 (1.24 g, 9 mmol, 3 eq.) were dissolved in 20 mL of CH_3CN. The reaction mixture was stirred at reflux for 20 minutes and then 1,2-dibromoethane (1.3 mL, 15 mmol, 5 eq.) was added dropwise. The reaction was refluxed overnight. After this time, the reaction was cooled down to r.t. and the crude was filtered to remove K_2CO_3. The filtrate was concentrated under reduced pressure and purified by column chromatography (SiO_2, gradient from CHX to CHX:EtOAc 98:2), affording **ES4** a colourless solid (243 mg, 26%). ^{1}H-NMR (400 MHz, $CDCl_3$,) δ: 7.06 (t, *J* = 1.6 Hz, 1H), 6.77 (d, *J* = 1.6 Hz, 2H), 4.31 (t, *J* = 6.3 Hz, 2H), 3.65 (t, *J* = 6.3 Hz, 2H), 1.32 (s, 18H). ^{13}C-NMR (100 MHz, $CDCl_3$) δ 157.85, 152.53, 115.84, 109.27, 67.98, 35.13, 31.57, 29.53. HRMS (m/z) calculated for $C_{16}H_{25}BrONa^+$ 335.0981, found 335.0976.

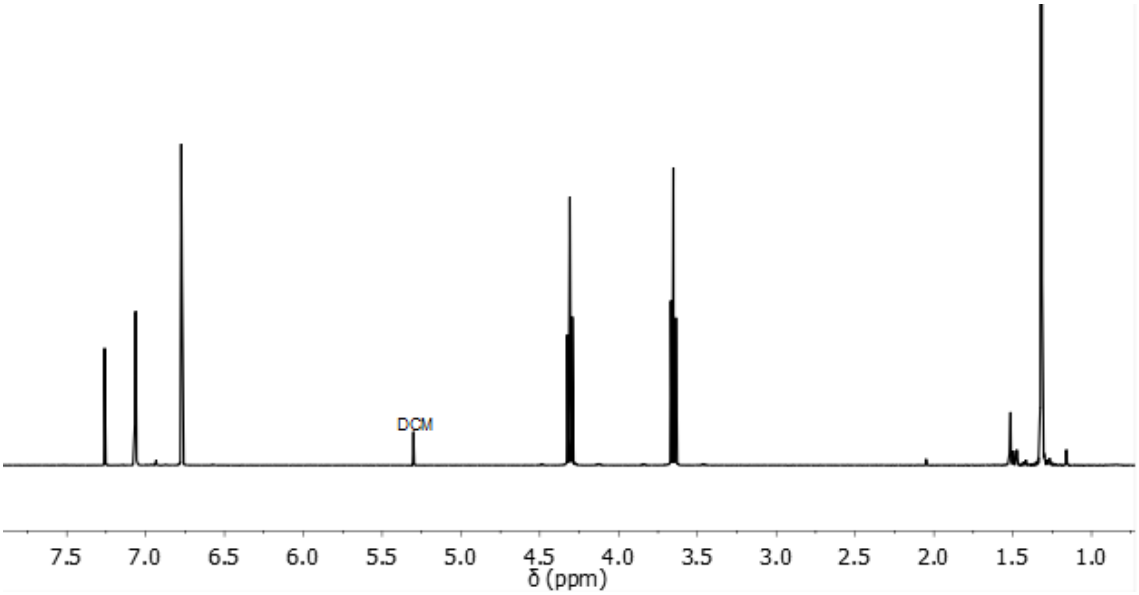

Figure 3.29. ^{1}H-NMR (400 MHz, $CDCl_3$) of **ES4**.

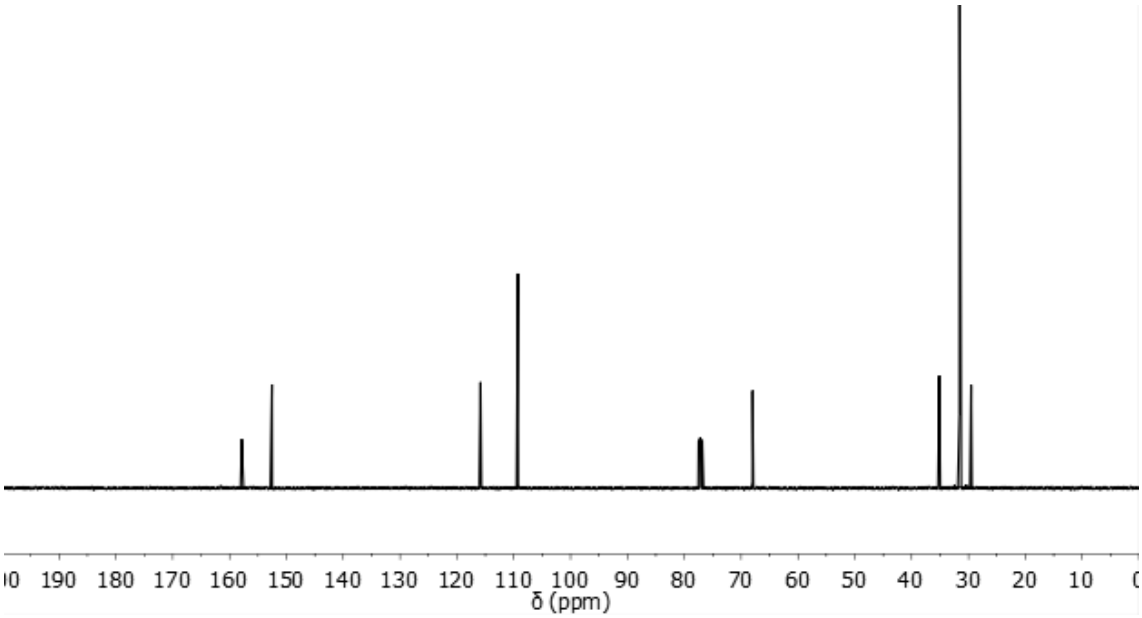

Figure 3.30. ^{13}C-NMR (100 MHz, $CDCl_3$) of **ES4.**

Synthesis of ES5.

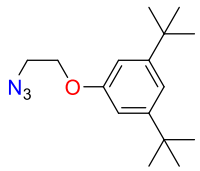

ES5

Compound **ES4** (205 mg, 0.654 mmol) and sodium azide (127 mg, 1.96 mmol, 3 eq.) were dissolved in dry DMF (3 mL) and the mixture was stirred at r.t. for 24 h. Water (30 mL) was added and the organic material was extracted with Et_2O (3 × 50 mL). The organic fractions were collected, washed with LiCl (5% aq.), dried over Na_2SO_4, and concentrated to give compound **ES5** as a colourless solid (173 mg, yield 96%). ^{1}H-NMR (400 MHz, $CDCl_3$) δ 7.09 (t, *J* = 1.6 Hz, 1H), 6.80 (d, *J* = 1.6 Hz, 2H), 4.19 (dd, *J* = 5.5, 4.6 Hz, 2H), 3.61 (dd, *J* = 5.5, 4.6 Hz, 2H), 1.34 (s, 18H). ^{13}C-NMR (100 MHz, $CDCl_3$) δ 158.00, 152.52, 115.78, 109.14, 66.95, 50.50, 35.14, 31.57. HRMS (m/z) calculated for $C_{16}H_{25}N_3ONa^+$ 298.1890, found 298.1888.

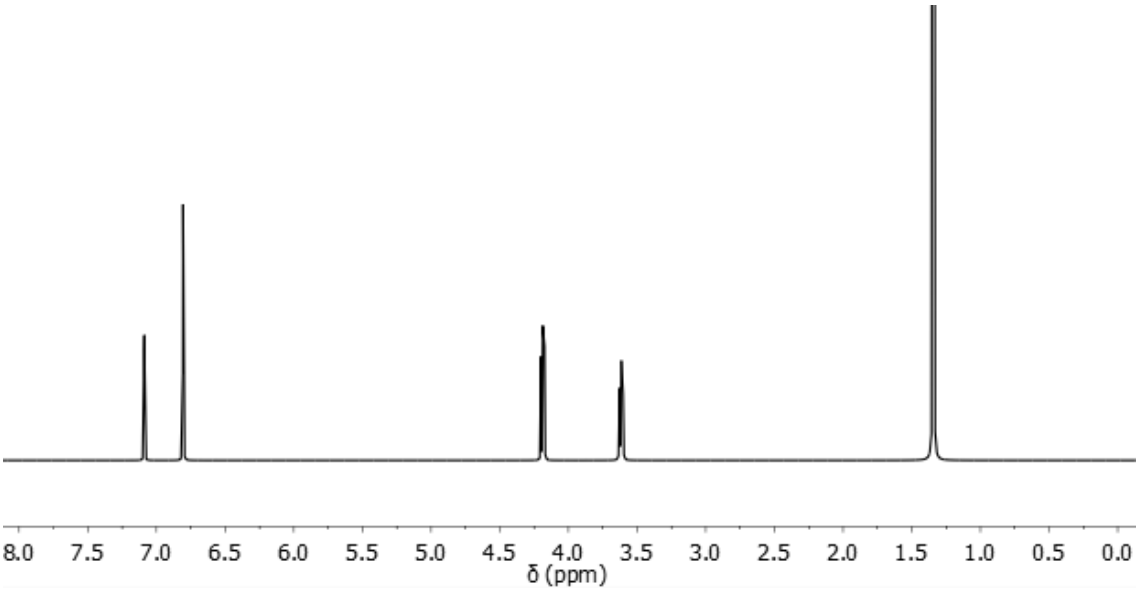

Figure 3.31. ^{1}H-NMR (400 MHz, $CDCl_3$) of **ES5**.

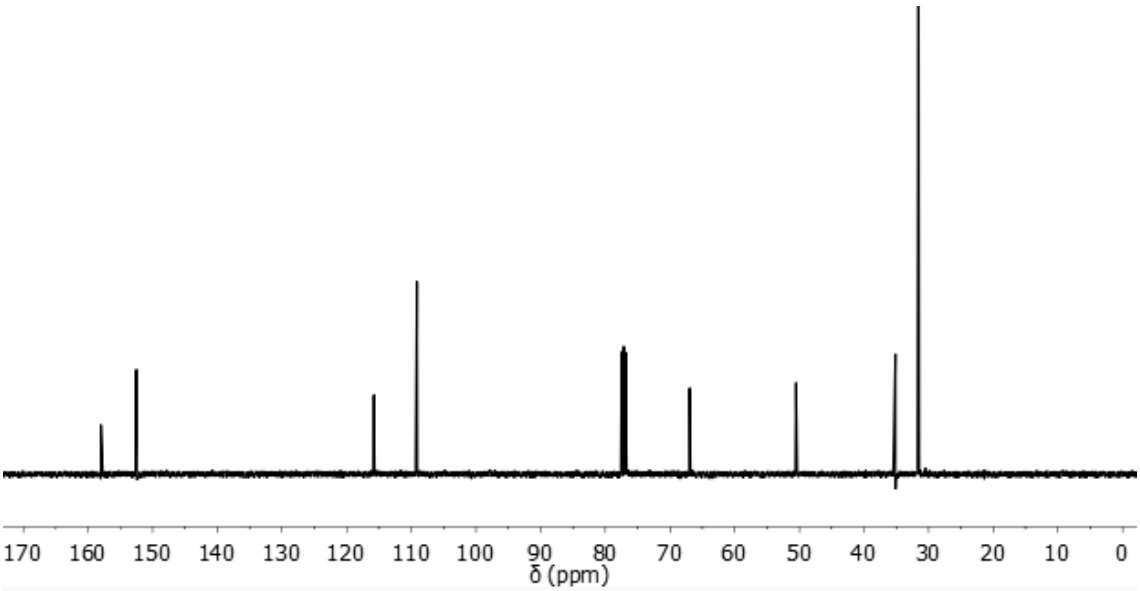

Figure 3.32. ^{13}C-NMR (100 MHz, $CDCl_3$) of **ES5.**

Synthesis of ES6.

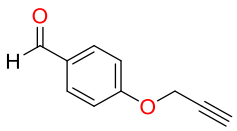

ES6

4-hydroxybenzaldehyde (1 g, 8.2 mmol) was dissolved in CH_3CN (40 mL). Then, K_2CO_3 (1.6 g, 11.5 mmol, 1.4 eq.) was added and the mixture was refluxed for 30 minutes before propargyl bromide (1.8 mL, 16.4 mmol, 2 eq.) was added. After the

addition, the mixture was refluxed for 2 h, then the solvent was removed under reduced pressure. The obtained solid was dispersed in water and extracted with EtOAc (4 × 100 mL). The combined organic layers were washed with brine, dried over Na_2SO_4, filtered, and the solvent removed in vacuo, affording compound **ES6** as a yellowish solid (1.27 g, yield 97%). ^{1}H-NMR (400 MHz, $CDCl_3$) δ: 9.90 (s, 1H), 7.90 – 7.81 (m, 2H), 7.13 – 7.05 (m, 2H), 4.78 (d, J = 2.4 Hz, 2H), 2.57 (t, J = 2.4 Hz, 1H). ^{13}C-NMR (100 MHz, $CDCl_3$,) δ 190.90, 162.51, 132.03, 130.75, 115.32, 77.68, 76.49, 56.09. HRMS (m/z) calculated for $C_{10}H_8O_2Na^+$ 183.0417, found 183.0416. Data consistent with that previously reported in literature.[220]

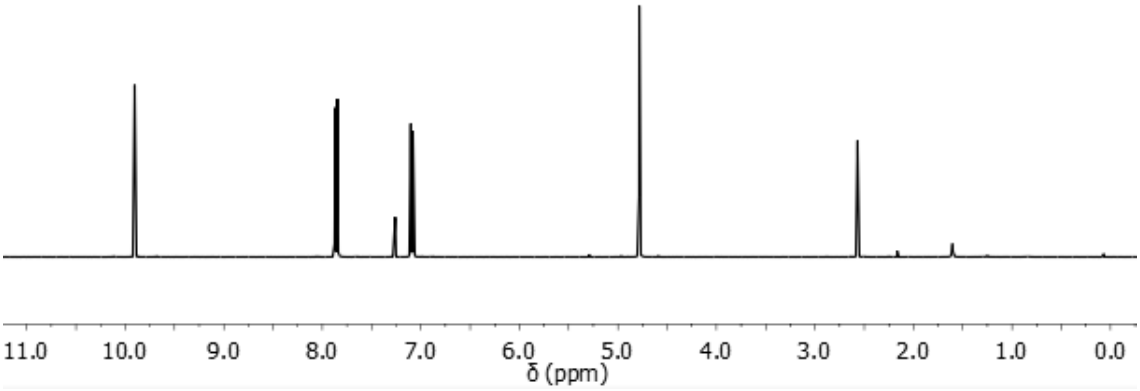

Figure 3.331. ^{1}H-NMR (400 MHz, $CDCl_3$) of **ES6**.

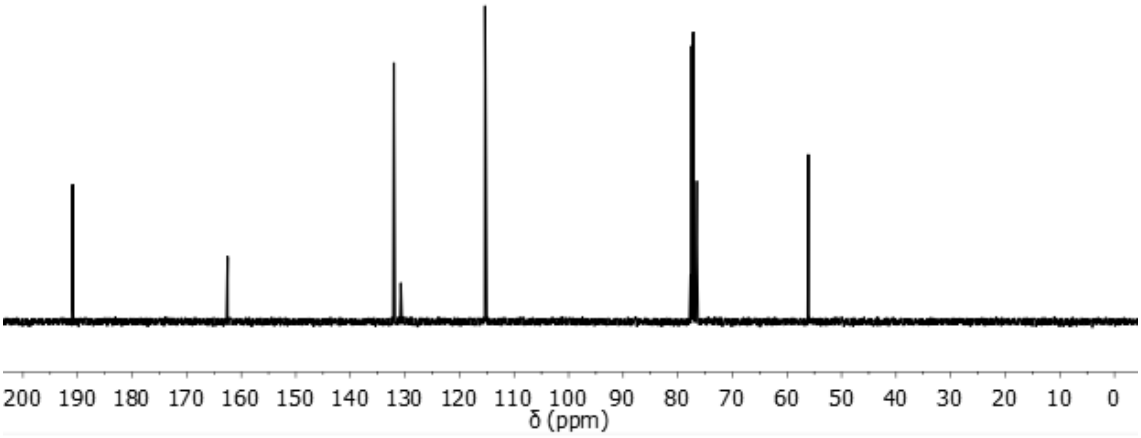

Figure 3.34.^{13}C-NMR (100 MHz, $CDCl_3$) of **ES6**.

Synthesis of ES7.

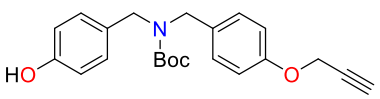

ES7

4-hydroxy benzylamine (431 mg, 3.5 mmol) and compound **ES6** (560 mg, 3.5 mmol) were dissolved in anhydrous MeOH (60 mL) with 10 mg of Na_2SO_4 and the reaction mixture was heated to reflux overnight. Formation of the imine intermediate was checked via TLC (eluent: DCM/MeOH 9:1). The reaction mixture was then filtered, concentrated under reduced pressure, and then diluted with dry THF/MeOH 1:1 (60 mL). $NaBH_4$ (530 mg, 4 eq.) was added in 5 portions over 1 h and the reaction mixture was stirred at r.t. for 6 h, while monitoring its progress via TLC. Once complete, the reaction was quenched with saturated NH_4Cl (10 mL). The organic solvents were removed under reduced pressure. The residue was dispersed with 50 mL of H_2O. The aqueous phase was extracted with EtOAc (3×30 mL) and the combined organic layers were washed with brine (20 mL), dried over Na_2SO_4, and filtered. The solvent was removed under reduced pressure, affording the intermediate amine as a yellowish oil (928 mg), used in the next step without any further purification. The intermediate compound (928 mg, 3.5 mmol) was dissolved in dry MeOH (20 mL) and $NaHCO_3$ (1.18 g, 14 mmol, 1.15 eq.) was added. Boc_2O (870 mg, 4 mmol, 1.1 eq.) was then dissolved in 10 mL of dry MeOH and added dropwise to the reaction mixture that was stirred for 6 h, while monitoring the reaction via TLC (eluent PE:EtOAc 7:3). MeOH was removed under reduced pressure and the residue resuspended in 50 mL H_2O. The aqueous phase was extracted with 3×30 mL EtOAc, then the organic phases were collected, washed with 60 mL of brine, dried over Na_2SO_4, filtered, and the solvent was removed under reduced pressure. The crude was purified by column chromatography (SiO_2, eluent PE:EtOAc 7:3) to afford a pale-yellow oil, that was with Et_2O to afford **ES7** as a white a solid. (866 mg, 67% over two steps) ^{1}H NMR (500 MHz, CD_3CN) δ 7.21 – 7.03 (m, 4H), 6.97 – 6.87 (m, 2H), 6.86 (s, 1H), 6.79 – 6.72 (m, 2H), 4.72 (d, *J* = 2.4 Hz, 2H), 4.32 – 4.22 (brd, 4H), 2.79 (t, *J* = 2.4 Hz, 1H), 1.45 (s, 9H). ^{13}C NMR (126 MHz, CD_3CN) δ 157.69, 157.06, 156.62, 132.56, 130.60, 130.08, 129.90, 116.10, 115.77, 80.40, 79.82, 76.71, 56.53, 49.87, 49.57, 28.62. HRMS (m/z) calculated for $C_{22}H_{25}NO_4Na^+$ 390.1676, found 390.1677.

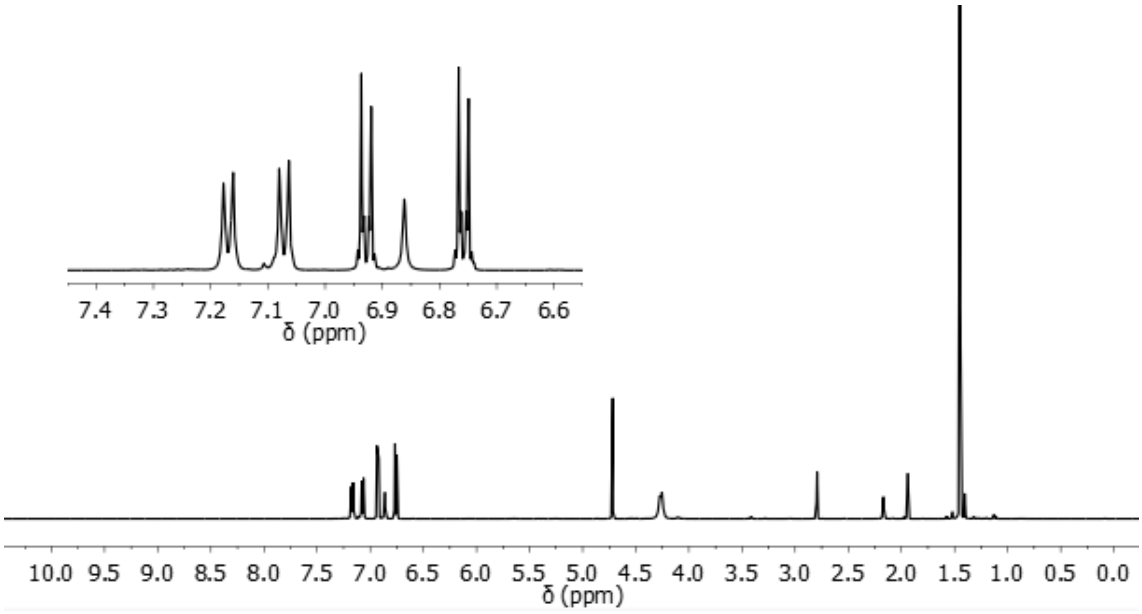

Figure 3.352. ^{1}H-NMR (500 MHz, CD_3CN) of **ES7**.

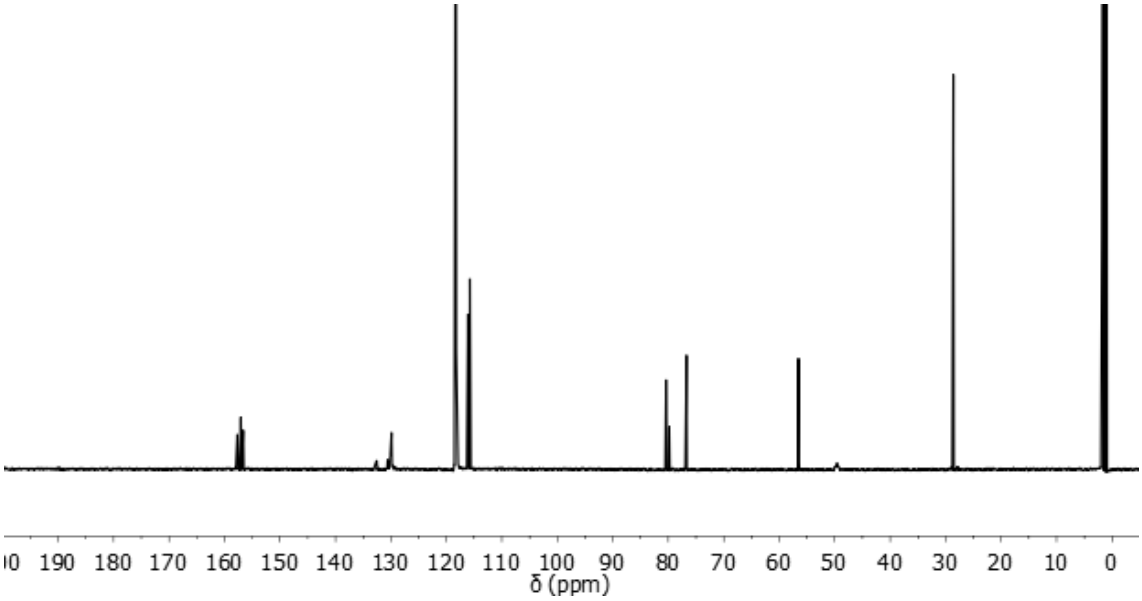

Figure 3.363. ^{13}C-NMR (126 MHz, CD_3CN) of **ES7**.

Synthesis of ES8.

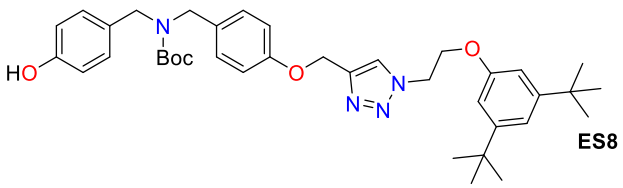

Compound **ES8** was synthetized according to an adjusted literature protocol used for similar compound.[221] Compound **ES7** (200 mg, 0.544 mmol, 1 eq.), compound **ES5**

(225 mg, 0.816 mmol, 1.5 eq.), $Cu[(CN)_4]PF_6$ (170 mg, 0.544 mmol, 1 eq.), and 2,6-lutidine (6.3 µL, 0.0544 mmol, 0.1 eq.) were dissolved in dry CH_2Cl_2 (10 mL) and stirred at r.t.. After 24 h, the mixture was diluted with CH_2Cl_2 (10 mL) and washed with EDTA (0.1 M aq.). The organic fraction was collected, dried over Na_2SO_4, and concentrated under reduced pressure. The crude product was purified by column chromatography (SiO_2, eluent PE/EtOAc 7:3 to 1:1) to afford a pale-yellow oil, which was triturated with Et_2O to afford **ES8** as a white solid. (238 mg, 68%). ^{1}H-NMR (500 MHz, $CDCl_3$,) δ 7.89 (s, 1H), 7.17 – 6.98 (m, 5H), 6.93 (d, J = 8.3 Hz, 2H), 6.73 (d, J = 8.3 Hz, 2H), 6.73 (d, J = 1.6 Hz, 2H), 6.66 – 6.52 (br s, 1H), 5.20 (s, 2H), 4.79 (t, J = 5.0 Hz, 2H), 4.39 (t, J = 5.0 Hz, 2H), 4.28 (br d, 4H), 1.50 (s, 9H), 1.31 (s, 18H). ^{13}C-NMR (126 MHz, $CDCl_3$,)157.62, 157.58, 156.19, 155.59, 152.74, 144.37, 130.86, 129.57, 129.06, 124.18, 116.19, 115.59, 114.92, 109.04, 80.26, 66.43, 62.11, 50.25, 48.65, 48.40, 35.13, 31.53, 28.64. HRMS (m/z) calculated for $C_{38}H_{50}N_4O_5Na^+$ 665.3673, found 665.3675.

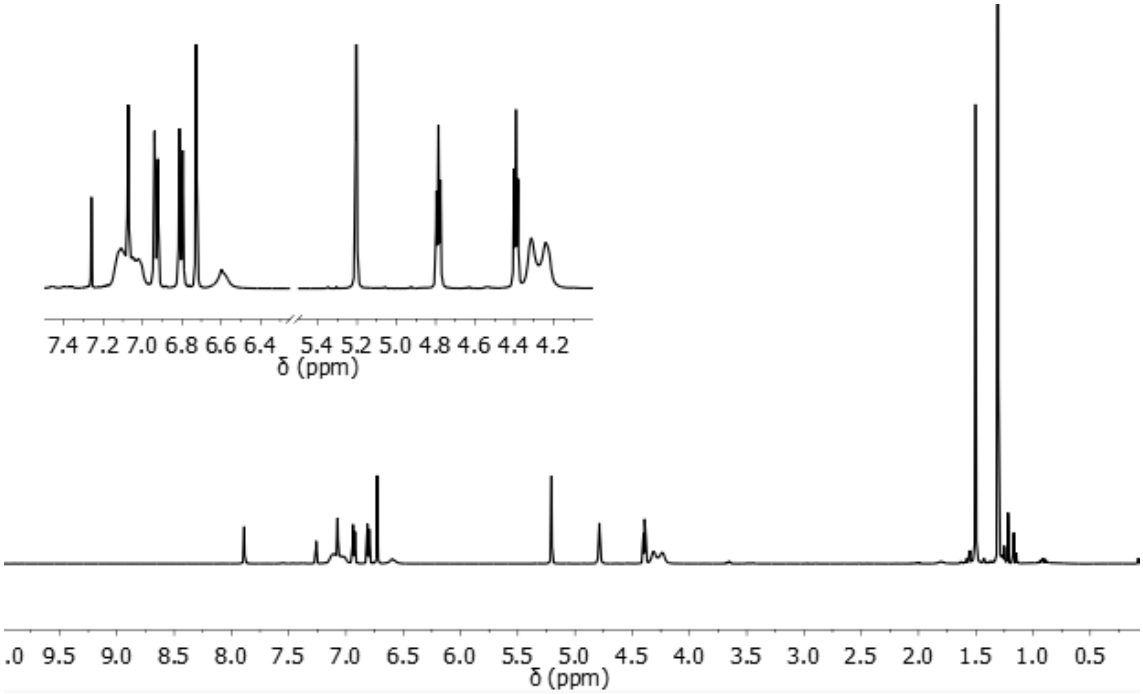

Figure 3.374. ^{1}H-NMR (500 MHz, $CDCl_3$) of **ES8**.

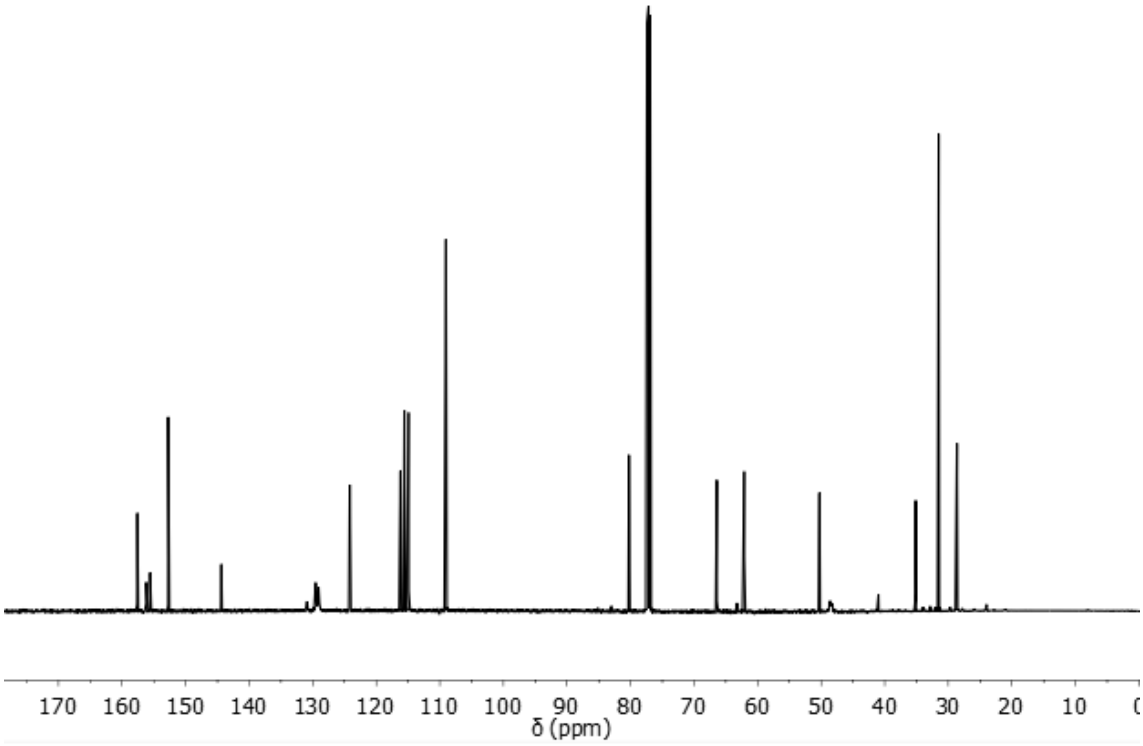

Figure 3.385. ^{13}C-NMR (126 MHz, $CDCl_3$) of **ES8**.

Synthesis of ES9.

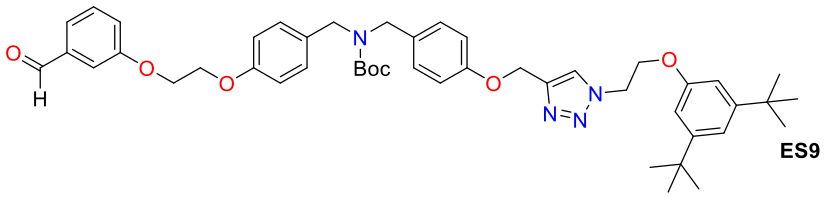

Compound **ES8** (193 mg, 0.3 mmol) and K_2CO_3 (145 mg, 1.05 mmol, 3.5 eq.) were dissolved in dry DMF (4 mL). Subsequently, compound **ES1** (225 mg, 0.816 mmol, 1.5 eq.) was dissolved in dry DMF (4 mL) and added dropwise. The reaction mixture was heated at 80 °C for 24 h, under stirring. The solvent was removed under reduced pressure, dissolved in EtOAc, and washed with water twice. The organic phases were collected, dried over Na_2SO_4, filtered, and the solvent was removed under reduced pressure. The crude product was purified by column chromatography (SiO_2, eluent DCM/acetone 100:0 to 95:5) to afford a pale-yellow oil, which was triturated with Et_2O to afford **ES9** as a white-off solid. (193 mg, 81%). ^{1}H NMR (400 MHz, CD_3CN) δ 9.96 (s, 1H), 7.97 (s, 1H), 7.53 – 7.44 (m, 3H), 7.30 – 7.24 (m, 1H), 7.15 (br d, *J* =6.9 Hz, 4H), 7.07 (t, J = 1.7 Hz, 1H), 6.98 – 6.89 (m, 4H), 6.73 (d, *J* = 1.7 Hz, 2H), 5.14 (s, 2H), 4.73 (t, *J* = 5.2 Hz, 2H), 4.42 – 4.25 (m, 10H), 1.44 (s, 9H), 1.28 (s, 18H). ^{13}C NMR (100 MHz, CD_3CN) δ 193.38, 160.34, 158.97, 158.87, 158.65, 156.64, 153.48, 144.49,

139.18, 132.03, 131.41, 130.04, 130.01, 125.53, 123.86, 122.41, 118.69, 116.60, 115.73, 115.54, 114.65, 110.10, 80.45, 68.07, 67.62, 67.44, 62.52, 50.75, 49.74, 49.65, 35.67, 31.63, 28.64. HRMS (m/z) calculated for $C_{47}H_{58}N_4O_7Na^+$ 813.4197, found 813.4195.

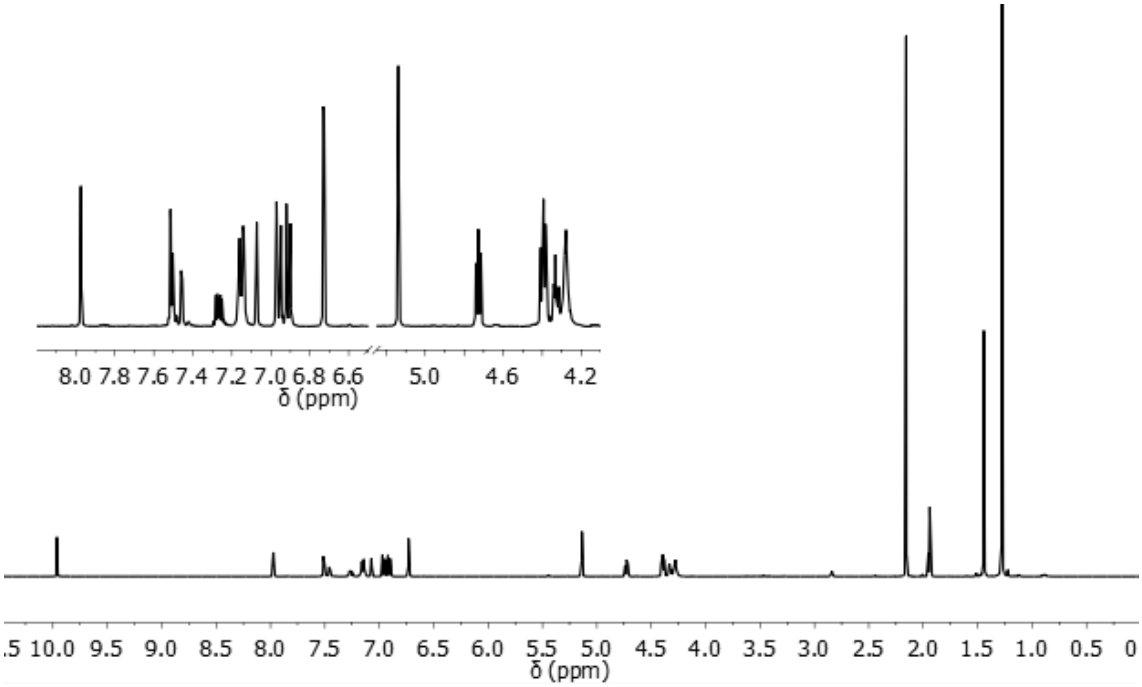

Figure 3.396. ^{1}H-NMR (400 MHz, CD_3CN) of **ES9**.

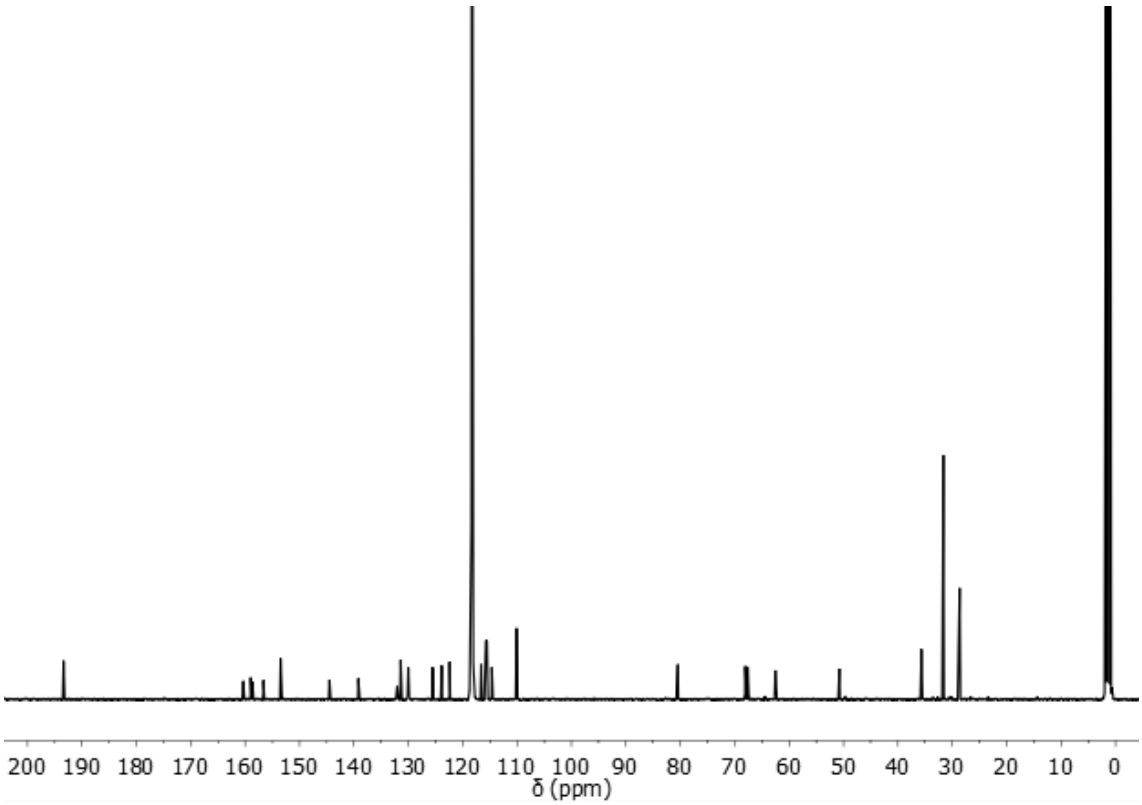

Figure 3.407. ^{13}C-NMR (100 MHz, CD_3CN) of **ES9**.

Synthesis of ES10.

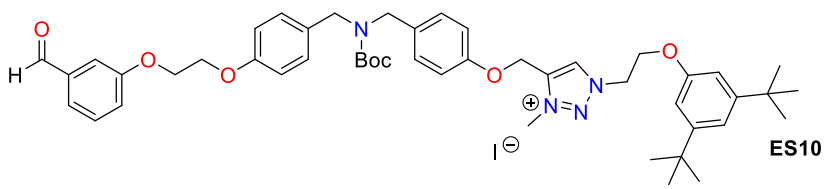

Compound **ES10** was synthetized according to an adjusted literature protocol used for similar compounds.[222] Compound **ES9** (42 mg, 0.053 mmol) was dissolved in CH_3I (4 mL) and stirred at 40°C for 4 d, under inert atmosphere. Then, the solution was concentrated under reduced pressure and the residue was dissolved in other 4 mL of CH_3I. The reaction was stirred at 40°C for additional 4 d. Then, the solution was concentrated and the crude product was purified by column chromatography (SiO_2, eluent DCM/acetone 95:5 to DCM:MeOH 9:1) to afford a pale-yellow oil, which was triturated with Et_2O to afford **ES10** as a yellow solid. (47 mg, 95%). ^{1}H NMR (400 MHz, $CDCl_3$) δ 9.97 (s, 1H), 9.41 (s, 1H), 7.50 - 7.43 (m, 3H), 7.26 – 7.22 (m, 1H), 7.21 – 7.09 (br s, 4H), 7.07 (t, J = 1.6 Hz, 1H), 7.01 – 6.95 (m, 2H), 6.93 – 6.87 (m, 2H), 6.73 (d, J = 1.6 Hz, 2H), 5.54 (s, 2H), 5.17 (t, J = 4.5 Hz, 2H), 4.56 (t, J = 4.6 Hz, 2H), 4.44 (s, 3H), 4.41 – 4.21 (m, 8H), 1.49 (s, 9H), 1.29 (s, 18H). ^{13}C NMR (126 MHz, $CDCl_3$) δ 192.18, 159.36, 157.94, 157.02, 156.11, 156.02, 152.91, 139.85, 137.92, 132.61, 131.66, 130.64, 130.29, 129.67, 129.57, 129.36, 128.99, 124.04, 122.29, 116.55, 114.95, 114.86, 113.01, 109.08, 80.26, 77.41, 77.16, 76.91, 66.97, 66.61, 64.95, 59.16, 54.43, 48.76, 48.21, 39.94, 35.17, 31.52, 28.61. HRMS (m/z) calculated for $C_{48}H_{61}N_4O_7^+$ 805.4540, found 805.4538.

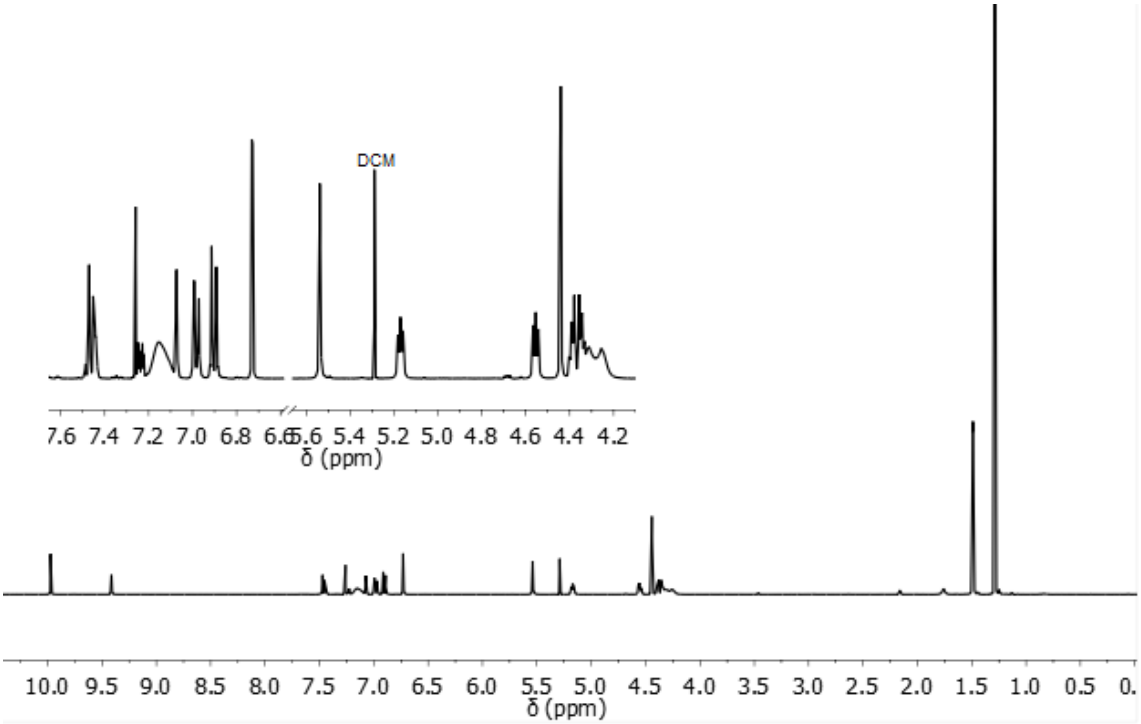

Figure 3.418. ^{1}H-NMR (400 MHz, $CDCl_3$) of **ES10**.

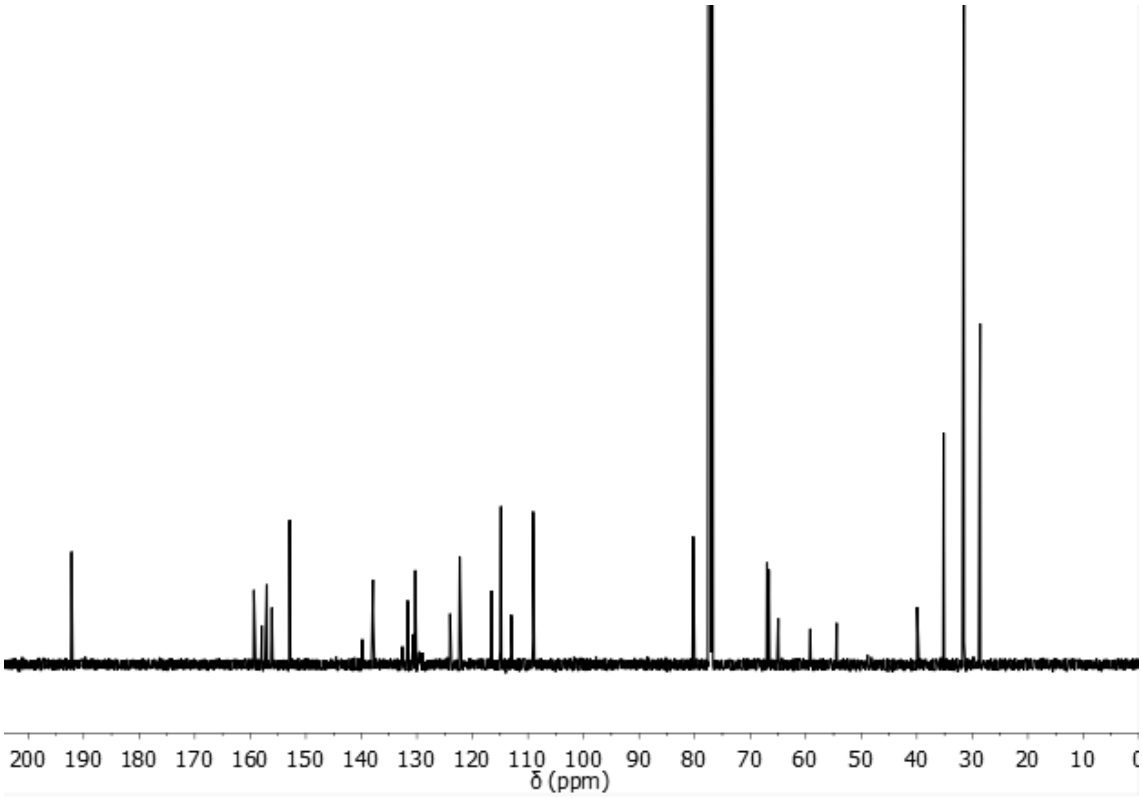

Figure 3.429. ^{13}C-NMR (126 MHz, $CDCl_3$) of **ES10.**

Synthesis of 1bHPF_6.

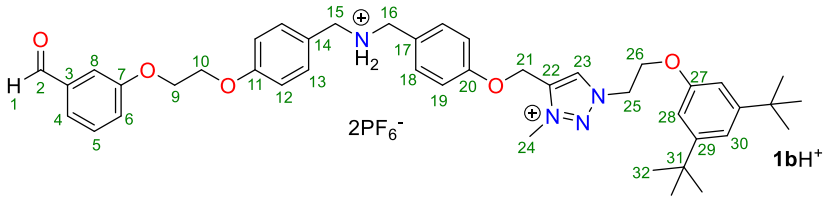

Compound **1b** was synthetized according to an adjusted literature protocol used for similar compounds.[222] Compound **ES10** (50 mg, 0.054 mmol) was dissolved in a solution 1:1 DCM:TFA (10 mL) and stirred at r.t. for 4 h. Then, the solvent was removed under reduced pressure. The residue was dissolved in 1 mL of THF and a saturated NH_4PF_6 aq. (5 mL) was added while stirring. The mixture suddenly turned foamy, and the suspension was stirred overnight. The suspension was extracted with DCM (10 mL × 3). The organic fractions were gathered, washed with brine, and dried over Na_2SO_4 and then the solution was concentrated under reduced pressure. The obtained residue was dissolved in the minimum amount of CH_3CN and transferred to a 50 mL centrifuge tube. Et_2O (20 mL) was added and. the suspension was centrifuged at 3000 rpm for 5 min. After removal of the supernatant, a yellow oil was obtained, which was further triturated with Et_2O to afford **1b**HPF_6 as a pale-yellow solid. (54 mg, quantitative).

^{1}H NMR (500 MHz, CD_3CN) δ 9.97 (s, 1H, 1), 8.59 (s, 1H, 23), 7.56 – 7.49 (m, 2H, 4+6), 7.49 – 7.38 (m, 5H, 13+18+8), 7.31 – 7.23 (m, 1H, 5), 7.14 – 7.08 (m, 3H, 30+12), 7.07 – 7.00 (m, 2H, 19), 6.78 (d, J = 1.6 Hz, 2H, 28), 5.33 (s, 2H, 21), 4.95 (t, J = 4.7 Hz, 2H, 25), 4.46 (t, J = 4.9 Hz, 2H, 26), 4.44 – 4.34 (m, 4H, 9+10), 4.27 (s, 3H, 24), 4.18 (d, J = 4.2 Hz, 4H, 15+16), 1.29 (s, 18H, 32).

^{13}C NMR (126 MHz, CD_3CN) δ 193.39 (2), 160.74 (11), 160.24 (7), 159.20 (20), 158.44 (27), 153.66 (29), 140.44 (22), 139.18 (3), 133.08 (13), 132.97 (18), 131.45 (4/6), 131.38 (23), 125.24 (14), 124.14 (4/6), 123.64 (17), 122.39 (5), 117.02 (30), 116.14 (12), 115.98 (19), 114.38 (8), 110.07 (28), 67.91 (9/10), 67.73 (9/10), 65.96 (26), 59.10 (21), 54.74 (25), 51.90 (16), 51.51 (15), 39.61 (24), 35.70 (31), 31.58 (32). HRMS (m/z) calculated for $C_{43}H_{53}N_4O_5^{2+}$ 353.2042, found 353.2042.

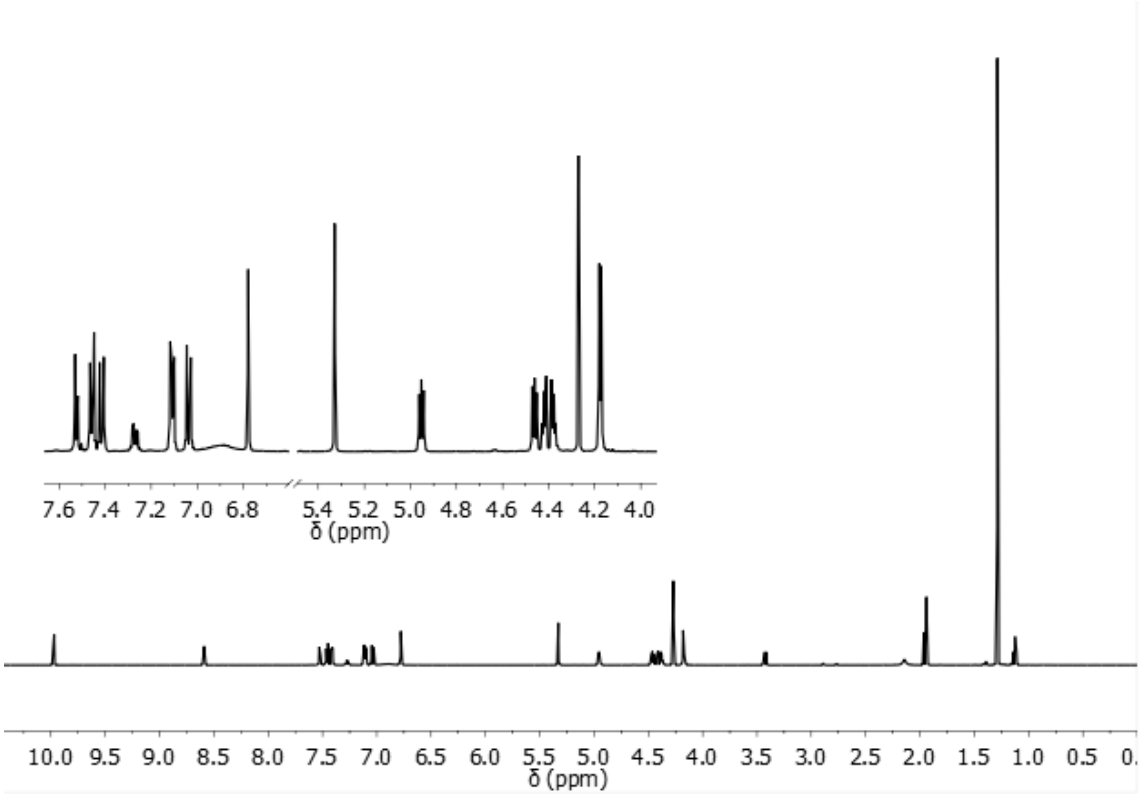

Figure 3.43. ^{1}H-NMR (500 MHz, CD_3CN) of **1b**HPF_6.

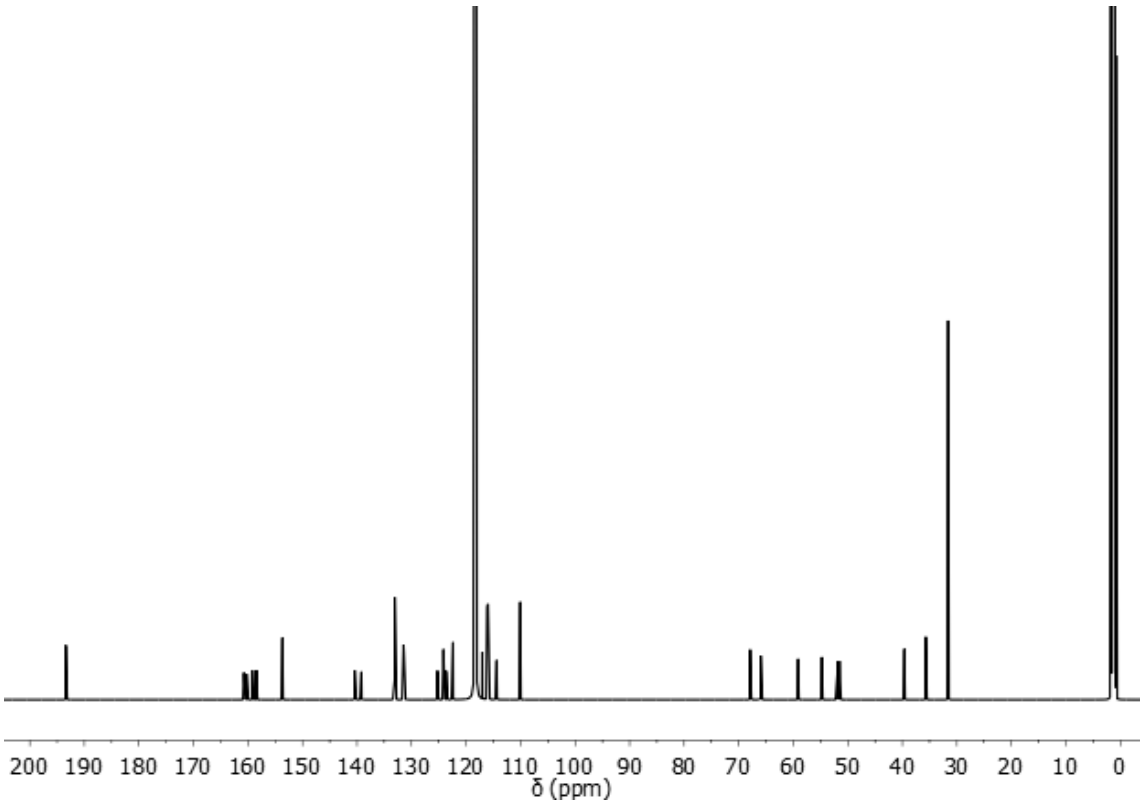

Figure 3.44. ^{13}C-NMR (126 MHz, CD_3CN) of **1b**HPF_6.

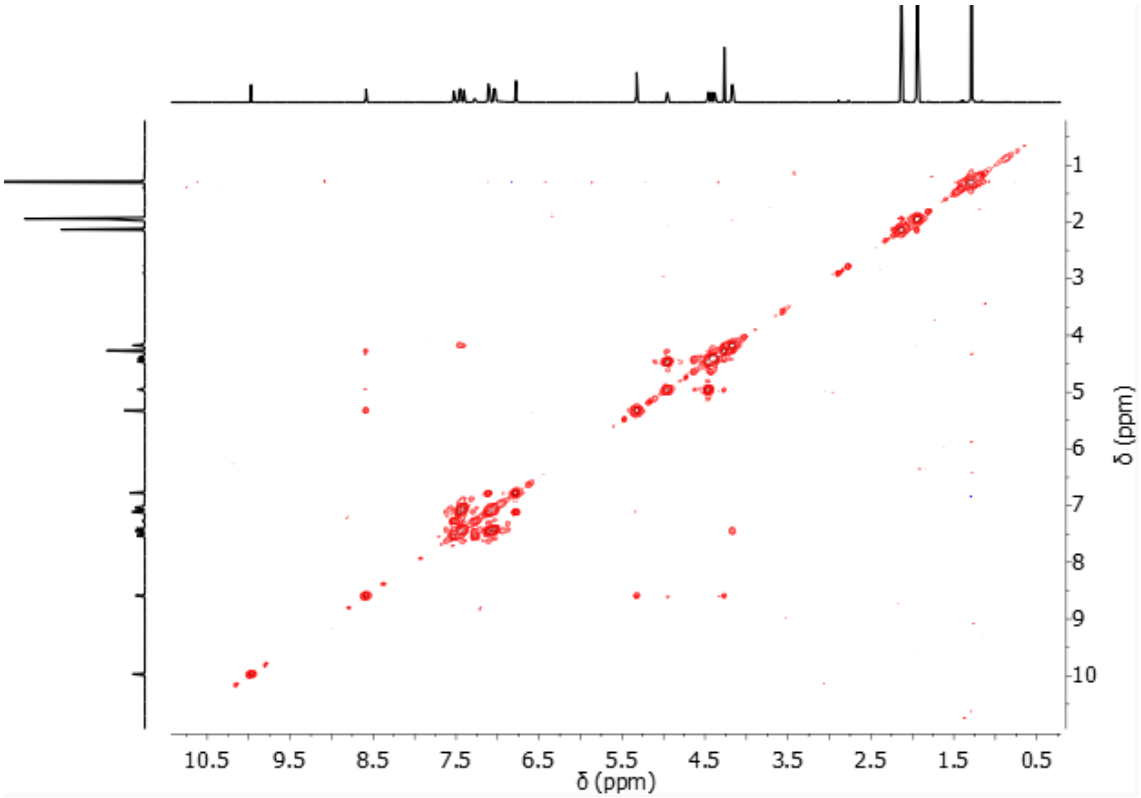

Figure 3.45. ^{1}H-^{1}H COSY (126 MHz, CD_3CN) of **1b**HPF_6.

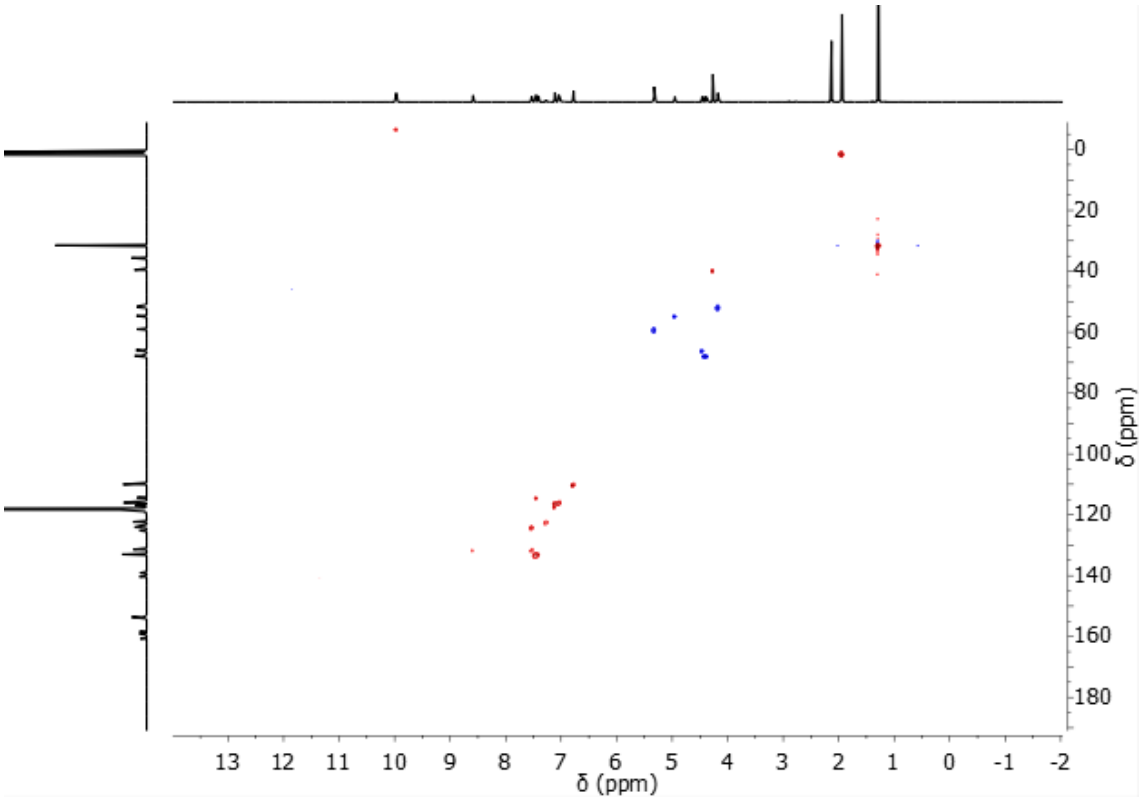

Figure 3.4610. ^{1}H-^{13}C HSQCAD (CD_3CN) of **1b**HPF_6.

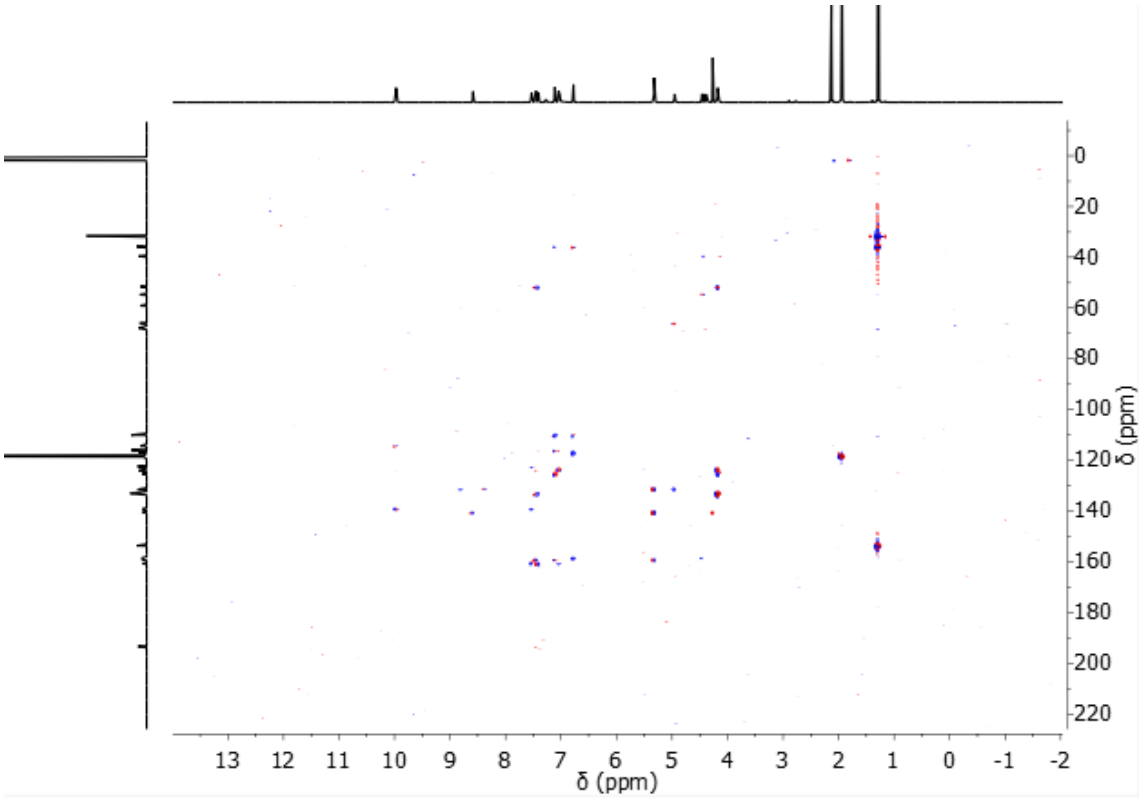

Figure 3.4711. ^{1}H-^{13}C HMBCAD (CD_3CN) of **1b**HPF_6.

3.3 Synthesis of hydrazides 2

Synthesis of ES11.

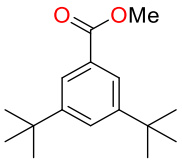

ES11

Concentrated H_2SO_4 (0.4 mL) was added drop by drop to a solution of 3,5-di-tert-butylbenzoic acid (506 mg, 2.16 mmol, 1 eq.) in MeOH (24 mL). The reaction mixture was heated at reflux during 16 h. After this time, the reaction was cooled to r.t. and the solvent was removed under reduced pressure. The crude was purified by column chromatography, using a PE/EtOAc (5/1) mixture as eluent. The final product was obtained as a white solid (515 mg, 96%). ^{1}H-NMR (500 MHz, $CDCl_3$), δ: 7.90 (d, J = 1.9 Hz, 2H), 7.63 (t, J = 1.9 Hz, 1H), 3.92 (s, 3H), 1.36 (s, 18H). ^{13}C-NMR (126 MHz, $CDCl_3$), δ: 167.8, 151.0, 129.5, 127.1, 123.8, 52.0, 34.9, 31.4. HRMS (m/z) calculated for $C_{16}H_{24}O_2Na^+$ 248.1776, found 271.1669.

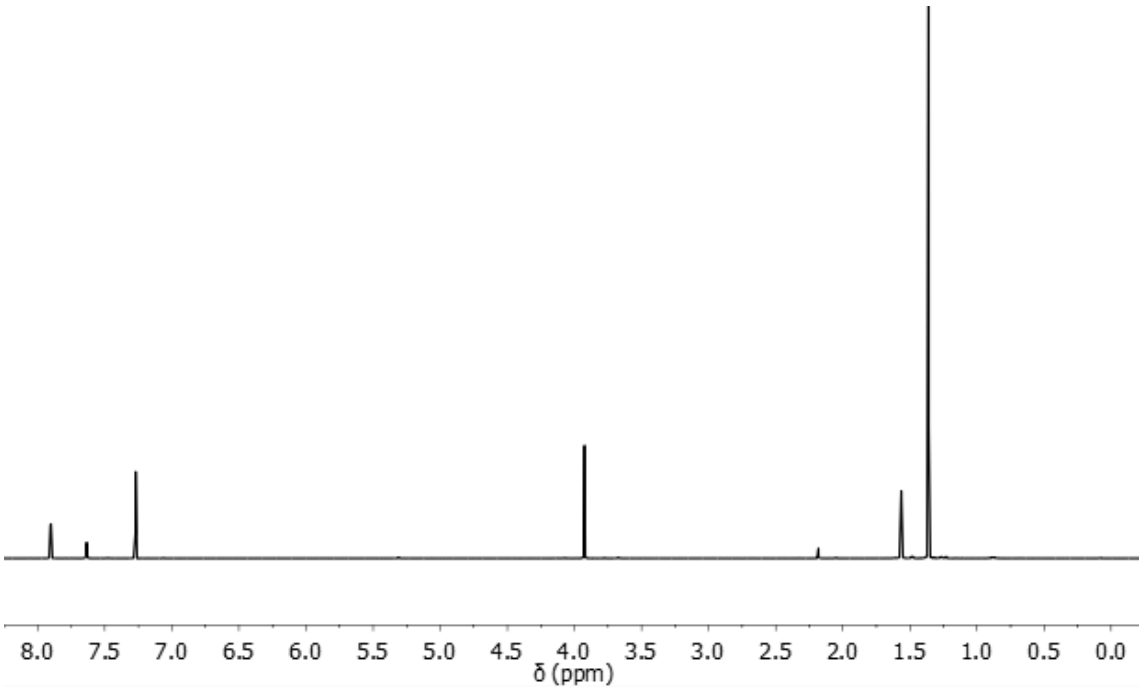

Figure12 **3.48**13. ^{1}H-NMR (500 MHz, $CDCl_3$) of **ES11**.

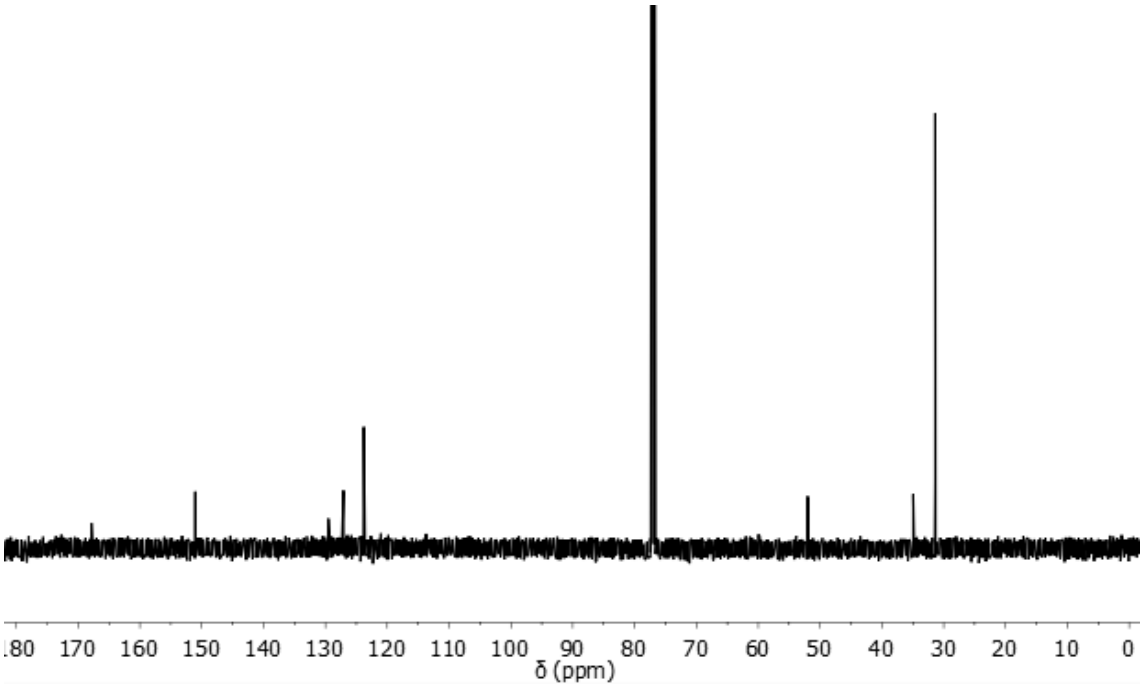

Figure 3.49. ^{13}C-NMR (126 MHz, $CDCl_3$) of **ES11**.

Synthesis of 2a.

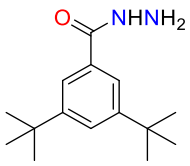

2a

Hydrazine hydrate (3 mL, 57.8 mmol, 76 eq.) was added drop by drop to a solution of **ES11** (265.8 mg, 1.07 mmol, 1 eq.) in MeOH (24 mL). The reaction mixture was heated at reflux during 24 h and after this time, it was cooled to r.t.. Then, water was added and the crude was extracted with Et_2O three times. The combined organic layers were washed with $NaHCO_3$ (sat) and brine, dried with Na_2SO_4, filtered and the solvent was removed under reduced pressure. The final product was obtained as a white solid (250 mg, 94%). ^{1}H-NMR (500 MHz, CD_2Cl_2), δ: 7.60 (t, J = 1.8 Hz, 1H), 7.55 (d, J = 1.8 Hz, 2H), 7.43 (s, 1H), 4.08 (s, 2H), 1.34 (s, 18H). ^{13}C-NMR (126 MHz, CD_2Cl_2), δ: 169.2, 151.4, 132.6, 125.9, 120.9, 34.9, 31.1. HRMS (m/z) calculated for $C_{15}H_{24}N_2O$ H^+ 248.1889, found 249.1961.

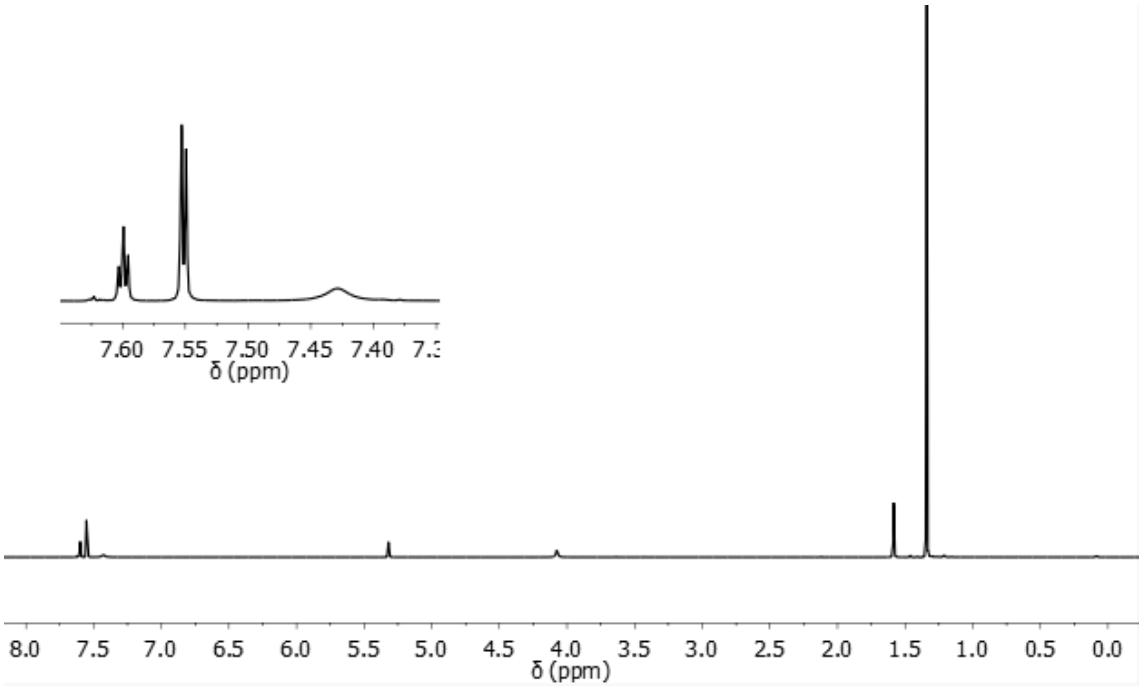

Figure 3.50 14. ^{1}H-NMR (500 MHz, CD_2Cl_2) of **2a.**

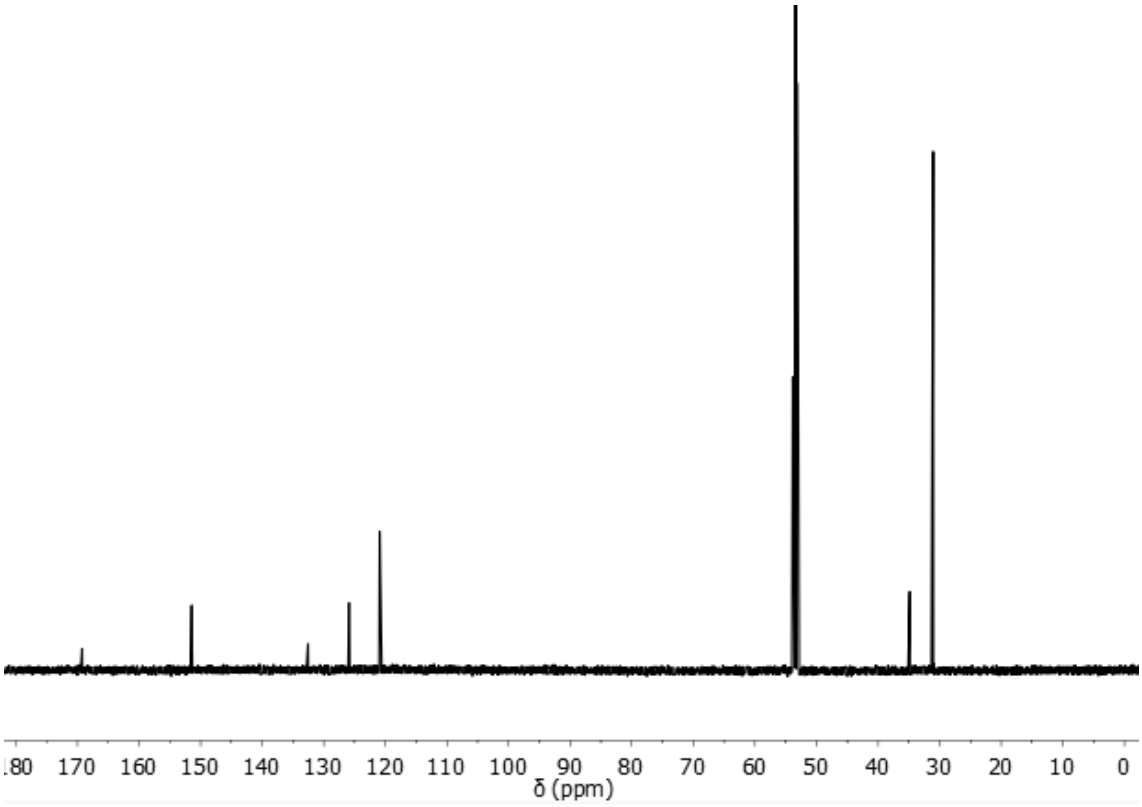

Figure 3.5115. ^{13}C-NMR (126 MHz, CD_2Cl_2) of **2a.**

Synthesis of 2c.

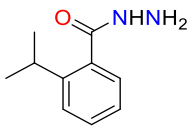

2c

5 mL of thionyl chloride were added to 2-isopropylbenzoic acid (0.125 g, 0.761 mmol, 1 eq.) in a two necked round bottom flask. The mixture was refluxed during 3 h. The excess of thionyl chloride was removed under reduced pressure. The resulting product was used without further purification. The obtained acyl chloride was dissolved in MeOH (10 mL) and hydrazine hydrate (3 mL, 57.8 mmol, 76 eq.) was added dropwise. The reaction mixture was heated at reflux for 5 d, monitoring reaction progress by TLC (hexane/DCM 1:1). Two additional aliquots of 1 mL of hydrazine hydrate were added after 24 and 48 h from the start of the reaction. After 5 d, the reaction mixture was cooled at r.t. and concentrated under reduced pressure. Hexane was added to the crude. A precipitate formed, which was filtered to obtain **2c** as a white powder (85.5 mg, 63%). ^{1}H-NMR (500 MHz, CD_3CN), δ: 7.73 (s, 1H), 7.44-7.36 (m, 2H), 7.26-7.16 (m, 2H), 4.10 (s, 2H), 3.22 (hept, J= 6.9 Hz, 1H), 1.21 (d, J = 6,9 Hz, 6H). ^{13}C-NMR (126 MHz, CD_3CN), δ: 170.1, 146.8, 135.1, 129.9, 126.9, 125.7, 125.5, 117.3, 29.8, 23.3. HRMS (m/z) calculated for $C_{10}H_{15}N_2O^+$ 178.1106, found 179.1179.

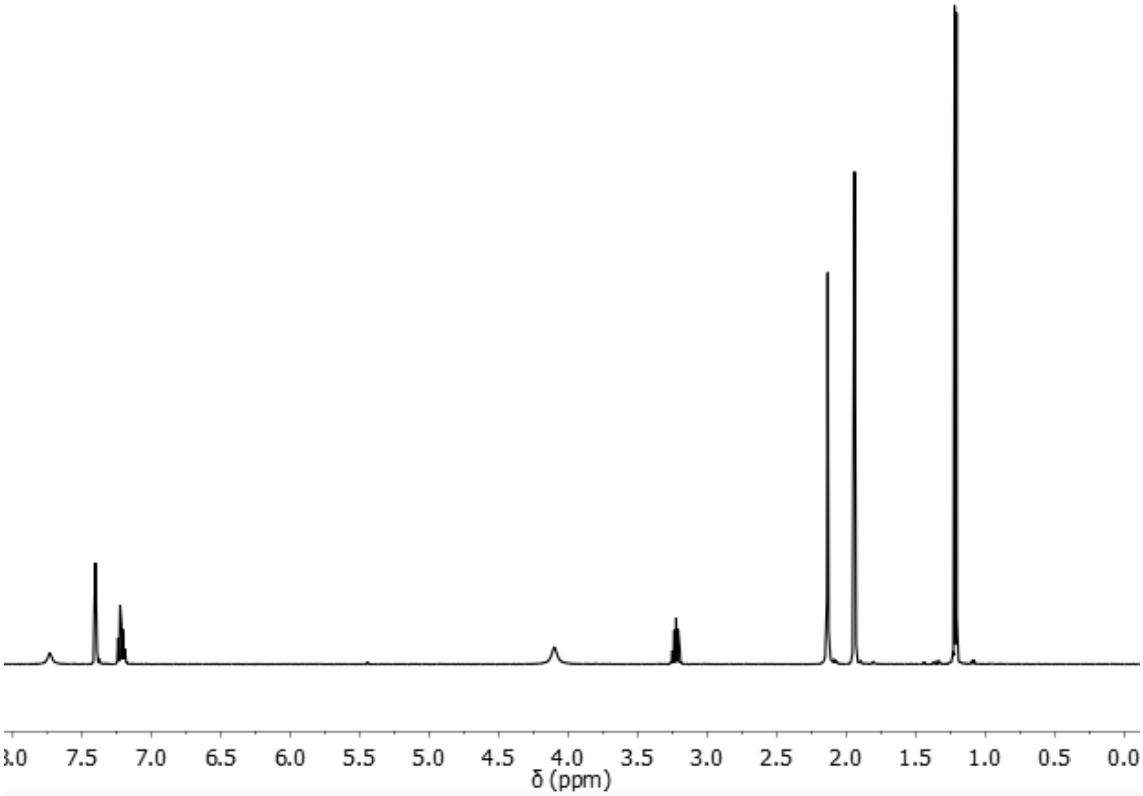

Figure 3.52 16. ^{1}H-NMR (500 MHz, CD_3CN) of **2c**.

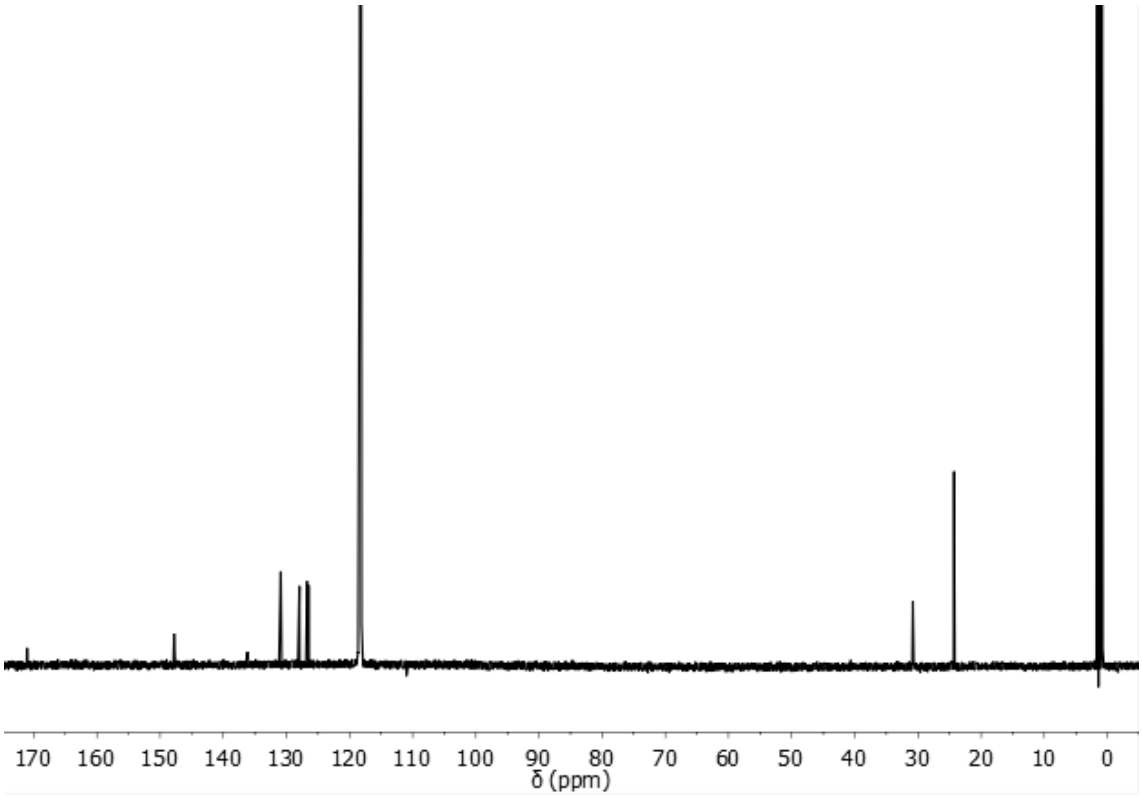

Figure 3.53. ^{1}H-NMR (126 MHz, CD_3CN) of **2c**.

Synthesis of 2d.

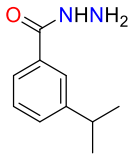

2d

5 mL of thionyl chloride were added to 3-isopropylbenzoic acid (0.125 g, 0.761 mmol, 1 eq.) in a two necked round bottom flask and the mixture was refluxed for 3 h. The excess of thionyl chloride was removed under reduced pressure. The resulting product was used without further purification. To a solution of the total crude acyl chloride in MeOH (24 mL), hydrazine hydrate (3 mL, 57.8 mmol, 76 eq.) was added dropwise. The reaction mixture was heated at reflux for 5 d, monitoring reaction progress by TLC (hexane/DCM 1:1). Two additional aliquots of 1 mL of hydrazine hydrate were added after 24 and 48 h from the start. After this time, the reaction mixture was cooled at r.t. and the solvent was removed under reduced pressure. Hexane was added to the crude. A precipitate formed, which was filtered to obtain **2d** as a white powder (122.1 mg, 90%). ^{1}H-NMR (500 MHz, CD_3CN), δ: 8.12 (s, 1H), 7.63 (td, J = 1.8, 0.6 Hz, 1H), 7.56 (dt, J = 7.5, 1.8 Hz, 1H), 7.43-7.39 (m, 1H), 7.37 (td, J = 7.5, 0.6 Hz, 1H), 4.11 (s, 2H), 2.97 (hept, J= 7.0 Hz, 1H), 1.26 (d, J = 7.0 Hz, 6H). ^{13}C-NMR (125 MHz, CD_3CN), δ: 167.6,

149.4, 133.5, 129.6, 128.5, 124.9, 124.5, 117.3, 33.9, 23.2. HRMS (m/z) calculated for $C_{10}H_{15}N_2O^+$ 178.1106, found 179.1180.

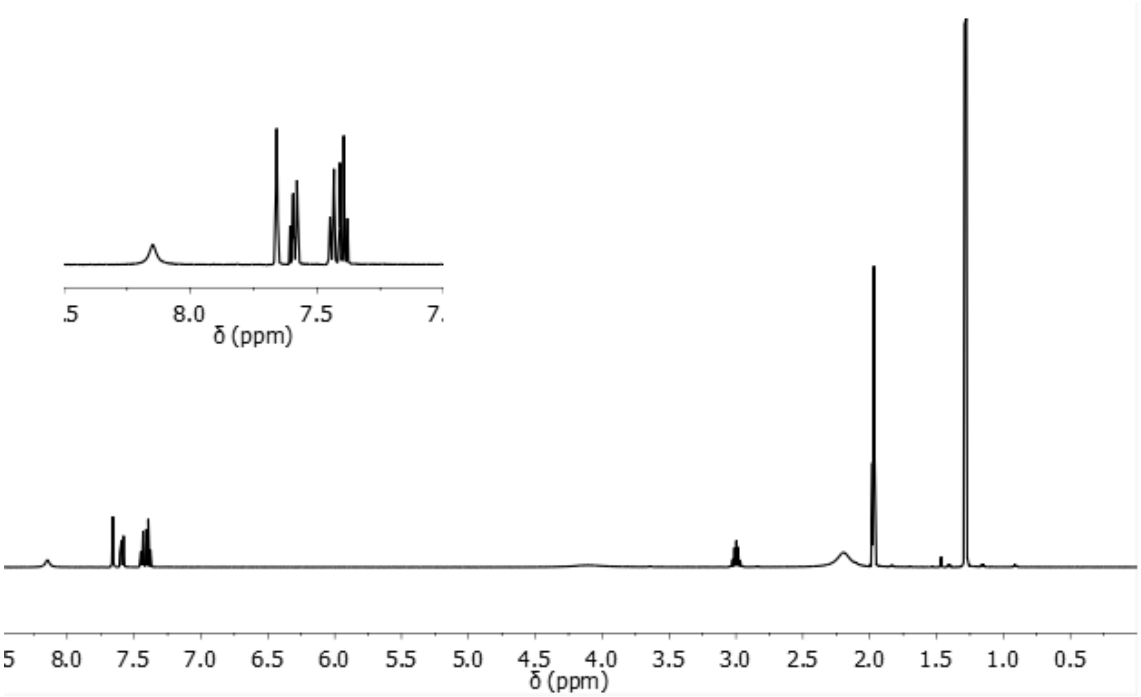

Figure 3.541718. ^{1}H-NMR (500 MHz, CD_3CN) of **2d**.

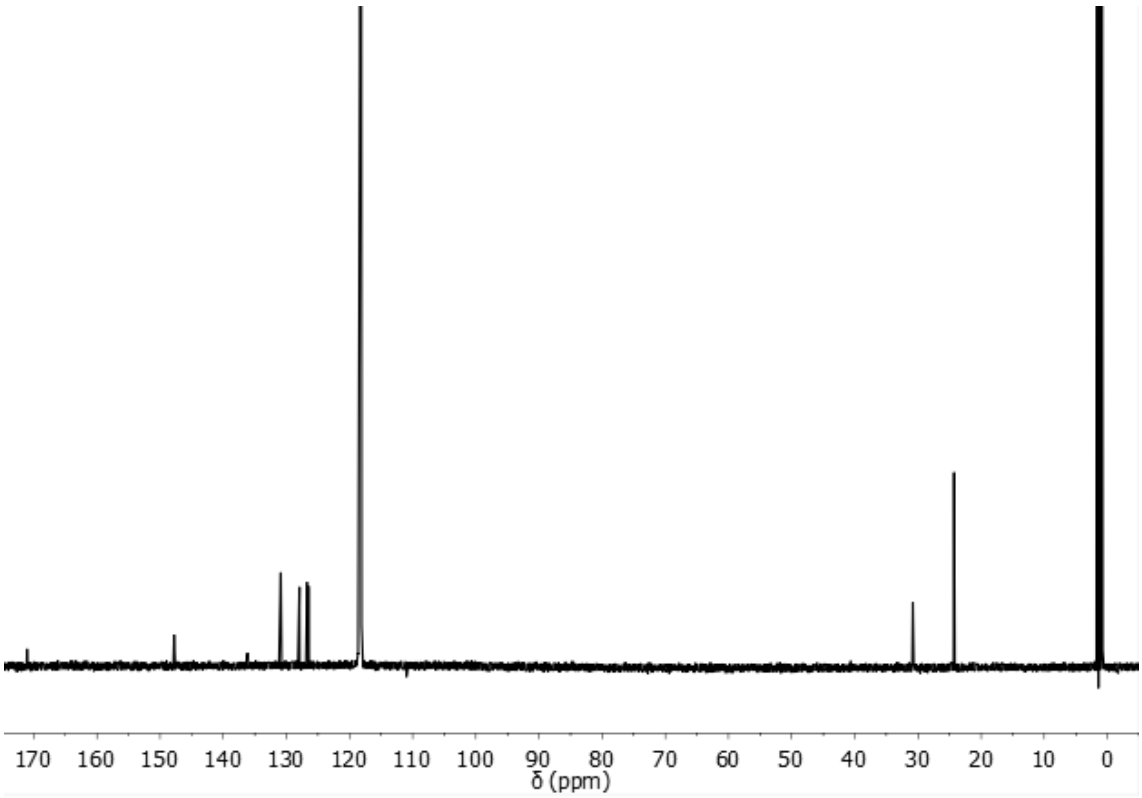

Figure 3.5519. ^{13}C-NMR (126 MHz, CD_3CN) of **2d**.

Synthesis of ES12.

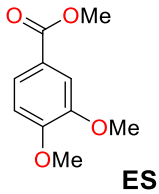

ES12

3,4-dimethoxybenzoic acid (0.5 g, 2.74 mmol, 1 eq.) was dissolved in 50 mL of MeOH and cooled in an ice bath for 15 min. After this time, 0.6 mL (3 eq.) of thionyl chloride were added dropwise and the reaction mixture was stirred at r.t. for 3 d. Solvent and thionyl chloride were removed under reduced pressure, the residue was disssolved in EtOAc, washed with saturated $NaHCO_3$ aq. and brine, dried over Na_2SO_4, and filtered. The solvent was removed under reduced pressure to obtain **ES12** as a white solid (467.7 mg, 87%). ^{1}H-NMR (400 MHz, $CDCl_3$), δ: 7.69 (dd, J = 8.4, 2.0 Hz, 1H), 7.55 (d, J = 2.0 Hz, 1H), 6.89 (d, J = 8.4 Hz, 1H), 3.94 (d, J = 1.4 Hz, 6H), 3.90 (s, 3H). ^{13}C-NMR (100 MHz, $CDCl_3$), δ: 166.9, 152.9, 148.6, 123.6, 122.7, 111.9, 110.2, 56.0, 55.9, 52.0. HRMS (m/z) calculated for $C_{10}H_{12}O_4Na^+$ 196.0736, found 219.0627.

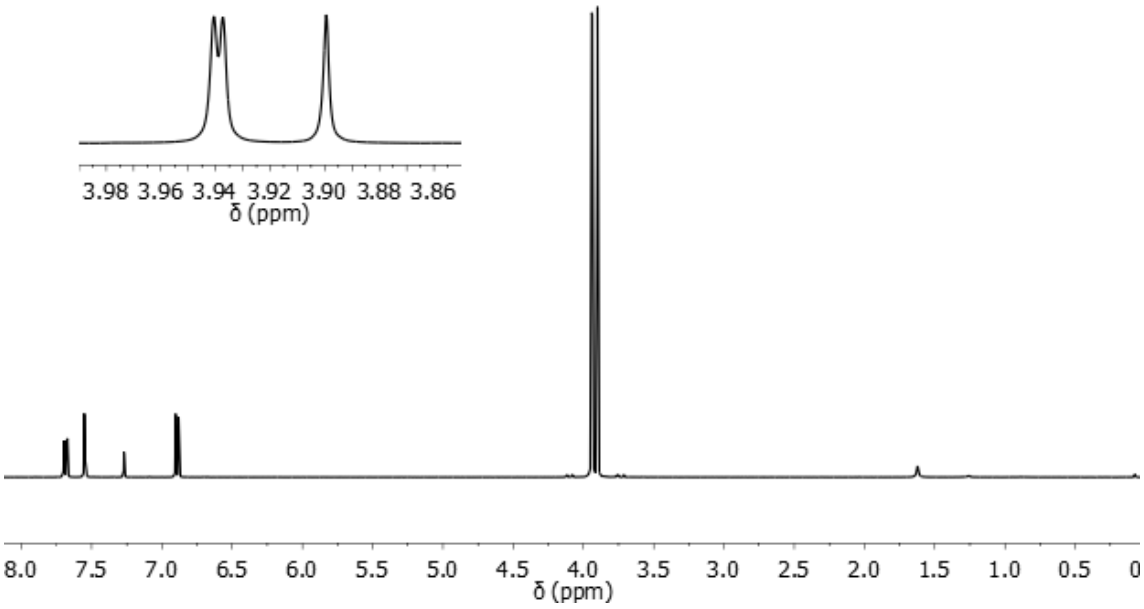

Figure 3.5620. ^{1}H-NMR (400 MHz, $CDCl_3$) of **ES12**.

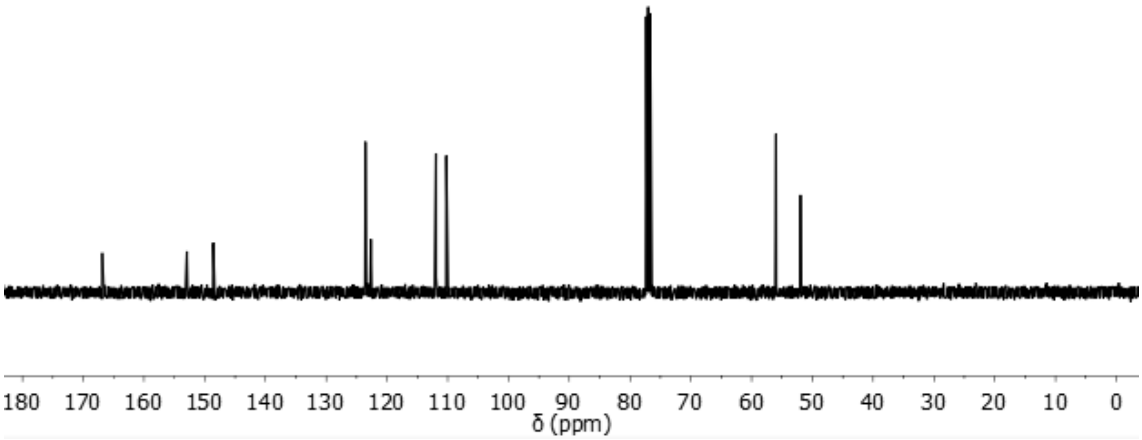

Figure 3.57. ^{1}H-NMR (100 MHz, $CDCl_3$) of **ES12**.

Synthesis of 2k.

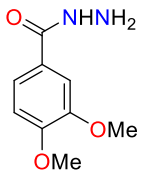

2k

Hydrazine hydrate (3 mL, 57.8 mmol, 76 eq.) was added dropwise to a solution of **ES12** (131.5 mg, 0.67 mmol, 1 eq.) in EtOH (24 mL). The reaction mixture was heated at reflux for 3 d. After this time, the reaction mixture was cooled to r.t. and the solvent and the hydrazine were removed under reduced pressure. The minimum amount of MeOH was used to dissolve the residue and hexane was added. The solution kept at -20 °C overnight, leading to the formation of a precipitate. The precipitate was filtered to obtain **2k** as white solid (81.5 mg, 62%). ^{1}H-NMR (500 MHz, CD_3CN), δ: 8.11 (s, 1H), 7.36 (dd, J = 8.3, 2.1 Hz, 1H), 7.33 (d, J = 2.1 Hz, 1H), 6.96 (d, J = 8.3 Hz, 1H), 4.09 (s, 2H), 3.84 (s, 3H), 3.84 (s, 3H). ^{13}C-NMR (126 MHz, CD_3CN), δ: 167.1, 151.9, 148.9, 125.7, 120.0, 110.9, 110.3, 55.4, 55.4. HRMS (m/z) calculated for $C_9H_{12}N_2O_3Na^+$ 196.0848, found 219.0739.

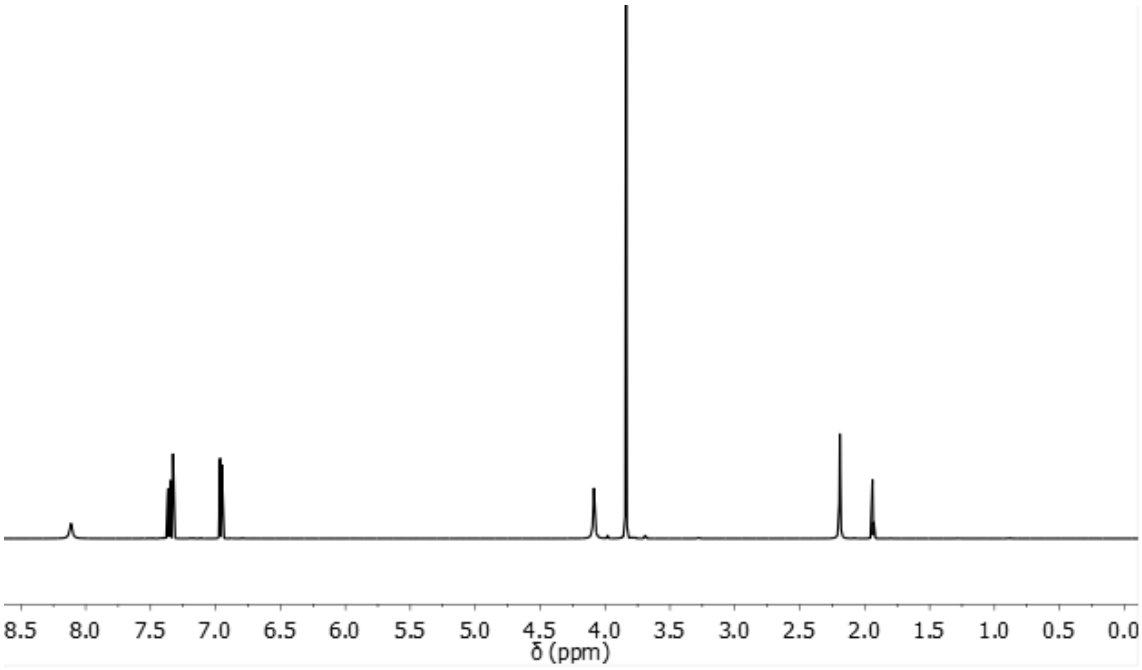

Figure 3.58. ^{1}H-NMR (500 MHz, CD_3CN) of **2k**.

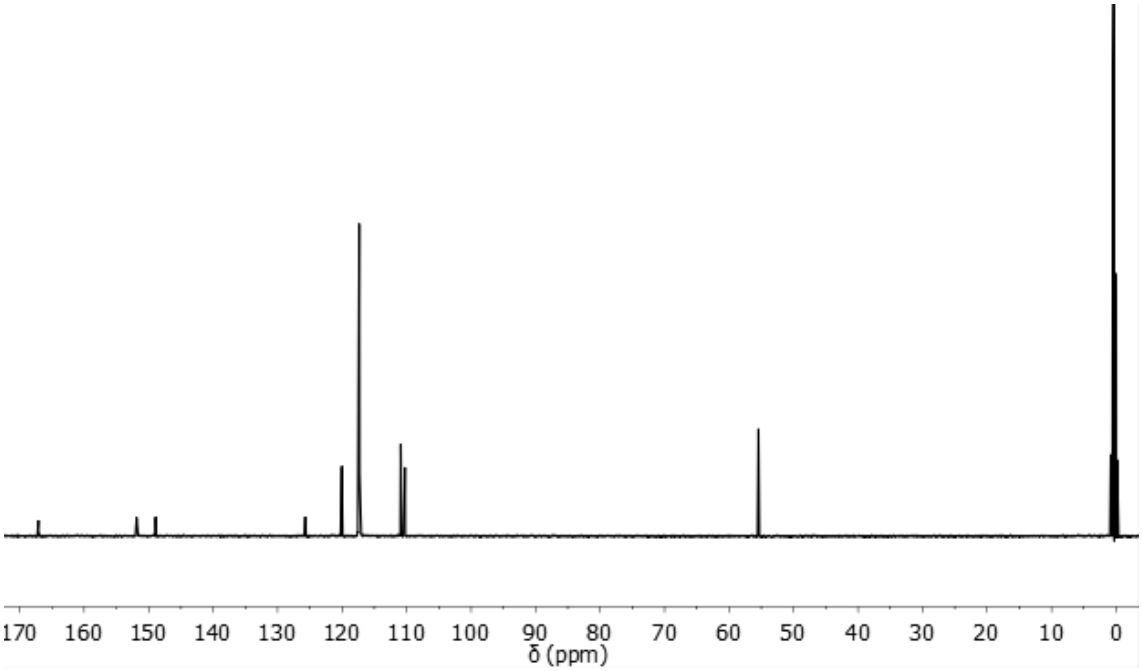

Figure 3.59. ^{13}C-NMR (126 MHz, CD_3CN) of **2k**.

Synthesis of 2l.

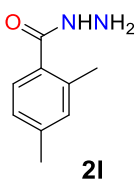

2l

Hydrazine hydrate (3 mL, 57.8 mmol, 76 eq.) was added drop by drop to a solution of methyl 2,4-dimethylbenzoate (124.80 mg, 0.76 mmol, 1 eq.) in MeOH (24 mL). The reaction mixture was heated at reflux for 3 d, monitoring the reaction by TLC analysis (hexane/DCM 1:1). Two additional aliquots of 2 mL of hydrazine hydrate were added after 24 and 48 hours. After this time, the reaction mixture was cooled at r.t. and the solvent was removed under reduced pressure. Hexane was added to the crude. A precipitate formed, which was filtered to obtain **2l** as a white powder (87.4 mg, 70%). ^{1}H-NMR (400 MHz, CD_3CN), δ: 7.69 (s, 1H), 7.21 (d, J = 7.7 Hz, 1H), 7.07 (m, 1H), 7.03 (d, J = 7.7 Hz, 1H), 4.07 (s, 2H), 2.33 (s, 3H), 2.31 (s, 3H). ^{13}C-NMR (100 MHz, CD_3CN), δ: 169.8, 139.9, 136.2, 132.4, 131.4, 127.2, 126.1, 20.2, 18.8. HRMS (m/z) calculated for $C_9H_{13}N_2O^+$ 164.0950, found 165.1021.

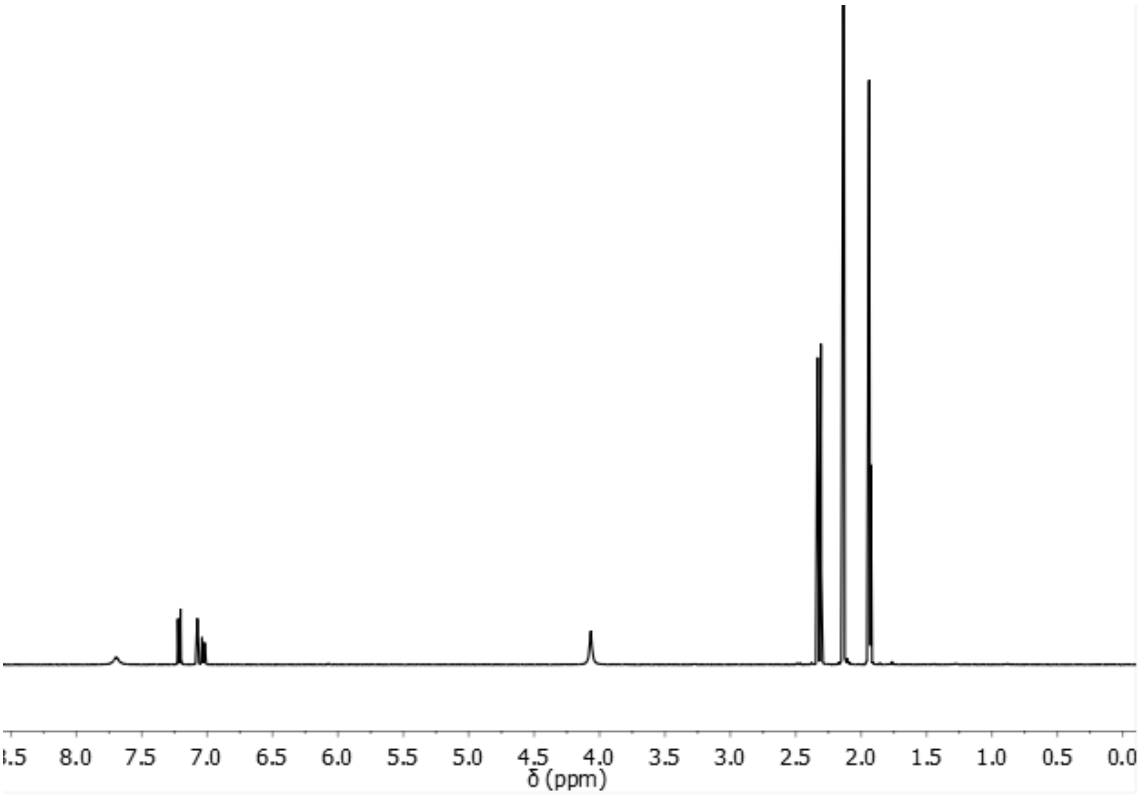

Figure 3.6021. ^{1}H-NMR (400 MHz, CD_3CN) of **2l**.

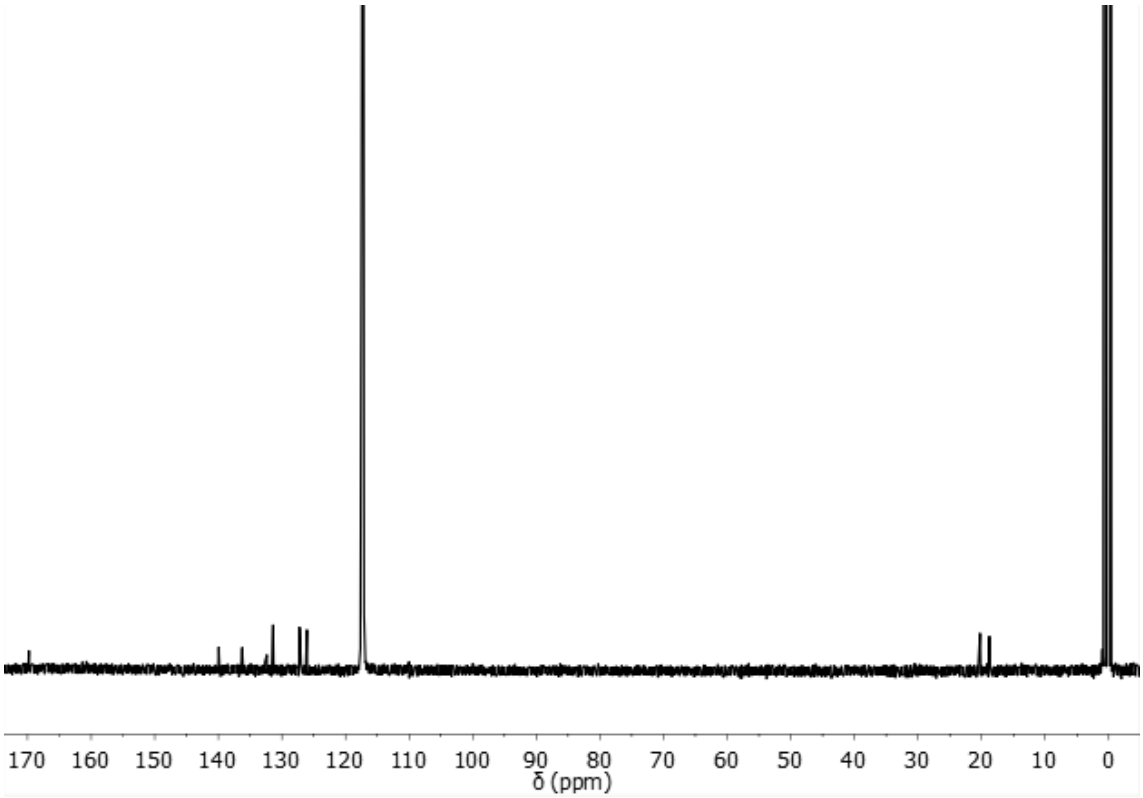

Figure 3.61. ^{13}C-NMR (100 MHz, CD_3CN) of **2l**.

Conclusions

The broad field of nanotechnology, the interdisciplinary science including physics, chemistry, biology, and engineering, has deeply impacted everyday life. An example is given by smartphones and personal computers that are constantly used. The circuits of these devices can be fabricated by the manipulation of matter at the nanoscale, *via* a so-called top-down approach. The miniaturization of bulk materials using this strategy is conceptually simple, but it also carries on some physical limits to produce nanomaterials. An opposite method that has attracted researchers for a long time is the bottom-up approach, which allows producing nanomaterials with fine-tuned features from molecularly engineered "building blocks". In this Thesis, this strategy has been explored from two complementary perspectives: on one side, a traditional bottom-up approach for the synthesis of zero-dimensional carbon-based nanostructures, *i.e.* CNDs; on the other side, leveraging on supramolecular chemistry, a bottom-up strategy consisting in the use of artificial molecular machines. *Chapter 1* introduced the nanoworld of CNDs, and molecular machines, supported by selected examples.

In *Chapter 2* a bottom-up strategy was employed for the preparation of CNDs. These luminescent nanomaterials can be obtained in a simple and fast way from small molecular precursors, which transfer their features from the molecular scale to the nanoscale. Our work focused on customizing CPL, a property that remained elusive for long. The problem has been tackled by leveraging atropoisomeric molecular precursors. The versatility of these chiral molecules has been demonstrated: indeed, it was possible to obtain two families of CNDs with advanced chiroptical properties from citric acid, binaphthyl diamine, and eventually a molecular dopant. Remarkably, using 1,4-benzoquinone as dopant, CNDs displaying intrinsic CPL were obtained.

In *Chapter 3*, a supramolecular-based bottom-up approach was employed to build molecularly-defined systems performing tasks at the nanoscale, namely artificial molecular machines. These molecular systems can be engineered to achieve a variety of functions. A direct inspiration for the synthesis of artificial machines comes from Nature. However, while biomolecular machines, are able to accomplish energetically-demanding. (*i.e.* endergonic) functions, according to a ratchet mechanism, few of the artificial counterparts are capable of doing so. A step forward has been done using a minimal molecular machine. An asymmetric axle was engineered to allow the formation of a pseudorotaxane complex, which can be dynamically stoppered, modulating the formation of a rotaxane. Powered by acid/base inputs, machine operation was studied, confirming the importance of stoppering molecular fragment to achieve energetically-demanding trapping of the macrocyclic component of the rotaxane in a high-energy state, according to an energy ratchet mechanism. Importantly, multiple dissipative

dethreading kinetics can be obtained, simply tuning solvent polarity in which operation is performed, confirming machine operation according to the unidirectional exploration of a square reaction network.

Overall, this Thesis has expanded the potential of two bottom-up approaches to nanotechnology. Intriguingly, both involved the study of objects of ca. 3.5 nm. A bottom-up approach was employed to advance the intrinsic properties of CNDs, laying the ground for the fabrication of engineered CNDs with superior chiral and emitting features. In a complementary fashion, bottom-up method was adopted to enhance the functionality of a minimal artificial machine, paving the way for the fabrication of ratchet-based functional nanomaterials.

References

(1) Nano on Reflection. *Nat. Nanotechnol.* **2016**, *11* (10), 828–834.
(2) Roco, M. C. Nanoscale Science and Engineering: Unifying and Transforming Tools. *AIChE J.* **2004**, *50* (5), 890–897.
(3) Roco, M. C. N. S.; Unifying, E.; Tools, T. *AIChE J.* **2004**. *50* (5), 890–897.
(4) Lu, W.; Lieber, C. M. Nanoelectronics from the Bottom Up. *Nat. Mater.* **2007**, *6*, 841–850.
(5) Palma, C.-A.; Samorì, P. Blueprinting Macromolecular Electronics. *Nat. Chem.* **2011**, *3* (6), 431–436.
(6) Iqbal, P.; Preece, J. A.; Mendes, P. M. Nanotechnology : The "Top-Down" and "Bottom-Up" Approaches. In *Supramolecular Chemistry: From Molecules to Nanomaterials*; John Wiley & Sons, Ltd., 2012; pp 1–14.
(7) Isaacoff, Benjamin P., Brown, K. A. Progress in Top-Down Control of Bottom-Up Assembly. *Nano Lett.* **2017**, *17*, 6508–6510.
(8) Vieu, C., Carcenac, F., Pépin, A., Chen, Y., Mejias, M., Lebib, A., Manin-Ferlazzo, L., Couraud, L., & Launois, H. Electron Beam Lithography: Resolution Limits and Applications. *Appl. Surf. Sci.* **2000**, *164* (1–4,), 111–117.
(9) Kawata, S.; Sun, H.-B.; Tanaka, T.; Takada, K. Finer Features for Functional Microdevices. *Nature* **2001**, *412*, 697–698.
(10) Abid, N.; Khan, A. M.; Shujait, S.; Chaudhary, K.; Ikram, M.; Imran, M.; Haider, J.; Khan, M.; Khan, Q.; Maqbool, M. Synthesis of Nanomaterials Using Various Top-down and Bottom-up Approaches, Influencing Factors, Advantages, and Disadvantages: A Review. *Adv. Colloid Interface Sci.* **2022**, *300* (2), 102597.
(11) *Molecular Building Blocks for Nanotechnology: From Diamondoids to Nanoscale Materials and Applications*, 1st ed.; Mansoori, G. A., George, T. F., Lahsen, A., Zhang, G., Eds.; Springer New York, NY: New York, NY, 2007.
(12) Feynman, R. There's Plenty of Room at the Bottom. *Eng. Sci.* **1960**, *23* (5), 22–36.
(13) Andreo, J.; Ettlinger, R.; Zaremba, O.; Peña, Q.; Lächelt, U.; de Luis, R. F.; Freund, R.; Canossa, S.; Ploetz, E.; Zhu, W.; Diercks, C. S.; Gröger, H.; Wuttke, S. Reticular Nanoscience: Bottom-Up Assembly Nanotechnology. *J. Am. Chem. Soc.* **2022**, *144* (17), 7531–7550.
(14) Rizzo, C.; Arcudi, F.; Đorđević, L.; Dintcheva, N. T.; Noto, R.; Anna, F. D.; Prato, M. Nitrogen-Doped Carbon Nanodots-Ionogels: Preparation, Characterization, and Radical Scavenging Activity. *ACS Nano* **2018**, *12* (2), 1296–1305.
(15) Schäfer, C.; Ragazzon, G.; Colasson, B.; La Rosa, M.; Silvi, S.; Credi, A. An Artificial Molecular Transporter. *ChemistryOpen* **2016**, *5*, 120–124.
(16) Bruns, C. J.; Stoddart, J. F. Rotaxane-Based Molecular Muscles. *Acc. Chem. Res.* **2014**, *47* (7), 2186–2199.
(17) De Bo, G.; Gall, M. A. Y.; Kitching, M. O.; Kuschel, S.; Leigh, D. A.; Tetlow, D. J.; Ward, J. W. Sequence-Specific β-Peptide Synthesis by a Rotaxane-Based Molecular Machine. *J. Am. Chem. Soc.* **2017**, *139* (31), 10875–10879.
(18) Balzani, V. Nanoscience and Nanotechnology: A Personal View of a Chemist. *Small* **2005**, *1* (3), 278–283.

(19) Busseron, E.; Ru, Y.; Moulin, E.; Giuseppone, N. Nanoscale Supramolecular Self-Assemblies as Functional Nanomaterials. *Nanoscale* **2013**, *5*, 7098–7140.
(20) Li, Q.; Fuks, G.; Moulin, E.; Maaloum, M.; Rawiso, M.; Kulic, I.; Foy, J. T.; Giuseppone, N. Macroscopic Contraction of a Gel Induced by the Integrated Motion of Light-Driven Molecular Motors. *Nat. Nanotechnol.* **2015**, *10* (2), 161–165.
(21) Goujon, A.; Lang, T.; Mariani, G.; Moulin, E.; Fuks, G.; Raya, J.; Buhler, E.; Giuseppone, N. Bistable [C2] Daisy Chain Rotaxanes as Reversible Muscle-like Actuators in Mechanically Active Gels. *J. Am. Chem. Soc.* **2017**, *139* (42), 14825–14828.
(22) Kroto, H. W.; Heath, J. R.; O'Brien, S. C.; Curl, R. F.; Smalley, R. E. C60: Buckminsterfullerene. *Nature* **1985**, *318* (6042), 162–163.
(23) Iijima, S. Helical Microtubules of Graphitic Carbon. *Nature* **1991**, *354* (6348), 56–58.
(24) Iijima, S.; Ichihashi, T. Single-Shell Carbon Nanotubes of 1-Nm Diameter. *Nature* **1993**, *363* (6430), 603–605.
(25) Novoselov, K. S.; Geim, A. K.; Morozov, S. V.; Jiang, D.; Zhang, Y.; Dubonos, S. V.; Grigorieva, I. V.; Firsov, A. A. Electric Field in Atomically Thin Carbon Films. *Science* **2004**, *306* (5696), 666–669.
(26) Xu, X.; Ray, R.; Gu, Y.; Ploehn, H. J.; Gearheart, L.; Raker, K.; Scrivens, W. A. Electrophoretic Analysis and Purification of Fluorescent Single-Walled Carbon Nanotube Fragments. *J. Am. Chem. Soc.* **2004**, *126* (40), 12736–12737.
(27) Georgakilas, V.; Perman, J. A.; Tucek, J.; Zboril, R. Broad Family of Carbon Nanoallotropes: Classification, Chemistry, and Applications of Fullerenes, Carbon Dots, Nanotubes, Graphene, Nanodiamonds, and Combined Superstructures. *Chem. Rev.* **2015**, *115* (11), 4744–4822.
(28) Vázquez, E.; Giacalone, F.; Prato, M. Non-Conventional Methods and Media for the Activation and Manipulation of Carbon Nanoforms. *Chem. Soc. Rev.* **2014**, *43* (1), 58–69.
(29) Li, H.; Kang, Z.; Liu, Y.; Lee, S. T. Carbon Nanodots: Synthesis, Properties and Applications. *J. Mater. Chem.* **2012**, *22* (46), 24230–24253.
(30) Park, Y.; Yoo, J.; Lim, B.; Kwon, W.; Rhee, S.-W. Improving the Functionality of Carbon Nanodots: Doping and Surface Functionalization. *J. Mater. Chem. A* **2016**, *4* (30), 11582–11603.
(31) Arcudi, F.; Đorđević, L.; Prato, M. Design, Synthesis, and Functionalization Strategies of Tailored Carbon Nanodots. *Acc. Chem. Res.* **2019**, *52* (8), 2070–2079.
(32) Zhu, P.; Tan, K.; Chen, Q.; Xiong, J.; Gao, L. Origins of Efficient Multiemission Luminescence in Carbon Dots. *Chem. Mater.* **2019**, *31* (13), 4732–4742.
(33) Ragazzon, G.; Cadranel, A.; Ushakova, E. V.; Wang, Y.; Guldi, D. M.; Rogach, A. L.; Kotov, N. A.; Prato, M. Optical Processes in Carbon Nanocolloids. *Chem* **2021**, *7* (3), 606–628.
(34) Papaioannou, N.; Marinovic, A.; Yoshizawa, N.; Goode, A. E.; Fay, M.; Khlobystov, A.; Titirici, M.-M.; Sapelkin, A. Structure and Solvents Effects on the Optical Properties of Sugar-Derived Carbon Nanodots. *Sci. Rep.* **2018**, *8* (1), 6559.
(35) Baker, S. N.; Baker, G. A. Luminescent Carbon Nanodots: Emergent Nanolights. *Angew. Chem. Int. Ed.* **2010**, *49* (38), 6726–6744.

(36) Yatom, S.; Bak, J.; Khrabryi, A.; Raitses, Y. Detection of Nanoparticles in Carbon Arc Discharge with Laser-Induced Incandescence. *C* **2017**, *117*, 154–162.
(37) Hu, S.-L.; Niu, K.-Y.; Sun, J.; Yang, J.; Zhao, N.-Q.; Du, X.-W. One-Step Synthesis of Fluorescent Carbon Nanoparticles by Laser Irradiation. *J. Mater. Chem.* **2009**, *19* (4), 484–488.
(38) Li, H.; Liu, R.; Kong, W.; Liu, J.; Liu, Y.; Zhou, L.; Zhang, X.; Lee, S.-T.; Kang, Z. Carbon Quantum Dots with Photo-Generated Proton Property as Efficient Visible Light Controlled Acid Catalyst. *Nanoscale* **2014**, *6* (2), 867–873.
(39) Manioudakis, J.; Victoria, F.; Thompson, C. A.; Brown, L.; Movsum, M.; Lucifero, R.; Naccache, R. Effects of Nitrogen-Doping on the Photophysical Properties of Carbon Dots. *J. Mater. Chem. C* **2019**, *7* (4), 853–862.
(40) Otten, M.; Hildebrandt, M.; Kühnemuth, R.; Karg, M. Pyrolysis and Solvothermal Synthesis for Carbon Dots: Role of Purification and Molecular Fluorophores. *Langmuir* **2022**, *38* (19), 6148–6157.
(41) Đorđević, L.; Arcudi, F.; Cacioppo, M.; Prato, M. A Multifunctional Chemical Toolbox to Engineer Carbon Dots for Biomedical and Energy Applications. *Nat. Nanotechnol.* **2022**, No. 17, 112–130.
(42) Sciortino, A.; Cannizzo, A.; Messina, F. Carbon Nanodots: A Review—From the Current Understanding of the Fundamental Photophysics to the Full Control of the Optical Response. *C* **2018**, *4* (4), 67.
(43) Arcudi, F.; Đorđević, L.; Prato, M. Synthesis, Separation, and Characterization of Small and Highly Fluorescent Nitrogen-Doped Carbon Nanodots. *Angew. Chem. Int. Ed.* **2016**, *55* (6), 2107–2112.
(44) Yang, P.; Zhao, J.; Zhang, L.; Li, L.; Zhu, Z. Intramolecular Hydrogen Bonds Quench Photoluminescence and Enhance Photocatalytic Activity of Carbon Nanodots. *Chem. Eur. J.* **2015**, *21* (23), 8561–8568.
(45) Xu, Y.; Wu, M.; Liu, Y.; Feng, X.-Z.; Yin, X.-B.; He, X.-W.; Zhang, Y.-K. Nitrogen-Doped Carbon Dots: A Facile and General Preparation Method, Photoluminescence Investigation, and Imaging Applications. *Chem. Eur. J.* **2013**, *19* (7), 2276–2283.
(46) Shi, Q.-Q.; Li, Y.-H.; Xu, Y.; Wang, Y.; Yin, X.-B.; He, X.-W.; Zhang, Y.-K. High-Yield and High-Solubility Nitrogen-Doped Carbon Dots: Formation, Fluorescence Mechanism and Imaging Application. *RSC Adv.* **2014**, *4* (4), 1563–1566.
(47) Meng, X.; Wang, Y.; Liu, X.; Wang, M.; Zhan, Y.; Liu, Y.; Zhu, W.; Zhang, W.; Shi, L.; Fang, X. Supramolecular Nanodots Derived from Citric Acid and Beta-Amines with High Quantum Yield and Sensitive Photoluminescence. *Opt. Mater. (Amst).* **2018**, *77*, 48–54.
(48) Sahu, S.; Behera, B.; Maiti, T. K.; Mohapatra, S. Simple One-Step Synthesis of Highly Luminescent Carbon Dots from Orange Juice: Application as Excellent Bio-Imaging Agents. *Chem. Commun.* **2012**, *48* (70), 8835–8837.
(49) Hutton, G. A. M.; Martindale, B. C. M.; Reisner, E. Carbon Dots as Photosensitisers for Solar-Driven Catalysis. *Chem. Soc. Rev.* **2017**, *46* (20), 6111–6123.
(50) Li, L.; Dong, T. Photoluminescence Tuning in Carbon Dots: Surface Passivation or/and Functionalization, Heteroatom Doping. *J. Mater. Chem. C* **2018**, *6* (30), 7944–7970.

(51) Li, D.; Jing, P.; Sun, L.; An, Y.; Shan, X.; Lu, X.; Zhou, D.; Han, D.; Shen, D.; Zhai, Y.; Qu, S.; Zbořil, R.; Rogach, A. L. Near-Infrared Excitation/Emission and Multiphoton-Induced Fluorescence of Carbon Dots. *Adv. Mater.* **2018**, *30* (13), 1705913.
(52) Strauss, V.; Margraf, J. T.; Dolle, C.; Butz, B.; Nacken, T. J.; Walter, J.; Bauer, W.; Peukert, W.; Spiecker, E.; Clark, T.; Guldi, D. M. Carbon Nanodots: Toward a Comprehensive Understanding of Their Photoluminescence. *J. Am. Chem. Soc.* **2014**, *136* (49), 17308–17316.
(53) Schneider, J.; Reckmeier, C. J.; Xiong, Y.; Von Seckendorff, M.; Susha, A. S.; Kasak, P.; Rogach, A. L. Molecular Fluorescence in Citric Acid-Based Carbon Dots. *J. Phys. Chem. C* **2017**, *121* (3), 2014–2022.
(54) Bartolomei, B.; Bogo, A.; Amato, F.; Ragazzon, G.; Prato, M. Nuclear Magnetic Resonance Reveals Molecular Species in Carbon Nanodot Samples Disclosing Flaws. *Angew. Chem. Int. Ed.* **2022**, *61* (20), e202200038.
(55) Mazzier, D.; Favaro, M.; Agnoli, S.; Silvestrini, S.; Granozzi, G.; Maggini, M.; Moretto, A. Synthesis of Luminescent 3D Microstructures Formed by Carbon Quantum Dots and Their Self-Assembly Properties. *Chem. Commun.* **2014**, *50* (50), 6592–6595.
(56) Đorđević, L.; Arcudi, F.; Prato, M. Preparation, Functionalization and Characterization of Engineered Carbon Nanodots. *Nat. Protoc.* **2019**, *14* (10), 2931–2953.
(57) Liu, W.; Li, C.; Ren, Y.; Sun, X.; Pan, W.; Li, Y.; Wang, J.; Wang, W. Carbon Dots : Surface Engineering and Applications. *J. Mater. Chem. B* **2016**, *4*, 5772–5788.
(58) Madonia, A.; Martin-Sabi, M.; Sciortino, A.; Agnello, S.; Cannas, M.; Ammar, S.; Messina, F.; Schaming, D. Highly Efficient Electron Transfer in a Carbon Dot–Polyoxometalate Nanohybrid. *J. Phys. Chem. Lett.* **2020**, *11* (11), 4379–4384.
(59) Reale, M.; Chandra, S.; Buscarino, G.; Emanuele, A.; Cannas, M.; Ikkala, O.; Sciortino, A.; Messina, F. Photoinduced Charge Separation in Functional Carbon–Silver Nanohybrids. *Phys. Chem. Chem. Phys.* **2022**, *24* (21), 12974–12983.
(60) Cadranel, A.; Strauss, V.; Margraf, J. T.; Winterfeld, K. A.; Vogl, C.; Luka, Đ.; Arcudi, F.; Hoelzel, H.; Jux, N.; Prato, M.; Guldi, D. M. Screening Supramolecular Interactions between Carbon Nanodots and Porphyrins. *J. Am. Chem. Soc.* **2018**, *140* (3), 904–907.
(61) Sciortino, A.; Ferrante, F.; Gonçalves, G.; Tobias, G.; Popescu, R.; Gerthsen, D.; Mauro, N.; Giammona, G.; Buscarino, G.; Gelardi, F. M.; Agnello, S.; Cannas, M.; Duca, D.; Messina, F. Ultrafast Interface Charge Separation in Carbon Nanodot–Nanotube Hybrids. *ACS Appl. Mater. Interfaces* **2021**, *13* (41), 49232–49241.
(62) Du, F.; Ming, Y.; Zeng, F.; Yu, C.; Wu, S. A Low Cytotoxic and Ratiometric Fluorescent Nanosensor Based on Carbon-Dots for Intracellular PH Sensing and Mapping. *Nanotechnology* **2013**, *24* (36), 365101.
(63) Ferrer-Ruiz, A.; Scharl, T.; Rodríguez-Pérez, L.; Cadranel, A.; Herranz, M. Á.; Martín, N.; Guldi, D. M. Assessing the Photoinduced Electron-Donating Behavior of Carbon Nanodots in Nanoconjugates. *J. Am. Chem. Soc.* **2020**, *142* (48), 20324–20328.

(64) Yan, Y.; Sun, J.; Zhang, K.; Zhu, H.; Yu, H.; Sun, M.; Huang, D.; Wang, S. Visualizing Gaseous Nitrogen Dioxide by Ratiometric Fluorescence of Carbon Nanodots–Quantum Dots Hybrid. *Anal. Chem.* **2015**, *87* (4), 2087–2093.
(65) Cui, X.; Zhu, L.; Wu, J.; Hou, Y.; Wang, P.; Wang, Z.; Yang, M. A Fluorescent Biosensor Based on Carbon Dots-Labeled Oligodeoxyribonucleotide and Graphene Oxide for Mercury (II) Detection. *Biosens. Bioelectron.* **2015**, *63*, 506–512.
(66) Arcudi, F.; Strauss, V.; Đorđević, L.; Cadranel, A.; Guldi, D. M.; Prato, M. Porphyrin Antennas on Carbon Nanodots: Excited State Energy and Electron Transduction. *Angew. Chem. Int. Ed.* **2017**, *56* (40), 12097–12101.
(67) Cacioppo, M.; Scharl, T.; Đorđević, L.; Cadranel, A.; Arcudi, F.; Guldi, D. M.; Prato, M. Symmetry-Breaking Charge-Transfer Chromophore Interactions Supported by Carbon Nanodots. *Angew. Chem. Int. Ed.* **2020**, *59* (31), 12779–12784.
(68) Đorđević, L.; Haines, P.; Cacioppo, M.; Arcudi, F.; Scharl, T.; Cadranel, A.; Guldi, D. M.; Prato, M. Synthesis and Excited State Processes of Arrays Containing Amine-Rich Carbon Dots and Unsymmetrical Rylene Diimides. *Mater. Chem. Front.* **2020**, *4* (12), 3640–3648.
(69) Carrara, S.; Arcudi, F.; Prato, M.; De Cola, L. Amine-Rich Nitrogen-Doped Carbon Nanodots as a Platform for Self-Enhancing Electrochemiluminescence. *Angew. Chem. Int. Ed.* **2017**, *56* (17), 4757–4761.
(70) Đorđević, L.; Arcudi, F.; D'Urso, A.; Cacioppo, M.; Micali, N.; Bürgi, T.; Purrello, R.; Prato, M. Design Principles of Chiral Carbon Nanodots Help Convey Chirality from Molecular to Nanoscale Level. *Nat. Commun.* **2018**, *9* (1), 3442.
(71) Döring, A.; Ushakova, E.; Rogach, A. L. Chiral Carbon Dots: Synthesis, Optical Properties, and Emerging Applications. *Light Sci. Appl.* **2022**, *11* (1), 1–23.
(72) Filippini, G.; Amato, F.; Rosso, C.; Ragazzon, G.; Vega-Peñaloza, A.; Companyó, X.; Dell'Amico, L.; Bonchio, M.; Prato, M. Mapping the Surface Groups of Amine-Rich Carbon Dots Enables Covalent Catalysis in Aqueous Media. *Chem* **2020**, *6* (11), 3022–3037.
(73) Yan, H.; Cacioppo, M.; Megahed, S.; Arcudi, F.; Zhu, D.; Schulz, F.; Prato, M.; Parak, W. J. Influence of the Chirality of Carbon Nanodots on Their Interaction with Proteins and Cells. *Nat. Commun.* **2021**, No. 12, 1–14.
(74) Arcudi, F.; Đorđević, L.; Prato, M. Rationally Designed Carbon Nanodots towards Pure White-Light Emission. *Angew. Chem. Int. Ed.* **2017**, *56* (15), 4170–4173.
(75) Rigodanza, F.; Đorđević, L.; Arcudi, F.; Prato, M.; Rigodanza, F; Đorđević, L.; Arcudi, F.; Prato, M.; Rigodanza, F.; Đorđević, L.; Arcudi, F.; Prato, M. Customizing the Electrochemical Properties of Carbon Nanodots by Using Quinones in Bottom-Up Synthesis. *Angew. Chem. Int. Ed.* **2018**, *57* (18), 5062–5067.
(76) Hutton, G. A. M. M.; Reuillard, B.; Martindale, B. C. M. M.; Caputo, C. A.; Lockwood, C. W. J. J.; Butt, J. N.; Reisner, E. Carbon Dots as Versatile Photosensitizers for Solar-Driven Catalysis with Redox Enzymes. *J. Am. Chem. Soc.* **2016**, *138* (51), 16722–16730.
(77) Rosso, C.; Filippini, G.; Prato, M. Use of Nitrogen-Doped Carbon Nanodots for the Photocatalytic Fluoroalkylation of Organic Compounds. *Chem. – A Eur. J.*

2019, *25* (70), 16032–16036.
(78) Lehn, J.-M. Supramolecular Chemistry—Scope and Perspectives Molecules, Supermolecules, and Molecular Devices (Nobel Lecture). *Angew. Chem. Int. Ed.* **1988**, *27* (1), 89–112.
(79) NobelPrize.org. The Nobel Prize in Chemistry 1987 https://www.nobelprize.org/prizes/chemistry/1987/summary/.
(80) Lehn, J.-M. Perspectives in Supramolecular Chemistry-From Molecular Recognition towards Molecular Information Processing and Self-Organization. *Angew. Chem. Int. Ed.* **1990**, *29* (11), 1304–1319.
(81) Lehn, J.-M. Toward Self-Organization and Complex Matter. *Science* **2012**, *295*, 2400–2403.
(82) *Supramolecular Chemistry: From Molecules to Nanomaterials, 2nd Ed.*; Steed, J. W., Gale, P. A., Eds.; John Wiley & Sons, Ltd.: Chichester, UK, 2012.
(83) Grzybowski, B. A.; Huck, W. T. S. The Nanotechnology of Life-Inspired Systems. *Nat. Nanotechnol.* **2016**, *11*, 585–592.
(84) Jean-François, L.; Makoto, O.; R., L. D.; Mitsuo, S. Sequence-Controlled Polymers. *Science* **2013**, *341* (6146), 1238149.
(85) Aida, T.; Meijer, E. W. Supramolecular Polymers – We've Come Full Circle. *Isr. J. Chem.* **2020**, *60* (1–2), 33–47.
(86) Gazit, E. Reductionist Approach in Peptide-Based Nanotechnology. *Annu. Rev. Biochem.* **2018**, *87* (1), 533–553.
(87) Buddingh', B. C.; Van Hest, J. C. M. Artificial Cells: Synthetic Compartments with Life-like Functionality and Adaptivity. *Acc. Chem. Res.* **2017**, *50* (4), 769–777.
(88) Balzani, V.; Credi, A.; Venturi, M. The Bottom-Up Approach to Molecular-Level Devices and Machines. *Chem. Eur. J.* **2002**, *8* (24), 5524–5532.
(89) Kinbara, K.; Aida, T. Toward Intelligent Molecular Machines: Directed Motions of Biological and Artificial Molecules and Assemblies. *Chem. Rev.* **2005**, *105* (4), 1377–1400.
(90) Abendroth, J. M.; Bushuyev, O. S.; Weiss, P. S.; Barrett, C. J. Controlling Motion at the Nanoscale : Rise of the Molecular Machines. *ACS Nano* **2015**, No. 8, 7746–7768.
(91) Goodsell, D. S. *The Machinery of Life*, 2nd Ed.; Copernicus New York, NY: New York, NY, 2010.
(92) Sobti, M.; Ishmukhametov, R.; Bouwer, J. C.; Ayer, A.; Suarna, C.; Smith, N. J.; Christie, M.; Stocker, R.; Duncan, Thomas M. Stewart, A. G. Cryo-EM Reveals Distinct Conformations of E. Coli ATP Synthase on Exposure to ATP. *Elife* **2019**, *8*, e43864.
(93) Xu, T.; Pagadala, V.; Mueller, D. M. Understanding Structure , Function , and Mutations in the Mitochondrial ATP Synthase. *Microb. Cell* **2015**, *2* (4), 105–125.
(94) Drexler, E. K. *Engines of Creation : The Coming Era of Nanotechnology*; Anchor Books: New York, NY, 1986; Vol. 1986.
(95) Astumian, R. D. Design Principles for Brownian Molecular Machines : How to Swim in Molasses and Walk in a Hurricane. *Phys. Chem. Chem. Phys* **2007**, *9* (37), 5067–5083.
(96) Tasbas, M. N.; Sahin, E.; Erbas-Cakmak, S. Bio-Inspired Molecular Machines and Their Biological Applications. *Coord. Chem. Rev.* **2021**, *443*, 214039.

(97) Balzani, V.; Credi, A.; Venturi, M. *Molecular Devices and Machines: Concepts and Perspectives for the Nanoworld, 2nd Ed.*; Wiley-VCH Verlag: Weinheim, 2008.
(98) Cram, D. J.; Cram, J. M. Host-Guest Chemistry. *Science* **1974**, *183* (4127), 803–809.
(99) Xia, D.; Wang, P.; Ji, X.; Khashab, N. M.; Sessler, J. L.; Huang, F. Functional Supramolecular Polymeric Networks: The Marriage of Covalent Polymers and Macrocycle-Based Host–Guest Interactions. *Chem. Rev.* **2020**, *120* (13), 6070–6123.
(100) Nicoli, F.; Baroncini, M.; Silvi, S.; Groppi, J.; Credi, A. Direct Synthetic Routes to Functionalised Crown Ethers. *Org. Chem. Front.* **2021**, *8*, 5531–5549.
(101) Harada, A. Cyclodextrin-Based Molecular Machines. *Acc. Chem. Res.* **2001**, *34* (6), 456–464.
(102) Bruns, C. J.; Stoddart, J. F. *The Nature of the Mechanical Bond - From Molecules to Machines*; Wiley: Hoboken, New Jersey, 2017.
(103) Stoddart, J. F. Mechanically Interlocked Molecules (MIMs)—Molecular Shuttles, Switches, and Machines (Nobel Lecture). *Angew. Chem. Int. Ed.* **2017**, *56* (37), 11094–11125.
(104) Balzani, V.; Credi, A.; Ferrer, B.; Silvi, S.; Venturi, M. Artificial Molecular Motors and Machines : Design Principles and Prototype Systems. *Top. Curr. Chem.* **2005**, *262*, 1–27.
(105) La Rosa, M.; Baroncini, M.; Silvi, S.; Credi, A. Manufacturing at Nanoscale: From Molecular Machines to Transducers. In *Advances in Nanostructured Materials and Nanopatterning Technologies*; Guarino, V., Focarete, M. L., Focarete, D., Eds.; Elsevier Inc., 2020; pp 41–63.
(106) Lutz, J. F.; Lehn, J. M.; Meijer, E. W.; Matyjaszewski, K. From Precision Polymers to Complex Materials and Systems. *Nat. Rev. Mater.* **2016**, *1* (16024), 1–14.
(107) Anelli, P. L.; Spencer, N.; Stoddart, J. F. A Molecular Shuttle. *J. Am. Chem. Soc.* **1991**, *113* (13), 5131–5133.
(108) Jeong, M.; Park, J.; Kwon, S. Molecular Switches and Motors Powered by Orthogonal Stimuli. *Eur. J. Org. Chem.* **2020**, *2020* (47), 7254–7283.
(109) Bissell, R. A.; Córdova, E.; Kaifer, A. E.; Stoddart, J. F. A Chemically and Electrochemically Switchable Molecular Shuttle. *Nature* **1994**, *369* (6476), 133–137.
(110) Coskun, A.; Banaszak, M.; Astumian, R. D.; Stoddart, J. F.; Grzybowski, B. A. Great Expectations: Can Artificial Molecular Machines Deliver on Their Promise? *Chem. Soc. Rev.* **2012**, *41* (1), 19–30.
(111) Aprahamian, I. The Future of Molecular Machines. *ACS Cent. Sci.* **2020**, *6* (3), 347–358.
(112) Heard, A. W.; Goldup, S. M. Simplicity in the Design, Operation, and Applications of Mechanically Interlocked Molecular Machines. *ACS Cent. Sci.* **2020**, *6* (2), 117–128.
(113) Erbas-Cakmak, S.; Leigh, D. A.; McTernan, C. T.; Nussbaumer, A. L. Artificial Molecular Machines. *Chem. Rev.* **2015**, *115* (18), 10081–10206.
(114) Kassem, S.; Van Leeuwen, T.; Lubbe, A. S.; Wilson, M. R.; Feringa, B. L.; Leigh, D. A. Artificial Molecular Motors. *Chem. Soc. Rev.* **2017**, *46* (9), 2592–2621.

(115) Dattler, D.; Fuks, G.; Heiser, J.; Moulin, E.; Perrot, A.; Yao, X.; Giuseppone, N. Design of Collective Motions from Synthetic Molecular Switches , Rotors , and Motors. *Chem. Rev.* **2020**, *120*, 310−433.
(116) Feng, Y.; Ovalle, M.; Seale, J. S. W.; Lee, C. K.; Kim, D. J.; Astumian, R. D.; Stoddart, J. F. Molecular Pumps and Motors. *J. Am. Chem. Soc.* **2021**, *143* (15), 5569–5591.
(117) Feynman, R. P.; Leighton, R. B.; Sands, M. Ratchet and Pawl. In *The Feynman Lectures on Physics*; Addison-Wesley Publishing Company Inc.: Reading, MA, 1965; Vol. 1, pp 46.1-46.9.
(118) Koumura, N.; Zijlstra, R. W. J.; van Delden, R. A.; Harada, N.; Feringa, B. L. Light-Driven Monodirectional Molecular Rotor. *Nature* **1999**, *401* (6749), 152–155.
(119) Koumura, N.; Geertsema, E. M.; Gelder, M. B. Van; Meetsma, A.; Feringa, B. L. Second Generation Light-Driven Molecular Motors. Unidirectional Rotation Controlled by a Single Stereogenic Center with Near-Perfect Photoequilibria and Acceleration of the Speed of Rotation by Structural Modification. *J. Am. Chem. Soc.* **2002**, *124* (18), 5037–5051.
(120) Kistemaker, J. C. M.; Peter, S.; Roke, D.; Wolters, A. T.; Heideman, G. H.; Chang, M.; Meulen, P. Van Der; Visser, J.; Otten, E.; Feringa, B. L. Third-Generation Light-Driven Symmetric Molecular Motors. *J. Am. Chem. Soc.* **2017**, *139* (28), 9650–9661.
(121) Feringa, B. L. The Art of Building Small: From Molecular Switches to Motors (Nobel Lecture). *Angew. Chem. Int. Ed.* **2017**, *56* (37), 11060–11078.
(122) Zhang, Q.; Qu, D. H.; Tian, H.; Feringa, B. L. Bottom-Up: Can Supramolecular Tools Deliver Responsiveness from Molecular Motors to Macroscopic Materials? *Matter* **2020**, *3* (2), 355–370.
(123) Serreli, V.; Lee, C.; Kay, E. R.; Leigh, D. A. A Molecular Information Ratchet. *Nature* **2007**, *445* (February), 523–527.
(124) Leigh, D. A.; Wong, J. K. Y.; Dehez, F.; Zerbetto, F. Unidirectional Rotation in a Mechanically Interlocked Molecular Rotor. *Nature* **2003**, *424*, 174–179.
(125) Wilson, M. R.; Solà, J.; Carlone, A.; Goldup, S. M.; Lebrasseur, N.; Leigh, D. A. An Autonomous Chemically Fuelled Small-Molecule Motor. *Nature* **2016**, *534* (7606), 235–240.
(126) Borsley, S.; Leigh, D. A.; Roberts, B. M. W. A Doubly Kinetically-Gated Information Ratchet Autonomously Driven by Carbodiimide Hydration. *J. Am. Chem. Soc.* **2021**, *143* (11), 4414–4420.
(127) Astumian, R. D. Kinetic Asymmetry Allows Macromolecular Catalysts to Drive an Information Ratchet. *Nat. Commun.* **2019**, No. 10, 1–14.
(128) Balzani, V.; Clemente-Leon, M.; Credi, A.; Ferrer, B.; Venturi, M.; Flood, A. H.; Stoddart, J. F. Autonomous Artificial Nanomotor Powered by Sunlight. *Proc. Natl. Acad. Sci. U.S.A.* **2006**, *99* (8), 4763–4768.
(129) Nicoli, F.; Curcio, M.; Tran, M.; Paltrinieri, E.; Silvi, S.; Baroncini, M.; Credi, A. Photoinduced Autonomous Nonequilibrium Operation of a Molecular Shuttle by Combined Isomerization and Proton Transfer Through a Catalytic Pathway. *J. Am. Chem. Soc.* **2021**.
(130) Ragazzon, G.; Baroncini, M.; Silvi, S.; Venturi, M.; Credi, A. Light-Powered Autonomous and Directional Molecular Motion of a Dissipative Self-Assembling System. *Nat. Nanotechnol.* **2015**, *10* (1), 70–75.

(131) Borsley, S.; Kreidt, E.; Leigh, D. A.; Roberts, B. M. W. Autonomous Fuelled Directional Rotation about a Covalent Single Bond. *Nature* **2022**, *604*, 80–85.
(132) Baroncini, M.; Casimiro, L.; Vet, C. De; Groppi, J. Making and Operating Molecular Machines : A Multidisciplinary Challenge. *ChemistryOpen* **2018**, No. 7, 169–179.
(133) Qiu, Y.; Feng, Y.; Guo, Q. H.; Astumian, R. D.; Stoddart, J. F. Pumps through the Ages. *Chem* **2020**, *6* (8), 1952–1977.
(134) Baroncini, M.; Silvi, S.; Venturi, M.; Credi, A. Photoactivated Directionally Controlled Transit of a Non-Symmetric Molecular Axle. *Angew. Chem. Int. Ed.* **2012**, *51* (17), 4223 –4226.
(135) Corra, S.; Casimiro, L.; Baroncini, M.; Groppi, J.; La Rosa, M.; Tranfić Bakić, M.; Silvi, S.; Credi, A. Artificial Supramolecular Pumps Powered by Light. *Chem. Eur. J.* **2021**, *27* (43), 11076–11083.
(136) Canton, M.; Groppi, J.; Casimiro, L.; Corra, S.; Baroncini, M.; Silvi, S.; Credi, A. Second-Generation Light-Fueled Supramolecular Pump. *J. Am. Chem. Soc.* **2021**, *143* (29), 10890–10894.
(137) Corra, S.; Curcio, M.; Baroncini, M.; Silvi, S.; Credi, A. Photoactivated Artificial Molecular Machines That Can Perform Tasks. *Adv. Mater.* **2020**, *1906064*, 1–22.
(138) Baroncini, M.; Silvi, S.; Credi, A. Photo- and Redox-Driven Artificial Molecular Motors. *Chem. Rev.* **2020**, *120*, 200−268.
(139) Cheng, C.; Mcgonigal, P. R.; Liu, W.; Li, H.; Vermeulen, N. A.; Ke, C.; Frasconi, M.; Stern, C. L.; Iii, W. A. G.; Stoddart, J. F. Energetically Demanding Transport in a Supramolecular Assembly. *J. Am. Chem. Soc.* **2014**, *2*, 10–13.
(140) Cheng, C.; McGonigal, P. R.; Schneebeli, S. T.; Li, H.; Vermeulen, N. A.; Ke, C.; Stoddart, J. F. An Artificial Molecular Pump. *Nat. Nanotechnol.* **2015**, *10* (6), 547–553.
(141) Zhang, Q.; Qu, D. Artificial Molecular Machine Immobilized Surfaces : A New Platform To Construct Functional Materials. *ChemPhysChem* **2016**, *17*, 1759–1768.
(142) Feng, L.; Qiu, Y.; Guo, Q.-H.; Chen, Z.; Seale, J. S. W.; He, K.; Wu, H.; Feng, Y.; Farha, O. K.; Astumian, R. D.; Stoddart, J. F. Active Mechanisorption Driven by Pumping Cassettes. *Science* **2021**, *374* (6572), 1215–1221.
(143) Carlone, A.; Goldup, S. M.; Lebrasseur, N.; Leigh, D. A.; Wilson, A. A Three-Compartment Chemically-Driven Molecular Information Ratchet. *J. Am. Chem. Soc.* **2012**, *9*, 8321–8323.
(144) Goldup, S. M.; Leigh, D. A.; Slawin, A. M. Z. A Chemically-Driven Molecular Information Ratchet. *J. Am. Chem. Soc.* **2008**, *15*, 1836–1838.
(145) Erbas-Cakmak, S.; Fielden, S. D. P.; Karaca, U.; Leigh, D. A.; Mcternan, C. T.; Tetlow, D. J.; Wilson, M. R. Rotary and Linear Molecular Motors Driven by Pulses of a Chemical Fuel. *Science* **2017**, *343* (October), 340–343.
(146) Thomas, D.; Tetlow, D. J.; Ren, Y.; Kassem, S.; Karaca, U.; Leigh, D. A. Pumping between Phases with a Pulsed-Fuel Molecular Ratchet. *Nat. Nanotechnol.* **2022**.
(147) Bai, J.; Yuan, G.; Zhu, Y.; Huang, Z.; Zhang, L.; Wang, X.; Wu, S.; Ren, L. Study on the Origin of Fluorescence by Using Dual-Emission Carbon Dots. *J. Phys. Chem. C* **2021**, *125* (33), 18543–18551.
(148) Hola, K.; Zhang, Y.; Wang, Y.; Giannelis, E. P.; Zboril, R.; Rogach, A. L. Carbon Dots - Emerging Light Emitters for Bioimaging , Cancer Therapy and

Optoelectronics. *Nano Today* **2014**, *9* (5), 590–603.
(149) Yuan, F.; Li, S.; Fan, Z.; Meng, X.; Fan, L.; Yang, S. Nano Today Shining Carbon Dots : Synthesis and Biomedical and Optoelectronic Applications. *Nano Today* **2016**, *11* (5), 565–586.
(150) Li, X.; Rui, M.; Song, J.; Shen, Z.; Zeng, H. Carbon and Graphene Quantum Dots for Optoelectronic and Energy Devices: A Review. *Adv. Funct. Mater.* **2015**, *25* (31), 4929–4947.
(151) Wang, F.; Pang, S.; Wang, L.; Li, Q.; Kreiter, M.; Liu, C. Y. One-Step Synthesis of Highly Luminescent Carbon Dots in Noncoordinating Solvents. *Chem. Mater.* **2010**, *22* (16), 4528–4530.
(152) Panniello, A.; Di Mauro, A. E.; Fanizza, E.; Depalo, N.; Agostiano, A.; Curri, M. L.; Striccoli, M. Luminescent Oil-Soluble Carbon Dots toward White Light Emission: A Spectroscopic Study. *J. Phys. Chem. C* **2018**, *122* (1), 839–849.
(153) Choi, Y.; Choi, Y.; Kwon, O. H.; Kim, B. S. Carbon Dots: Bottom-Up Syntheses, Properties, and Light-Harvesting Applications. *Chem. Asian J.* **2018**, *13* (6), 586–598.
(154) Wu, M.; Zhan, J.; Geng, B.; He, P.; Wu, K.; Wang, L.; Xu, G.; Li, Z.; Yin, L.; Pan, D. Scalable Synthesis of Organic-Soluble Carbon Quantum Dots: Superior Optical Properties in Solvents, Solids, and LEDs. *Nanoscale* **2017**, *9* (35), 13195–13202.
(155) Wang, Q.; Gao, Y.; Wang, B.; Guo, Y.; Ahmad, U.; Wang, Y.; Wang, Y.; Lu, S.; Li, H.; Zhou, G. S,N-Codoped Oil-Soluble Fluorescent Carbon Dots for a High Color-Rendering WLED. *J. Mater. Chem. C* **2020**, *8* (13), 4343–4349.
(156) Minervini, G.; Panniello, A.; Fanizza, E.; Agostiano, A.; Curri, M. L.; Striccoli, M. Oil-Dispersible Green-Emitting Carbon Dots: New Insights on a Facile and Efficient Synthesis. *Materials* **2020**, *13* (17), 10–14.
(157) Yang, H.; Liu, Y.; Guo, Z.; Lei, B.; Zhuang, J.; Zhang, X.; Liu, Z.; Hu, C. Hydrophobic Carbon Dots with Blue Dispersed Emission and Red Aggregation-Induced Emission. *Nat. Commun.* **2019**, *10*, 1789.
(158) De Medeiros, T. V.; Manioudakis, J.; Noun, F.; Macairan, J. R.; Victoria, F.; Naccache, R. Microwave-Assisted Synthesis of Carbon Dots and Their Applications. *J. Mater. Chem. C* **2019**, *7* (24), 7175–7195.
(159) Sun, Y.-P. *Carbon Dots*; Springer Nature Switzerland AG: Cham, Switzerland, 2020.
(160) Reckmeier, C. J.; Schneider, J.; Susha, A. S.; Rogach, A. L. Luminescent Colloidal Carbon Dots : Optical Properties and Effects of Doping. *Opt. Express* **2016**, *24* (2), 312–340.
(161) Hu, C.; Li, M.; Qiu, J.; Sun, Y. P. Design and Fabrication of Carbon Dots for Energy Conversion and Storage. *Chem. Soc. Rev.* **2019**, *48* (8), 2315–2337.
(162) Goto, T.; Okazaki, Y.; Ueki, M.; Kuwahara, Y.; Takafuji, M.; Oda, R.; Ihara, H. Induction of Strong and Tunable Circularly Polarized Luminescence of Nonchiral, Nonmetal, Low-Molecular-Weight Fluorophores Using Chiral Nanotemplates. *Angew. Chem. Int. Ed.* **2017**, *56* (11), 2989–2993.
(163) Li, A.; Zheng, D.; Zhang, M.; Wu, B.; Zhu, L. Chirality Transfer in Carbon Dot-Composited Sol-Gel Systems for Excitation-Dependent Circularly Polarized Luminescence. *Langmuir* **2020**, *36* (30), 8965–8970.
(164) Chekini, M.; Prince, E.; Zhao, L.; Mundoor, H.; Smalyukh, I. I.; Kumacheva, E. Chiral Carbon Dots Synthesized on Cellulose Nanocrystals. *Adv. Opt. Mater.*

2020, *8* (4), 1901911.
(165) Ru, Y.; Sui, L.; Song, H.; Liu, X.; Tang, Z.; Zang, S.-Q.; Yang, B.; Lu, S. Rational Design of Multicolor-Emitting Chiral Carbonized Polymer Dots for Full-Color and White Circularly Polarized Luminescence. *Angew. Chem. Int. Ed.* **2021**, *60* (25), 14091–14099.
(166) Zou, C.; Qu, D.; Jiang, H.; Lu, D.; Ma, X.; Zhao, Z.; Xu, Y. Bacterial Cellulose: A Versatile Chiral Host for Circularly Polarized Luminescence. *Molecules* **2019**, *24* (6), 1008.
(167) Xu, M.; Wu, X.; Yang, Y.; Ma, C.; Li, W.; Yu, H.; Chen, Z.; Li, J.; Zhang, K.; Liu, S. Designing Hybrid Chiral Photonic Films with Circularly Polarized Room-Temperature Phosphorescence. *ACS Nano* **2020**, *14* (9), 11130–11139.
(168) Rosini, C.; Franzini, L.; Raffaelli, A.; Salvadori, P. Synthesis and Applications of Binaphthylic C2-Symmetry Derivatives as Chiral Auxiliaries in Enantioselective Reactions. *Synthesis* **1992**, *6*, 503–517.
(169) Bringmann, G.; Mortimer, A. J. P.; Keller, P. A.; Gresser, M. J.; Garner, J.; Breuning, M. Atroposelective Synthesis of Axially Chiral Biaryl Compounds. *Angew. Chem. Int. Ed.* **2005**, *44* (34), 5384–5427.
(170) Kumarasamy, E.; Raghunathan, R.; Sibi, M. P.; Sivaguru, J. Nonbiaryl and Heterobiaryl Atropisomers: Molecular Templates with Promise for Atropselective Chemical Transformations. *Chem. Rev.* **2015**, *115* (20), 11239–11300.
(171) Liu, Z.; Jiang, Z.; He, C.; Chen, Y.; Guo, Z. Circularly Polarized Luminescence from Axially Chiral Binaphthalene-Bridged BODIPY. *Dyes and Pigments* **2020**, *181* (June), 108593.
(172) Tanaka, H.; Inoue, Y.; Mori, T. Circularly Polarized Luminescence and Circular Dichroisms in Small Organic Molecules: Correlation between Excitation and Emission Dissymmetry Factors. *ChemPhotoChem* **2018**, *2* (5), 386–402.
(173) Ludmerczki, R.; Mura, S.; Carbonaro, C. M.; Mandity, I. M.; Carraro, M.; Senes, N.; Garroni, S.; Granozzi, G.; Calvillo, L.; Marras, S.; Malfatti, L.; Innocenzi, P. Carbon Dots from Citric Acid and Its Intermediates Formed by Thermal Decomposition. *Chem. Eur. J.* **2019**, *25* (51), 11963–11974.
(174) Shockravi, A.; Javadi, A.; Abouzari-Lotf, E. Binaphthyl-Based Macromolecules: A Review. *RSC Adv.* **2013**, *3* (19), 6717–6746.
(175) Patel, D. C.; Woods, R. M.; Breitbach, Z. S.; Berthod, A.; Armstrong, D. W. Tetrahedron : Asymmetry Thermal Racemization of Biaryl Atropisomers. *Tetrahedron: Asymmetry* **2017**, *28* (11), 1557–1561.
(176) Ng, H. M.; Saidi, N. M.; Omar, F. S.; Ramesh, K.; Ramesh, S.; Bashir, S. Thermogravimetric Analysis of Polymers. In *Encyclopedia of Polymer Science and Technology*; John Wiley & Sons, Inc., 2018; pp 1–29.
(177) Ratkovic, S.; Peica, N.; Thomsen, C.; Bukur, D. B.; Boskovic, G. Thermal Stability Evolution of Carbon Nanotubes Caused by Liquid Oxidation. *J. Therm. Anal. Calorim.* **2014**, *115* (2), 1477–1486.
(178) Stejskal, J.; Bober, P.; Trchová, M.; Horský, J.; Pilař, J.; Walterová, Z. The Oxidation of Aniline with P-Benzoquinone and Its Impact on the Preparation of the Conducting Polymer, Polyaniline. *Synth. Met.* **2014**, *192*, 66–73.
(179) Essner, J. B.; Kist, J. A.; Polo-Parada, L.; Baker, G. A. Artifacts and Errors Associated with the Ubiquitous Presence of Fluorescent Impurities in Carbon Nanodots. *Chem. Mater.* **2018**, *30* (6), 1878–1887.

(180) Victoria, F.; Manioudakis, J.; Zaroubi, L.; Findlay, B.; Naccache, R. Tuning Residual Chirality in Carbon Dots with Anti-Microbial Properties. *RSC Adv.* **2020**, *10* (53), 32202–32210.
(181) Zhang, Z.; Wang, W.; Liu, S.; Chen, D. Experimental and Density Functional Theory Calculation Studies on Raman and Infrared Spectra of 1,1′-Binaphthyl-2,2′-Diamine. *Chinese J. Chem. Phys.* **2017**, *30* (1), 7–15.
(182) T. Kinuta, N. Tajima, M. Fujiki, M. Miyazawa, Y. I. Control of Circularly Polarized Photoluminescent Property via Dihedral Angle of Binaphthyl Derivatives. *Tetrahedron* **2012**, *68*, 4791–4796.
(183) Reichardt, C. Solvatochromic Dyes as Solvent Polarity Indicators. *Chem. Rev.* **1994**, *94*, 2319–2358.
(184) Naito, M.; Iwahori, K.; Miura, A.; Yamane, M.; Yamashita, I. Circularly Polarized Luminescent CdS Quantum Dots Prepared in a Protein Nanocage. *Angew. Chem. Int. Ed.* **2010**, *49* (39), 7006–7009.
(185) Tohgha, U.; Deol, K. K.; Porter, A. G.; Bartko, S. G.; Choi, J. K.; Leonard, B. M.; Varga, K.; Kubelka, J.; Muller, G.; Balaz, M. Ligand Induced Circular Dichroism and Circularly Polarized Luminescence in CdSe Quantum Dots. *ACS Nano* **2013**, *7* (12), 11094–11102.
(186) Shi, Y.; Duan, P.; Huo, S.; Li, Y.; Liu, M. Endowing Perovskite Nanocrystals with Circularly Polarized Luminescence. *Adv. Mater.* **2018**, *30*, 1705011.
(187) Sang, Y.; Han, J.; Zhao, T.; Duan, P.; Liu, M. Circularly Polarized Luminescence in Nanoassemblies: Generation, Amplification, and Application. *Adv. Mater.* **2019**, *32* (41), 1900110.
(188) Zhang, M.; Li, K.; Zang, S. Progress in Atomically Precise Coinage Metal Clusters with Aggregation-Induced Emission and Circularly Polarized Luminescence. *Adv. Opt. Mater.* **2020**, *8*, 1902152.
(189) Zinna, F.; Bruhn, T.; Guido, C. A.; Ahrens, J.; Bröring, M.; Di Bari, L.; Pescitelli, G. Circularly Polarized Luminescence from Axially Chiral BODIPY DYEmers: An Experimental and Computational Study. *Chem. Eur. J.* **2016**, *22*, 16089-16098.
(190) Pezzato, C.; Cheng, C.; Stoddart, J. F.; Astumian, R. D. Mastering the Non-Equilibrium Assembly and Operation of Molecular Machines. *Chem. Soc. Rev.* **2017**, *46* (18), 5491–5507.
(191) Liang, Z.; Vanesa, M.; A., L. D. Molecular Machines with Bio-Inspired Mechanisms. *Proc. Natl. Acad. Sci.* **2018**, *115* (38), 9397–9404.
(192) Chatterjee, M. N.; Kay, E. R.; Leigh, D. A. Beyond Switches: Ratcheting a Particle Energetically Uphill with a Compartmentalized Molecular Machine. *J. Am. Chem. Soc.* **2006**, *128* (12), 4058–4073.
(193) Astumian, R. D.; Bier, M. Mechanochemical Coupling of the Motion of Molecular Motors to ATP Hydrolysis. *Biophys. Chem.* **1996**, *70*, 637–653.
(194) Amano, S.; Fielden, S. D. P.; Leigh, D. A. A Catalysis-Driven Artificial Molecular Pump. *Nature* **2021**, *594* (7864), 529–534.
(195) Amano, S.; Borsley, S.; Leigh, D. A.; Sun, Z. Chemical Engines: Driving Systems Away from Equilibrium through Catalyst Reaction Cycles. *Nat. Nanotechnol.* **2021**, *16* (10), 1057–1067.
(196) Cesario, M.; Guilhem, J.; Pascard, C.; Dietrich, C. O.; Edel, A.; Sauvage, J. P.; Kintzinger, J. P. Topological Enhancement of Basicity: Molecular Structure and Solution Study of a Monoprotonated Catenand. *J. Am. Chem. Soc.* **1986**, *108*

(20), 6250–6254.
(197) Kihara, N.; Tachibana, Y.; Kawasaki, H.; Takata, T. Unusually Lowered Acidity of Ammonium Group Surrounded by Crown Ether in a Rotaxane System and Its Acylative Neutralization. *Chem. Lett.* **2000**, No. 5, 506–507.
(198) Ragazzon, G.; Schäfer, C.; Franchi, P.; Silvi, S.; Colasson, B.; Lucarini, M.; Credi, A. Remote Electrochemical Modulation of PKa in a Rotaxane by Co-Conformational Allostery. *Proc. Nat. Acad. Sci. U. S. A.* **2018**, *115* (38), 9385–9390.
(199) Fialkowski, M.; Bishop, K. J. M.; Klajn, R.; Smoukov, S. K.; Campbell, C. J.; Grzybowski, B. A. Principles and Implementations of Dissipative (Dynamic) Self-Assembly. *J. Phys. Chem. B* **2006**, *110* (6), 2482–2496.
(200) Van Rossum, S. A. P.; Tena-Solsona, M.; Van Esch, J. H.; Eelkema, R.; Boekhoven, J. Dissipative Out-of-Equilibrium Assembly of Man-Made Supramolecular Materials. *Chem. Soc. Rev.* **2017**, *46* (18), 5519–5535.
(201) Rieß, B.; Grötsch, R. K.; Boekhoven, J. The Design of Dissipative Molecular Assemblies Driven by Chemical Reaction Cycles. *Chem* **2020**, *6*, 1–27.
(202) Singh, N.; Formon, G. J. M.; De Piccoli, S.; Hermans, T. M. Devising Synthetic Reaction Cycles for Dissipative Nonequilibrium Self-Assembly. *Adv. Mater.* **2020**, *32* (20), 1906834.
(203) De, S.; Klajn, R. Dissipative Self-Assembly Driven by the Consumption of Chemical Fuels. *Adv. Mater.* **2018**, *30* (41), 1–6.
(204) Penocchio, E.; Rao, R.; Esposito, M. Thermodynamic Efficiency in Dissipative Chemistry. *Nat. Commun.* **2019**, *10* (1), 3865.
(205) Biagini, C.; Di Stefano, S. Abiotic Chemical Fuels for the Operation of Molecular Machines. *Angew. Chem. Int. Ed.* **2020**, *59* (22), 8344–8354.
(206) Mariottini, D.; Del Giudice, D.; Ercolani, G.; Di Stefano, S.; Ricci, F. Dissipative Operation of PH-Responsive DNA-Based Nanodevices. *Chem. Sci.* **2021**, *12* (35), 11735–11739.
(207) Raymo, F. M.; Houk, K. N.; Stoddart, J. F. The Mechanism of the Slippage Approach to Rotaxanes. Origin of the "all-or-Nothing" Substituent Effect. *J. Am. Chem. Soc.* **1998**, *120* (36), 9318–9322.
(208) Groppi, J.; Casimiro, L.; Canton, M.; Corra, S.; Jafari-Nasab, M.; Tabacchi, G.; Cavallo, L.; Baroncini, M.; Silvi, S.; Fois, E.; Credi, A. Precision Molecular Threading/Dethreading. *Angew. Chem. Int. Ed.* **2020**, *59* (35), 14825–14834.
(209) Ashton, P. R.; Campbell, P. J.; Glink, P. T.; Philp, D.; Spencer, N.; Stoddart, J. F.; Chrystal, E. J. T.; Menzer, S.; Williams, D. J.; Tasker, P. A. Dialkylammonium Ion/Crown Ether Complexes: The Forerunners of a New Family of Interlocked Molecules. *Angew. Chem. Int. Ed.* **1995**, *34* (17), 1865–1869.
(210) Gasa, T. B.; Valente, C.; Stoddart, J. F. Solution-Phase Counterion Effects in Supramolecular and Mechanostereochemical Systems. *Chem. Soc. Rev.* **2011**, *40* (1), 57.
(211) Coutrot, F. A Focus on Triazolium as a Multipurpose Molecular Station for PH-Sensitive Interlocked Crown-Ether-Based Molecular Machines. *ChemistryOpen* **2015**, *4* (5), 556–576.
(212) Belot, V.; Farran, D.; Jean, M.; Albalat, M.; Vanthuyne, N.; Roussel, C. Steric Scale of Common Substituents from Rotational Barriers of N-(o-Substituted Aryl)Thiazoline-2-Thione Atropisomers. *J. Org. Chem.* **2017**, *82* (19), 10188–

10200.
(213) Ashton, P. R.; Baxter, I.; Fyfe, M. C. T.; Raymo, F. M.; Spencer, N.; Stoddart, J. F.; White, A. J. P.; Williams, D. J. Rotaxane or Pseudorotaxane? That Is the Question! *J. Am. Chem. Soc.* **1998**, *120* (10), 2297–2307.
(214) Papadakis, R.; Deligkiozi, I. Solvent Effects in Supramolecular Systems. In *Solvents, Ionic Liquids and Solvent Effects*; Glossman-Mitnik, D., Maciejewska, M., Eds.; IntechOpen: Rijeka, 2019.
(215) Panman, M. R.; Bakker, B. H.; den Uyl, D.; Kay, E. R.; Leigh, D. A.; Buma, W. J.; Brouwer, A. M.; Geenevasen, J. A. J.; Woutersen, S. Water Lubricates Hydrogen-Bonded Molecular Machines. *Nat. Chem.* **2013**, *5* (11), 929–934.
(216) Douarre, M.; Martí-Centelles, V.; Rossy, C.; Pianet, I.; McClenaghan, N. D. Regulation of Macrocycle Shuttling Rates in [2]Rotaxanes by Amino-Acid Speed Bumps in Organic–Aqueous Solvent Mixtures. *Eur. J. Org. Chem.* **2020**, *2020* (36), 5820–5827.
(217) Liu, P.; Chipot, C.; Shao, X.; Cai, W. Solvent-Controlled Shuttling in a Molecular Switch. *J. Phys. Chem. C* **2012**, *116* (7), 4471–4476.
(218) Adrian, J. C.; Wilcox, C. S. Chemistry of Synthetic Receptors and Functional Group Arrays. 15. The Effects of Added Water on Thermodynamic Aspects of Hydrogen Bond Based Molecular Recognition in Chloroform. *J. Am. Chem. Soc.* **1991**, *113* (2), 678–680.
(219) Connors, K. A. *Binding Constants: The Measurement of Molecular Complex Stability*; Wiley-Interscience: New York, NY, 1987.
(220) Coutrot, F.; Busseron, E. A New Glycorotaxane Molecular Machine Based on an Anilinium and a Triazolium Station. *Chem. Eur. J.* **2008**, *14* (16), 4784–4787.
(221) Ragazzon, G.; Credi, A.; Colasson, B. Thermodynamic Insights on a Bistable Acid–Base Switchable Molecular Shuttle with Strongly Shifted Co-Conformational Equilibria. *Chem. Eur. J.* **2017**, *23* (9), 2149–2156.
(222) Corra, S.; De Vet, C.; Groppi, J.; La Rosa, M.; Silvi, S.; Baroncini, M.; Credi, A. Chemical On/Off Switching of Mechanically Planar Chirality and Chiral Anion Recognition in a [2]Rotaxane Molecular Shuttle. *J. Am. Chem. Soc.* **2019**, *141* (23), 9129–9133.

Ringraziamenti

Questa tesi è la conclusione di un capitolo lungo quasi quattro anni, che è stato reso possibile grazie alla presenza, al supporto e all'aiuto di molte persone. Spero che poche parole bastino per poter esprimere la mia profonda gratitudine.

La prima persona che ringrazio è il Prof. Maurizio Prato per avermi dato l'enorme opportunità di poter fare ricerca nel suo gruppo. Grazie per la stima che ha avuto nei miei confronti, per avermi spronato quando non vedevo vie d'uscita e per avermi insegnato "che non si possono fare cose facili, perché le cose facili le hanno già fatte gli altri. Rimangono le cose difficili, che alcune volte vengono e altre no. Però non bisogna mai arrendersi: alla fine, in un modo o in un altro, riusciamo sempre a vincere".

Una menzione a parte va al Dr. Ragazzon. Giulio, sono stato fortunato ad incontrarti. Se non ci fossi stato durante questo percorso, non starei scrivendo questi ringraziamenti. Grazie per avermi sopportato e per avermi dato prospettive diverse con cui poter guardare le cose. Sei un'ispirazione per chiunque desideri fare questo mestiere. Presente, organizzato, *consistent*, ma soprattutto una persona buona. Sono orgoglioso di aver lavorato con te. Spero di poter restituire il favore.

Al Prof. Gianluca Farinola, che ha visto in me qualcosa che io ancora non vedevo. Non sarei qui, senza il suo supporto.

Grazie a tutto il gruppo di ricerca del Prof. Prato per aver condiviso le gioie e i tanti dolori del lab. Tutti, dai ricercatori ai tesisti, mi avete insegnato a maturare sia scientificamente che personalmente. Senza fare torti a nessuno, ringrazio in particolare Beatrice, Cristian e Marina G. per aver condiviso tempo, conoscenze e focacce.

Grazie a Ottavia, a Cristina e a Eva per la gentilezza con cui mi hanno accolto.

Grazie a Mario e Marcello per essere dei buoni amici.

Grazie ad Anna per avermi dato la possibilità di vivere Trieste.

Grazie a Ticco, Emanuele, Mario e Matteo. E un abbraccio soprattutto a Riccardo. Siete arte-maestria-sapienza-sacrificio-professionalità.

Grazie a Laura, Luisa, Vito, Pierpaolo e Giovanni. Nonostante le poche volte in cui si siamo visti in questi anni, la vostra vicinanza è stata enorme.

Grazie a tutta la mia numerosa famiglia, a mia nonna Maria, a Graziana, a mamma e a papà. Siete le mie colonne.